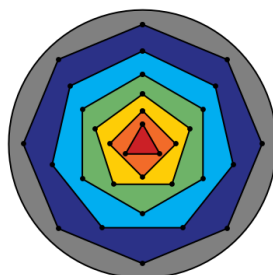


Simulating Self-Assembly of Organic Molecules & Classifying Intermolecular Dispersion

BY: MATT BUMSTEAD, *B.Sc. Astrophysics*



A Thesis
Submitted to the School of Graduate Studies
In Partial Fulfillment of the Requirements
for the Degree Doctor of Philosophy

Address and Information:
McMaster UNIVERSITY
Hamilton, Ontario, Canada
email: bumstema@mcmaster.ca

Committee Members:
Dr. Ayse TURAK
Dr. Alejandro DIAZ ORTIZ
Dr. Erik SORENSEN

DOCTOR OF PHILOSOPHY (2017)
Engineering Physics

McMaster University
Hamilton, Ontario

TITLE: Simulating Self-Assembly of Organic Molecules &
Classifying Intermolecular Dispersion

AUTHOR: Matt Bumstead, B.Sc. Astrophysics (University of Calgary)

SUPERVISOR: Dr. Ayse Z. Turak

NUMBER OF PAGES: 129

Preface

The work in this thesis has been previously published in the form of peer-reviewed journal entries. Manuscripts are prefaced with the main motivation and conclusions while followed by extra information in the form of expanded explanations and subtleties not expressed in the paper.

Paper 1: “disLocate: tools to rapidly quantify local intermolecular structure to assess order in self-assembled systems”, *Matt Bumstead, Kunyu Liang, Gregory Hanta, Lok Shu Hui, Ayse Turak*, In Review (2017)

Paper 2: “Reproducing morphologies of disorderly self-assembling planar molecules with static and dynamic simulation methods by matching density”, *M. Bumstead, B. Arnold, A. Turak*, *Physica A: Statistical Mechanics and its Applications*, Vol 471, (2017)

Paper 3: “Steric self-assembly of laterally confined organic semiconductor molecule analogues”, *A.D. Ortiz, B. Arnold, M. Bumstead, A. Turak*, *Physical Chemistry Chemical Physics*, (2014)

Paper 4: “Similar morphology but different molecule shape: self-assembly simulations with varying steric potentials”, *M. Bumstead, A. Turak*, In Preparation for Special Issue Publication: “Advances in Computational Methods for Soft Matter Systems”, *European Physical Journal E (EPJ E)* with Submission Before: 15th December 2017

Abstract

Mechanisms for charge transport in organic electronics allows them to perform with disordered internal morphology, something which is not possible for traditional crystalline semiconductors. Improvements to performance can occur when the materials change their relative positions to each other, resulting as a different spatial dispersion with lower electrical loss over the device area.

A numerical method has been developed using interaction models for molecules from colloidal self-assembly. Colloids are rigid particles with a volume which is embodied by their shape and their collective behaviour depends on its density. The self-assembly mechanism used is condensation, which increases the density by removing the spaces between molecules while they lose thermal energy due to the increasing steric interactions with neighbours. The molecular chemical structure determines the spatial probability of electron orbitals that (for a given energy) outlines their geometric shape. Because these shapes are localized onto the molecule, their intermolecular positions determine how close these orbitals can be to each other which is important for electron charge transport.

During operation, the organic active layer may have thermal energy to cause molecular reorganization before cooling, which increases the probability to find disordered states within the device. A comprehensive suite of tools has been developed which can classify disorder in the physical characteristics of morphology; such as density, internal spacing, and angular orientation symmetry. These tools were used to optimize the experimental preparations for depositing nanoparticle dispersions on surfaces within organic electronic devices. These have also been used to quantify the statistical variations in structure between configurations produced from our Monte Carlo method and a similar molecular dynamics approach. Simulated self-assembly within highly confined areas showed repeatedly sampled microstates, suggesting that at thermodynamic equilibrium confined particles have quantized density states. We conclude with morphologies resulting from non-circular shapes and systems of donor-acceptor type molecules.

Acknowledgements

I would like to thank all of those who have helped and directed this project to its completion. It is my honour to present the results of this project as novel research.

I would like thank Dr. Ayse Turak for giving me the opportunity to pursue my dreams and career. As one of her first students at McMaster, I've been part of many projects over the years. Involvement in these has really inspired me to develop a wide understanding of all aspects of modern computational and laboratory research. For this, I am grateful.

Thank you to the committee members: Dr. Ayse Turak, Dr. Alejandro Diaz Ortiz, and Dr. Erik Sorensen for proving their valuable input and time. Presenting the progress of this thesis over the years has been a pleasure. Comments from these members have helped me refine my understanding of peer review and expectations for researchers. Additional thanks goes to the external reviewer for my defence, Dr. Jolanta Lagowski, who raised very welcoming and intelligent questions.

An additional mention is needed for Dr. Alejandro Diaz Ortiz. The extra meetings on new ideas and scientific discussions was a key factor in the success of this project. Many of the results presented in this manuscript were the direct product of his hard work and dedication to solving questions. His unique perspective on my project has allowed my own creativity to grow into something novel. Thank you for this help.

I would like to thank all my collaborators and coauthors for sharing their expertise of experimental techniques and their ability to produce high quality data. Notable graduate student group members include: Lok Shu Hui, Kunyu Liang, Gregory Hanta, Erinn van Wynsberghe, Hyeonghwa Yu, and Hrishu Das Gupta. Thank you for all the extra time you spent listening to practise presentations and asking questions that really pushed my understanding. A special thank you to Bjorn Arnold for providing the basic roots of the project, with building the first iteration of the simulation code used in this thesis. Finally, thanks go to the undergraduate summer researchers Lindsay Vasilak, Eve Yi, Kaijie Zhang, and Mike Zamboni who shared their enthusiasm for creative explorations with us. Thanks to my friends Mary Jane, Tina, Molly, and Lucy for their late night motivational support. Thank you to SCARCNET at Compute Canada for allowing us computational time on their cluster.

Contents

Preface	i
Abstract	ii
1 Introduction	1
1.1 Organic Electronic Devices and Intermolecular Dispersion	1
1.2 Brief Outline of Thesis	2
2 Literature and Motivations	3
2.1 Quantifying Interfacial Morphology	3
2.2 Entropy Driven Condensation of Particulates	4
2.3 The shape of an excluded-volume region	6
2.4 Polydisperse Distributions of Molecules	9
3 Method used to Simulate Organic Molecules	12
3.1 Monte Carlo Condensation	12
3.2 Entropy Driven Microstates	13
3.3 Modelling Molecules with Polygons	14
3.4 Resolution of Polygons: Circular Approximation	14
4 Quantifying disorder in planar systems	16
4.1 My Contributions	17
4.2 Overview of Manuscript (in Submission - 2017)	17
4.3 The importance of visualization: mapping physics onto molecules using colour schemes	18
4.4 Expectation values for global planar structure metrics	20
4.4.1 Pair Correlation Function - $g(r)$	20
4.4.2 Voronoi tessellations and local area variation	21
4.4.3 Bond order parameter - q_ℓ	22
4.5 The Relation Between Edge Effects and Neighbours	23
4.6 Publication: “disLocate: tools to rapidly quantify local intermolecular structure to asses order in self-assembled systems” (Submitted - 2017)	25
5 Comparing morphology between ensembles of many configurations with similar density	43
5.1 My Contributions	44
5.2 Overview of Manuscript (Physica A - 2017)	45
5.3 Event-Driven Molecular Dynamics simulations	46
5.3.1 Finding Protocols that Produce Similar Area Fraction Probability Distributions	46
5.3.2 Changes in Area Fraction from varying EDMD initial conditions	46
5.3.3 Discussion of Performance and Parallel Execution	47
5.4 Matched Protocols	48
5.5 Monovacancies and the Bond Order Parameter	49

5.6	Publication: “Reproducing morphologies of disorderly self-assembling planar molecules with static and dynamic simulation methods by matching density” (Physica A - 2017)	51
6	Directing Self-Assembly with Confinement	66
6.1	My Contributions	67
6.2	Overview of Manuscript (PCCP - 2014)	67
6.3	Pattern Matching Microstates into Parcels	68
6.4	Confined Molecules of Varying Shape	70
6.5	Publication: “Steric self-assembly of laterally confined organic semiconductor molecule analogues” (PCCP - 2014)	71
7	Morphologies of Molecules with Anisotropic Steric Interactions	80
7.1	My Contributions	81
7.2	Overview of Manuscript (For Submission - 2017)	81
7.3	Morphology of Circular Molecules with Low Resolution	82
7.4	Publication: “Similar morphology but different molecule shape: self-assembly simulations with varying steric potentials” (For Submission - 2017)	85
8	Simulating Morphologies with Multiple Molecular Species	95
8.1	Morphological Variation in Organic Electronic Devices	96
8.2	Expansions to the Monte Carlo Simulation Method	96
8.2.1	Types of Systems that can be Simulated	97
8.2.2	Overview of the Main Algorithm	99
8.3	Molecular Confinement and Boundary Conditions	102
8.3.1	Hard Boundary Condition - (hard)	102
8.3.2	Homeotropic Boundary Condition - (soft)	103
8.3.3	Periodic Boundary Condition	104
8.3.4	Benchmarking CPU Times for Confined Monodisperse Systems	105
8.4	Molecular Monte Carlo Interactions	107
9	Summary and Outlook	109
9.1	Concluding Remarks	109
9.2	Expanding Upon this Research	110
9.2.1	Image Charge Boundary and Circular Confinement	110
9.2.2	Voronoi Coordination Shells and the Pair Correlation	110

List of Figures

2.1	Cross section of an organic photovoltaic device. (a) Nanoparticles are introduced to modify the interfacial work function. (b) Organic active layer consisting of donor/acceptor materials. Adapted with permission from [18]. Copyright (2007) John Wiley and Sons.	3
2.2	Self-assembled morphologies land somewhere between highly ordered systems (i) and one with very low density (ii). Two key factors at classifying disorder are simultaneously in competition with each other: limitations on perception misguides us into seeing patterns in randomness while our imprecise ability to distinguish between similar patterns misses subtle differences. To remove unwanted bias, numerical order metrics are utilized to characterize the morphology located at particle positions: pair correlation function (a & d), Voronoi tessellations (b & e), and the bond order parameter (c & f).	4
2.3	Self-assembly can be directed by imposing boundaries onto the system. By reducing the area, the particles arrange into discrete patterns which limits the variation of expected particle positions.	5
2.4	Maximally dense packing of a) pentagons b) “fat crosses” c) convex curved triangles d) concave curved triangles e) “moonlike shape”. The darker colour set of shapes indicates the unit cell. Adapted with permission from Ref. [53]. Copyrighted by the American Physical Society.	7
2.5	a) Circular approximation to molecular shape with simulated morphology. b) Complex polygon approximation of the star-shaped chemical structure. c) STM image of star-shaped organic molecule oligo(p-phenylenevinylene)-substituted hexaarylbenzene on 1-phenyloctane-HOPG. Reproduced with permission from [64]. Copyright 2007 American Chemical Society.	8
2.6	Schematic outlining the influence that a change the morphology from a) linearly ordered pattern to b) a “checker-board” pattern could have on charge extraction. Excitons (spark-shape) are formed when photons are absorbed and disassociate to produce electron-hole charge carriers that move through the pathway as indicated by the arrows. a) Molecules may form long pathways for charges to move easily between or b) cause excess intermolecular orbital hopping which increases likelihood of recombination. Insets are STM images adapted from [15].	9
3.1	Monte Carlo simulation method to generate condensed dispersions of planar organic molecules. (A) The initial state A has density ϕ_A . (i) Density is increased by inflating particles. (ii) Monte Carlo displacement of particle. (iii) Trial move results in overlap so it is rejected and another move is selected. (iv) Other particles find accepted positions. Translational, rotational, or a mixture of both operations can occur. (B) The result is the condensed microstate B with a higher density ϕ_B	12
3.2	Regular polygons approximating a mathematical circle. In each case, the number of sides (n) is displayed within the polygon while the name, the normalized (to the circle) area, and the rolling resistance, respectively, are listed below. In all counts, heptagons and even tetracontagons, are indistinguishable from analytic (mathematical) circles.	15

3.3	The effect of normalizing the shape to have its farthest point be at a distance of 1 for closed and open definitions of polygons. (a) Circular polygon with 100 sides and (b) Rodonea curve with 36 points.	15
4.1	Mapping colour onto particle positions to indicate local order. a) Standard rendering of monochromatic molecules gives no additional information. However, variations of local Voronoi tessellations can quantify (b) the bond order parameter relative to the hexagonal lattice, (c) number of neighbours as defined by number of Voronoi facets, (d) the angle each molecule is orientated at relative to the x-axis, and (e) the area deviation from an expected hexagonal lattice with the same number density.	18
4.2	(a) Expected radial distribution functions from a hexagonal lattice, a square lattice, and a hexatic lattice. Insets show particle configurations as well as the radial width associated with the neighbour shells. (b) Fourier transforms of the particle positions that produced the associated pair correlation functions.	20
4.3	Effect of random displacements away from lattice positions. (a) Pair correlation function for the hexagonal and hexatic lattice. Inset shows the relative displacement needed to broaden the $g(r)$ peaks. (b) A series of hexatic lattices with increasing mean square displacement. Lines directly connect the $g(r)$ to the (c) Voronoi tessellations of the displaced hexatic lattice. Tiles are colour coded (left to right): area deviation from an expected hexagonal lattice with the same number density, coordination number of neighbours as defined by number of Voronoi facets, and the bond order parameter relative to the hexagonal lattice.	22
4.4	Edge definitions of virtual particles effect the statistics of disorder metrics (a) coordination number, (b) bond order q_6 , and (c) Voronoi area deviation	24
5.1	Optimizing folders for large data sets to search parameter space. (a) Varying two parameters X and Y by $\pm\Delta$ creates a grid. (b) Data is more accessible when it is stored within a hierarchical subfolder system of protocols.	45
5.2	Effect on the PDF for area fractions using non-optimized parameters with 36 particles. (a) Effect of pressure with constants: events=120 and growth=0.01. (b) Effect of events with constants: pressure=400 and growth=0.01. (c) Effect of growth with constants: pressure=1000 and events=80.	47
5.3	Probability density distributions (PDF) of the area fractions (ϕ) of circular molecules contained within square boundaries. Above are the root mean square residual spectra which were used to determine the relative closeness in probability. The numbers of molecules are: a) 16, b) 25, c) 36, d) 49, e) 64, and f) 81.	48
5.4	A configuration from event-driven molecular dynamics that contains point defects. (Left) Rendering of the configuration using the bond order colouring scheme, with darker colouring representing a lower value for local hexagonal packing: q_6^i/q_6^{hex} . (Right) Voronoi tessellations of the same configuration with a colour scheme that describes the area fluctuation as a percent deviation from the expected hexagonal lattice of the same density. Monovacancies are highlighted in red circles on both configurations.	49
5.5	Voronoi tiles of (a) perfect hexagonal lattice, (b) monovacancy at lattice site 1, (c) two monovacancies at lattice site 1 and 2. Blue lines indicates the boundaries of the Voronoi tiles corresponding to each particle. The red lines are the associated Delaunay triangulations that define nearest neighbours for the bond order parameter. Insets visually define the particle positions and where point defects are.	50

6.1	Reducing an ensemble of configurations into parcels of patterns. (a) Global effect of confinement can be seen in the point cloud where all centroids of all molecules of all configurations are combined and plotted together. (b) Individual configurations which were successfully classified as similar by pattern matching are grouped together into a parcel. These configurations can still be jumbled (i.e. pre-symmetry operations). (c) Configurations in the parcel are rotated and mirrored relative to each other so their positions have the lowest amount of deviation. Finally, the characteristic parcel pattern emerges at the end, showing the spatial distributions molecules are directed into by confinement effects.	68
6.2	Enumeration of microstates with non-zero parcel sizes for N=25 circular molecules confined within a box. The pattern with the most parcel members is in the top left - the square packed configuration. Parcels decreasing in size are shown left to right, where the bottom right has the fewest members. The registry map to the left of the configuration shows the planar probability of centroids for that parcel as coloured histograms.	70
6.3	The influence of confinement on 49 complexly shaped molecules confined within a square box. Polygons include: (a) Circle, (b) Reuleaux, (c) Epicycloid, (d) Alhambra, (e) Hypocycloid, (f) Rodonea. The most common pattern found within the ensemble is shown on top. Point clouds of superimposed molecular centroids from 4032 configurations are plotted below.	71
7.1	Planar configurations of polygonal shaped molecules as viewed using STM. Above each image is the chemical structure associated with that molecule as well as its geometric approximation. Chemical names: a) star-shaped 2,4,6-tris(4,4,4-trimethylphenyl)-1,3,5-triazine [113] b) Copper phthalocyanine [114] c) pentachloro-corannulene derivative [115] d) Coronene [116] e) C60 fullerene [117].	82
7.2	Statistics of bulk systems of molecules (N=1024) defined by simple steric potentials. (a-f) Simulated configurations of "almost circular" molecules in bulk phase. Colour overlaid as the local bond order q_6 . (e) Probable distribution of area fractions for ensembles with 4032 patterns. (f) Pair correlation functions with intermolecular distances being normalized by the length of the largest distance from the molecular centroid to vertex of the regular polygon.	83
8.1	Example output configuration from simulating CuPc + DIP molecules (N=100 each) inside a hexagonal container with homeotropic boundary walls. (a) Rendered configuration with CuPc in orange and DIP in blue. (b) Charge percolation paths for each molecular species is plotted on top of the configuration. Black indicates the donor path while green is the acceptor. (c) Objects are removed for clarity, showing the regions of charge favourability and donor/acceptor interfaces. Thicker percolation paths indicate higher steric overlap - leading to a higher probability for charges to transfer between those molecules.	97
8.2	Flow chart of the "Morphologies" simulation procedure.	99
8.3	Comparing Monte Carlo simulations under confined boundaries. (a) Area fraction distributions of confined circular particles. (b) Point clouds associated each distribution. Ensembles contain 4032 configurations.	103
8.4	Comparing Monte Carlo simulations under homeotropic boundaries. (a) Area fraction distributions for 25, 36, and 49 circular particles. (b) Example of the most probable configuration from "Morphologies". Area fractions are calculated using only the portions of molecules contained within the square box, denoted as blue sections. (c) Point clouds from "Morphologies". Ensembles contain 4032 configurations.	104
8.5	Comparison between Monte Carlo simulations of 1024 circular molecules within periodic boundaries. (a) Density profile of the covering area. (b) Pair correlation function and (c) Voronoi tessellations with bond order colouring for the most probable configuration	105

8.6	Periodic boundaries that are available in “Morphologies”. (a) Square and (b) Hexagonal periodic tiling. The orange particle inside the centre dark gray areas are translated by a set of basis vectors, adding and placing virtual particles that influence the rejection criteria for the Monte Carlo displacement. Note that only the green virtual particles influence the molecules inside the container, with the opaque gray particles being translated too far outside the system to interact sterically and thus can be ignored.	106
8.7	Example of how the probability distribution of possible Monte Carlo trial is spatially displaced to incorporate the effect of a constant background field (along the x-axis). a) No field. b) Constant field.	107
8.8	Example configuration with a constant background field (along the x-axis) with $N=1024$ molecules (512:512). Blue particles have an opposite charge to the Orange ones, hence the segregation of molecules. Field strengths relative to the thermal agitation: (a) Zero field (b) 0.1 kT, (c) 0.2 kT	108
9.1	Examples of Voronoi tessellations and boundary corrections. (a) Configuration of 37 circular particles simulated inside a circularly confining boundary. (b) Truncated boundaries are applied as usual, with tiles extending outside the automatically detected binding box being excluded. This removes the outer particles in touch the channel walls, causing the particles under steric frustration to be neglected. (c) Periodic boundaries introduces large Voronoi tiles at the corners, causing errors in both the expected shape and expected number density. (d) Regular image charge boundaries within “disLocate” explicitly assume a rectangular confinement space. (e) The general routine for image charge boundaries is applied showing that Voronoi edges approximate the box at the boundary.	110
9.2	(a) Voronoi tessellations of a disordered packing. The central particle is surrounded by a series of “neighbour shells”. (b) The pair correlation function can be subdivided to capture the information about specific caging influences. Colours of the shells in the Voronoi diagram represent the $g(r)$ of the same colour.	111

List of Tables

4.1	Comparison of peak positions of the Radial Distribution Function for exact lattices (hexagonal and square) with normalized first neighbour distance as 1 diameter. .	21
4.2	Absolute values of Voronoi weighted bond order parameter for varying symmetry ℓ for $n = \ell$ neighbours spaced evenly at $2\pi/\ell$ angles.	23
5.1	Optimized parameters of EDMD found to match ensembles produced from Monte Carlo. For $N = 64$ and 81 particles, systems were not found to have minimized area fraction difference ($\Delta\phi_{rms}$) with repacking cycles. Note that $N = 16$ contains finite a localized states at the $n \times n$ square lattice with a discrete value for the area fraction, therefore $\Delta\phi_{rms}$ is meaningless (discontinuous PDF), and only coincidence of the area fractions at those values were considered.	49
5.2	Absolute (non-normalized) local bond order parameter (q_ℓ) with symmetry ℓ corresponding to each particle within the configuration shown in Figure 5.5. See Eqn. 4.9 for calculation details.	50
6.1	Enumeration and probability for microstates shown in the top row of Fig 6.2 (left to right $\rightarrow 1$ to 6). Data is from ensembles of 4032 randomly generated microstates of $N=25$ circular molecules in a square container.	70
6.2	Enumeration of the most probable microstate shown in Figure 6.3. Data is from ensembles of 4032 randomly generated microstates of 49 complexly shaped molecules in a square container.	71
8.1	List of major release features and their limitations over various iterations of our Monte Carlo simulation method.	98
8.2	Examining execution time and RAM usage for Monte Carlo simulations of circular molecules inside both a hard and periodic square.	105

Chapter 1

Introduction

1.1 Organic Electronic Devices and Intermolecular Dispersion

Organic electronic devices such as organic photovoltaics (OPV) and organic light emitting diode (OLED) are technologies with emerging popularity. Recent portable electronics, such as mobile phones, demand their components to be as thin and lightweight as possible. Electronic components based on organic molecules can be extremely thin and is a desired trait when used for technologies such as solar energy collection and mobile communication devices. Silicon and GaAs require the regular internal structure of a lattice to function at peak performance which poses a challenge to manufacturing microscopic components. Organics on the other hand, can still perform with a disordered internal morphology resulting from a simpler self-assembly fabrication method. Mechanisms of charge transport in organic electronics allows for this benefit, which is not possible with traditional crystalline semiconductors. An additional benefit is the reduced toxicity of organic molecules compared to other semiconducting materials such as gallium, arsenide, tellurium, and antimony, [1, 2] making organic material an attractive alternative for consumer goods with planned obsolescence.

The main drawback on these systems is that they are currently much less efficient than silicon-based devices [3, 4]. Silicon-based semiconductors still dominate the market due to the natural abundance of raw material and the highly refined manufacturing processes of crystalline silicon [5, 6]. Optimization of organic electronic devices often involves selecting new molecules and subjecting them to many expensive experiments inside highly controlled environments. This leaves the technology undesirable for companies, since these preparation techniques are too costly for large scale fabrication.

Self-assembly of components is an attractive solution because it means that molecules use their own internal properties to naturally form into useful macromolecular arrangements rather than needing to be intentionally placed into the correct positions. For OPV devices that use the interface between acceptor and donor molecules to separate charges, the way that these molecules self-assemble can have a large impact on the efficiency [7]. The device is made up of many different interfacial connections between active materials and by varying the morphology of the material, the device characteristics will change [8]. Thus, it is important to explore methods that can optimize the efficiency from tuning the organization of the composite material [9].

Bulk heterojunctions are devices that can utilize donor/acceptor molecules by mixing the two at their interface and has shown to increase device performance over non-mixed films [10, 11, 12, 13, 14, 15]. One approach that has been explored to improve the amount of donor-acceptor interfacial area by choosing candidate materials which are complementary shaped. One reported device uses the spherical geometry of fullerenes to create a ball which sits inside the socket joint shaped molecule of hexabenzocoronene [12]. The interlocking between ball and joint shapes of the molecules improves device performance by geometrically linking more donor/acceptor pairs, causing increased dissociation of excitons. Additional experiments have been performed by depositing varying amounts of donor/acceptor type molecules onto planar metallic substrates

and depending on the ratio amounts of molecule species used, their tiling patterns show different configurations [16]. This gives an indication that shape of the acceptor and donor molecules can be consciously selected to effect a wide range of possible geometric distributions. Experimental evidence also suggests that the orientation of these organic molecules may effect the charge mobility [17]. The thermodynamic binding energy changes depending on the which side of the molecule interacts with the substrate. This would be yet another indication that geometry of objects has a wide implication on organic devices.

The overall focus of this thesis is to quantify the role that shape has on morphology by isolating the steric potential and observing its influence on self-assembled molecular analogs via Monte Carlo simulation. It can simulate the condensation of polydisperse molecules which interact through a steric potential on a planar substrate which results in a static glassy state morphology. This protocol forms the basis of simulation algorithms which we used to explore the influence of molecular shape on the resulting morphology by explicitly limiting the amounts and types of interactions. The ability to distinguish between different morphologies can be done by classifying the internal arrangements of molecules with structural signatures and order metrics. This thesis describes how I have integrated various analysis methods together into comprehensive suite of tools which can classify different physical characteristics of the morphology; such as density, internal spacing, and angular orientation symmetry. This distributable package can quantify variations in morphological outcomes and inform which experimental methods lead to dispersions desired self-assembled patterns. Both the simulation and analysis package open the door to novel explorations of unique and undiscovered molecular arrangements with the capability of predicting possible morphologies of highly complex molecular geometry. Quantifying nanoparticle dispersions and optimizing molecular morphology has been at focus for researchers at the Organic Electronic Interfaces lab in the Department of Engineering Physics at McMaster University, many of which have benefited directly from the work outlined in this thesis.

1.2 Brief Outline of Thesis

This document is meant to be a combination of a traditional and sandwich thesis, and consists of four (4) published manuscripts. Each of the chapters are meant to encapsulate a central topic of scientific contribution. Chapters start with a visual abstract figure to introduce the overarching topic covered in the chapter, with any additional research not included in the publication presented before finally finishing with the manuscript. The final chapter outlines unpublished work done documenting simulations, data, benchmarking, and highlights of new advancements from the development of Monte Carlo simulations that model polydisperse molecules. The thesis is finished by suggesting possible starting points for continuation into planar morphologies of condensed material.

Chapter 1: Introduction.

Chapter 2: Literature and Motivations.

Chapter 3: Method used to Simulate Organic Molecules.

Chapter 4: Publication: “disLocate: tools to rapidly quantify local intermolecular structure to asses order in self-assembled systems” in Review - 2017.

Chapter 5: Publication: “Reproducing morphologies of disorderly self-assembling planar molecules with static and dynamic simulation methods by matching density” in Physica A - 2017.

Chapter 6: Publication: “Steric self-assembly of laterally confined organic semiconductor molecule analogues”, in Physical Chemistry Chemical Physics - 2014.

Chapter 7: Manuscript: “Similar morphology but different molecule shape: self-assembly simulations with varying steric potentials”, In Preparation for Special Issue Publication (EPJ E) - 2017.

Chapter 8: Simulating Morphologies with Multiple Molecular Species

Chapter 9: Summary and Outlook.

Chapter 2

Literature and Motivations

2.1 Quantifying Interfacial Morphology

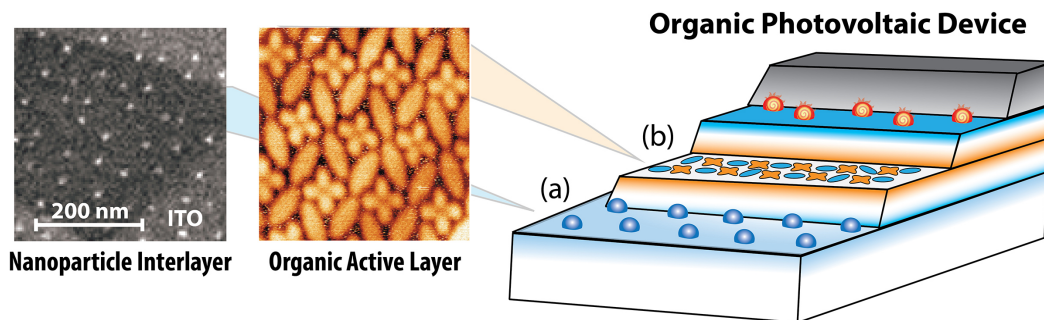


Figure 2.1: Cross section of an organic photovoltaic device. (a) Nanoparticles are introduced to modify the interfacial work function. (b) Organic active layer consisting of donor/acceptor materials. Adapted with permission from [18]. Copyright (2007) John Wiley and Sons.

To predict the influence that localized spatial arrangements of nanoparticles has on electronic devices, we must rely on the ability to accurately classify the type and amount of ordering observed from self-assembly. The ability to quantify order is important because the dispersion of nanoparticles at an interface can change the electronic properties. A typical schematic of an OPV device is shown in Figure 2.1 with two of the interfaces explored within the thesis where the device can improve performance by modifying (a) the electrode interface with nanoparticles [8] and/or (b) controlling the morphology of molecules within the organic active layer [9].

The collective arrangement of nanoscale objects can change the interfacial properties of materials to produce macroscopic phenomena. Engineered nanostructures that mimic those found on the exterior membranes of biological entities have been shown to have super wetting properties which relate to the arrangement of these features [19]. The ability for liquid material to adhere to a surface (wettability) can be changed using nanoscale structures with repeated structures that form 2D Bravais lattice patterns [20]. Their internal spacing and relative size can be used to define a surface roughness which has been theorized to describe contact angles of a droplet [21, 22, 23]. An important test of this claim came from an experiment that compared the contact angle of a droplet resting on nanoparticles within a small area directly underneath the center of the droplet to both full and empty surface coverages [24]. In this case, the contact angles from both empty and partially covered surfaces were the same, implying that the nanoparticles changed the water droplet shape at a location of the 3-phase interface contact line [25]. Nanostructures with radial dispersions have been compared to the square lattice to investigate the effect on contact angle and found that the droplets were pinned to the posts as

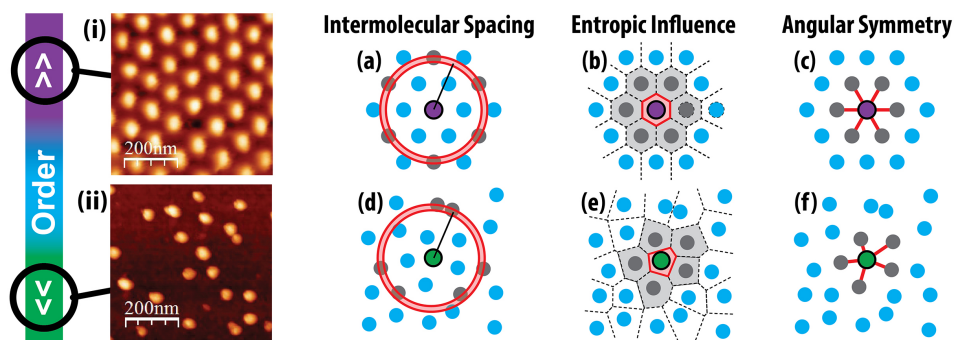


Figure 2.2: Self-assembled morphologies land somewhere between highly ordered systems (i) and one with very low density (ii). Two key factors at classifying disorder are simultaneously in competition with each other: limitations on perception misguides us into seeing patterns in randomness while our imprecise ability to distinguish between similar patterns misses subtle differences. To remove unwanted bias, numerical order metrics are utilized to characterize the morphology located at particle positions: pair correlation function (a & d), Voronoi tessellations (b & e), and the bond order parameter (c & f).

the liquid evaporated [26]. Additionally, this triple line has shown to produce square lattice configurations of nanoparticles from the motion caused by evaporation [27]. This is a direct example of how knowing the surface morphology and dispersion of objects is critical to understanding the underlying physical mechanisms directing interfacial material properties.

Different experimental preparation methods can produce intermolecular dispersions which are seem visually similar to each other and there needs to be a meaningful way to quantify the differences between morphologies to judge whether their configurations are actually similar. Multiple specific types of ordering needed to be quantified and analyzed together since two patterns can show disordered structure metrics in one domain of order but not another. This case is exemplified in liquid crystals which can have angular order without also having translational order [28, 29, 30]. This high level of analysis allows for deep quantification and detection of slight differences that might be missed by causal observers. In Chapter 4, we discuss the parameters that can be used to quantify the organization of planar objects in relation to the expected results for highly ordered states in 2D.

Figure 2.2 highlights the analysis tools which I have coded together into a cohesive package that can quantify differences in morphologies. Each metric has a set of expected values for the densest known phase of circular particles in the plane (the hexagonal lattice) which is shown in Figure 2.2 i). These images show planar arrangements of micelle nanoparticles deposited onto silicon and imaged using Atomic Force Microscopy (AFM). Since the hexagonal arrangement is the densest possible pattern for spheres in the plane, deviations away from these values characterize the amount of quantifiable disorder within the system. This disordered pattern is represented in Figure 2.2 ii) and can be clearly distinguished from the ordered state i) by the apparent difference in number density. Numerical methods outlined Figure 2.2 are best used when two images have similar density but slightly recognizable differences in the order. In this case, computation routines remove any observer bias to define internally consistent metrics between samples. More detail on how these analysis metrics work is outlined in the publication (under peer-review) within Chapter 4.

2.2 Entropy Driven Condensation of Particulates

The main property that describes the internal morphology is the density, and as such, there is much overlap between the behaviour of the hard-sphere model and granular material [31, 32]. This system of particles is considered to be a granular material and it consists of a large number

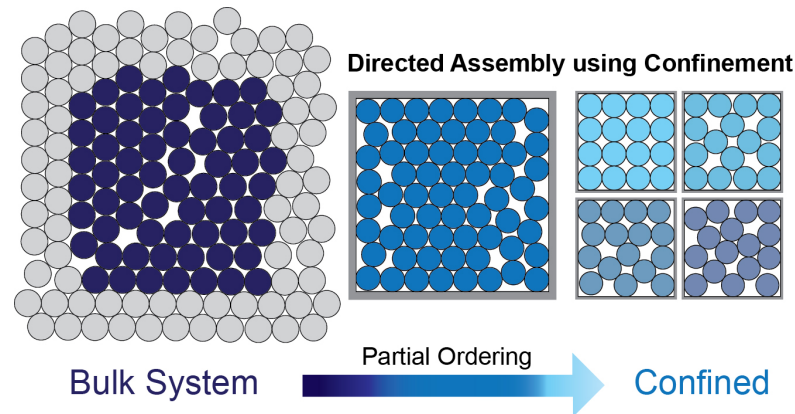


Figure 2.3: Self-assembly can be directed by imposing boundaries onto the system. By reducing the area, the particles arrange into discrete patterns which limits the variation of expected particle positions.

of hard particles that interact through collisions. Granular particles are typically macro-sized objects that can have collective motions which resemble flow of a liquid but also settle into static states that resemble solids [33]. The classic example of this would be silica sand, which can be poured from a height and results with a sand pile that forms a stable cone-like static structure.

Density is a property that describes the amount of objects there are within a given amount of volume. When particles with shape are described, their volume must be factored in to the density to fully encompass the amount of free space for the particles to move within. The simplest geometric shape that embodies volume is a sphere and that each entity with volume cannot embody the same regions of space. This simplification provides insight into the role of density by minimizing the influence of anisotropic particle volumes.

Several ideas developed from granular materials can be used across fields to expand our ability to classify the morphology of planar particles. If objects with volume and complementary shape (i.e. lego blocks) were able to fill the contents of a drawer by the deposition method of randomly tossing them within the confined area, the resulting microstate would be one of the many possible equilibrium state configurations where in which these particles could have assembled differently while still at this density. Imagine however, taking out these objects and then consciously changing the arrangement by stacking them into an ordered arrangement with positions that minimizes the distance between sequential additions. In this case, we would get the same density (objects per area) but the distribution of free space would be maximized to allow for more particles if necessary. At a certain point, particles embody enough excluded-volume to prevent the sequential addition of another particle because the available “free”-volume is less than the space needed to fit this particle into. At this point, the density describes not only information about how many particles fit into confined spaces, but also the local arrangements these particles needed to take when reaching this density. This example highlights the entropic component for self-assembly of objects with shape. The configuration we obtain is dependent on the probability of all possible microstates for that given volume fraction.

Simulations are a robust way to access experimental information that may remain inaccessible during fabrication processes [34]. Using computational methods and models, these various possible complex dynamics of particle interactions can be isolated to determine which interactions produce the types of morphologies observed in experiment [35]. We have been exploring the role of molecular shape as the main intermolecular interaction that drives resulting morphology. To do this, we have made simulations of molecular self-assembly by substituting the complex dynamical equations of motions of particles with randomized displacements of molecules. This model allows for arbitrarily-shaped particles to be simulated on the same level footing as simple circularly-shaped ones.

Our approach is one based on a Monte Carlo simulation where particles’ shapes are approx-

imated by planar polygons [36], and the interactions are modelled by purely geometric, hard wall potentials. This approach has the advantage of modelling particles with complex shapes when the implementation of excluded-volume interactions poses serious challenges for molecular dynamics due to the non-smooth (non-analytical) nature of particles shapes (for instance, ones that resemble fractals). An important aspect of implementing such an approach is to validate it against standard techniques in limiting cases.

Event-driven molecular dynamics (EDMD) is a simulation technique that uses kinematic equations of motion to collide sets of condensing hard spheres within a container [37, 38]. This method is good enough if the molecules of interest are symmetric. The circular approximation breaks down at some point when the geometry of the molecules become the driving impact on morphology. In Chapter 5, we test the validity of our Monte Carlo approach against event-driven molecular dynamics to study if the different approach to modelling molecular movement leads to a quantifiable difference in morphology. This is done by finding a comparable set of simulation outcomes that have probability density distributions of molecular covering density (area fraction) which are similar. This manuscript highlights the importance of open access software and data for researchers who might not be able to generate their own sets of statistical samples.

One key approach to improving the efficiency of organic electronic devices is by directing the supramolecular self-assembly to obtain preferred morphologies [39, 40, 41, 15]. Confinement is one possible way to direct the self-assembly of molecules into desired configurations [36]. This long-range effect shows the importance of morphological control on varying length scales, not just at the level of intermolecular interaction. Figure 2.3 shows how the external influence of confinement changes the resulting morphologies of circular molecules when the available space for objects to self-assemble into is limited. In Chapter 6, circular molecular analogs are simulated under the influence of confinement and its potential utility as an external influence to direct self-assembly is discussed. We find that specific patterns can be found by using the channel walls to limit the possible free-volume these molecules can occupy and have a stable configuration. By understanding these types of confining effects, new possibilities emerge for optimization of nano-sized electronic devices that have lengths of only a few semiconducting molecules. The manuscript highlights the reduction in possible microstates into finite and countable patterns as the available area decreases from bulk systems. Sections within this chapter include details on optimizing pattern matching algorithm and how it was used to detect faults in the previous versions of our Monte Carlo simulation code which miscalculated molecular centroids of complexly shaped molecules.

2.3 The shape of an excluded-volume region

The shape of an object may seem self-evident since objects are sometimes used synonymously for their shape. For example, the word “bell” describes both colloquial use of a unique shape (“bell curve”), but also whose reference could be identified either in context of a shape (Gaussian distribution) or an object (Liberty Bell). However, unlike the Liberty bell, shape is not a unique quality of only one object since many objects of different material properties can have similar shapes. Shape is also scale invariant since the relative structure defined by the objects constituents can span across varying length scales. This intertwine between a physical object and a generalized notation of shape suggests that a precise definition is needed.

Physical objects embody volume. Shape manifests as a physical property of objects through partitioning the surrounding volume with geometric contours that confine the spatial distributions of material as a localized aggregate which collectively acts a single body. The interface between the surrounding environment and the excluded-volume of the object defines a conformal outline of the shape. Shape is a result of the collective behaviour of all constituents that compose of the material that acts as a single object. For instance, the iron atoms can collectively form intermolecular bonds into a rigid shaped object at the macroscale implying the material should also have similar rigidity until the size of the shape becomes comparable to the length scales of the bonds.

A particle is steric if it acts as a rigid body. This property implies that the intermolecular bonds connecting the internal pieces of the object are strong relative to the external object

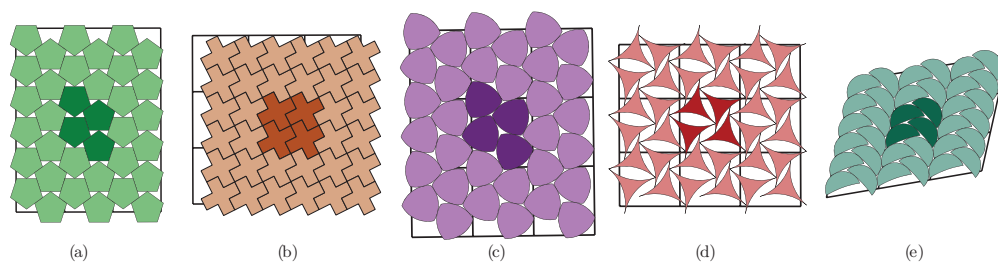


Figure 2.4: Maximally dense packing of a) pentagons b) “fat crosses” c) convex curved triangles d) concave curved triangles e) “moonlike shape”. The darker colour set of shapes indicates the unit cell. Adapted with permission from Ref. [53]. Copyrighted by the American Physical Society.

interactions (collisions between grains) and these bonds are stable on timescales which are longer than the time needed to observe any internal fluctuation of its constituents (bending/vibration). This applies consistently as the sizes of the objects shrink until the length scales at which the steric interactions become comparable to atomistic intermolecular influences.

What happens when the objects interact at a distance and can a steric potential (shape) still be defined as an excluded-volume interaction? There has been a lot of work describing potentials that use intermolecular distances to define physical properties within a system of many particles [42, 43, 44]. Models like density functional theory calculates potentials by using a correlation function between atoms to form a description of the charge density in molecular orbitals [45]. This has is practical importance for organic electronic devices since it is able to calculate HOMO and LUMO energy states. These energy states can have areas of high probability of occupation that are separated spatially from each other. Particles that act at a distance through repulsive potentials can have a steric potential drawn using contours of constant energy potentials [46]. Molecular orbital contours are then accessible from experimental techniques since individual molecules can be imaged using scanning tunnelling microscopy [47]. These contours are what we would consider to be the molecular shape.

Supramolecular modelling using molecular dynamics (MD) [48, 49, 50] and Monte Carlo (MC) [49, 51, 52] approaches to atomistic interactions have been fairly successful in predicting molecular tiling patterns for a variety of molecules. However, these simulations rely on computationally expensive calculations for the interaction potentials, typically modelling each atom in the system, limiting the approach to small unit cells and fairly simple molecules [48, 49, 50, 52]. This not only includes the deposition material, but also the substrate in which the particles are adsorbed onto. One successful simulation code, Self Assembly of Nano Objects (SANO) [52], uses this such method. Molecular movements are chosen using a grand canonical Monte Carlo scheme that minimizes the configurational energy and maximizes entropy. Both chemical potential and temperature are set constants for these simulations. Systems of interests are modeled by including potential energy calculation for both substrate and molecule. This simulation technique has reported success in modeling different organic molecules, such as: octachloro-zinc-phthalocyanines (ZnPcCl_8), copper-phthalocyanines-fluorinated (CuPcF_{16}), penta-tert-butylcorannulene (PTBC), and di-indenoperylene (DIP). The surfaces that are explored are silver ($\text{Au}_{(111)}$) as well as gold ($\text{Ag}_{(111)}$). Using this method, it is possible to explore how the substrate can affect the morphology.

The use of a grid is one way to model highly complex interaction potentials by restricting the shape to only occupy quantized spaces and translations. However, this comes at the cost of limiting the positional degrees of freedom, constraining the molecules to occupy only select grid points. This limitation of single grid point occupation can also form the basis of molecule shape. In this case, particles fixed to the grid have predefined morphology from grid-point locations. Because of this limitation on positional freedom, the possible permutations for a set of particles can be completely enumerated. This method can allow for the inclusion of many different interaction potentials to move molecules around on the grid, however, the grid mainly

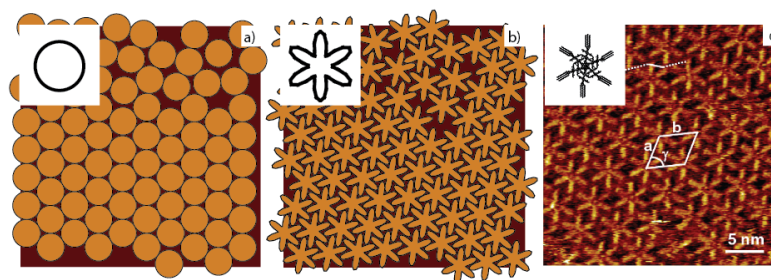


Figure 2.5: a) Circular approximation to molecular shape with simulated morphology. b) Complex polygon approximation of the star-shaped chemical structure. c) STM image of star-shaped organic molecule oligo(*p*-phenylenevinylene)-substituted hexaarylbenzene on 1-phenyloctane-HOPG. Reproduced with permission from [64]. Copyright 2007 American Chemical Society.

acts as the geometric link between intermolecular interaction potential and the thermodynamic microstates allowable for particles of that shape and density.

Three-armed organic molecules have been modelled as rigid planar objects that occupy positions on a grid [54]. The molecule that was explored is 1,3,5-tris-(1,1-biphenyl-4-yl)benzene (TBB). These molecules move around a triangular lattice, with segment points that align the molecule with the grid points. The interaction energy from the surface and the molecule is assumed to be zero, which simplifies the simulations. Randomly chosen Monte Carlo moves are accepted if the segments of the molecule do not share the same lattice points as another molecule. These conditions produce a system that is an example of the excluded-volume model. Another organic molecule that has been explored using a grid method has been pentacene [55]. The motivation for this study was to explore how the molecules arrange themselves on the surface of substrates after thermal deposition. This molecule has an elongated shape and can occupy two spots on a rectangular grid. Molecule-substrate and molecule-molecule density functional theory interactions are solved with Gaussian software for potential energies used with Monte Carlo acceptance.

For organic molecules with “almost circular” chemical structures, such as fullerene and coronene, circles can be used to as a first order approximation to their shape [56, 57]. However, molecules that have potential use in photovoltaic devices, such as pentacene [58, 59] and PTCDA (3,4,9,10-perylene-tetracarboxylic-dianhydride) [60], are observed to have a shape that resembles an ellipsoid [61, 62]. As a result, molecules of complex shape have the possibility self-assemble into configurations of localized states that would not be seen in systems of molecules with simple circular shape [63]. Figure 2.4 shows a series varying shapes that have been explored through adaptive shrinking cell simulation method. These configurations have been generated using a randomized movement scheme that rejects movements that result in overlapping objects while the confining area geometrically transforms to minimize the density (packing fraction) [53]. The goal was to explore the maximally dense packing configurations that correspond to these various shapes, with each unit cell shown as darkened objects inside each section in Figure 2.4. Understanding the crystallization unit cell is important when trying attribute order in systems with non-circular particles. If this can be qualitatively solved, then it is possible to develop algorithms that are able to detect positional and angular arrangement of these maximally dense regions in disordered states.

Circular approximations are commonly used to represent particles within simulations, since this geometry can model many symmetric objects. However, organic molecules do not necessarily have this kind of circular shape associated with their chemical structure. The electronic orbitals of the molecule create an interaction volume that can resemble a shape that can be similar to its chemical structure [65]. One of the reasons that this Monte Carlo method was developed was to explore disordered states beyond those assembled using simple circles into morphologies from molecules with arbitrarily complex shapes. For instance, one molecule that can be modelled is the six-sided molecule (Figure 2.5 c), which has a shape that differs from a circle (Figure 2.5

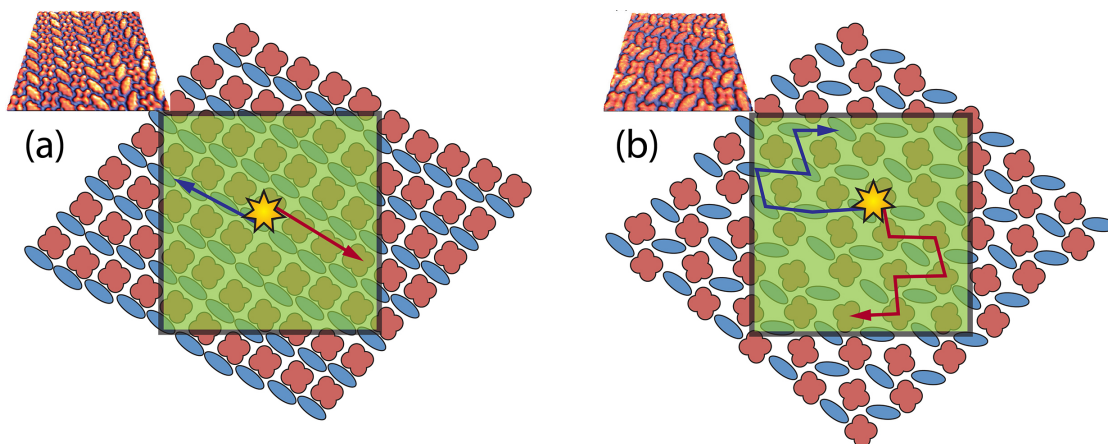


Figure 2.6: Schematic outlining the influence that a change the morphology from a) linearly ordered pattern to b) a “checker-board” pattern could have on charge extraction. Excitons (spark-shape) are formed when photons are absorbed and disassociate to produce electron-hole charge carriers that move through the pathway as indicated by the arrows. a) Molecules may form long pathways for charges to move easily between or b) cause excess intermolecular orbital hopping which increases likelihood of recombination. Insets are STM images adapted from [15].

a) and cannot accurately be described by this approximation. We can further introduce more geometric complexity by using a polygon defined from approximations to what is observed (Figure 2.5 b). While approximating these molecules with circles may be a good starting point, the influence of molecular arrangement caused by any anisotropic shape is not captured properly with the circular approximation. We ultimately wish to explore analog particles that resemble the observed molecular shape as closely as possible. In Chapter 7, we explore bulk systems of monodisperse complexly shaped molecules that were chosen to approximate the molecule shown in Figure 2.5 c). Each candidate we explore has a unique geometric deviation from a circle that could also possibly represent this molecules shape. The chapter reveals how the space-filling method used in our Monte Carlo simulations requires a standard calibration for measuring intermolecular distance to accurately compare across ensembles of analog candidates. This distance directly relates to the strength of the intermolecular steric interaction between neighbouring molecules. Similarly, the standard definition of the packing fraction loses meaning for particles with complex shape due to the degeneracy of covering area between differently shaped molecules. This problem is solved by utilizing Voronoi tessellations to define a local number density which incorporates structural information into their probability density distributions.

2.4 Polydisperse Distributions of Molecules

Organic photovoltaic devices work on the same principle as typical silicon-based photovoltaic devices, the only difference is the absorbing material [66]. Incident photons are absorbed within the organic active layer which results in an energetic excitation of an electron into a higher energy state. The electron leaves the highest occupied molecular orbital (HOMO) and enters the lowest unoccupied molecular orbital (LUMO) resulting in the formation of an exciton [13]. This exciton may separate into corresponding electron/hole pairs at the interface of the donor/acceptor type materials and can be collected as energy before these charge carriers quench within the material. This interface becomes important for charge transport [12] since there are many different permutations of positional arrangement possible for organic molecules. Molecules with anisotropic shape can be rearranged differently relative to each other (i.e. rotated) and this different placement can change the interface between donor/acceptor molecules [17]. The LUMO and HOMO energy states of the donor/acceptor molecules have particular spatial distributions within the molecule, meaning the charge separation can potentially be improved from repositi-

tioning molecules such that these states are geometrically closer together.

The utility of complementary shapes can be seen at the macroscale in everyday objects within the system of a lock and key. Here, the proper arrangement of excluded-volume contours along one edge (i.e. the teeth on the keys) is the determining factor for selecting access through the lock. These two objects form a system of complementary shapes that allows for their features to interdigitate between grooves, where the reduction of intermediate free-area between these shapes lets them come together such that the rotating mechanism of the lock allows the key to turn without resistance. Imagine that the incorrect key was entered into the lock, the steric influence between mis-matching jagged edges would prevent the combination to collapse into the correct state for rotation. The interlocking features of steric contact between the donor/acceptor molecules forms an interface that should also be considered as a means for device improvement.

Not only is the interface important, how the charge moves through the device after disassociation can also affect the performance [10]. Figure 2.6 outlines two different morphologies with the same ratio of donor/acceptor molecules while changing only their relative intermolecular positional arrangement and angular orientations. In both panels of Figure 2.6, scanning tunnelling microscopy (STM) images of deposited organic molecules are shown along with the representative schematic [15]. This imaging technique can detect positions of individual molecules and allows for experimental observation of how molecules self-assemble into particular patterns depending on substrate and intermolecular interactions. To produce current in the device, percolation of the charge carriers needs to occur from inside the active layer and out to the electrodes. For this, there needs to be a path for the charge to follow without being allowed to recombine and quench at another interface [67]. In each configuration of molecules, the patterns that form may result in different charge mobilities through the morphology, which will in turn affect the performance of the electrical device [66]. Figure 2.6 a) shows a stripe pattern with linear rows of molecules which create pathways for each of the charge carriers to move through. Bulk heterojunction devices have been fabricated with similar striped pattern of donor/acceptor material and the increased performance is attributed to the smoothed paths for charge carriers, even when the separated active layers are micrometres in length [68]. As the morphology changes, so will the ability for charge carriers to move within the active layer. Figure 2.6 b) shows a different morphology of the same material, however, molecules are arranged such that the interfaces between donor/acceptor molecules impedes the direct movement of charges through the device. In this case, the charge carriers must manoeuvre around adjacent donor/acceptor molecules while travelling to the electrodes. Since the paths each carrier takes is dependent on the neighbouring molecule position, each move increases the possibility for recombination at the molecule interface [60]. Performance in these devices will depend on how the molecules self-assemble into patterns, which can be improved through morphological tuning [69].

One unique feature of organic material is that different molecules can have the same effective shape (geometric structure) but are chemically and electrically distinct. For instance, the same flower shape pattern is seen from STM images from Copper phthalocyanine (CuPc) [70] and Zinc phthalocyanine (ZnPc) [71]. This has the potential to optimize the electrical properties of a system by selecting a different molecule but keeping the same effective shape. Device performance can change by swapping out one molecule for another with favourable electrical properties without changing the expected tiling pattern. Conversely, it is likely that a change in chemical structure will change the molecule-surface interaction resulting in a different morphology. For example, the flower shaped molecules in each inset of Figure 2.6 are different, with a) having $F_{16}CuPc$ and b) CuPc and with both morphologies STM imaged on gold Au(111). In this case, the observed molecular dispersions are a result of the difference in surface interactions between the fluorine atoms in $F_{16}CuPc$ and the hydrogen terminated ends in CuPc molecules. This can be further supposed with the observation of different morphologies produced when the same molecule is deposited onto different substrates [72]. From this perspective, it is crucial to understand how the shape of the molecules will influence the molecular configurations when the intermolecular interactions are stronger than the substrate-molecule interactions. In this way, it is possible to predict how the molecules will self-assemble according to their effective shape and choose donor/acceptor molecules with complementary chemical permutations that will most likely favour charge separation and movement.

Understanding the interactions that govern how these objects behave can pave a way into directing their self-arrangement by exploiting the molecular shape. The complex interactions between molecules and the substrates need to be separated and analyzed separately to gain full information on the molecular self-assembly. Separating the influence that intermolecular and substrate-molecule interactions has on the self-assembly is not a trivial task since both potentials are always present in nature. Computer simulations can provide insight into systems that may be inaccessible to direct observation, such as self-assembly during thermal evaporation and deposition. Numerical modelling of molecular self-assembly can help predict which interactions dictate the resulting morphologies, since these interactions can be artificially turned off and explored using simulations in a way that cannot be done experimentally. In Chapter 8, the details on the newest iteration of our Monte Carlo simulation code is outlined in terms of its algorithm and new improvements which allow for greatly expanded systems which were not possible in previous versions. Molecular polydispersity, new boundaries, and additional interactions are described by contextualizing the actions taken to implement these constraints into a working simulation. Benchmarking of this new simulation code, named “morphologies”, is conducted against the previous version “gransim” and is shown to execute at a faster speed with all other protocols being similar.

Chapter 3

Method used to Simulate Organic Molecules

3.1 Monte Carlo Condensation

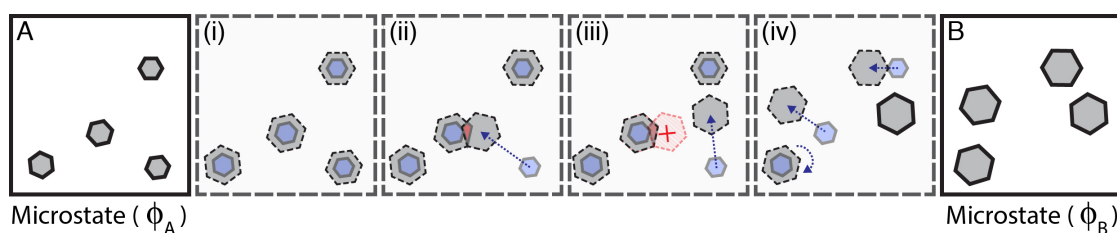


Figure 3.1: Monte Carlo simulation method to generate condensed dispersions of planar organic molecules. (A) The initial state A has density ϕ_A . (i) Density is increased by inflating particles. (ii) Monte Carlo displacement of particle. (iii) Trial move results in overlap so it is rejected and another move is selected. (iv) Other particles find accepted positions. Translational, rotational, or a mixture of both operations can occur. (B) The result is the condensed microstate B with a higher density ϕ_B

The simulations begin by preparing the systems of polygon-rendered particles in the dilute phase, i.e., N particles are randomly deposited in a simulation box of area A while avoiding overlaps (see Figure 3.1 (A)). For a general polygonal shape, each particle is defined by the position of its geometric center r_i and its orientation θ_i ($i=1, \dots, N$).

The order in which the different steps are applied during the simulations is as follows: First an increase of density is performed. We have found that changes in the simulation box size can be easily achieved by introducing a rescaled set of coordinates, i.e., mapping the particles positions and polygon vertexes to a unit square simulation box. In other words, to increase the particle density each particle is expanded within a fixed simulation box size (see Figure 3.1 (i)), instead of shrinking the simulation box for a fixed particle size. This rescaling of coordinates greatly simplifies the implementation of the various boundary conditions. Naturally, the rate of compression of the box is directly related to the rate of expansion of the polygonal particles.

If the increase in density results in overlaps, all N particles are randomly displaced and rotated in an attempt to remove the existing overlaps. Since we are considering systems with only hard-core interactions, the acceptance criterion of our Monte Carlo method is straightforward: All moves are accepted when they do not result in overlaps.¹ In order to sample the phase space, for a constant number of particles and area of the simulation box, we have implemented two

¹That is, overlaps between molecules or between a molecule and the container wall.

types of Monte Carlo trial moves: translation and rotation. The magnitude of the translational displacement vector is calculated as $\delta r_i = (\delta x_i, \delta y_i)$ with elements $(\delta x_i, \delta y_i)$ chosen randomly from probability distributions $P(\delta x_i), P(\delta y_i)$ uniquely defined for translational x-y dimensions. The simulations use non-uniform probability distributions to incorporate diffusive motion into the Monte Carlo selector by. This motion can be captured with Gaussian distributions with zero mean and standard deviations σ_r and σ_θ .

$$\delta r_i = [\delta x_i^2 + \delta y_i^2]^{1/2} \quad (3.1a)$$

$$p(\delta x_i) = \frac{1}{\sigma_r \sqrt{2\pi}} \exp\left(\frac{-\delta x_i^2}{2\sigma_r^2}\right), \quad (3.1b)$$

$$p(\delta y_i) = \frac{1}{\sigma_r \sqrt{2\pi}} \exp\left(\frac{-\delta y_i^2}{2\sigma_r^2}\right), \quad (3.1c)$$

The amplitude of the rotational displacement $\delta\theta_i$ is also selected with a Gaussian probability.

$$p(\delta\theta_i) = \frac{1}{\sigma_\theta \sqrt{2\pi}} \exp\left(\frac{-\delta\theta_i^2}{2\sigma_\theta^2}\right), \quad (3.2a)$$

This move is accepted if it does not produce any overlaps between the particles or between the particles and container walls in the case of hard-wall boundary conditions. When a move results in an overlap (Figure 3.1 (ii)), it is rejected and a new position is sampled (Figure 3.1 (iii)). There are set number of trial attempts to find an acceptable move after which the object is left at its current position if none are found. If the simulation cannot reposition any of the particles, the order in which each particle is shaken is randomly permuted and the scheme is repeats. The process of increasing the density and removing the overlaps by displacing the particles is repeated until the density cannot be increased further. That is, the density will increase until the total overlap, defined as the sum of overlapping areas between pairs of polygons, cannot be resolved below a given threshold. The result is a dispersion of N particles with area A that were randomly arranged on a surface area A_{box} with characteristic density $\phi = NA/A_{\text{box}}$ (Figure 3.1 (B)).

The magnitude of the trial displacement moves $\delta r_i = (\delta x_i, \delta y_i)$ and $\delta\theta_i$ are allowed to change during the runs according to the following rule: The initial displacements are kept until the density cannot be increased further, at this point they are reduced to one tenth of their current values and the simulation continues. This reduction to the randomized displacement mimics the loss of thermal energy when cooled and allows the system to transition into a glass phase where the particles are maximally packed together. This process is repeated until no significant densification between two consecutive reduction cycles is achieved where usually 4 to 6 reduction cycles, involving ca. 10^6 – 10^7 Monte Carlo steps, are necessary to achieve dense configurations.

For the biased MC method, the initial conditions for all system sizes were set from those optimized for 1024 particles. These were chosen by determining which parameters allowed the large system to produce a disordered yet densified state. These were: a translational shaking amplitude (σ_r) that is proportional to the particle diameter and rotational amplitude (σ_θ) is proportional to one molecular rotation 2π . A growth rate which scales the molecular size by adding 10^{-5} radii per step was used. The number of trial shakes per particle (k) was set to 1000. The number of shaking cycle permutations was set to 10 per inflation step.

3.2 Entropy Driven Microstates

The model used for the simulation is based off properties of systems that have minimal interactions (short range) and are described statistically. The excluded-volume model of particles has the same properties of many models of gas. An ideal gas has the property of uniform structure throughout the volume it is contained within and its thermodynamic equation of state can be solved with entropy states using the microcanonical ensemble. A lattice gas would be the next model that explicitly forbids particles from occupying the same volume by only allowing one

gas particle to be on a single grid point. Here, the particles have an implied volume that is the equal distribution of volume left from excluding the number of unoccupied points from the total number possible. The equation of state can be solved for a specific density (number of particles per total available positions) and implies that the volume of a particle relative to the interior unoccupied free space determines the number of microstates expected at this density.

Since we are using a Monte Carlo scheme, the configuration produced should be one randomly selected from the possible equilibrium states. The entropy is the driving factor for molecular assembly and the systems can be solved for the number of possible permutations of particle positions. The microcanonical ensemble accounts for all possible variations to positions at equilibrium by having each microstate possess a different spatial dispersion of particles within. By continually sampling all the possible permutations available at this density, an average of the intermolecular structure can be extracted. In this sense, every accepted Monte Carlo configuration adds to the an equilibrium states for an excluded-volume gas with constant density.

3.3 Modelling Molecules with Polygons

The objects that are simulated are represented as polygons, which are input as two dimensional arrays of x-y coordinates. This list of coordinates defines the outline of the polygon and its volume comes from the continuous linear interpolation between sequential entries. Since the simulated objects are stored as arrays, all actions or influences done to the molecules can be solved using linear algebra. Simulated movements are functions that apply a displacement vector to the current position of the polygon. There are only two operations applied to model displacement, that being a radial translation away from the centroid and a rotation about its axis. To model condensation, increasing the density is mapped into the particles using a scaling operation to change their volume relative to the simulation area. The correct order to apply these operations in to: Scale, Rotate, then Translate.

Define the input polygon (\mathbf{M}) as a constant 2d matrix with n vertices. The scale transform s is a scalar value that multiplies the vertices to change relative size of the molecules while retaining its shape. This operation simplifies to a scalar multiplication when the polygon has a center of mass at the origin $(0, 0)$. The polygon rotates by applying the rotation transform R by the randomly selected angle (θ) onto the euclidean coordinates of the scaled polygon. The translation transformation adds the components of the displacement vector r to the vertices of the scaled rotated polygon. The resulting Monte Carlo trial polygon P is represented in the equation:

$$P_{MC} = R(\vec{\theta})[sP] + d\vec{r} \quad (3.3)$$

3.4 Resolution of Polygons: Circular Approximation

The number of points that make up the polygon has a significant impact on the polygon overlap detection in our Monte Carlo scheme, leading to increased simulation time. As the number of sides of a polygon increases, it become a better approximation of a mathematically perfect circle. To gauge how well a regular polygon describes a circle, in addition to a visual inspection, one can use the area ratio and the rolling resistance ($\mu = \frac{1}{4} \tan(\pi/2n)$ [73, 74]. As can be seen in Figure 3.2, visually, iscosagons are virtually indistinguishable from circles, with an area ratio of 0.9959 and resistance of 0.0787. However, there may be an impact of even such small deviations on the densified configurations and resultant particle density distributions. Due to the similarity of the particle density distributions above 100 sides, we chose the resolution of 100 sides to approximate circles.

If the initial polygon is off-center, the scaling causes a skew to the shape, the rotation will cause precession of the centroid around the origin, and the translation will miss by the distance of the origin offset. Figure 3.3 shows the resulting polygon that results from normalizing the polygon to have the longest distance to a vertex equal to one unit length. Two variations of polygon definitions exist, one that has the last point in the list equalling the first (closed) and without

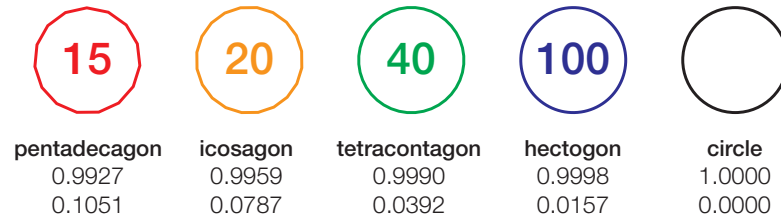


Figure 3.2: Regular polygons approximating a mathematical circle. In each case, the number of sides (n) is displayed within the polygon while the name, the normalized (to the circle) area, and the rolling resistance, respectively, are listed below. In all counts, hectagons and even tetracontagons, are indistinguishable from analytic (mathematical) circles.

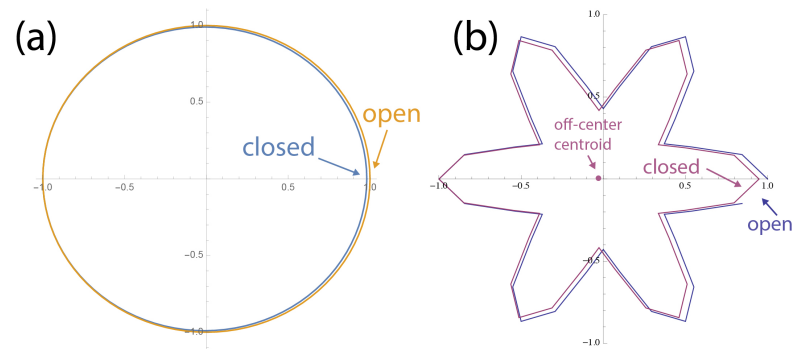
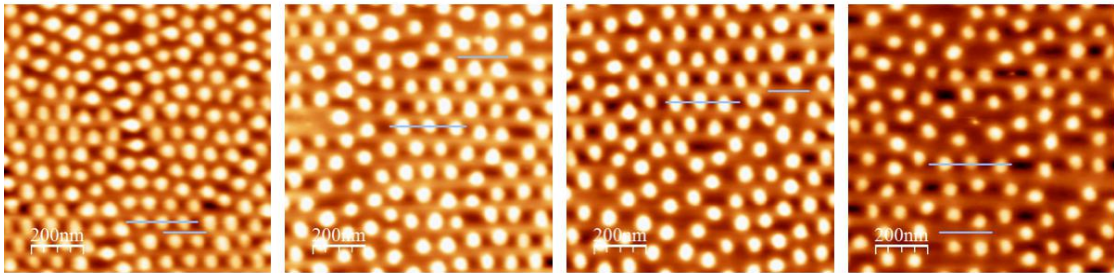


Figure 3.3: The effect of normalizing the shape to have its farthest point be at a distance of 1 for closed and open definitions of polygons. (a) Circular polygon with 100 sides and (b) Rodonea curve with 36 points.

this point (open). The initial version of the Monte Carlo code only normalizes open polygons properly and causes skew with closed ones. This has been changed in latest implementation, which can handle either definition and removes the rescaling of shape by keeping the lengths of the input polygon instead. This allows for polygons with size polydispersity (same shape, different lengths) to be simulated together while keeping their relative size ratio constant.

Chapter 4

Quantifying disorder in planar systems



A series of AFM images of monolayer micelles prepared with varied experimental methods. The quantification of disorder provides information about the impact each step has on directing the self-assembly. The variance of order within each configuration defines the reliability of the technique. Without this unbiased quantification of order, an observer might not be able pick out the subtle differences in dispersion.

4.1 My Contributions

My contributions for this publication came in the form of developing a package of tools to quantify disorder, determining the expected values these tools should provide, writing sections of the manuscript, and producing the figures. The other authors (besides: Matt Bumstead, Ayse Turak) were instrumental in providing the experimental outcomes and helped find bugs in the code that was used for the analysis and results. My work has brought together complementary metrics and combined them into a Mathematica package that will produce easily interpreted visual representations of complex intermolecular structure. Developing this package consisted of bringing together and testing numerical techniques which characterize structural order (see Chapter 5). This lets users quickly assess the order in self-assembled systems without reliance on observer interpretation or mathematical/technical ability.

One large contribution I made was to generate sets of expectation values for highly ordered intermolecular dispersions. Gathering and/or generating these expected values provides a concise reference of values for which others can use to gauge planar disorder from. Expectation values for these order metrics had been used and reported on in 3D [75, 76, 77, 78, 79], and had comparatively less emphasis on planar 2D systems. These values were used to benchmark the algorithms that I wrote for the Mathematica functions in “disLocate.m” and were a key factor in optimizing these tools for speed. My work has brought a wider range of structural descriptors together into a single place.

Another contribution I worked on was building a model of planar morphology that can classify the amount of disorder in planar arrangements of objects relative to a desired pattern. This model utilizes the most ordered configuration for planar spheres, the hexagonal lattice, and extracts the deviation in the order metrics relative to it. The variance uses the Voronoi tessellations to partition the space surrounding each particle to build a statistical sample from within a single pattern. This is beneficial for experimental images since scanning probe techniques (e.g. AFM) will require a long time to accurately rasterize surface features. This can impose a limit to the amount of positional data available for analysis to only one sample. This hard limitation was the main motivation to build a set of tools that can describe the probability for variation within intermolecular dispersions. This package has seen success in helping members of the Organic Electronic Interfaces lab determine methods which optimize monolayer coverage of micelle nanoparticles. These tools have resulted in faster development and prototyping of novel organic devices by rejecting experimental variations that do not favour a desired morphology in favour of those that can direct the self-assembly into specific arrangements of particles.

Another contribution that I made was to introduce a novel way to define neighbours of edge particles. The main motivation for this was to ensure accuracy of the order metrics in finite systems. The finite size effects are enhanced in these order metrics because only a small number of particles are often resolved when imaged using AFM (e.g. between 50 - 500). Many of these metrics rely on accurate positions of neighbouring particles, which poses a problem for particles near the edge. These particles have neighbours that extend outside the image area, which means they were not directly observed. I have worked on implementations of boundary conditions that can correct for this issue by removing their influence on the order metrics. One contribution I make is that the influence of neighbours can be inferred and included in these metrics for confined morphologies. My implementation of how edge neighbours in confined boxes can be defined is outlined in this chapter.

4.2 Overview of Manuscript (in Submission - 2017)

Observers may perceive that two separate images look the same but actually have quantifiably different intermolecular dispersions. This is due to our limited ability to differentiate deviations between two images that have similar densities of particles. The manuscript that follows outlines how we can quantify the internal structures of planar arrangements of particles simply by knowing their centroid positions relative to each other. The goal of this manuscript was to concatenate the tools that would best be able to quantify flat planar dispersions of particles and to implement them into an easily recognizable format where only a basic understanding of the metric will be

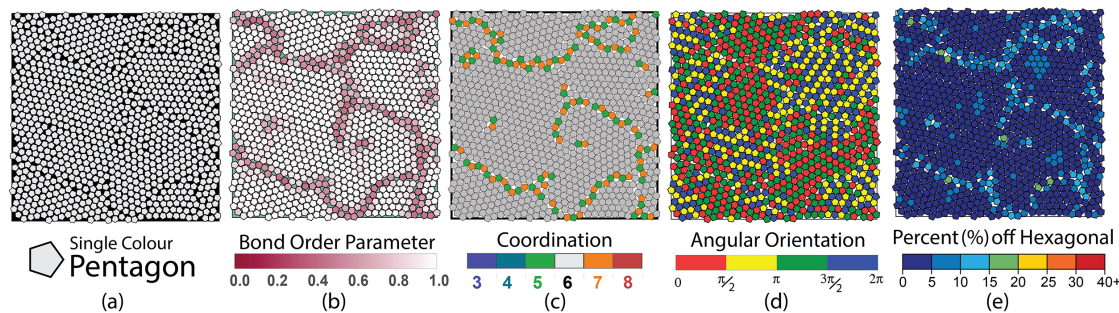


Figure 4.1: Mapping colour onto particle positions to indicate local order. a) Standard rendering of monochromatic molecules gives no additional information. However, variations of local Voronoi tessellations can quantify (b) the bond order parameter relative to the hexagonal lattice, (c) number of neighbours as defined by number of Voronoi facets, (d) the angle each molecule is orientated at relative to the x-axis, and (e) the area deviation from an expected hexagonal lattice with the same number density.

sufficient to interpret the results. The resulting outcome is a Mathematica package that focuses on the visualization of translational, entropic, and angular order metrics. In this publication, we outline how to use and interpret these structure metrics. The manuscript also describes a way to rank disorder between similarly dense patterns by using the local descriptions to obtain a statistical mean and variation. This benefits experimentalists by providing information on how changes to sample preparation impacts the intermolecular dispersion and separation distances of particles. This is meant to improve experimental techniques and methods which can direct self-assembly into specific desired patterns.

The sections below highlight portions of my research that did not appear in the manuscript and/or were part of the supporting information associated with this publication. Chapter 4 expands on the interpretation and implementation of the “disLocate” tool set. The importance of visualizing the local order metrics is discussed in section 4.3. Background for each metric is in section 4.4 which also presents the expected values for the highly ordered states from which disordered patterns can be ranked against. Section 4.5 discusses the influence of varying the boundary definition before applying the metrics and the influence it produces. The chapter finishes with the manuscript (in review).

4.3 The importance of visualization: mapping physics onto molecules using colour schemes

The power of mapping physical information onto particles is really the ability to highlight exactly the regions that deviate from the expected norm. A single picture or graph can be powerful enough to prove or disprove an entire scientific conclusion [80]. The quality for a well thought out picture or graph should be its ability to quickly and effectively convey the exact information the user is querying. For planar morphologies, additional information can be added to configurational renderings by overlaying physical information onto molecules by colouring them with a colour scheme that highlights structural deviations. This need for colourful visualization has been emphasized in a review of modern techniques for analyzing dislocations of deformed crystal structures, which showed that all twelve methods studied presented structural information with some kind of colour overlay [81]. To maximize the utility of this mapping technique, the choices of colour schemes should relate to the physical interpretation of the physical properties being explored and should naturally express the bounds and limitations of the analysis metrics.

Defining appropriate colour mappings is not a trivial task, as not only the physical parameters themselves must be considered, but also the possible range for expected variation. This concept is outlined in Figure 4.1, which shows different analysis metrics mapped onto a configuration of pentagonal molecules. In Figure 4.1 a) the monochromatic grey colour is assigned to each par-

title and leaves all information regarding intermolecular structure up to observer interpretation. Parameters with a continuous values should make use of gradient colour transitions as visual cues. For example, the bond order parameter is a scalar quantity that ranges from zero to one (i.e. complete disorder to maximum order) [75]. In Figure 4.1 b), the value of the bond order parameter is overlaid onto each molecule by converting the numerical value into a gradient scale. The localized bond order of each particle can be represented easily with a grayscale mapping, having the colour dark if it has little to no order while white represents a molecule in the ordered expectation state. The gradient colour scheme provides visual contrast between disordered darker coloured particles from the more ordered lighter coloured particles, with grain boundaries of the polycrystalline sites becoming visually distinguished from the bulk phase particles.

However, different order parameters might benefit from a different colouring scheme if their values are discrete or multidimensional. The local coordination number takes on discrete values, allowing for each value to be represented by a unique colour and is shown in in Figure 4.1 c). Each particle has a unique colour that is distinct and easily differentiated from the other possible values. The downside is that this colour scheme may not be as useful when there are too many discrete values to map colours onto.

Multiple mappings can be creatively combined by assigning colour to the Voronoi tessellations using a gradient to represent the local bond order parameter, while then also overlaying a discrete mapping of the coordination number as coloured centroids [82]. This presents the two metrics together on a single figure, allowing for regions of angular disorder and disclination lines (grain boundaries) to become visually correlated. In another example, local properties of Voronoi area fraction, bond order, and particle displacement have been used with binned colours to indicate their local values are within certain physical bounds [83].

In some cases, the order metric might be continuous, however, a preselected discrete number of colouring bins are chosen instead for practical reasons. The angular orientation of each molecule and the local Voronoi area deviation were both chosen to bin specific amounts of deviation together into a single colour. In Figure 4.1 d), molecules are coloured by their the angular orientation. The angle at which each pentagon is pointing relative to the box is a continuous function (between 0 and 2π), but is chosen to be represented with four discrete bins. The use of four colours represents set of perpendicular reference vectors that bins the angles into quadrants. This provides the distinction between neighbouring up-down pentagon pairs (seen as stripes of Red-Green/Yellow-Blue lines) which are associated with its crystal structure of the pentagonal molecules [84].

The Voronoi tessellations produced from dilute or disordered configurations will have local area partitions that are distributed around the expected Voronoi area of a hexagonal lattice with the same global number density [85]. A parameter that can have both negative or positive deviation from a mean should not use a gradient scale but instead use a colour metric that incorporates both possibilities. Figure 4.1 e) shows molecules coloured by the amount of area deviation each local Voronoi tile has with respect to a hexagonal lattice with the same number density. In this case, the colour scheme of Blue to Red was selected due to its physical interpretation from granular statistical mechanics, which utilizes the use of local volume as a proxy for local temperature [86, 87]. This is a reasonable metric to use since these steric particles do not fluctuate on noticeable timescales. High area deviation from the hexagonal pattern allows the local molecule more room to move and therefore more susceptible to particle displacement (more movement = “hotter”), whereas molecules with lower area deviations are expected to be in the closed-packed phase and unable to move (i.e. colder). As objects heat up, they change colour via black body radiation and eventually emit into the visible spectrum with red being the first colour seen. The sections of higher density-disorder appear in Orange and Red, colours which naturally stands out as being hotter from higher entropic movement. Particles in a non-hexagonal non-disordered state, such as the square lattice, binned with colours of Green and Yellow with this particular arrangement having an expected value for the Voronoi area deviation of 15.47%. The colour Blue is commonly interpreted with cold systems, which subconsciously links the behaviour of freezing liquids into a solid, glassy arrangement of molecules. Dark Blue sections describe local densities close to the expected result of a hexagonal lattice with the same number density. Any small deviations are likely local density frustration and not a physically dif-

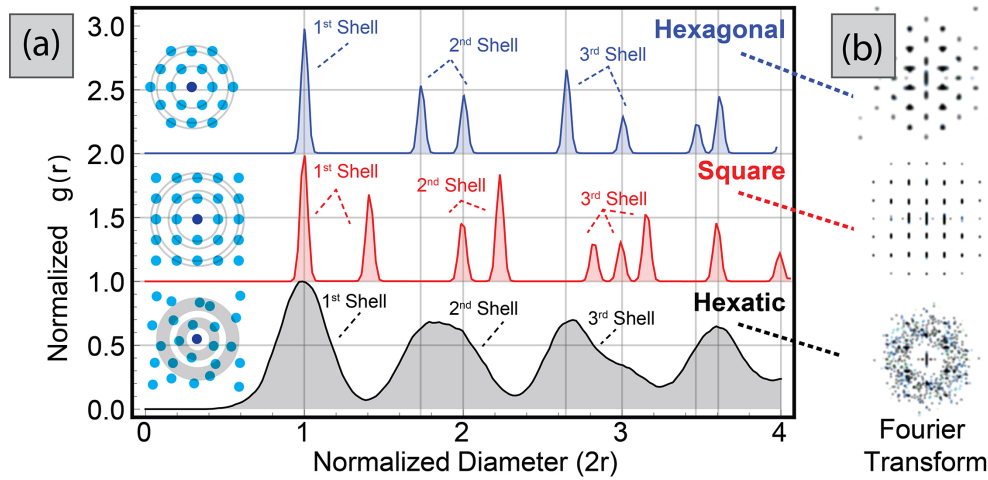


Figure 4.2: (a) Expected radial distribution functions from a hexagonal lattice, a square lattice, and a hexatic lattice. Insets show particle configurations as well as the radial width associated with the neighbour shells. (b) Fourier transforms of the particle positions that produced the associated pair correlation functions.

ferent type of disorder, thus these are coloured as a lighter shade of blue (more thermal agitation, not as “cold”). Naturally, these colour schemes are subjective and highly dependent on common human experience, however, they provide a stepping point in which artistic interpretation can be fused with investigation of physical phenomena. The next section outlines how these analysis metrics are calculated before colour mapping is applied.

4.4 Expectation values for global planar structure metrics

4.4.1 Pair Correlation Function - $g(r)$

The pair correlation function is one method that can quantify the translational order of intermolecular morphology. This function describes the probability to find other particles at varying distances away from each particle. The centre of each particle is chosen as the origin to measure the distance from. A circular shell of width dr expands from the centre to a radius distance r . Any particles inside a circular shell of width Δr are counted together and binned to produce the neighbour probability $n_n(r)$ as a function of distance. This probability is then normalized by the density of the configuration ρ , which then describes its deviation from an ideal gas. Since particles of an ideal gas have equal probability to be at any distance, its pair correlation function $g(r)$ is a flat line with slope 0 with probability 1.

$$g(r) = \frac{n_n(r)}{2\pi r \Delta r \rho} \quad (4.1)$$

This function is sometimes referred to as “the radial distribution function”, since it counts the distribution of neighbours over the radial dimension outwards from each particle. Short and long range translational order can be seen by the peaks in this distribution and provide probabilistic information about the relative intermolecular spacings between molecules, with minimums between peaks commonly denoting the boundaries of nearest neighbour “shells”. Pair correlation functions for highly ordered planar patterns are shown in Figure 4.2 a) for the triangular lattice, square lattice, and a disordered hexatic state and highlights the positions of each of the first three neighbouring shells. In highly ordered states, the internal structure is evenly spaced out at specific distances, meaning the pair correlation function of a periodically ordered array will produce delta functions at distances matching the length between lattice points. The distances between particles for hexagonal and square planar lattices are shown in Table 4.1 and are

normalized by the radius of particles at the densest configuration (non-overlapping). In morphologies that are in this hexatic state (i.e. randomly jammed glass), intermolecular distances vary throughout the configuration by only small deviations away from the expected lattice positions, causing the broadening of peaks. Figure 4.2 b) shows the Fourier transform of the same morphology, highlighting positional ordering of the lattices with bright spots and disordered states as distributions.

The equation below gives the exact values for the distances expected as peaks for the hexagonal lattice [88]:

$$r = (m^2 + mn + n^2)^{1/2} \quad (4.2)$$

where r is the radial distances, and m and n are integers (i.e. lattice vectors) that range from $(0, 0)$ to (m, n) . Exact values for the distances expected as peaks for the square lattice [88]:

$$r = (m^2 + n^2)^{1/2} \quad (4.3)$$

Diameter	1	2	3	4	5	6						
Lattice												
Hex.	1	1.732	2	2.645	3	3.461	4	4.358	5	5.196	6	6.082
								4.582		5.291		6.245
										5.567		6.557
												6.928
Square	1	1.414	2	2.236	3	3.1622	4	4.123	5	5.099	6	6.082
				2.828		3.605		4.242		5.385		6.324
								4.472		5.656		6.403
										5.830		6.708

Table 4.1: Comparison of peak positions of the Radial Distribution Function for exact lattices (hexagonal and square) with normalized first neighbour distance as 1 diameter.

4.4.2 Voronoi tessellations and local area variation

Intermolecular spacing and area fluctuation: A Voronoi tessellation partitions the substrate into sections by using the centroids of the particles. Each tile is defined by the set of perpendicular bisecting lines that are an equal distance between objects and with facets that occur at the midpoint of the line directly connecting the central particle to its neighbours [89]. This procedure produces localized partitions that express the maximum space each molecule can potentially possess. Disordered systems can be analyzed by comparing the Voronoi tessellations of observed configurations to those expected from highly ordered patterns. In disordered systems, one would expect to see a distribution in the size and shape of the local Voronoi tiles [90]. A set of closed packed circular particles will produce Voronoi tiles that are hexagonal and with an apothem equal to the twice the particle radius $2r_{\text{hex}}$ [91]. The expected mean radius of particles within the morphology $2r_{\rho}$ can be directly calculated generically from the global number density ρ [91]:

$$2r_{\rho} = \sqrt{2/(\sqrt{3}\rho)} \quad (4.4)$$

with the density ($\rho = n/A$) being the total number of objects n over the total area A . The expected area each particle should encompass is determined by the equipartition of volume for all particles: ($A^{\text{exp}} = 1/\rho$). The Voronoi area deviation is calculated as the absolute percent difference the local value is from the expected equipartition area:

$$\Delta A = |(A^{\text{vor}} - A^{\text{exp}})/A^{\text{exp}}| \quad (4.5)$$

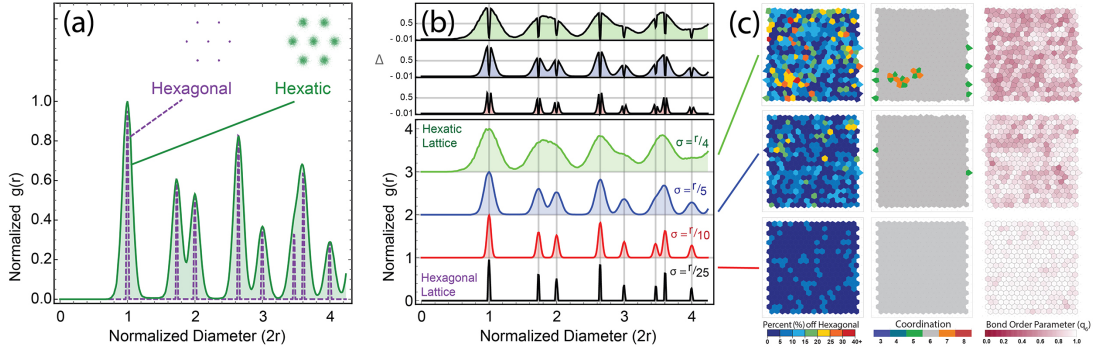


Figure 4.3: Effect of random displacements away from lattice positions. (a) Pair correlation function for the hexagonal and hexatic lattice. Inset shows the relative displacement needed to broaden the $g(r)$ peaks. (b) A series of hexatic lattices with increasing mean square displacement. Lines directly connect the $g(r)$ to the (c) Voronoi tessellations of the displaced hexatic lattice. Tiles are colour coded (left to right): area deviation from an expected hexagonal lattice with the same number density, coordination number of neighbours as defined by number of Voronoi facets, and the bond order parameter relative to the hexagonal lattice.

A similar radius can be calculated using the local area density instead. This can provide a distribution of local intermolecular distances using the volume fluctuations from the expected state. The hexatic radius can be found from the area of a tile (A^{vor}) [92].

$$r_{\text{hex}} = \sqrt{A^{\text{vor}} / (6 \tan(\pi/6))} \quad (4.6)$$

with similar consideration to the expected square lattice:

$$r_{\text{sqr}} = \sqrt{A^{\text{vor}}} / 2 \quad (4.7)$$

The intermolecular spacing d is calculated from the mean of the expected lattice diameters, $d = \text{Mean}(2r_{\text{lattice}})$. If the observed objects are close to the lattice configuration, the calculated $g(r)$ should have its first peak close to this distance. The hexatic lattice disorder parameter can be found using the variance in the local radius distribution (not diameters).

$$\Delta r^2 = \text{Var}(r_{\text{vor}}) \quad (4.8)$$

This value describes the approximate width of the $g(r)$. The benefit of this is that the amount of hexatic disorder can be calculated as a function of local distributions in area without using the explicit center-to-center distance. This can become important when particle positions have a large approximate error from experimental observation. Figure 4.3 a) shows the $g(r)$ from random displacements of the hexagonal lattice particles with probability to move this distance using a Gaussian probability distribution. As this distance increases, the pair correlation function spreads out, mimicking a liquid. Figure 4.3 b) shows the differences in $g(r)$ between patterns with random displacements of the hexagonal lattice particles of varying intensities. As the hexatic lattice disorder parameter rises, the broadening becomes clear in the peaks of the $g(r)$. Figure 4.3 c) shows the sequence of increasing disorder in the structural order as visualizations overlaid onto the Voronoi tessellations of each configuration. The area deviation and bond order q_6 are sensitive to the random fluctuations of points around their center, however the coordination number shows almost no change by keeping 6 neighbours throughout the fluctuations.

4.4.3 Bond order parameter - q_ℓ

The bond order parameter (q_ℓ) is a local structure metric that describes the spatial positions of neighbours as a function of relative angular distribution between a central particle and its adjacent neighbours [75]. Classifying arc-symmetry is key for understanding melting and phase

transitions of colloids [93, 94, 95] and has led to the detection of a “hexatic” phase in spherical gases [96]. Appropriate selection of neighbours is crucial when describing localized disorder, as the number of neighbours selected can influence the resulting analysis of the system. When selecting an appropriate distance for neighbour definition, it is possible to overshoot the closest neighbours in the first neighbour shell and take into account second shell neighbours. One method that has been used is to utilize a cutoff radius which defines neighbours as any particles within that intermolecular distance and excludes neighbours past [97, 98, 78]. This distance can be defined using a multiple of the particles diameter (usually 1.2 or 1.4 times) [75] or with the first minimum in the radial distribution function found between the first and second peaks. In submonolayer dispersions of nanoparticles, it is possible to acquire configurations where the distance between objects is much larger than the particles themselves. The use of a constant cutoff radius can provide inaccurate results by accounting for too many or too little numbers of neighbours. This would be a situation where the use of the radial distribution may not produce an accurate estimation of nearest neighbour distance. To overcome this issue, the Voronoi tile weighted definition of the bond order parameter [78] has gained our attention.

Voronoi tessellations can be used to help define the bond order parameter for very dilute systems [78]. The angle that each molecule has toward the central object can be weighted by the length of the Voronoi facet. This model allows for a continuous bond order when dealing with dilute systems. In this factor, $A(f)$ is the surface area of the Voronoi facet (f) separating the two neighbouring particles, and $A_{vor} = \sum_{f \in \mathcal{F}(a)} A(f)$ is the total surface area (perimeter length on 2D) of the Voronoi tile boundary $F(a)$ of particle a . Here, θ_f and ϕ_f are the spherical angles of outer normal vector \mathbf{n}_f of facet f .

$$q'_l(a) = \sqrt{\frac{4\pi}{2l+1} \sum_{m=-l}^l \left| \sum_{f \in \mathcal{F}(a)} \frac{A(f)}{A_{vor}} Y_{l,m}(\theta_f, \phi_f) \right|^2} \quad (4.9)$$

The densest configuration of circular particles is a hexagonal lattice which has six nearest neighbours around every particle at a regular interval of $2\pi/6$ radians. However, particles could arrange themselves into configurations with other symmetries than six-fold. Table 4.2 shows absolute values for the Voronoi weighted bond order parameter q_ℓ for $n = \ell$ neighbours spaced evenly at $2\pi/\ell$ angles. These results provide an expectation value for this maximum symmetry pattern and can be used to normalize localized values by to gauge the angular deviation from. A particle that has a normalized bond order with the least deviation (closest to one), will provide information about what kind of arc-symmetry is most probable within that configuration. This normalization factor and the use of symmetries other than $\ell = 4$ and 6 is useful in separating types of arc-symmetric angular ordering of particles that can be misclassified as disordered states.

q_3	q_4	q_5	q_6	q_7	q_8
0.7905	0.8290	0.7015	0.7408	0.6472	0.6837

Table 4.2: Absolute values of Voronoi weighted bond order parameter for varying symmetry ℓ for $n = \ell$ neighbours spaced evenly at $2\pi/\ell$ angles.

4.5 The Relation Between Edge Effects and Neighbours

Directing self-assembly can be done through molecular containment [36]. Larger volumes allow particles to settle into equilibrium states, whereas hard walls impose boundaries that frustrate internal particles. In many systems, the boundary conditions will influence the morphology inside the container. Analysis tools that rely on neighbour definitions, such as the bond order parameter, will provide inaccurate results when assumptions are made about objects that lay outside the boundary. In the “dislocate” package, the default edge definition is to ignore particles

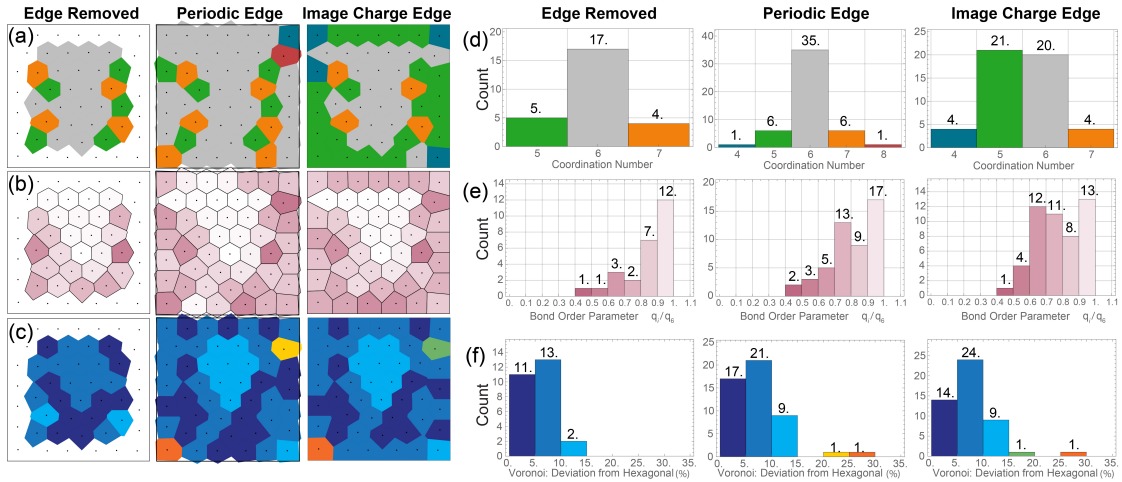


Figure 4.4: Edge definitions of virtual particles effect the statistics of disorder metrics (a) coordination number, (b) bond order q_6 , and (c) Voronoi area deviation

that have Voronoi tiles which extend outside the container. In this case, they still count toward metrics for particles within the bulk, but do not contribute the error associated with their unknown neighbours outside the observation window. This is the most accurate way to quantify experimental systems.

Truncated edges are ones in which objects on the boundaries are removed from the calculation. Here we make no assumptions about any unseen objects or the nature of the morphology outside the image. Figure 4.4 shows an example of how the edge particles are removed. Typically, particles are dispersed over a large area, however, only a small fraction of the morphology is actually contained within image. In this case, neighbours are calculated for all of the particles visible, however only a subset of those are used for calculating the structural signatures. Particles with Voronoi tiles that touch or extend outside the boundary are removed from the metric statistics but still contribute as neighbours to the interior. This is done to reduce errors associated with the unknown dispersions outside the image.

Periodic boundary conditions are ones in which objects on or near the edge are translated by a set of periodic basis vectors toward the opposite side. Figure 4.4 b) shows an example of how the Voronoi tessellations are influenced by periodic boundaries. Instead of truncation with calculating neighbours along the edge, periodic boundaries include virtual particles outside the image and are identical to the ones on the opposite side. This causes the tiles to protrude outside of the image box and is represented in Figure 4.4. One thing to note is that even though local tiles may extend outwards, the change in shape does not influence the global area, causing the sum total area of the Voronoi tiles to be exactly similar to the original area of the image itself. This seems to cause the order metrics to recognize these virtual particles as having more hexagonal order. This is because the periodic translations cause the particles to keep their local structure, with most particles already in the hexagonal state.

Hard boundary conditions are ones in which there is a fixed container that holds the samples. This correction changes the number of neighbours that objects on the boundary have. For some analysis methods, it is crucial that the number of neighbours is properly defined. This hard edge correction imposes a set of virtual particles outside of the boundary that are equidistant and perpendicular to the wall. Conceptually, this is similar to the method of image charges. For the electric field to be zero at the boundary of a conductor, the system can be estimated by substituting in a virtual particle with opposite charge that is equidistant from the boundary. In this case, the constraint of the container can be replaced with objects outside that would produce the same steric influence as a hard box. This neighbour definition forces the Voronoi tessellation to exactly calculate tiles that are within the container. This essentially mimics clipping an unbounded Voronoi tessellation into an area but adds information about neighbours outside the image and is shown in Figure 4.4. The added information from these virtual particles provides

a more accurate idea of how neighbouring particles need to be arranged such that they impose the same steric influences as the box. This seems to influence the order metrics to recognize these virtual particles as causing more disorder. This is because the reflecting translations cause particles to mirror flip their local structure, which produces a fixed shape to one side of the Voronoi polygon. This seems to remove the two facets which appear with periodic boundary conditions.

Defining Neighbours using Method of Image Charges

The method of image charges was borrowed from the concept developed for electromagnetic physics problems [99]. The idea is that a charge that is close to a perfectly conducting wall (metal) will induce a mirror-charge that is opposite in charge and equidistant away from the conductor boundary. This produces satisfactory boundary conditions that exactly sets the electric field to zero at the conductor interface. This method can be extended into the excluded-volume potential. Instead of image particles inducing a charge, they induce a volume-interaction which equally and oppositely imposes the particles at the boundary. This has been a very useful concept when conceptualizing and numerically implementing hard boundary conditions for analyzing intermolecular dispersions. In “disLocate”, the boundaries are replaced with a set of virtual particles that have the exact same influence as the container, allowing for a more accurate understanding of confined morphology. This is the proper procedure in how to generate image charge virtual particles. Any particles within one or two particle radius of a hard wall edge are moved perpendicularly and equidistant away from the edge. This cutoff is needed to reduce computational cost, but to also reduce any errors that could come from having a complex boundary (concave polygon sections) that could move image particles onto of each other. This accounts for most of the system, but the most important part is to include image charges that produce the sharp corners. To do this, for every corner take the absolute closest particle and apply the same procedure using the corner point as the mirror edge. This will result in Voronoi tiles at the edges that are exactly similar in shape to the container.

4.6 Publication: “disLocate: tools to rapidly quantify local intermolecular structure to asses order in self-assembled systems” (Submitted - 2017)

disLocate: tools to rapidly quantify local intermolecular structure to assess order in self-assembled systems

Matt Bumstead^{1,**}, Kunyu Liang¹, Gregory Hanta¹, Lok Shu Hui¹, and Ayse Turak^{1,*}

¹McMaster University, Department of Engineering Physics, Hamilton, L8S 4L7, Canada

*turaka@mcmaster.ca

**bumstema@mcmaster.ca

ABSTRACT

Order classification is particularly important in photonics, optoelectronics, nanotechnology, biology, and biomedicine, as self-assembled and living systems tend to be ordered well but not perfectly. Engineering sets of experimental protocols that can accurately reproduce specific desired patterns can be a challenge when (dis)ordered outcomes look visually similar. Robust comparisons between similar samples, especially with limited data sets, need a finely tuned ensemble of accurate analysis tools. Here we introduce our numerical Mathematica package **disLocate**, a suite of tools to rapidly quantify the spatial structure of a dispersion of objects. The full range of tools available in **disLocate** give different insights into the quality and type of order present in a given dispersion, accessing the translational, orientational and entropic order. The utility of this package allows for researchers to extract the variation and confidence range within finite sets of data (single images) using different structure metrics to quantify local variation in disorder. Containing all metrics within one package allows for researchers to easily and rapidly extract many different parameters simultaneously to make robust conclusions on the order of a given system, quantifying the experimental trends which produce desired morphologies and engineer novel methods which can direct self-assembly.

1 Introduction

1.1 Structural order drives properties

Order is particularly important in a wide variety of fields ranging from optics and nanotechnology, to biology and biomedicine. Self-assembled nanoscale systems with low interaction, such as colloids, tend to long range, yet not perfect, order due to the competition between kinetic and thermodynamic driving forces¹. The same is true in nature, as living systems tend to be ordered well but not perfectly². Such deviations from perfect order have widespread implications from enhancing optical transmission using quasi-periodic³ or slightly disordered⁴ arrays of holes, controlling the plasmonic response using disorder in two-dimensional arrays of nanoparticles⁵, or weevils producing two-colour bands on their wings from a quasi- rather than perfectly ordered photonic crystal⁶. Understanding and harnessing such effects rely on the accurate quantitative description of the extent of order in a given spatial arrangement.

The texturing of surfaces with dispersions of nanoscale objects (e.g. nanoparticles, micelles, quantum dots) is a particularly effective design strategy for controlling surface properties. The number, availability and spatial arrangement of such objects has been used to control metamaterial polarizability⁷, cell growth and apoptosis⁸, plasmonic enhancement⁵, cell spreading and locomotion^{9,10}, transparent oxide surface work function¹¹, photovoltaic conversion efficiency¹², cell attachment on a variety of substrates¹³⁻¹⁵, and templated nanowire growth¹⁶.

The ability to quantitatively describe relative structure and ordering is highly valuable particularly to those who rely on image analysis to understand and probe experimental systems. A precise quantitative description of the local and global arrangement are critical to consistently reproducing the correct spatial patterns for a given application. Figure 1 shows a set of AFM images of polystyrene-block-poly-2-vinylpyridine (PS-b-P2VP) diblock copolymer micelles distributed on a Si wafer surface with three different deposition approaches. Such micelle nanoreactors are typically used to form two dimensional arrays of a variety of nanoparticle materials¹⁷⁻²⁰. It is relatively easy for observers to identify that these patterns are not in a perfectly hexagonal arrangement (highly ordered) nor are they arranged with complete randomness. The distributions of particle spacing appear to land somewhere between these two extremes.

Variations in preparation methods have an influence on the density or relatively spatial distribution of the objects (see for example²¹⁻²³). Techniques such as varying the deposition spin speed is known to have this effect with diblock copolymer micelles^{21,23}. In such experiments, the observable outcomes can look visually similar, as suggested by the inset Fourier

transforms in Fig. 1 for these three micrographs. However, most observers can also perceive some intuitive difference in order among the three images², even if it is not immediately apparent what those differences are.

Assessing these differences requires an accurate and unbiased detection of the structural features of the objects. A common practice in image analysis is to make decisions on the relative order through a combination of user choice and computationally driven filtering, with a program such as ImageJ²⁴. However, human observers often perceive order from randomness, a psychological phenomena called apophenia. Even when order does exist, human perception has difficulty in distinguishing between relatively similar ordering². In order to overcome this limitation, convenient computational techniques can be used to automate research. Allowing the computer to make value judgments about experimental observations is a powerful way to save time while producing a reliable and constantly unbiased analysis. However, though computational approaches are efficient in selecting an easily measurable global mean or expectation value, the effect of variances or local descriptions still rely largely on human interpretation²⁵.

Self-assembling molecular or nanoparticle systems always contain a certain amount of variation, from unavoidable measurement errors or imperceptible variations in variables at the macroscale that have visible ramifications at the micro or nanoscale. In general, rather than a perfect crystal, many self-assembling and biological systems have a polycrystalline structure – areas of high order, separated by defects and localized disorder, analogous to grain boundaries in an atomic crystal– or mesophases such as liquid crystals or plastic-crystalline systems where some of the degrees of freedom are lost²⁶⁻²⁹. Thus their quantification poses an issue: distinguishing any real trends can be challenging if there are limitations on sample preparation or replication due to the high cost of materials, limited quantities, or long processing times. Optimization of protocols and recipes require highly accurate quantitative justification for how likely a system is to have predictable and reproducible outcomes, and how much those outcomes vary naturally, in response to changes in experimental methods. The quantitative classification of naturally occurring limits thereby provides a road-map to reproducibly produce a desired result.

In this contribution, we outline a series of tools and metrics that can be used for a fine grained understanding of both global and local spatial order patterns, within the package "disLocate" (**D**etecting **I**ntermolecular **S**tructure **L**ocated at particle positions). This provides a convenient tool, using a variety of numerical techniques, for researchers to quantify the relative disorder of objects and engineer desired outcomes to a higher degree of specificity. This approach goes beyond common techniques by providing access to a combination of structural metrics which estimate the amount of intermolecular order, and also introduces a way in which local fluctuations of disorder can be used as confidence range to rank protocols and experimental interventions against each other.

To outline the utility of these tools, we use an illustrative fictitious goal for spatial organization: to determine if it is possible to direct the self-assembly of our diblock co-polymer micelles from solution shown in Fig. 1 into a polycrystalline hexagonal periodic arrangement with internal spacing of two micelle diameters between particles using the spin coating speed. In this example, we use the realistic scenario where the data set from which to draw conclusions is limited to AFM micrographs from three experiments of varying spin speed. This leaves the next possible experiment within three choices to achieve our goal: 1) decrease the spin speed below 2000rpm, 2) refine the spin speed between 2000 and 8000 rpm or 3) increase the spin speed above 8000 rpm. Each of the tools available in the package will be used consecutively on the experimental data, described in relation to a conclusion based solely on observation, contrasted against an interpretation based on the numerical metrics. Using the full range of information available in "disLocate", we are able to distinguish between the three images with a degree of specificity that allows us to determine if it is feasible to reach our fictitious goal with this experimental procedure.

Based on the procedure described in the following sections, we were able to use **disLocate** to identify that increasing speed will increase the intermolecular spacing at the expense of the angular periodicity, and that an intermediate speed may be sufficient for our purposes. The full range of tools available in **disLocate** gave different insight into the quality and type of order present in the various samples. Using **disLocate** for spatial analysis would also allow us to quickly change experimental tactics if necessary (such as modifying solvents, temperature, or polymer) by providing an accurate trend with a limited amount of data.

2 Brief overview of "disLocate"

The **disLocate** package was developed to provide a series of automated tools to quantify the varying degrees of order that can exist within a given spatial distribution pattern. Though highly ordered patterns are relatively easy to classify, disordered or nearly ordered states as exist in a variety of biological and nanoscale systems are much more difficult to distinguish effectively.

Additionally, the trend in nanoscale research is for higher resolution images of smaller surface features. This limits the number of objects observed, which truncates the information each image has and decreases the effectiveness of a statistical approach. The resulting loss of information from limited long range order curtails the use of standard numerical techniques. It is entirely possible for researchers to mis-classify and assign a false positive to the reproducibility of their experiments by simply adapting generally used metrics designed for systems of many objects. This issue can be avoided by adopting a new set

of techniques which consist of structural metrics that can distinguish local differences in the observable structural order rather than solely relying on global averages of samples (though those are also available directly from the package if so desired).

Order on the local scale can be sub-categorized into three distinct types:

- Translational order occurs when every particle in the system has an exact position that repeats at a specific distance, defined by a specific translation period.
- Entropic order is the the amount of free volume (sections unoccupied by particle mass) encompassed by the system, where highly ordered systems have the lowest possible free volume (maximum density).
- Angular order relies on relative arc-separation of the "bonds" between a particle and its neighbours.

The expectation value for complete periodicity occurs when neighbours for any give particle have the same arc symmetry as well as being equidistant, with maximized covering area due to the equivalent position of each particle relative to all others. If any one of these types of order are not met, the system can be considered in a mesophase²⁸, such as that observed for plastic crystals (limited orientational or rotational order, but long range translational order)³⁰ or liquid crystals (limited translational order but long range angular order)³¹.

Each of these types of order requires a different tool to extract the desired information, as shown schematically in Figure 2. Positional order can be described probabilistically using the pair correlation function³² (Fig. 2 a & d). This tool counts the number of objects within a small shell at a distance away from a central particle and averaged over all particles in the system. Local free volume and the complementary metric, covering area³³, can be calculated by partitioning the substrate into a Voronoi tessellation around each individual particle (Fig. 2 a & d)³⁴. This routine draws a perpendicular line at the midpoint along the line-of-sight vector connecting nearest neighbours around every particle. Angular order can be calculated by using the bond order parameter³⁵, which compares the angle between the central particle and its closest neighbours against a specified symmetry basis vectors (Fig. 2 c & f). All of these methods have been widely used to characterize disorder, identify polycrystalline and disordered sections, and extract the probability of intermolecular spacings^{36,37}.

For comprehensive analysis, all of these techniques are bundled together as a set of tools in a freely distributable Mathematica package (disLocate.m) (available in the Supporting Information) to build sets of hierarchal metrics that can distinguish morphological subtleties. Table 1 outlines specific physical parameters that describe types of structural order within planar morphologies that can be analyzed with this package. The main thread that ties these tools together is the partitioning of space into local Voronoi tessellations around each particle as a basis for critical decision making on extent of order. The variation in each of the above metrics can be provided by the information contained within the Voronoi polygons unique to each particle. This provides the statistical basis for quantifying different dispersions with a confidence range that may be inaccessible due to the limited numbers of prepared samples.

3 Results

3.1 It is harder to distinguish differences in positional order when experiments have similar density

When defining order, the most common feature that humans consider quantifying is the positional structure – i.e. the relative distances between objects arranged in a particular pattern. Variations in density are typically the first noticeable feature observed between sets, before confirmation with counting of each individual object. Standard analytics such as number count (N), mean radius ($\langle r \rangle$), and the covering area (ϕ) are global structure metrics that describe density of a morphology on a surface. Table SI (Supporting information) outlines the calculated global values for the micelle system extracted from ImageJ. In each case, the number and covering density decrease with spin speed, but that is all the information we can extract. To extract the positional and symmetry data, a standard approach is to take the fast fourier transform (FFT) of the image^{38,39}. However, systems where these features are similar, such as the micellar systems in Fig. 1, require other tools to describe the varying types of order.

The positional structure of a dispersion describes how the number density of objects behave as a function of relative distances. One of the key measures is the average internal spacing between the centroid of objects. If the objects are evenly spaced out at specific distances by lateral translations of a repeated unit (unit cell), the periodic order can be easily understood and quickly recognized by observers. For two dimensional systems, these translations are limited to one of five Bravais lattices. For our fictitious goal to quantify and objectively distinguish the ideal experimental condition, the aim is to form a hexagonal (triangular) disperse lattice. In such hexagonal lattice, the distance between the object centres are all of the same length, separated by an angle of $2\pi/6$, such that a single object is surrounded by six equidistant neighbours. If the objects are touching (i.e. in a closed-packed array) the distance to finding another object is easily determined as twice the radius of the particle. This distance sets the minimum separation that can be between spherical objects. As the objects are not exactly touching in our desired arrangement, the centre to centre distance can instead be described by an effective radius (r_{hex}), half the distance between the object centres.

If the objects are arranged in a predictable lattice pattern (see Fig. 2i), the local density is identical to the global average density of particles, and is correlated to this radius. However, if there is no correlation between positional arrangement and density (as in Fig. 2ii), the pattern corresponds to a condition of complete spatial randomness. In such a condition, the position of each object is unrelated to any of the neighbour positions, suggesting no interactions between objects. The mean density does not correlate to any important structural feature, and as the pattern is arbitrary, there is no expectation that any experimental intervention will be able to reliably reproduce the observed pattern.

In between these two extremes, the spatially disordered systems can be characterized by internal distances between particles which vary slightly throughout the system. This implies that the density changes at a localized scale while retaining the average global density.

The pair correlation function $g(r)$ describes the radially averaged density as a global function of positional distance away from every particle (see Fig. 2a&d and Methods 4.4). In a perfect hexagonal lattice, this would result in delta functions with no positional variation at radial distances where neighbours are located on the unit lattice with known values⁴⁰ (see Fig. 3).

One way of quantifying the inter-object spacing is to use the maximum of the first peak of the pair correlation function, which are plotted in Figure 3(a). The values for these are outlined in Table SII (Supporting Information) which shows a trend of increasing spacing as the spin speed is increased, as expected. However, we require an accurate and reproducible value for this spacing to determine if our goal has been met in increasing the spacing to two micelle diameters. Instead of relying only on a single global value of probable spacing from the $g(r)$, we also implement a set of routines that can extract the mean local spacing from the Voronoi tessellations. Voronoi tessellations partition the space into sections that encompass the centroids of the objects in the system. This produces localized partitions that express the maximum space each particle can potentially possess. Each individual particle will produce a unique tessellation that corresponds directly to the relative position of its neighbours, which can give information on localized preferential structural order (see also section 3.2).

This method can be used to extract the mean expected spacing ($\langle 2r_{hex}^{vor} \rangle$) using the local density without measuring any distances between particles. The area of the Voronoi cells can additionally be used to directly calculate the effective radius $2r_{hex}$ that a hexagonal lattice would have to possess to have the same local Voronoi area.

This approach based on local Voronoi areas also provides a statistical distribution in the local density for which the variance in localized translational disorder can be extracted. We designate the intermolecular variance using the density located at particle positions as the bond disorder parameter (Δr). This variance information is generally difficult to extract directly from the $g(r)$.

As seen in Table SII (Supporting information), the mean expected localized spacing, ($\langle 2r_{hex}^{vor} \rangle$) is larger than the globally derived spacing from the effective radius or the $g(r)$. This is a direct result of global edge artifacts. As the particles in the image represent a subunit of a larger surface, the particles on the edge have neighbours outside the image that should contribute to the calculation of density. With an unknown local area outside of edge of the image, including edge particles resulting in an artificially lower total particle number and density, due to the increased ratio between the number of particles and the observed area. The Voronoi tessellation reduces the error associated with particles on the image edge, by allowing for the removal of such edge particles, to more accurately define the intermolecular area located at particle positions.

Using this refined effective intermolecular spacing, we observe that increasing the spin speed to 6000rpm achieves a value ~ 100 nm (see supporting information Table SII). As each micelle has an approximate diameter of 50 (nm) (supporting information Table SI), this spacing corresponds to our goal of achieving a sparse lattice of approximately two micelle diameters.

Having established that increasing the spin speed beyond 6000 rpm is effective in increasing the spacing, which was relatively easy to determine even using only the global metrics from the pair correlation function, one now needs to establish how well the translational order was preserved under those same conditions.

One key metric for order comes from the pair correlation function: the extent or degree of order can be inferred from the number of peaks that appear — each peak corresponds to another further neighbour. A delta function at twice, three or more times the effective radius, for example, would suggest that the order is long range. High probability of finding further neighbours where the lattice translations would predict them to be, as shown by peaks in the $g(r)$, is suggestive of order. As can be seen in the rest of Figure 3 (a), none of the $g(r)$ distributions for the micelles systems under different experimental conditions conform to a perfectly ordered lattice at the bottom (calculated using the number density of the 2000 rpm micelle image). However, as the density for each image is slightly different, it is difficult to make direct comparisons of the pair correlation function to judge any changes to the ordering from the change to the spin speed.

To accurately determine the degree of order, it is necessary to separate the information regarding relative spacing of particles from their probability for translational disorder. By normalizing the real-space distances to the intermolecular effective radius (the first nearest neighbour effective radius expectation value), it is possible to evenly quantify the deviation in positional order amongst samples. Figure 3 (b) outlines this normalization, such that all functions now share the first maximum peak at the same distance. The package automatically extracts the residual difference spectrum, $\Delta g(r)$,⁴¹ (figure 3 (b) top panel), which allows researchers to quickly determine the relative amount of positional fluctuation of particles relative to any reference data

set. Areas above the curve indicate more probability for particles to be at this normalized distance compared to the reference. The maximum $\Delta g(r)$ difference between the reference lattice occurs when the data has complete spatial randomness (i.e. no spatial correlation) and is minimized when the data exactly matches the reference.

As the hexagonal lattice is strictly defined by exact spatial translations in two dimensions, deviations necessarily mean that positional order is lost. However, with only slight disorder, the global features of near order are easily recognizable to most human viewers. It is common for researchers to use the spatial order classifications of “quasi-hexagonal”⁴² and “hexatic”^{43,44} to define systems that are close to hexagonal, often using spatial symmetry to define such a system (see section 3.3). In the pair correlation function, slight deviations of the particles in the vicinity of the global lattice positions will not change the mean particle spacings, and hence the neighbour peak positions; however, each of these peaks do experience a broadening of the peak widths to account for how the small fluctuations increase the chance for neighbours to be found at a different distance. The approach to determining the $\langle 2r_{hex}^{vor} \rangle$ intermolecular spacing provides a powerful tool to understand this behaviour. With the local Voronoi areas, a statistical distribution in the local density is found for which the variance in localized translational disorder can be extracted. We designate this as the bond disorder parameter (Δr). We propose, therefore, that the pair correlation function can also be used to quantitatively distinguish differences between patterns by systematic normalization to a new lattice: the “hexatic” lattice.

Using our tool set, a “hexatic” lattice is determined through an ensemble average of a hexagonal lattice which has been modified by randomly displacing the particles from their center with a mean distance relative to a normal probability distribution. The lattice disorder parameter (Δr) directly relates the random intermolecular displacement to the expected hexagonal spacing.

A larger value of Δr between one sample relative to another indicates more translational disorder (i.e. less positional correlation) by having higher spreads in the intermolecular distances. This way it provides a model to use the local density for quantifying random displacements located at particle positions. For the series of micelles deposited at different spin speeds, the lattice disorder parameter (Δr) (supporting information Table SII) increases with greater spin coating speed, suggesting that peaks are broadening in the pair correlation function, as is observed.

A single overlay comparison between a simulated hexatic lattice with the disorder parameter and an experimental micelle $g(r)$ is shown in Fig. 3 (c) with the distances normalized by the expected hexagonal spacing. To quantify differences in disorder outside the first neighbours, the $g(r)$ functions are also normalized by their maximum value (i.e. highest probability is at first neighbour diameter). The $\Delta g(r)$, pair correlation difference spectrum, again gives a snapshot view of how the experimental data deviates from the reference spectrum, in this case the slightly disordered hexatic lattice.

Hexagonal ordering has a unique feature in the $g(r)$ that corresponds to a splitting of the second shell of neighbours into two peaks, seen in Fig. 3 for both the hexagonal and hexatic lattices. If the second neighbour peaks overlap almost completely, and there are peaks in the pair correlation function centred around 1.75 and 2 normalized diameters, the system is much more likely to have long-range global hexagonal periodic order. This feature can be used as a quick test to determine if a pattern is likely to be hexatic, rather than possess another type of order. However, this examination is not definitive, as defects, polycrystallinity and disorder can also lead to splitting in the pair correlation function peaks⁴⁵⁻⁴⁷. Fig. 3(c) suggests that the 2000 rpm micelle data has hexatic order as indicated by large overlap between functions at both the second neighbour expected hexagonal spacings. The splitting of the second order peak exists, though the fitting is not as good for the peak centred around 2 normalized diameters, suggesting some sections that may have other spatial symmetries (square lattice, twinning defects, etc)⁴⁵⁻⁴⁷. The appearance of a peak close to that expected for the third nearest neighbour is also suggestive of global hexagonality, but the deviations between the experimental data and the hexatic lattice grow more pronounced as the distances increase, suggesting a large number of defects and grain boundaries. In data sets of limited particles, the pair correlation begins to fail at long distances, due to the missing information of particles who have intermolecular distances which lie outside the image. The region between the first and second neighbour shells (cross-hatched area in Fig. 3 (c)) also suggests that the micelles have more disorder than a pure hexatic lattice at these distances. Overall, the comparison to the hexatic lattice for the micelle data does suggest that there is a high degree of “hexatic” character for 2000 rpm spin speed, at least to the level of the second nearest neighbour shell, but with some defects.

For spin speed as a parameter, the local fluctuations in spatial positions increase as the hexagonal lattice spacing increases, leading to less “hexatic” character. The best fit “hexatic” lattice for the other spin speeds is given in supporting information Figure S1. With such a large Δr for 8000 rpm, the hexatic peaks broaden to the extent that there is almost an equal likelihood of finding a particle at any distance, similar to a liquid or glass. This is also supported by the average mean square displacement from the difference spectra, Δr_{ms} which increases as the hexagonal lattice spacing increases, due to the relative broadening of all the $g(r)$ peaks ($\Delta g(r)$ spectrum Fig. 3). This behaviour suggests that the spin-speed has multiple effects on the spatial order: the higher centripetal forces with increasing spin speed increases the intermolecular spacing while also increasing the amount of fluctuation between neighbours distances. This might suggest that the positional order is somewhat sacrificed when increasing the spacing using this approach. This is most evident for the highest spin speeds, which achieves the goal of increasing the spacing to twice the micelle radius, but appears to completely lose most of the positional hexagonal order. Lower

spin speeds, however, retain a hexatic formation while increasing the spacing by a lower amount. Using a combined method of implying both local and global density metrics, it is possible to amplify the key influence that experimental variation has on intermolecular spacing.

3.2 Extracting entropic force information by grouping particles with similar local bond structures

As described in section 3.1, the translational separation within point patterns is relatively easily recognized by both human and algorithmic observers if the metric is relaxed enough to allow for some small fluctuations. The variance in positional order is particularly helpful in determining the usefulness of particular experimental interventions. The lattice disorder parameter, however, only gives a global metric relating the deviations from a perfect lattice. It does not reveal if the deviations are uniformly dispersed, if these systems are polycrystalline – systems with areas of local order separated by defects – or if they exist in a mesophase, where some type of order (translational, entropic, or angular) is not satisfied.^{28,48} Though spatial disorder is fairly intuitive to classify, distinguishing between systems consisting of other types of order can be challenging for researchers.

The entropic order is related to the unoccupied areas in a given dispersion, that is, the free volume available. Necessarily, when the free volume is in the lowest possible state (i.e. maximum density), the system is in a highly ordered state. The drive to minimize the free volume, the entropic order, can therefore be harnessed to drive self-assembly, as has been observed recently for a variety of systems^{29,48-52}.

Particularly, in anisotropic systems (i.e. with non-spherical shapes^{48,51,53} or asymmetrically functionalized coated spheres^{52,54}), there is a driving force that aligns faceted or functionalized particles so as to maximize the system entropy by minimizing the free volume^{50,53}. The so called directional entropic force^{51,55} drives systems to complex structures. The anisotropic probability distribution describing the likely positions of neighbouring particles is analogous to that observed for chemical valence states⁵³.

In chemical systems, the valence defines the coordination number of an object: i.e. the number of neighbours to which the object is bonded. In the absence of bonds, as in our micelle systems, the entropic force yields a similar “coordination number” defined through the number of nearest neighbours. The drive to maximize local entropy is therefore related to the number of nearest neighbours, even for systems without any intrinsic anisotropy.

Observers have a hard time distinguishing the extent to which the free volume is minimized in a particular system. Due to the various neighbour definitions that exist⁵⁶, defining the neighbours correctly also poses challenges. The selection of neighbours is truly a binary selection criteria: it either fits the definition and is counted as a neighbour or it is rejected from analysis. Utilizing numerical methods allows for a more refined and accurate detection of neighbours than achievable by an observer alone. However, subtle differences in particle positions (i.e. numerical accuracy) can lead to the computer providing a neighbour list that may differ from ones provided by the qualitative decisions of an observer, leading to large differences in the classification of structures.

To achieve consistency in algorithmic classification, methodological numerical consistency should be favoured across comparators rather than variable definitions⁵⁷ that can change depending on the sample. In our package, the Voronoi tessellation are chosen as a robust method to calculate neighbours due to their invariability with respect to particle size and shape. Such an approach yields an unbiased definition for the coordination number for each object when the distance between particles is much larger than its size (low density)⁵⁶. The coordination number is defined through the number of Voronoi cell facets which contain the particle (see Fig. 2b & e). By partitioning each particle, Voronoi tessellations can be used to accurately calculate the entropic order through the minimization of the free volume around each particle.

Figure 4 outlines probability histograms for local coordination numbers for each spin speed of our micelle system, defined for ease of identification at the far left-hand side. Above (left hand side for each panel), the Voronoi tessellations for each image used to generate the histograms are shown. They are overlaid on a representation of the particle centroids, plotted using a colour scheme that highlights the positional arrangement of particles with similar coordination number.

For our micelle systems, which have roughly hexagonal symmetry arrangements, the coordination number for each particle is expected to be six (6) indicated in gray. All three systems show regions with the gray Voronoi cells of high hexagonal entropic order, within a larger area that is not globally perfectly hexagonal, (as already seen from the pair correlation analysis from section 3.1). With defects or local disorder, the steric frustration at the boundaries between large hexagonal sections will form pairs of Voronoi cells with alternating 5 and 7 sides. These are the so called “disclination” defects⁵⁸, where the local number of neighbours is violated. In an analogy with dislocations, which is a defect in positional order, a collection of such defects can define “grain boundaries” or areas of higher local free volume, between entropically ordered sections of the spatial distribution⁵⁹ (see Figure 5b). Further frustration of the free volume minimization can result in even further deviations from the ideal coordination number, with 4 or even 8 neighbour particles suggesting large entropic disorder.

The coordination histograms from Fig. 4 indicates that the lowest spin speed (2000 rpm) results in relatively more six neighbour particles than at higher spin speeds, supporting the finding from the positional order that the system is basically hexatic. Using the coordination number frequency alone, however, suggests that the higher spin speeds are basically indistinguishable

since the probability between having six neighbours and either 5 or 7 neighbours are similar.

The first neighbour maps (top right hand side) in Figure 4 shows how likely it is for the configuration to have particles with neighbours in a specific arc symmetry. This bond order⁵² or entropic valence⁴⁸ diagram is a similar representation to a 2D pair correlation function³¹ and has been used to measure disordered magnetic moments⁶⁰.

To build such a map, all particles are moved to a common origin, bringing with them the relative structure of neighbouring entropic “bonds” i.e. the coordination number and arc-separation angle. For each particle, each neighbour contributes a set of points to build up a probability distribution in space. The rigid objects that describe the entropic distributions are then rotated to have a common orientation. The position and angle of each neighbour is then plotted as a probability map, outlining the areas of preferred relative positions. The number of points each particle contributes is equal to its local coordination number. Regions of bright spots indicate higher chances of neighbours being at these positions.

Using the probability maps in Fig. 4 (top-right panel), it is now clear that the highest spin speeds lead to an isotropic distribution of particles, with the probability spread with little trends in angular order. On the other hand, the samples prepared with 2000 rpm and 6000 rpm spin-speeds are in a hexatic state as shown by the evenly spaced intensity of points around the particle at angles of $2\pi/6$.

The highest density entropic order is found if each neighbour is spaced evenly at angles of $\theta = 2\pi/\ell$ (also known as the angular order, described in more detail in section 3.3). In such cases, the coordination number, ℓ defines an expected arc-periodicity for neighbours, and can be used to determine the angular symmetry of the system.

This angular map can be further broken down by isolating subsets of particles based on their coordination number and grouping them together for analysis of the relative structure of set numbers of neighbours. This can allow for a high level comparison between the specific angular ordering that happens at the local particle level. This is particularly useful for the 5- and 7-fold disclination defects to indicate if there is some correlation between defects, through their angular distribution. Using this approach, therefore, exposes the hidden rotational symmetry of defects. These subset entropic valence maps are shown for the 5-, 6- and 7-neighbour angular distributions in the middle panels of Fig. 4. The common origin is coloured to identify the expected coordination number, using the colour scheme from the Voronoi tessellations.

For both the lowest and highest spin speeds, the five fold defects have no clear separation of intensity at the expected angles, suggesting that they are randomly distributed over the surface. However, the intermediate spin speeds, some symmetry can be observed for the five fold defects. This suggests that the defects are clustered together, leaving large areas of entropic hexagonal order in the system.

Using this entropic order analysis based on the coordination number and entropic valence maps, the various structures can be classified as follows: the low spin speeds yield a mesophase structure of high hexatic order, with random defects. The intermediate spin speed results in a “polycrystalline” system, with defects segregated to “grain boundaries” between regions of higher order. The Voronoi tessellation diagram indicates that there is one large hexagonal region, surrounded on three sides by areas of higher free volume. Higher speeds ultimately prevent the formation of even those regions, with random defects distributed randomly over the surface.

By using the Voronoi tessellations and entropic valence maps, it is clear that lower speeds are more favourable to extracting a mesophase hexatic system, where entropic order is preserved even though translational order is lost, as we desired in our fictitious goal. By segregating the ensemble into portions using the coordination number, the amount and distribution of defects can be extracted to separate specific local information from the ensemble average.

3.3 Detecting angular symmetry using the localized bond order

As discussed above, the highest density entropic order is found if each neighbour is spaced evenly at angles of $\theta = 2\pi/\ell$, where ℓ is the entropically or enthalpically derived coordination number. Angular orientation order describes the likelihood of finding an object at a given angular arc-separation between neighbouring particles, most commonly thought of as the symmetry state of a system.

Symmetry can be understood in the context of periodical translational order, where objects are separated by fixed distances, in a given direction. The Bravais lattices are defined by type, number and direction of the allowable translations defining the symmetry space group (i.e. in a square lattice, objects can have a neighbour above, below, to the left or to the right, yielding four-fold symmetric allowable translations). Similar to the description of entropic order, the coordination number or number of nearest neighbours, ℓ , drives the angular order, and this was taken advantage of in the previous section to describe the correlation of defects. Unlike for entropic order, which was related to the minimization of free space, the angular order relaxes the condition of maximal density; however, it imposes the condition that each neighbour is spaced evenly at angles of $\theta = 2\pi/\ell$.

Humans are particularly adept at recognizing symmetry, as it is the basis of human pattern recognition^{61,62}. If there are only a few particles or the positions have not deviated too far from the expected lattice positions, observers can usually extrapolate and distinguish if there is a different local symmetry at a given point (see Fig. 2 (c & f)). This perception and correct classification is highly dependent on a robust and consistent definition of the coordination number. However, as described in

section 3.2, algorithms are sometimes limited in their ability to distinguish neighbours by interpolating localized periodicity in the same way an observer might. Simultaneously, observers may introduce bias by selecting or rejecting improper neighbours though inconsistency. Unwanted bias by either approach can be introduced using only bond-network neighbour descriptions, such as the Delaunay neighbour definition for the coordination number⁵⁶. To overcome this problem, the bond order parameter q_ℓ can be utilized together with the coordination neighbours to explicitly distinguish particles which have the arc-symmetry we wish to tailor experiments toward. Specifically, we use the Voronoi-weighted Minkowski definition of the bond order parameter⁵⁶, which reduces the influence from neighbours that have metastable edges.

Defining the bond order in this way provides a benefit for researchers who are exploring particles arrays that have ordering arc-symmetries other than that for $\ell = 4$ (i.e. square lattices) and $\ell = 6$ (i.e. hexagonal lattice). Sections of particles with local 5-fold symmetry have been observed along disordered edges of self-assembled hard-spheres^{63,64}. Also, planar arrays of colloidal particles subjected to quasiperiodic light fields of 5-fold arrangement of lasers have been shown to direct the self organization into quasicrystalline colloids^{65,66}. These are dispersions of particles where the mix of multiple odd-integer symmetries of the lattices form complex structures that could easily be mis-classified by observers. In the next example, we emphasize a model system with two types of order to highlight the utility of using the bond order in "disLocate" to explore these hidden symmetries as ℓ is varied. This is done to precisely outline this complex behaviour, since in disordered material the effects are much more difficult to resolve.

In Figure 5(a), we present a simulated configuration of ($N = 256$) micelle particles under square confinement⁴¹. This type of self-assembly causes internal frustration of the particles and leads to a different ordering in the center than that around the wall⁶⁷. Hexagonal ordering can be observed at the walls while the square configuration imposed by steric frustration is in the center. As before, Voronoi tessellation of the centroids was taken and plotted using the colour scheme that highlights the coordination number (Fig. 5b). The majority of the system turns gray (6 neighbours) while disclination lines of alternating green/orange (5 and 7 neighbours respectively), separate the ordered "grains", originating at the corners. The steric frustration from interacting neighbours at arc-angles different than the expected $2\pi/6$ results in the local defects with 5 and 7-fold rotational symmetry. One thing that clearly stands out is the lack of Voronoi cells with 4 sides (dark blue) at the center. One consequence of using the coordination number definition for neighbours is that it may incorrectly over-count due to the metastable square Voronoi cell⁶⁸. In this case, subjective classification of local symmetry due to steric frustration is quickly seen while the numerical definition inaccurately identifies false neighbours using the expected particle spacings.

Fig. 5(c) shows an overlay of the the bond order parameter in symmetry basis $\ell = 4, 5, 6, 7$. These values are normalized by the expectation value for the given symmetry (see last entry of Table SIII (Supporting information) onto the same Voronoi tessellation shown in the coordination map shown in Fig. 5(b). Here, the dark shade represents bond order parameters that are heavily deviated away from the expected value while lighter and whiter sections are ones where in which they are closer to expectation values in that symmetry basis. Separating the rotational symmetries allows for an observer to judge the reliability of the internal structure as described by metrics using the coordination definition of neighbours. The expectation values for the hexagonal and square lattices are given in Table SIII (Supporting information).

In general, 6-fold bond order values (q_6) are reported in research without consideration for other symmetry values, as close packing of circles yields a hexagonal configuration. Looking only at q_6 in Fig. 5, most of the system is closer to white, suggesting that the system is relatively hexagonal as expected. The mean bond order parameter value in Table SIII (Supporting information) also gives a similar indication – that the system is mostly hexagonally ordered, with some disorder. One consequence with using only q_6 , however, is that disordered sections can take on values similar to that of the square pattern in the center, making it difficult to classify if there is angular ordering other than the 6-fold – all are just deviations from the expected value of q_6 for a hexagonal lattice. Table SIII (Supporting information) shows how different symmetry operations can take on non-zero values even for perfect lattices. Using the Voronoi tessellation coloured by 4-fold bond order values, q_4 , the 4-fold square configuration in the center can be isolated, as shown in the left-most panel of Fig. 5c.

However, disordered systems have variations in their intermolecular structures. There will be high probability for particles with coordination other than six, dispersed throughout the sample. Disordered states should produce bond orders values that converge towards a similar value in all symmetry basis. Table SIII (Supporting information) lists the values for a simulated dispersion of ($N = 5000$) pseudo-random point-particles to show the possible values when examining the fully disordered system. When dealing with disordered states with partial internal ordering, however, there can be correlations or distributions that are not captured solely by the single mean value (see Fig. 4). Experimentally, 5-fold localized structures have been observed to have correlations in partially disordered systems where 6-fold symmetry is expected⁶⁹. The exploration of multiple different symmetry types can reveal information often missed by either observers and/or computers⁷⁰ (also see section 3.2). In Fig. 5c, the 5-fold pentagonal configurations, q_5 matches almost exactly to the calculated 5 sided Voronoi cells. The 7-fold bond order parameter similarly targets the cells with coordination number of 7. The combination of 5 and 7-fold bond orders highlight the disordered boundaries that separate the square and hexagonal crystallites from each other, targeting the transition between highly ordered hexagonal and square states.

With that general framework, we can apply the same approach to the experimental micelle spin-speed series data. Table SIII (Supporting information) reports the mean values for the normalized bond orders for the three experimental data sets. For any given data set, the values do not seem very different from the randomly generated pattern. However, the trend in changing bond order parameters as the spin speed increases does give some insights into the angular ordering behaviour.

Using only q_4 and q_6 , as would be a common approach in the literature, suggests that low spin-speed produces relatively hexagonal packings with some low probability for square packing. By increasing this speed, the limited data set would suggest that the system transitions from hexagonal into a square lattice (as determined by the decrease in q_6 and increase in q_4). However, it is clear that q_5 and q_7 also increase with increasing spin speed. In general, if there is an increase in order or the transition from one type of order to another, higher ordered states will converge to the expected value for the maximum symmetry while decreasing all others. On the other hand, disordered states will produce bond orders values that converge towards a similar value in all symmetry bases, due to the broken local symmetry. This would also appear as an isotropic distribution of intensity in the entropic force map (see top panels of Fig. 4) for disordered systems; for ordered systems, the new symmetry state would emerge in the probability map (i.e. a square pattern would emerge if there were a transition from hexagonal to square). Therefore, from the trend of all four parameters, it can be concluded that increasing speeds cause a loss of hexagonal order in favour of more localized disorder, supporting the conclusions using the previous tools.

For the experimental data, the Voronoi maps coloured with the localized bond order (see supporting information Fig. S2) reflect the trends already identified – lowest spin speeds result in the largest regions of hexagonal order; as spin speed increases the disorder becomes randomized. The q_7 map, which is more useful in highlighting grain boundaries, gives a little more insight compared to the entropic analysis alone – the random defects at the lowest spin speed are actually more like a “grain boundary” separating two large hexagonal regions.

By using the Voronoi tessellations and bond order parameter, it is again clear that lower speeds are more favourable to extracting a mesophase hexatic system, where angular symmetry is preserved, as we desired in our fictitious goal. By examining the ensemble with both global and local bond order parameters of various arc-symmetry, the nature of the defects at lower speeds can be determined to be analogous to “grain boundaries” separating regions of higher order; at high speeds, due to the random distribution of defects, these dispersions are closer to complete spatial randomness.

4 Concluding remarks on combining numerical methods and visualizations

Structural characterization is a key aspect of reproducible experiments which allows for critical insight into the external factors which drive self-assembly. Robust comparisons between similar samples, especially with limited data sets, need a finely tuned ensemble of accurate analysis tools. We have combined a range of tools as a freely distributable Mathematica package (`disLocate.m`) which can be applied to any data set that contains spatial information.

Using the full range of tools available in **disLocate**, we examined as a representative example of AFM images of polystyrene-block-poly-2-vinylpyridine (PS-*b*-P2VP) diblock copolymer micelles distributed on a Si wafer surface with three different deposition approaches. From an analysis of the structures, we are able to distinguish them with a high degree of specificity, from a variety of perspectives. To illustrate the power of the tools in allowing a user to come to critical decisions about experimental protocols based on limited information, we established a fictitious goal: can the spin speed alone be used to increase the internal spacing of two micelle diameters between particles, while maintaining mostly hexagonal angular order, separated by limited regions of disorder or defects, making the surface polycrystalline. Based on our analysis of all the global mean and local variance information on the structure of each data set, it is clear that further experiments with varying spin speeds would not lead to our desired outcome, due to the conflicting influences on the various types of order in the micellar system. The slower spin speeds encourage the formation of a nearly hexagonal order, with some contained defects, but brings the particles closer together to increase the entropic order. Higher spin speeds are able to increase the spacing, but at the expense of angular order, resulting in a system that appears almost like complete spatial randomness. An intermediate spin speed seems to fulfill most of the requirements set out. Even though there are similar numbers of defects as at higher speeds, there are still regions of high hexatic order. However, this number of defects may be too high, as the hexagonal regions are about the same size as the disordered regions. Each piece of information gained by the tools gave different insight into the type and quality of the order. Based on the analysis provided by **disLocate**, we were able to narrow our choices for next methodological improvement depending on the desired importance of each ordering. If hexagonal dispersions are highly desired, then slower spin speeds are needed. If the priority is for larger intermolecular spacing, then higher speeds are necessary. To achieve different types of ordering with a density that was observed, then other factors may need to accompany the refinement in spin speeds (like temperature, or solvents) when it is set between these two ranges. By identifying that increasing speed will increase the intermolecular spacing at the expense of the angular periodicity, using **disLocate** for spatial analysis allows us to quickly change experimental tactics by providing an accurate trend with a limited amount of data.

Using the tools in the **disLocate** package, different structure metrics of single image patterns can be compared to quantify local variation in disorder through a variety of methods. Though researchers may use one or some of the tools outlined in this

contribution, the complete package allows one to easily and rapidly extract all of the different parameters in Table 1 to make robust conclusions on the order of a given system. Each state variable can be defined either as a single global description or as a local average value with uncertainties determined using internal variation as suits the intended purpose. We strove to remove unintentional user-introduced bias by advocating and implementing metrics based on the local variation in Voronoi tessellations as a way to promote consistency within the numerical analysis and interpretation of state variables between experimental setups. This package has been made available freely online. Using this package, researchers can quickly and easily quantify the experimental trends which produce desired morphologies and engineer novel methods which can direct self-assembly.

Methods

4.1 Software Availability

The code included with this manuscript is written as a (*.m) Mathematica Package. It currently supports Version 10 and above. Some highly optimized functions may require a local C compiler (such as Visual Studio, Clang, etc) for execution at full speed. Calling the package may cause a warning to appear, but these functions will still run without the compiler. The user manual is included with the package.

4.2 Data Availability

The raw AFM data that was used in this manuscript is bundled as example data inside the dislocate.zip file in Supporting Information. It also includes the xy positions extracted from imageJ and the height profiles from post-processing.

4.3 Experimental details

Polystyrene-block-poly-2-vinylpyridine (PS-b-P2VP) diblock co- polymer (Polymer source, P1330-S2VP) was dissolved in o-xylene (CALEDON) to form core-corona reverse micelles and kept under vigorous stirring for 18 h. Dynamic spin-coating (Speciality Coating Systems, SCS G3) at 2000, 6000 and 8000 rpm was used to produce an 2D monolayer array on 1cm Si(100) substrates with native oxide, diced from 6" wafers. The substrates were cleaned with acetone and ethanol in an ultrasonic bath, rinsed with deionized water, and dried in an N2 stream. Images of the micelle dispersions were analyzed using atomic force microscopy (AFM) in air in tapping mode with a phase locked loop (PLL) dynamic measurement board (NanoScopeIIIa, Veeco). The non-contact silicon tips were PPP-FMR-50 (NanosensorsTM) with a resonance frequency of 45-115kHz, a force constant of 0.5-9.5N/m and a tip radius of curvature ρ 10 nm. The AFM images were processed with WSxM (NanoTec).

4.4 Pair Correlation Function

The pair correlation function is a tool to analyze positional order. It is calculated using the probability of all distances between particles internal to the system. Every particle has a list of distances from its center to its sequential nearest neighbouring shells. An initial central particle a is chosen as the origin. A circular shell of width dr expands from the center to a radius distance r . Any particles inside a circular shell of width Δr are counted together and binned to produce the neighbour probability $n_n(r)$ as a function of distance.

$$g(r) = \frac{n_n(r)}{2\pi r \Delta r \rho} \quad (1)$$

As such, this function is sometimes described as "the radial distribution function", since it counts the distribution of neighbours over the radial spatial dimension. With this definition, information on angular orientation is lost in favour of positional probability.

The pair correlation function is not very well defined when samples consist of less than a few hundred particles. The micelle samples analyzed here are these kind of systems. To overcome these challenges, we've implemented a bootstrap technique to generate artificial systems that slightly deviate between them. This benefit allows for the smoothing of sharp features in the $g(r)$ which are artifacts of the finite number of intermolecular distances. Each micelle configuration was subjected to the same hexatic lattice procedure, where the molecules are randomly displaced around their centers by a fixed standard deviation. This value is associated with the experimental error, where particle centers are uncertain to within one pixel. Ensembles can be generated from randomly displacing the particles by the experimental error. For the micelle case, this ensemble was generated with 1000 independently shaken patterns with a Gaussian probability distribution using variance of half the experimental pixel size width (2.44 nm/pixel). This technique produces data that is analogous to multiple observations of the same area over different time periods. Slight variations in each observation will produce a set of particle coordinates that are not exactly identical. This is a key aspect in removing spurious peaks in the pair correlation function caused from finite data sets. These ensembles are solved together in a global average $g(r)$, the small displacements allow particles to hop between bins which smooths the probability distribution.

4.5 Hexatic Lattice

Density is correlated to the average intermolecular spacing between particles. Generating a proper periodic point pattern for an accurate comparison reference depends on a few key components. One is the number of particles (N) inside the window and the other is the area encompassed by that window (A_{box}). This number of particles per area defines the intensity (λ) and can be used to calculate the average spacing between neighbouring particles in the hexagonal state. $\lambda = \frac{N}{A_{box}}$

The goal is to find the radius of circular particle that would produce a Voronoi cell with exactly similar area to the one solved at the particle location.

The distance between two objects can be represented as close-packed (touching) circles with diameter ($2r_{hex}$) can be solved geometrically for the *hexagonal lattice spacing*. This equation is derived by solving for the apothem of a hexagon with area equal to the local Voronoi cell. $2r_{hex} = \sqrt{2/(\lambda\sqrt{3})}$

The total area of all the Voronoi cells must equal the total area from which the number of particles has been observed. $\lambda = \sum^N \frac{1}{A_{vor}}$

The resulting variation in local Voronoi volumes translates into a distribution of possible particle sizes, which can be estimated with a mean and variance. This mean is effective distance where in which intermolecular interactions and density are equalized. The variation in this effective distance represents the relative positional agitation of each particle at their location (i.e. the entropic portion of random local movements). The number of particles is constant while the the area changes. The local hexagonal radius at location i is a function of local Voronoi area (A_{vor}) only.

$$r_{hex}^i = \sqrt{A_{vor}^i (2\sqrt{3})^{-\frac{1}{2}}} \quad (2)$$

The uncertainty in mean intermolecular distance (Δr) can be calculated using a method of error propagation, using the Voronoi cell areas as the independent variable in the lattice spacing function (r_{hex}) and the standard deviation (Δu_r).

$$\Delta r = \sqrt{\left(\frac{\partial(r_{hex})}{\partial A_{vor}} \Delta u_r\right)^2} \quad (3)$$

The result can be modeled as a system where particles have a global mean spacing ($2r_{hex}$) but also fluctuate around the center ($r_0 = 0$) with a mean square displacement proportional to the local density variation.

$$(\Delta r)^2 = \langle r - r_0 \rangle^2 = Var(r_{hex})$$

4.6 Bond Order Parameter

The bond order parameter uses the angles between neighbours to calculate a metric that describes their arc distribution relative to a central particle. A reference frame needs to be chosen to properly assign angles and typically the horizontal (x)-axis is a common choice. Rotational symmetry can be exploited to define the bond order parameter in terms of any arbitrary axis using spherical harmonic functions. Consider a particle a which has a set of nearest neighbours $n_n = (b, c, d, \dots)$. Each neighbour is at an angle $\theta_{a(n_n)}$ relative to the reference frame vector and the neighbour vector.

$$q_\ell(i) = \left[\frac{4\pi}{2\ell+1} \sum_{m=-\ell}^{\ell} |Y_{\ell m}|^2 \right]^{1/2}, \quad (4)$$

where $Y_{\ell m}$ is spherical harmonic function with degree ℓ and order m .

$$|Y_{\ell m}|^2 = \left| \sum_{n_n} \frac{1}{n_n} Y_{\ell m}(\theta, \phi) \right|^2 \quad (5)$$

In the case of neighbours being defined using Voronoi coordination, the value of n_n (i.e. 1 / the number of classified neighbours) is replaced by a weighting function, determined by the length of the Voronoi facet (p_a) passing through its bond vector. This is then divided by the total sum of Voronoi facets from neighbours (p_{a_b}) / $\sum(p_{a_{n_n}})$ ⁵⁶, so that the total probability remains at unity. In two dimensions, the sum of Voronoi facets is the perimeter of the Voronoi cell and each facet is the line segment between central particle and its neighbour. The configuration average is the mean value of each local bond order associated with the particles in the system.

$$\langle q_\ell \rangle = \frac{1}{N} \sum_i^N q_\ell(i) \quad (6)$$

The normalized bond order is solved by dividing the mean bond order by the bond order associated with the highest neighbour configuration symmetry q_{ℓ}^{sym} which has ℓ neighbours with arc separation angle ($\theta = 2\pi/\ell$).

References

1. Boles, M. A., Engel, M. & Talapin, D. V. Self-Assembly of Colloidal Nanocrystals: From Intricate Structures to Functional Materials. *Chem. Rev.* **116**, 11220–11289 (2016). DOI 10.1021/acs.chemrev.6b00196.
2. Protonotarios, E. D., Baum, B., Johnston, A., Hunter, G. L. & Griffin, L. D. An absolute interval scale of order for point patterns. *J. The Royal Soc. Interface* **11** (2014).
3. Ebbesen, T. W., Lezec, H. J., Ghaemi, H. F., Thio, T. & Wolff, P. A. Extraordinary optical transmission through sub-wavelength hole arrays. *Nat.* **391**, 667–669 (1998). DOI 10.1038/35570.
4. Quint, S. B. & Pacholski, C. Getting real: Influence of structural disorder on the performance of plasmonic hole array sensors fabricated by a bottom-up approach. *J. Mater. Chem. C* **2**, 7632–7638 (2014). DOI 10.1039/C4TC01244E.
5. Augu  , B. & Barnes, W. L. Diffractive coupling in gold nanoparticle arrays and the effect of disorder. *Opt. Lett., OL* **34**, 401–403 (2009). DOI 10.1364/OL.34.000401.
6. Pouya, C., Stavenga, D. G. & Vukusic, P. Discovery of ordered and quasi-ordered photonic crystal structures in the scales of the beetle *Eupholus magnificus*. *Opt. Express, OE* **19**, 11355–11364 (2011). DOI 10.1364/OE.19.011355.
7. Albooyeh, M. *et al.* Resonant metasurfaces at oblique incidence: Interplay of order and disorder. *Sci. Reports* **4**, 4484 (2014). DOI 10.1038/srep04484.
8. Chen, C. S., Mrksich, M., Huang, S., Whitesides, G. M. & Ingber, D. E. Geometric Control of Cell Life and Death. *Sci.* **276**, 1425–1428 (1997). DOI 10.1126/science.276.5317.1425.
9. Cavalcanti-Adam, E. A. *et al.* Cell Spreading and Focal Adhesion Dynamics Are Regulated by Spacing of Integrin Ligands. *Biophys. J.* **92**, 2964–2974 (2007). DOI 10.1529/biophysj.106.089730.
10. Lehnert, D. *et al.* Cell behaviour on micropatterned substrata: Limits of extracellular matrix geometry for spreading and adhesion. *J. Cell Sci.* **117**, 41–52 (2004). DOI 10.1242/jcs.00836.
11. Ow-Yang, C. *et al.* Work function tuning of tin-doped indium oxide electrodes with solution-processed lithium fluoride. *Thin Solid Films* **559**, 58–63 (2014). DOI 10.1016/j.tsf.2013.11.035. The International Symposium on Transparent Oxide and Related Materials for Electronics and Optics. May 13–15, 2013.
12. Turak, A., Aytun, T. & Ow-Yang, C. W. Solution processed LiF anode modification for polymer solar cells. *Appl. Phys. Lett.* **100**, 253303 (2012). DOI 10.1063/1.4729932.
13. Kruss, S. *et al.* Stimulation of Cell Adhesion at Nanostructured Teflon Interfaces. *Adv. Mater.* **22**, 5499–5506 (2010). DOI 10.1002/adma.201003055.
14. Graeter, S. V. *et al.* Mimicking Cellular Environments by Nanostructured Soft Interfaces. *Nano Lett.* **7**, 1413–1418 (2007). DOI 10.1021/nl070098g.
15. Selhuber, C., Bl  mmel, J., Czerwinski, F. & Spatz, J. P. Tuning Surface Energies with Nanopatterned Substrates. *Nano Lett.* **6**, 267–270 (2006). DOI 10.1021/nl052256e.
16. Mbenkum, B. N., Barrera, E., Kelsch, M. & Dosch, H. Selective Growth of Organic 1-D Structures on Au Nanoparticle Arrays. *Nano Lett.* **6**, 2852–2855 (2006). DOI 10.1021/nl062057a.
17. K  stle, G. *et al.* Micellar Nanoreactors—Preparation and Characterization of Hexagonally Ordered Arrays of Metallic Nanodots. *Adv. Funct. Mater.* **13**, 853–861 (2003). DOI 10.1002/adfm.200304332.
18. Pileni, M. P. Reverse micelles as microreactors. *The J. physical chemistry* **97**, 6961–6973 (1993).
19. Spatz, J. P. *et al.* Ordered Deposition of Inorganic Clusters from Micellar Block Copolymer Films. *Langmuir* **16**, 407–415 (2000). DOI 10.1021/la990070n.
20. Yu, H. & Turak, A. Nanoreactors or nanoscale stabilizers: Routes for solution processed indium tin oxide nanoparticles by reverse micelle deposition. *Can. J. Phys.* **92**, 797–801 (2014). DOI 10.1139/cjp-2013-0549.
21. Gu, X., Gunkel, I. & Russell, T. P. Pattern transfer using block copolymers. *Phil. Trans. R. Soc. A* **371**, 20120306 (2013). DOI 10.1098/rsta.2012.0306.
22. Hur, J. & Won, Y.-Y. Fabrication of high-quality non-close-packed 2D colloid crystals by template-guided Langmuir–Blodgett particle deposition. *Soft Matter* **4**, 1261–1269 (2008). DOI 10.1039/B716218A.

23. Krishnamoorthy, S., Pugin, R., Brugger, J., Heinzlmann, H. & Hinderling, C. Tuning the Dimensions and Periodicities of Nanostructures Starting from the Same Polystyrene-block-poly(2-vinylpyridine) Diblock Copolymer. *Adv. Funct. Mater.* **16**, 1469–1475 (2006). DOI 10.1002/adfm.200500524.
24. Schneider, C. A., Rasband, W. S. & Eliceiri, K. W. NIH Image to ImageJ: 25 years of image analysis. *Nat. Methods* **9**, 671–675 (2012). DOI 10.1038/nmeth.2089.
25. Stein, H. S., Jiao, S. & Ludwig, A. Expediting Combinatorial Data Set Analysis by Combining Human and Algorithmic Analysis. *ACS Comb. Sci.* **19**, 1–8 (2017). DOI 10.1021/acscombsci.6b00151.
26. Burda, C., Chen, X., Narayanan, R. & El-Sayed, M. A. Chemistry and Properties of Nanocrystals of Different Shapes. *Chem. Rev.* **105**, 1025–1102 (2005). DOI 10.1021/cr030063a.
27. Frenkel, D. Soft condensed matter. *PHYSICA A* **313**, 1–31 (2002).
28. Agarwal, U. & Escobedo, F. A. Mesophase behaviour of polyhedral particles. *Nat Mater* **10**, 230–235 (2011). DOI 10.1038/nmat2959.
29. Thapar, V., Hanrath, T. & Escobedo, F. A. Entropic self-assembly of freely rotating polyhedral particles confined to a flat interface. *Soft Matter* **11**, 1481–1491 (2015). DOI 10.1039/C4SM02641A.
30. Timmermans, J. Plastic crystals: A historical review. *J. Phys. Chem. Solids* **18**, 1–8 (1961). DOI 10.1016/0022-3697(61)90076-2.
31. Bernard, E. P. & Krauth, W. Two-Step Melting in Two Dimensions: First-Order Liquid-Hexatic Transition. *Phys. Rev. Lett.* **107**, 155704 (2011). DOI 10.1103/PhysRevLett.107.155704.
32. Kirkwood, J. G. & Boggs, E. M. The Radial Distribution Function in Liquids. *J. Chem. Phys.* **10**, 394–402 (1942). DOI 10.1063/1.1723737.
33. Williamson, J. J. & Evans, R. M. L. Measuring local volume fraction, long-wavelength correlations, and fractionation in a phase-separating polydisperse fluid. *The J. Chem. Phys.* **141**, 164901 (2014). DOI 10.1063/1.4897560.
34. Okabe, A., Boots, B., Sugihara, K. & Chiu, S. *Spatial Tessellations: Concepts and Applications of Voronoi Diagrams*. Wiley Series in Probability and Statistics (Wiley, Hoboken, NJ, USA, 2000).
35. Steinhardt, P. J., Nelson, D. R. & Ronchetti, M. Bond-orientational order in liquids and glasses. *Phys Rev B* **28**, 784–805 (1983). DOI 10.1103/PhysRevB.28.784.
36. Rankin, D. W. H., Mitzel, N. & Morrison, C. *Structural Methods in Molecular Inorganic Chemistry* (Wiley, Chichester, West Sussex, United Kingdom, 2013).
37. Ladd, M. & Palmer, R. *Structure Determination by X-Ray Crystallography* (Springer US, Boston, MA, 2013).
38. Magonov, S. N. & Whangbo, M.-H. *Surface Analysis with STM and AFM: Experimental and Theoretical Aspects of Image Analysis* (John Wiley & Sons, 2008). Google-Books-ID: nheUWMPiB5wC.
39. Bharati, M. H., Liu, J. J. & MacGregor, J. F. Image texture analysis: Methods and comparisons. *Chemom. Intell. Lab. Syst.* **72**, 57–71 (2004). DOI 10.1016/j.chemolab.2004.02.005.
40. Ebert, F., Keim, P. & Maret, G. Local crystalline order in a 2D colloidal glass former. *Eur. Phys. J. E* **26**, 161–168 (2008). DOI 10.1140/epje/i2007-10270-8.
41. Bumstead, M., Arnold, B. & Turak, A. Reproducing morphologies of disorderly self-assembling planar molecules with static and dynamic simulation methods by matching density. *Phys. A: Stat. Mech. its Appl.* **471**, 301–314 (2017). DOI 10.1016/j.physa.2016.12.075.
42. Gonzalo-Juan, I. *et al.* Dipole moment-tuned packing of TiO₂ nanocrystals into monolayer films by electrophoretic deposition. *Appl. Phys. Lett.* **105**, 113108 (2014). DOI 10.1063/1.4896133.
43. Nelson, D. R. Reentrant melting in solid films with quenched random impurities. *Phys. Rev. B* **27**, 2902–2914 (1983). DOI 10.1103/PhysRevB.27.2902.
44. Halperin, B. I. & Nelson, D. R. Theory of Two-Dimensional Melting. *Phys. Rev. Lett.* **41**, 121–124 (1978). DOI 10.1103/PhysRevLett.41.121.
45. Egami, T. & Poon, S. J. Atomic structure of quasicrystals. *Mater. Sci. Eng.* **99**, 323–329 (1988). DOI 10.1016/0025-5416(88)90350-3.
46. Barnard, A. S. Modelling of nanoparticles: Approaches to morphology and evolution. *Rep. Prog. Phys.* **73**, 086502 (2010). DOI 10.1088/0034-4885/73/8/086502.

47. Zhang, K., Li, H., Li, L. & Bian, X. F. Why does the second peak of pair correlation functions split in quasi-two-dimensional disordered films? *Appl. Phys. Lett.* **102**, 071907 (2013). DOI 10.1063/1.4793187.
48. van Anders, G., Klotsa, D., Karas, A. S., Dodd, P. M. & Glotzer, S. C. Digital Alchemy for Materials Design: Colloids and Beyond. *ACS Nano* **9**, 9542–9553 (2015). DOI 10.1021/acsnano.5b04181.
49. Young, K. L. *et al.* A Directional Entropic Force Approach to Assemble Anisotropic Nanoparticles into Superlattices. *Angew. Chem. Int. Ed.* **52**, 13980–13984 (2013). DOI 10.1002/anie.201306009.
50. Agarwal, U. & Escobedo, F. A. Effect of quenched size polydispersity on the ordering transitions of hard polyhedral particles. *The J. Chem. Phys.* **137**, 024905 (2012). DOI 10.1063/1.4734021.
51. Damasceno, P. F., Engel, M. & Glotzer, S. C. Crystalline Assemblies and Densest Packings of a Family of Truncated Tetrahedra and the Role of Directional Entropic Forces. *ACS Nano* **6**, 609–614 (2012). DOI 10.1021/nn204012y.
52. Damasceno, P. F., Engel, M. & Glotzer, S. C. Predictive Self-Assembly of Polyhedra into Complex Structures. *Sci.* **337**, 453–457 (2012). DOI 10.1126/science.1220869.
53. van Anders, G., Ahmed, N. K., Smith, R., Engel, M. & Glotzer, S. C. Entropically Patchy Particles: Engineering Valence through Shape Entropy. *ACS Nano* **8**, 931–940 (2014). DOI 10.1021/nn4057353.
54. Cayre, O., Paunov, V. N. & Velev, O. D. Fabrication of asymmetrically coated colloid particles by microcontact printing techniques. *J. Mater. Chem.* **13**, 2445–2450 (2003). DOI 10.1039/B308817K.
55. van Anders, G., Klotsa, D., Ahmed, N. K., Engel, M. & Glotzer, S. C. Understanding shape entropy through local dense packing. *Proc. Natl. Acad. Sci.* **111**, E4812–E4821 (2014). DOI 10.1073/pnas.1418159111.
56. Mickel, W., Kapfer, S. C., Schröder-Turk, G. E. & Mecke, K. Shortcomings of the bond orientational order parameters for the analysis of disordered particulate matter. *The J. Chem. Phys.* **138**, 044501 (2013). DOI 10.1063/1.4774084.
57. Higham, J. & Henchman, R. H. Locally adaptive method to define coordination shell. *The J. Chem. Phys.* **145**, 084108 (2016). DOI 10.1063/1.4961439.
58. Murayama, M., Howe, J. M., Hidaka, H. & Takaki, S. Atomic-Level Observation of Disclination Dipoles in Mechanically Milled, Nanocrystalline Fe. *Sci.* **295**, 2433–2435 (2002). DOI 10.1126/science.1067430.
59. Barón, M. Definitions of basic terms relating to low-molar-mass and polymer liquid crystals (IUPAC Recommendations 2001). *Pure Appl. Chem., PAC* **73**, 845–895 (2001). DOI 10.1351/pac200173050845.
60. Beleggia, M. & Frandsen, C. Measuring magnetic correlations in nanoparticle assemblies. *J. Physics: Conf. Ser.* **521**, 012009 (2014). DOI 10.1088/1742-6596/521/1/012009.
61. van der Helm, P. A. & Leeuwenberg, E. L. J. Goodness of visual regularities: A nontransformational approach. *Psychol. Rev.* **103**, 429–456 (1996). DOI 10.1037/0033-295X.103.3.429.
62. Wagemans, J. Characteristics and models of human symmetry detection. *Trends Cogn. Sci.* **1**, 346–352 (1997). DOI 10.1016/S1364-6613(97)01105-4.
63. Karayiannis, N. C., Malshe, R., de Pablo, J. J. & Laso, M. Fivefold symmetry as an inhibitor to hard-sphere crystallization. *Phys. Rev. E* **83**, 061505 (2011). DOI 10.1103/PhysRevE.83.061505.
64. Karayiannis, N. C., Malshe, R., Kröger, M., de Pablo, J. J. & Laso, M. Evolution of fivefold local symmetry during crystal nucleation and growth in dense hard-sphere packings. *Soft Matter* **8**, 844–858 (2012). DOI 10.1039/C1SM06540H.
65. Mikhael, J. *et al.* Proliferation of anomalous symmetries in colloidal monolayers subjected to quasiperiodic light fields. *PNAS* **107**, 7214–7218 (2010). DOI 10.1073/pnas.0913051107.
66. Mikhael, J., Gera, G., Bohlein, T. & Bechinger, C. Phase behavior of colloidal monolayers in quasiperiodic light fields. *Soft Matter* **7**, 1352–1357 (2011). DOI 10.1039/C0SM00486C.
67. Díaz Ortiz, A., Arnold, B., Bumstead, M. & Turak, A. Steric self-assembly of laterally confined organic semiconductor molecule analogues. *Phys. Chem. Chem. Phys.* **16**, 20228 (2014). DOI 10.1039/C4CP02331E.
68. McDonald, M. J., Yethiraj, A. & Beaulieu, L. Y. A method to characterize structure and symmetry in low-resolution images of colloidal thin films. *Meas. Sci. Technol.* **23**, 045606 (2012). DOI 10.1088/0957-0233/23/4/045606.
69. Wochner, P. *et al.* X-ray cross correlation analysis uncovers hidden local symmetries in disordered matter. *Proc. Natl. Acad. Sci.* **106**, 11511–11514 (2009).
70. Cliffe, M. J. & Goodwin, A. L. Quantification of local geometry and local symmetry in models of disordered materials. *Phys. Status Solidi B* **250**, 949–956 (2013). DOI 10.1002/pssb.201248553.

Acknowledgements

The authors would like to thank the staff at Compute Canada in helping with and providing the computational resources that were essential to this study. This work was made possible by the facilities of the Shared Hierarchical Academic Research Computing Network (SHARCNET: www.sharcnet.ca) and Compute/Calcul Canada. The authors also thank A. Diaz-Ortiz for helpful discussions and suggestions and E. Cranston for access to the AFM for measurements. This research was supported by 436100-2013 RGPIN, 384889-2010 CREAT, and ER15-11-123.

Author contributions statement

M.B wrote the **disLocate** package and performed all the analysis. K.L, G.H, L.S.H produced the samples and images used. A.T. and M.B. conceived the project and wrote the paper. All authors reviewed the manuscript.

Additional information

Competing financial interests

The author(s) declare no competing financial interests.

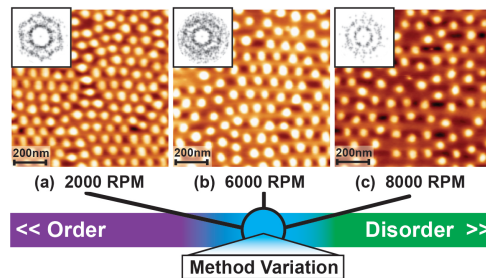


Figure 1. (colour online) Atomic force micrographs of diblock copolymer reverse micelles (PS-b-P2VP) with varying spin-coating spin-speed (a) 2000 RPM, (b) 6000 RPM, and (c) 8000 RPM, showing varying spatial order. AFM images are inset with Fourier transforms of the micelle centers, showing similar planar topographies.

Table 1. Summary of physical observables and the tool within "disLocate" that has the ability quantify them. The global observable refers to an invariant between different observers, either by simplicity of counting or common routines. The mean local reference utilizes the internal properties of the single data set to determine an expected mean for the physical properties. The variations are products of defining these metrics with as localized parameters. It should be noted that additional confidence in specific metrics can be enhanced by capturing the structural variation from another one of the analysis tools, since the variation will have a correlated influence between these through the Voronoi partitions.

	Global Observable	Mean Localized Reference	Disorder Variance and Confidence
Intermolecular Spacing	Pair Correlation $g(r)_{\max}^{\text{1st}}$	Expected Hexagonal Lattice $2r_{\text{hex}}$	Hexatic Mean Displacement Δr
Entropic Coordination	First Neighbour Shell $g(r)_{\text{shell}}^{\text{1st}}$	Coordination Bond Structure of symmetry ℓ Figure 4	Ratio of Coordination $N_{(\ell)}/N_{(\ell)_6}$
Angular Symmetry	Hexagonal Bond Order $\langle q_6 \rangle / q_6^{\text{hex}}$	ℓ -fold Bond Order $\langle q_\ell \rangle / q_\ell^{\text{sym}}$	Deviation in q_ℓ from Random $\Delta q_5 \Delta q_7$

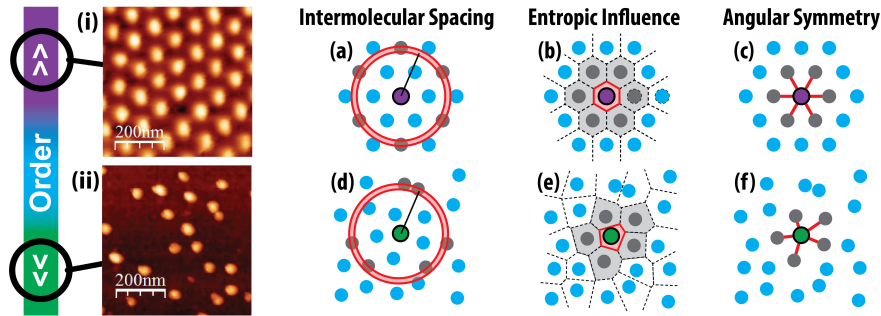


Figure 2. (left) Self-assembled morphologies land somewhere between highly ordered systems (top) and one with very low density (bottom). Two key factors at classifying disorder are simultaneously in competition with each other: limitations on perception misguides us into seeing patterns in randomness while our imprecise ability to distinguish between similar patterns misses subtle differences. To remove unwanted bias, numerical order metrics are utilized to characterize the morphology located at particle positions: pair correlation function (a & d), Voronoi tessellations (b & e), and the bond order parameter (c & f).

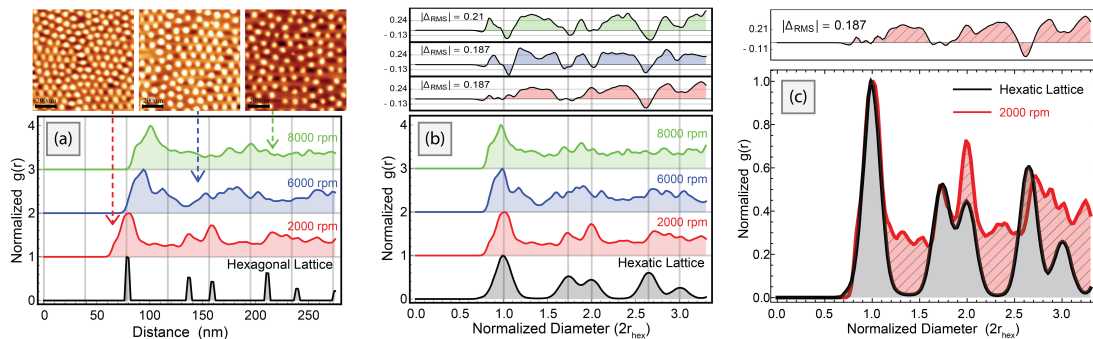


Figure 3. (colour online) Pair correlation functions of centroids obtained from AFM images of diblock copolymer reverse micelles PS-b-P2VP. (a) Measurements of objects shows that the peak positions are misaligned. This implies the average spacing between micelles changes. (b) Normalizing the distance to the average spacing ($2r_{\text{hex}}$) of a hexagonal lattice with the same number density (located at particle positions) collapses the distributions into a shared spatial reference frame where peak positions can easily be compared. (c) The differences in $g(r)$ is shown as red thatched sections on an overlay of both functions from 2000 rpm micelle distributions and the best matched hexatic lattice. The widths of these peaks correspond to the average mean displacement each particle has relative to this expected spacing. The inset above (b) and (c) shows the difference spectrum, which is the subtraction between a pair correlation function and the hexatic lattice.

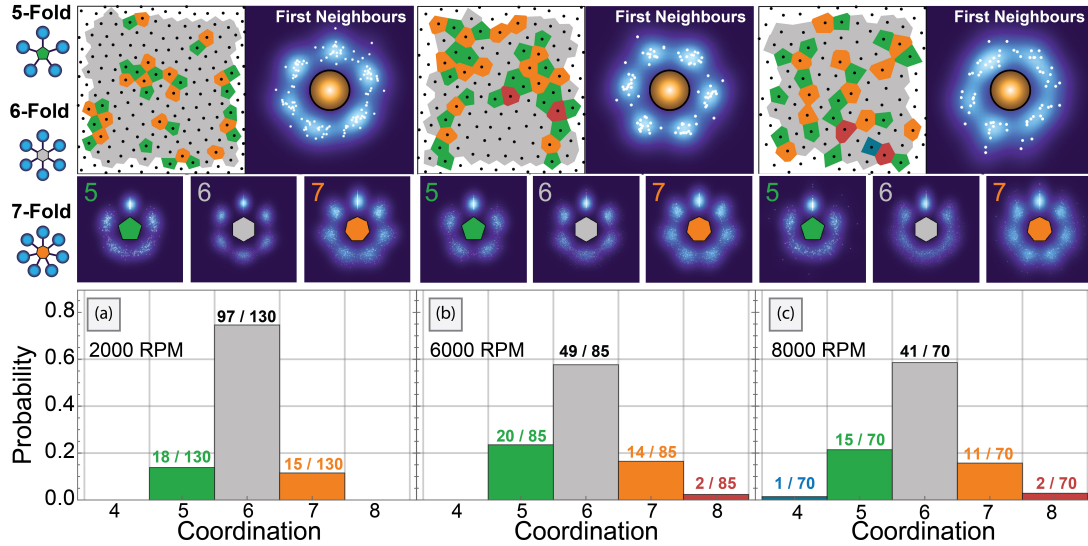


Figure 4. (colour online) Angular classification of coordination neighbours within micelle configurations observed by AFM. Coordination numbers are calculated using the Voronoi tessellations (top panels left), given in a histogram of the probabilities for each coordination number (bottom panels). Particles are translated to have a common origin so as to build a planar probability map of first neighbour (entropic force map) in relation to the particle center (top panels right). Particles are then separated by their coordination number and remapped to observe correlation between the expected angular symmetry (shown on the far left) and the rotational order of neighbours (middle panels). Bond-structures are rotated to have a common orientation (y-axis) so to show disordered states as blurred rings at the bottom (negative y-axis) and ordered states as sharp bright spots. Experimental spin speeds (a) 2000 rpm (b) 6000 rpm (c) 8000 rpm.

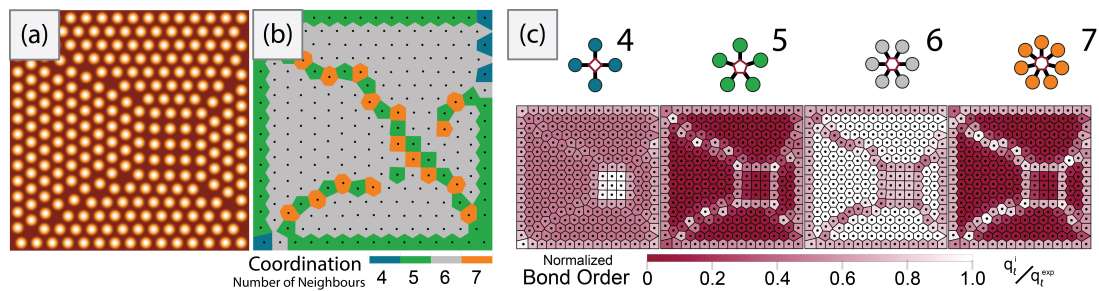
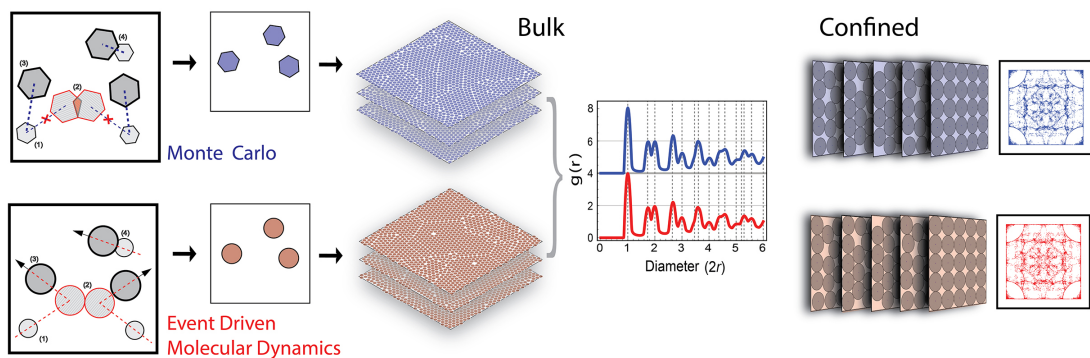


Figure 5. (colour online) (a) Simulated micelles in a confined square boundary. An observer may expect for particles in the center to have 4 neighbours, but this is not the case for the coordination number. (b) Voronoi tessellation of the micelle centroids coloured by the number of shared facets. (c) Voronoi tessellations coloured by the normalized bond order parameter for the type of symmetry (above). Whiter areas indicate particles that have high angular order in that symmetry basis. Particles with 5 and 7 neighbours highlight the grain boundaries and dislocation lines in their respective symmetry basis. The separation between square and hexagonal configurations are not detected in the Voronoi tessellation as having 4 neighbours, however it can be seen in the bond order with symmetry $\ell = 4$.

Chapter 5

Comparing morphology between ensembles of many configurations with similar density



Comparing morphologies from two simulation methods: Monte Carlo (blue) and Event-Driven Molecular Dynamics (red). When the density is fixed, will the resulting morphologies of bulk phase particles and confined patterns show similar structural trends?

5.1 My Contributions

My contributions to this publication was mainly in developing the simulation experiment to answer the question: do these two simulation methods (event-driven molecular dynamics and Monte Carlo) produce the same morphologies? The reason that this question needed to be answered is to gain confidence that our previously developed Monte Carlo simulation was accurately representing the natural phenomena of steric self-assembly. The main motivation was to simulate the condensation of molecules and observe the influence that molecular shape has on the resulting morphology. If it is not producing morphologies consistent with nature, then this method should be rejected in favour of one that does. The result of this investigation was a publication in *Physica A* that summarizes our findings.

Dr. Ayse Turak, Dr. Alejandro Diaz Ortiz, and Matt Bumstead collectively decided to benchmark our Monte Carlo code against a similar method that uses event-driven molecular dynamics (EDMD) to evolve the system [100]. The EDMD protocol tracks collisions with event-integrated positional movement of particles as the global density is reduced. Our Monte Carlo simulation interprets the positional uncertainty between sequential observations (simulation inflation steps) as being caused by thermal motion and implements random trial displacements surrounding the previously accepted positions to acquire an equilibrium microstate with higher density. It was unclear if our statistical mechanics approach to modelling condensation as a series of static states was continuously in equilibrium. If these two methods produce similar outcomes in the limit where they simulate the same objects to have the same density distribution, then we can say that when the objects are changed to embody complex shape then the resulting morphology should also be predictable with molecular dynamics techniques. In the work that I did for this manuscript, I determined that this was true for circular particles. This provided evidence that our Monte Carlo simulations are properly exploring the thermodynamic phases and allowed for new investigations into how morphology changes with molecular shape.

A set of criteria that can be normalized across both simulation methods was needed to isolate the influence of each simulation method by removing the influence from variations between protocols. Since each simulation has a different algorithmic implementation, there is no a set of standard protocols (user inputs, initial conditions) which represents the same assembly phenomena. Phase changes in hard glassy colloidal systems are density dependent [31], which suggests that density is main parameter which determines the resulting morphology. This observable parameter was used as a constant standard across each simulation to test the deviations between internal morphology. Large ensembles of configurations from both methods were produced such that the probability for them to generate patterns with the same density was statistically similar. By using an iterative optimization approach to generate ensembles with varying protocols, I found a set for EDMD which produced patterns that minimized the differences between covering density profiles from each of the two methods (see Section 5.3.1).

To assess structural similarity in both ensembles, I used analysis metrics such as the bond order parameter [97], the pair correlation function [101], and Voronoi tessellations. These tools were from external research groups and had open source implementations that where written in different coding languages, making them laborious to utilize fully and challenging to distribute updates to routines amongst the research group at the Organic Electronic Interfaces lab. Also, these single set functions were not exactly consistent among implementations and did not seem to work well when used together. My work has brought these different tools together to use in this publication and to start building our own tool set package “disLocate” (See: Chapter 4). This was a key component of my work since these external codes allowed me to test and benchmark the newer routines involving equations relating to new structure metrics. What we concluded was that the statistical description of the varying types of morphological order was similar between simulation methods in the case where the density distributions of tested configurations were fixed.

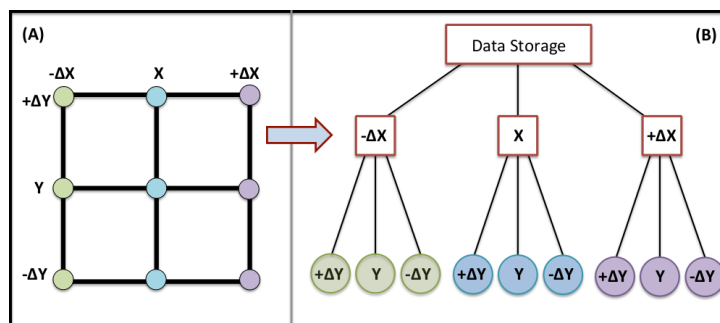


Figure 5.1: Optimizing folders for large data sets to search parameter space. (a) Varying two parameters X and Y by $\pm\Delta$ creates a grid. (b) Data is more accessible when it is stored within a hierarchical subfolder system of protocols.

5.2 Overview of Manuscript (Physica A - 2017)

Numerical simulations can provide a unique insight into the self-assembly of molecules. However, it is critically important that these simulations accurately describe behaviour observed in nature. The morphologies produced from simulations may not be fully physical and may lead to incorrect models. To make sure our own simulation method is correct, we benchmarked it against event-driven molecular dynamics [100] using the same internal restrictions, like number and shape of the particles. This was done to prove that for simple shapes, both codes would reproduce morphologies that are similar to each other. If these simulations produce the same morphologies with circular particles, then we have confidence that the configurations produced with complexly shaped particles would be one that is accurately described by natural process.

This manuscript outlines how we were able to quantify the internal structures of molecular dispersions produced using both simulation methods. Statistical ensembles of many independently run simulations were generated under a common protocol and their configurations were grouped together for analysis. Finding a common set of initial conditions between the two simulation methods was dropped in favour of protocols which could produce morphologies with the density and with the same probability. Once we were able to do this, structural analysis tools were used to directly compare the resulting morphologies by mapping the order-space of ensembles. We conclude that when the densities are the same, Monte Carlo and EDMD simulations modelling excluded-volume particles will produce configurations with similar intermolecular structure.

The sections below highlight portions of my research that did not appear in the manuscript and/or were part of the supporting information associated with this publication. Section 5.3 highlights information about the EDMD simulation and our experience with it. These topics include: how the density distributions were matched using an iterating protocol search, the behaviour of varying EDMD protocols, and the instability of EDMD and its execution timing. Section 5.4 presents the set of protocols we found for EDMD that produced configurations with similar densities and at similar frequencies to those generated with the Monte Carlo method. Section 5.5 outlines one noticeable difference in the morphologies which suggests it is unlikely for Monte Carlo to simulate point defects. These are also hard to quantify numerically, but extremely easy to find in the visual rendering of the pattern. Since this is clearly impractical to try to quantify with ensembles of over 4000 patterns, the bond order parameter might be able to detect these without observation.

5.3 Event-Driven Molecular Dynamics simulations

5.3.1 Finding Protocols that Produce Similar Area Fraction Probability Distributions

The goal here was to tune the initial conditions of the EDMD simulation (such as number of events, growth rate, and stopping pressure) to obtain a similar probability density function (PDF) of area fraction that was generated using our Monte Carlo method. Our motivation was not to find protocols that produced exact matches in this PDF, but to find a set that minimized this difference as much as possible. To compare similar results, the PDFs of area fractions were subtracted from each other and the root mean square of this difference was used as a metric to gauge similarity. The lower this value, the closer the particle density probabilities were to each other.

This quickly became an exercise in big data storage and management since we were looking to vary the protocols heavily and produce over 4000 configurations with each variation. To make the data easily accessible, I set these simulations to output data to a fractal-like hierarchy of file folders based on the protocol values. Figure 5.1 shows a schematic for the procedure, with a) showing how the change in protocol values from initial values (x, y, \dots) by adding/subtracting a small value ($\Delta x, \Delta y, \dots$) forms a grid in the parameter space of the simulation. Data from each simulation ensemble would normally be placed in its own unique folder. Instead, this fractal-based system stores all the ensembles with similar protocols together (Figure 5.1 b), allowing them to be easily accessed by data harvesting algorithms. One other benefit for this type of system is that it allows for easy addition to the ensembles. By determining how many final configurations are contained in the folder, the program can continue from the last known run number and update the ensemble if a bigger database is needed for analysis. For initial comparisons, ensembles of about 1000 runs were used to gauge the approximate distribution in particle densities. These were then expanded to 4032 simulations once protocols were found to have sufficiently close outcomes.

5.3.2 Changes in Area Fraction from varying EDMD initial conditions

This section outlines the general trends of how the change to one parameter will influence the resulting area fraction probability distribution (PDF). **Pressure:** This parameter greatly influences the particle density since it is used as the one of the halting conditions for EDMD [102]. In Figure 5.2 (a), as the pressure is varied, an increase to the pressure shifts the distribution to a higher particle density. When this parameter is set at a low value (< 10), we observe the system rarely produces a fully densified state where the particles do not fully expand and the simulation is stopped in a dilute phase. When this is set to a higher value, the simulation produces very crystalline states and changes the yield to prefer these states. Since this is used as the primary stopping condition, the simulation undergoes many more collisions when this has a large value.

Events per Cycle: This parameter also has an impact on the overall particle density but much less than the pressure. In Figure 5.2 (b), as the events are tuned from low to higher values, the relative intensity (structure) of the PDF does not vary drastically but instead does shift the particle density to a higher value. When this parameter is set high, the particles in the simulation can reach an equilibrium state quicker, allowing for smoother transitions to denser configurations. This is consistent with what has been observed previously as this parameter is used to define the halting condition for detection of the jammed state [102].

Growth Rate: This parameter is one that controls the morphology of the internal structure, with low growth rates producing crystalline dispersions [102] as is what we observe here. In Figure 5.2 (c), the growth rate is varied by increasing by a factor of 2 for each ensemble. This parameter does not seem to shift the overall structure of the area fraction PDF, however, it greatly enhances the probabilities for localization to a specific state, indicated by the sharpening of peaks at area fractions $\phi = 0.771$ and $\phi = 0.785$. By having a smaller expansion rate between cycles, the simulation allows particles to equilibrate the energy imposed from densification (pressure

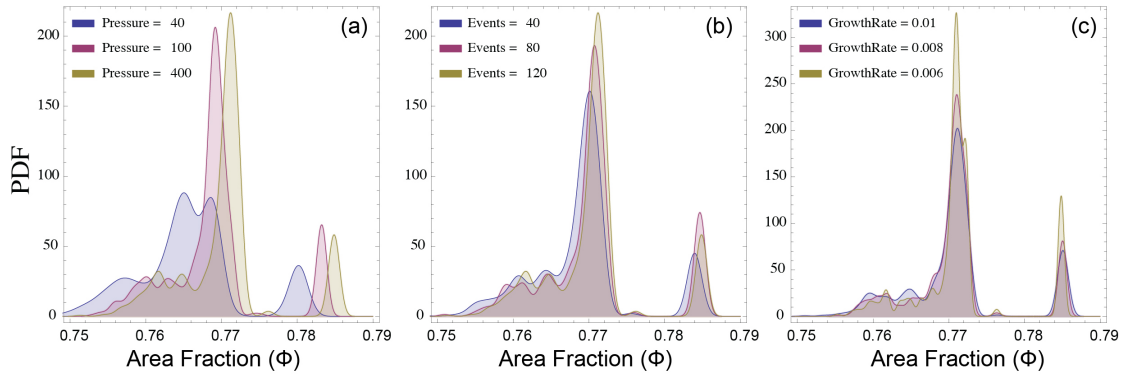


Figure 5.2: Effect on the PDF for area fractions using non-optimized parameters with 36 particles. (a) Effect of pressure with constants: events=120 and growth=0.01. (b) Effect of events with constants: pressure=400 and growth=0.01. (c) Effect of growth with constants: pressure=1000 and events=80.

from the reduction of free-volume), allowing for the particles to occupy the most energetically favourable configuration (i.e. least pressure and most dense) [103].

5.3.3 Discussion of Performance and Parallel Execution

One thing that has been noticed during usage is that EDMD is comparatively faster than our Monte Carlo simulations. The time taken to simulate 1024 particles with periodic boundaries takes approximately less than one second running on modern consumer grade desktop computers. When parallelized in a large group, the only restricting factor comes from the time separation between sequential runs. The published implementation uses a time seed for the generation of randomized initial positions and velocities of the spheres. If any of the nodes on a cluster have the same CPU time, the resulting configurations and distributions will match exactly as should be expected with a deterministic simulation method. This problem was overcome by amending this method to have the random number generator seed add the configuration number to the time (i.e. time + run number 1 of 4000). This allowed for ensemble generation on a single local machine running multiple instances of EDMD rather than outsourcing it onto supercomputer clusters.

When these systems become quite dense, EDMD spends a lot of time trying to determine an allowable position from the particle trajectories. For hard boxed boundary conditions, this time increased quite a bit and caused many of the simulations to crash. In EDMD, the growth rate needed to be considerably lower to allow for the interactions of the molecules and boundary. If the particles grow too fast between collisions, then they might expand outside the boundaries, causing unphysical overlap and will crash the simulation. This happened quite frequently when exploring the protocol space and the solution was to rerun the simulations until enough configurations were generated for the ensemble.

Specifically for the low particle limit, we found that exponentially more simulations from EDMD were needed to find disordered states. The fewer the amount of particles contained in the system, the harder it is for EDMD to result in a jammed metastable microstate. In the case of 9 particles, over 3.5 million EDMD simulations were launched and only 382 configurations resulted in a low probability microstate. Most of the molecular dynamic simulations for $n = 9$ particles produced the 3×3 square array. This is compared to our Monte Carlo method which was able to find 119 low density configurations in only 4032 runs. From this, it can be said that metastable configurations are much more easily found with our Monte Carlo method rather than EDMD. We attribute this to the static nature of the Monte Carlo microstate configurations. Since the Monte Carlo particles are not moving, patterns which are the result of balanced confinement pressures are not impacted by collisions from loose rattler particles which can disturb the metastability of

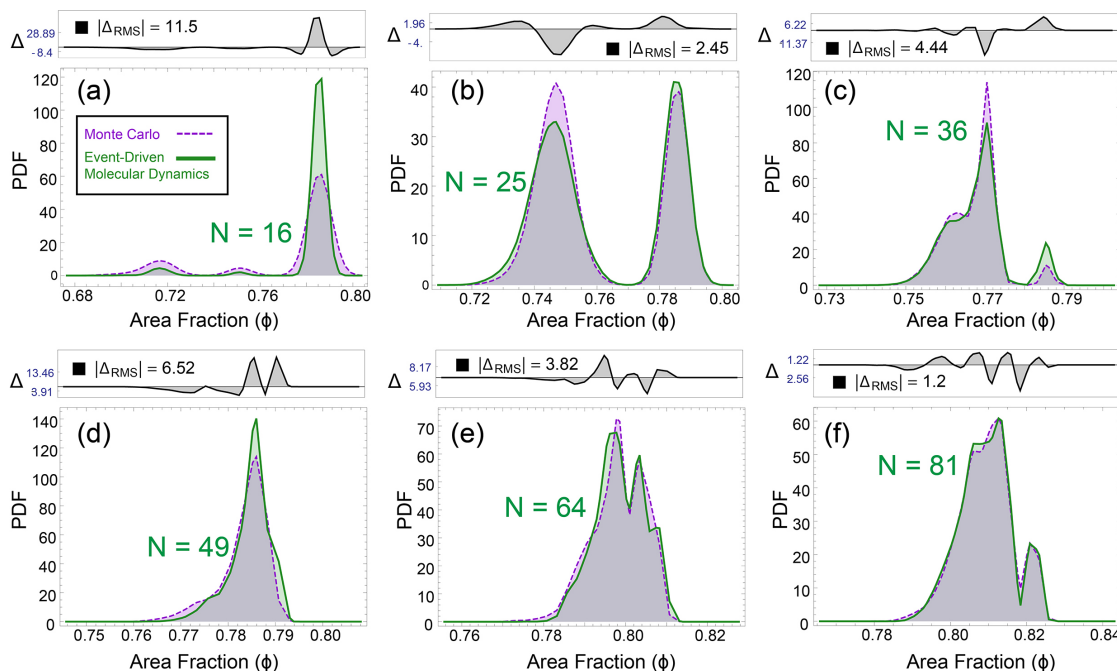


Figure 5.3: Probability density distributions (PDF) of the area fractions (ϕ) of circular molecules contained within square boundaries. Above are the root mean square residual spectra which were used to determine the relative closeness in probability. The numbers of molecules are: a) 16, b) 25, c) 36, d) 49, e) 64, and f) 81.

the microstate.

5.4 Matched Protocols

Monte Carlo Protocols: The initial conditions (protocols) that were used were: a shaking amplitude (σ) that is proportional to the particle diameter and an inflation growth rate of 10^{-5} times the molecular area per simulation step. The number of trial shakes (k) was set to 1000 with a number of cycles (ω) to 10. These parameters can be redefined within the “defaults.dat” file. One thing to note when importing polygon files, is make sure that the polygon is open (first and last vertex are different). When it is closed, it may cause the normalization of the polygon (longest length = 1) to have a centre of mass different from the origin (0,0). More information on technical details can be found within the document: [104] also available at: <http://organicelectronics.mcmaster.ca/ResearchFiles.html>

Release versions of the event-driven molecular dynamics (EDMD) code can be downloaded from: <http://cherrypit.princeton.edu/Packing/C++/>
An outline and tutorial of their code can be found on the website.

Particles (N)	Pressure	Events	Growth	Repressurization Cycles	$\Delta(\phi)_{rms}$
Periodic					
1024	70	60	0.025	—	4.93
Confined					
81	600	60	0.010	—	1.20
64	600	64	0.010	—	3.82
49	1,000,000	49	0.010	7	6.54
36	70	60	0.025	11	4.44
25	1000	100	0.100	5	2.45
16	70	60	0.025	6	11.5

Table 5.1: Optimized parameters of EDMD found to match ensembles produced from Monte Carlo. For $N = 64$ and 81 particles, systems were not found to have minimized area fraction difference ($\Delta\phi_{rms}$) with repacking cycles. Note that $N = 16$ contains finite a localized states at the $n \times n$ square lattice with a discrete value for the area fraction, therefore $\Delta\phi_{rms}$ is meaningless (discontinuous PDF), and only coincidence of the area fractions at those values were considered.

5.5 Monovacancies and the Bond Order Parameter

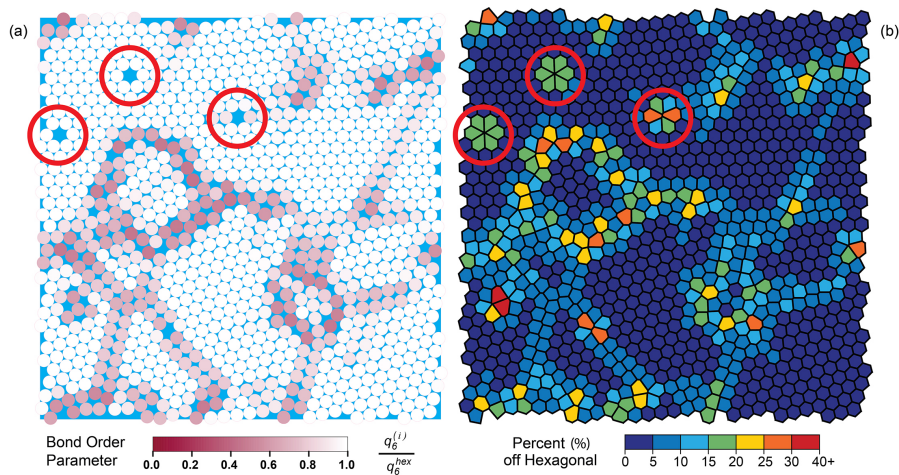


Figure 5.4: A configuration from event-driven molecular dynamics that contains point defects. (Left) Rendering of the configuration using the bond order colouring scheme, with darker colouring representing a lower value for local hexagonal packing: $q_6^{(l)}/q_6^{hex}$. (Right) Voronoi tessellations of the same configuration with a colour scheme that describes the area fluctuation as a percent deviation from the expected hexagonal lattice of the same density. Monovacancies are highlighted in red circles on both configurations.

This topic was briefly mentioned in the manuscript but expanded here as a brief study on using the bond order parameter (BOP) to detect these monovacancies. One notable difference that can be seen between the two simulation methods is the appearance of point defects or monovacancies. Molecular dynamics simulations tend to produce configurations with these defects; however, these are almost never seen in Monte Carlo simulations. When these configurations are viewed (Figure 5.4), the monovacancies are easily recognized as empty voids where particles should be. Red circles are plotted around the regions where the monovacancies are found. As can be seen, the Voronoi tiles of these neighbouring particles show long tails toward the defect, creating a 6 lobe flower-shape. Nearest neighbour particles around the point defect show an unexpected change in the bond order parameter for q_6 . To classify the relative frequency of occurrence, these defects

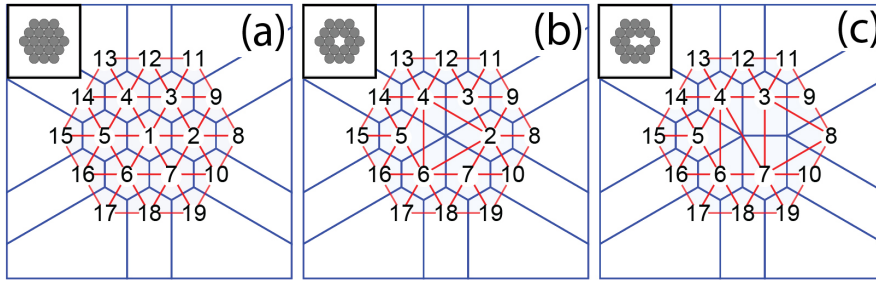


Figure 5.5: Voronoi tiles of (a) perfect hexagonal lattice, (b) monovacancy at lattice site 1, (c) two monovacancies at lattice site 1 and 2. Blue lines indicates the boundaries of the Voronoi tiles corresponding to each particle. The red lines are the associated Delaunay triangulations that define nearest neighbours for the bond order parameter. Insets visually define the particle positions and where point defects are.

would need to be detected within ensembles of over 4000 configurations and searching for them by eye is unfeasible. Delaunay triangulation and Voronoi tessellations have previously been used to track monovacancies [105] but the exact method in which this is done remains unclear. The authors seem to consider the identifiable characteristics of these vacancies as a ring of neighbours with alternating 5-7 coordination [106]. This is a characteristic of dislocation lines, however it does not necessarily distinguish monovacancies.

The Voronoi tessellation and Delaunay triangulation in Figure 5.5 shows a (a) perfect hexagonal lattice as well as (b) one and (c) two particle point defects. In this figure, there is indeed the 5-7 alternating coordination numbers at neighbouring sites. However, neighbours with a zero-length Voronoi edges and neighbours with Delaunay connectors crossing Voronoi edges not associated with that bond are removed from the list of neighbours. This leaves the ring of caging particles to have only 5 neighbours instead of 6.

Particle Site	2	3	4	5	6	7
Monovacancies						
Hexagonal (q_6)						
Zero	0.7408	0.7408	0.7408	0.7408	0.7408	0.7408
One	0.7652	0.7652	0.7652	0.7652	0.7652	0.7652
Two		0.5768	0.7652	0.7652	0.7652	0.5768
Square (q_4)						
Zero	0.375	0.375	0.375	0.375	0.375	0.375
One	0.4591	0.4591	0.4591	0.4591	0.4591	0.4591
Two		0.5948	0.4591	0.4591	0.4590	0.5948

Table 5.2: Absolute (non-normalized) local bond order parameter (q_ℓ) with symmetry ℓ corresponding to each particle within the configuration shown in Figure 5.5. See Eqn. 4.9 for calculation details.

One method we propose to detect point defects is to look at the bond order parameter of neighbouring particles. One hypothesis is that since a particle was missing, the BOP of nearest neighbours around the point defect should have a different value than q_6 for a hexagonal lattice. Table 5.2 outlines the non-normalized values of the local bond order parameter for each particle position in the configurations outlined in Figure 5.5. What can be seen is that neighbouring particles have local bond order values which change as a function of neighbours. In the case of monovacancies, the neighbour particles change from having six coordination neighbours to five. Routines that calculate the bond order using a fixed cutoff radius for neighbour definition are

unable to differentiate this subtlety since the monovacancy is neglected as a neighbour and the hexagonal arrangement of neighbours surrounding the particle dominates the calculation.

When solved using the weighted sides of the Voronoi tile, the value for q_6 around the monovacancy actually increases above the value for the hexagonal configuration. The bond order parameter in 2D has an expectation value of $q_6^{\text{hex}} = 0.7408$ for particles in a triangular lattice (see Chapter 4.4.3 for all expectation values). However, in the case when the central particle is removed, the bond order parameter becomes $q_6^{\text{mono}} = 0.7652$. This is surprising since a higher value of BOP usually implies a more crystalline configuration. The weighting of angles between neighbours using the Voronoi tile edges creates a bias toward neighbouring sites, manifesting as a long sided tile where the monovacancy is. Similarly, the particles on opposite sides of the point defects have an edge size equal to zero which removes their influence on the bond order calculation. Point defects studied using the cut-off radius definition of neighbours resulted in non-detection of the vacancies, giving local bond order equal to the hexagonal expectation $q_6 = q_6^{\text{hex}}$. When two point defects are removed in series, the local bond order of neighbours at the centre points between monovacancies is reduced by the removal of Voronoi tile edges while the outer neighbours continue to show this heightened value of q_6^{mono} .

In conclusion, the Voronoi weighted bond order parameter may be a possible way to determine if monovacancies are contained in a configuration. This can be done by determining if the particles which have local q_6 with a value higher than one expected for hexagonal patterns with a absolute value of $q_6^{\text{mono}} = 0.7652$. When using the normalized version of the bond order is considered, the monovacancy caging particles can be identified with a q_6 value above one: ($q_6^{\text{mono}}/q_6^{\text{hex}} = 1.033$) In the case of a singular monovacancy point defect, the number of particles with this higher bonder order should be six.

5.6 Publication: “Reproducing morphologies of disorderly self-assembling planar molecules with static and dynamic simulation methods by matching density” (Physica A - 2017)

Physica A 471 (2017) 301–314



Contents lists available at ScienceDirect

Physica A

journal homepage: www.elsevier.com/locate/physa

Reproducing morphologies of disorderly self-assembling planar molecules with static and dynamic simulation methods by matching density

M. Bumstead^{a,*}, B. Arnold^b, A. Turak^{a,*}^a McMaster University, Hamilton, Ontario, Canada^b INTRON GmbH, D-74523 Schwäbisch Hall, Germany

HIGHLIGHTS

- Monte Carlo and event-driven molecular dynamics approaches are discussed.
- Comparable and reproducible sets of configurations are key to validating methods.
- Statistical approaches should be used when analyzing simulated morphologies.
- When the density is fixed, static and dynamic configurations have the same structure.

ARTICLE INFO

Article history:

Received 1 September 2016

Received in revised form 23 November 2016

2016

Available online 23 December 2016

Keywords:

Entropy driven self-assembly

Excluded volume

Morphology

Monte Carlo

Event driven molecular dynamics

Repeatability

ABSTRACT

Monte Carlo and molecular dynamics simulations are the two main numerical approaches to modeling molecular self-assembly and ordering. Conceptually, however, each method explores different paths through the thermodynamic landscape. Molecular dynamics depends on the position and momentum terms. Monte Carlo is a static set, and thus the momentum term is replaced with an energy term that is dependent on the volume and entropy. Until now, it was unclear if a stochastic process of densifying particles would have the same internal structure as morphologies produced from classical mechanics. This paper provides a systematic (i.e., statistical) analysis of the outcomes of 4032 simulations for hard-core circular objects as a function of the number of molecules and the boundary conditions. Structural classification of the resultant ensembles (averaged pair correlation function, bond-order parameter, translational order parameter, and Voronoi diagrams) shows that stochastic and dynamic approaches do not alter the morphology of the steric molecules. We conclude that when the probability density of covering area fractions are matched, the ensembles produced from the two methods will show the same level of structural disorder and positional patterns. The resultant morphology from both models, therefore, is not a product of dynamic unrest, but that of the relaxation of entropic frustration from macromolecular crowding. Although statistically the two methods produce similar configurations, nuances arise from the static and dynamic nature of modeling. As a result, Monte Carlo is slightly better suited to modeling systems when the desired morphology is represented by a metastable state; molecular dynamics on the other hand is more suited to finding defects that can arise in morphologies. Regardless, a fixed density will result in similar morphologies from both techniques, driven by similar configurational entropy.

© 2016 Elsevier B.V. All rights reserved.

* Corresponding authors.

E-mail addresses: bumstema@mcmaster.ca (M. Bumstead), turaka@mcmaster.ca (A. Turak).<http://dx.doi.org/10.1016/j.physa.2016.12.075>

0378-4371/© 2016 Elsevier B.V. All rights reserved.

1. Introduction

The control of supramolecular self-assembly and morphology, especially of donor–acceptor pairs, is a key feature of molecular electronics [1]. The optimized movement of charge in such systems is heavily influenced by molecular organization and morphology [2–5]. The assembly of molecules into the desired ordered and continuous phases, however, poses a significant challenge. Predictive modeling of the phase diagram of possible supramolecular architectures is a critical tool in developing the next generation of device structures [6–8].

The interplay between molecule–substrate and intramolecular interactions yielding various morphologies are most complex in the first monolayer on the substrate surface. As such the molecular tiling of a single layer of planar molecules is the focus of significant interest in modeling to predict supramolecular organization. Both molecular dynamics [9–11] and Monte Carlo [10,12,13] approaches have been successful in predicting molecular tiling patterns for a variety of planar molecules. When these two approaches are used to model similar interaction potentials and planar environments, the final properties and final states are often taken as equivalent. The conceptual basis for each method is, however, very different. Monte Carlo (MC) simulations describe the structure of the system by stochastically yet statically sampling the configuration space. This is done by reorganizing molecules (displacing and/or rotating) to minimize an energy function under certain acceptance criterion for a fixed number of molecules and fixed volume (canonical ensemble). Molecular dynamics (MD), on the other hand, describes the time evolution of all the molecules in a deterministic way by solving dynamical equations of motion until the system reaches equilibrium.

Although it has been normally assumed that both methods provide equivalent static properties, to the best of our knowledge, a systematic analysis for statistically comparing these methods has yet to be explored. A comparison between MC and MD simulations cannot be based solely on fixing the same simulation conditions across methods. The Hamiltonian of each method is substantially different. Molecular dynamics depends on the position and momentum terms. Monte Carlo is a static set, and thus the momentum term is replaced with an energy term that is dependent on the volume and entropy. Due to their unique implementations of the initial parameters (e.g. the densification rate, molecule shape and number, or interaction), building sets of reproducible results from MC and MD is an involved process resting on the understanding of how the parameters can influence the production of states. Instead of the initial state being fixed, we explored systems where in which the final outcomes are the same. If the structural characteristics of these configurations are the same, then the morphology is not a product of dynamic unrest, but that of the relaxation of entropic frustration from macromolecular crowding.

The supramolecular patterns that arise from the self-assembly of molecules are the consequence of a wide variety of interactions which are possible in semiconducting organic molecular assemblies. In any simulation approach, there are many possible interaction potentials that can be chosen to model molecular behavior [14]. The inclusion of each additional potential will fundamentally change the morphology that is produced by the simulation, and increase the complexity of comparison across approaches [15].

The simplest implementation for a potential that represents the cooperativity of planar molecules on substrates is the steric interaction. In the same way the Ising model of a two-state ferromagnet is the simplest one used to describe phase transitions [16–19], this potential is the simplest that describes the self-organization of planar molecules, based on the basic principle of the lattice gas. The microstates of the lattice gas are occupied lattice points that are restricted to only having one particle. These occupied sites are excluded from the total available volume for which any particle can move into. The entropy can then be calculated from the multiplicity of all occupied lattice points. Sometimes denoted as the excluded volume interaction or hard-core potential, this steric interaction therefore excludes all complex interactions, leaving only the entropic description of the system to determine the energy. Entropically driven self-assembly refers to the rearrangement of molecules resulting from the relaxation of entropic frustration imposed by reducing the available free volume [20,21].

Entropy has been seen to drive phase behavior as rich and complex as that seen in enthalpy driven systems [22]. Though entropy driven control of morphology is not a new concept [23], pathways to exploiting entropic control for large aromatic π -systems [24] or fullerenes [25,26] are an emerging direction in morphology control. Fullerene miscibility, a key issue for bulk heterojunctions, is often described by such excluded volume potentials [27,28,26]. For planar systems, the subtle interplay between entropy and energy driven by the steric interactions have been exploited to produce switchable supramolecular structures of naphthalenediimides [21] and arylene ethylene macromolecules [29]. Steric interactions also played a key role in the amplification of a chiral morphology in trioctyl-functionalized triazatriangulenium molecules [30]. Though limiting the complexity in the description of the intermolecular potential focuses the comparison to the simulation methods representing the morphology, these entropically driven systems are also of technological interest in morphology control.

As structural order is the main property of interest when comparing configurations, a further necessary simplification is to focus on monodispersed circular shapes for the molecules. By simplifying the shape of the molecule to a circle, it is possible to gauge the resulting localized structures against the most ordered state of disks. These patterns are generally well characterized and freely available for comparison across a variety of system sizes [31]. One system of particular interest for organic electronics that can be described by such circular excluded volume approximations are buckminsterfullerenes (C_{60}) [32]. Other non-covalently bonded macromolecules, such as micelles or colloids [33], are also well described by such approximations. Particularly in a monolayer, these systems resemble mono-dispersed circular disks, with weak steric interactions.

For this study, dense polycrystalline and disordered states were purposely sampled for the comparison for two main reasons. Firstly, such systems closely resemble the morphological distributions of molecules in devices. Secondly, disordered systems provide a large basis of different configurations, rather than a limited set of crystalline packings. This allows a greater flexibility in drawing information about how initial conditions influence the outcomes in each simulation method, and gives more confidence in the reproducibility of the comparison. However, in general, it is more difficult to identify and classify disorder within morphology, rather than recognizing order. As such, we utilize a variety of analysis metrics and known states to benchmark structural order between the two simulation methods.

The reliability of these metrics allows us to judge to what extent systems have structural/physical properties that are similar and reproducible across various systems sizes and boundary conditions. Practices of reproducibility and reliability are important notions to consider within the realm of computational science, especially when dealing with different approaches to simulations [34–38]. These allow for transparency, re-use, and sharing of approaches among different disciplines. Simulation outcomes also often depend on technical choices (random-number generation, overlap detection, integration of the equations of motions, for instance), thus making available the information about data collection and model implementation [39] is vital for reproducibility. On the other hand, simulation outcomes and comparisons across methods need to be as independent as possible of idiosyncratic factors (e.g., unintentional bias on the selection of the outcomes) [40]. We addressed the latter by following a statistical approach to the comparison between MC and EDMD for the systems of interest, that is, by producing a large number of runs from each method for a given set of simulation parameters. To address the former, in the spirit of transparency, the computational parameters and methods are accessible along with the full raw data, as described in SI:Sec(A,B).

The layout of the rest of the paper is as follows: In Section 2.1 we briefly present the details of Monte Carlo and event-driven molecular dynamics of planar steric disks. Bulk systems are investigated in Section 3 where the different structural functions used to compare the simulation approaches, i.e., covering area fraction, pair correlation function, bond and translational order parameters, and Voronoi cells are introduced. Section 4.1 is devoted to finite systems in containers with hard square walls. In such systems, the analysis tools used for bulk systems become inaccurate due to boundary effects, so we explore enumeration of expected microstates by shape-matching the resulting patterns produced from positions of molecular centroids. We close the paper with a discussion of observed differences between methods and a summary of the structural order metrics within the prospect of repeatable results in Section 5.

2. Method

2.1. Simulation approaches: similarities and fundamental differences

In our systems for the purposes of this paper, the molecules that we are interested in modeling are represented by circular steric objects. One possible approach when describing the self-organization of steric objects is event-driven molecular dynamics (EDMD) [41–46], which is often denoted as “Lubachevsky–Stillinger” molecular dynamics, named after the authors. Another approach uses Monte Carlo methods (MC) [47–49] to simulate molecules. The approach to representing these molecules are slightly different yet important. Event driven molecular dynamics uses perfectly circular particles (excluded volume point particles) that have no angular momentum (spin). To approximate molecules, MC uses rasterized polygons that can freely rotate. To avoid confusion, throughout the manuscript, if the MD method is what is solely being described, EDMD objects are referred to as particles. If it is MC, objects are referred to as polygons. For all references to MC and EDMD at the same time, simulation objects are referred to as the more generic term: molecules or objects.

Both MC and EDMD approaches use a similar packing directive for objects to achieve an equilibrium configuration but vary in the approach towards the displacement of objects. Full details on both methods can be found in the supporting information (SI:Sec(B)). Briefly, objects start off dilute within the square simulation area, and then are allowed to self-assemble under densification. Instead of reducing the simulation area while holding a fixed object size, the alternative approach is to inflate the objects [50] in a fixed reference frame. In this way, the shape and center of mass (centroids) of all objects are mapped into a unit simulation box.

It is important to stress here that a main difference between schemes is how the objects move between densification steps. The behavior for EDMD is outlined in Fig. 1(b) where the three small light gray disks inflate (1) and collide, causing their trajectories to change (emphasized by the red dotted lines (2)). The particle at (4) continues uninterrupted during this event. The inflation rate for this event is dependent on the speeds of trajectories from the colliding molecules. If the speeds are lower, it takes longer for the particles to meet and thus will allow for more expansion between events. As the particles become denser, they will encounter more collisions. The inflation between event cycles soon becomes negligible as these collisions become more frequent, causing particles to converge to a densified final size where the method eventually halts.

Instead of deterministic trajectories, the Monte Carlo method displaces polygons randomly, where a MC trial move resulting in an unallowable amount of overlap is analogous to a collision event. In Fig. 1(a), the three small light-gray polygons (2) are discretely inflated and randomly displaced (outlined by the blue dotted lines (2)). When an overlap is encountered (red area in the center) the move is rejected and will undergo another MC trial move. If all positions are accepted (3), the polygons are discretely inflated again and the procedure repeats. Again, the polygon at (4) is one that does not encounter an event during this simulation step. The program halts after the set of all attempted moves for all simulated molecules are rejected. Note that the molecules in Fig. 1(a) are exaggerated to emphasize the polygonal nature

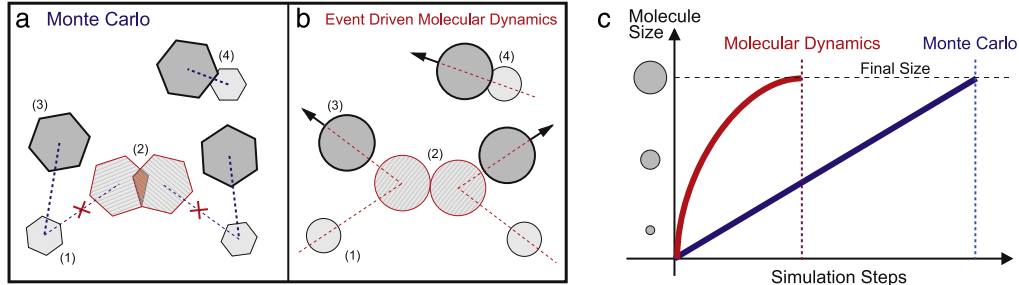


Fig. 1. (Color online) Schematics of (a) Monte Carlo (MC) and (b) event-driven molecular dynamics (EDMD) simulations on 3 molecules. Molecules start off dilute (1), and expand until an event is encountered (2). At this event a new random position is sampled (MC) or new trajectories are calculated (EDMD). In this case, both methods produce accepted configurations (3). The molecule at (4) is one that does not encounter a collision event during the simulation step. (c) Schematics of simulation growth rates as a function of number of simulation steps. Event-driven molecular dynamics (red line) expand rapidly during the initial part of the simulation swiftly converging as molecules become large enough to encounter many collisions during the same inflation rate. Monte Carlo molecules expand at a constant rate at every simulation step (blue line). Note: Molecules rendered in MC are exaggerated to emphasize their polygonal nature.

of the representation of objects in MC. In the simulations described in subsequent sections, molecules were rendered as tetracontagons (40 sides) or hectagons (100 sides), which are indistinguishable from analytic circles [7] (see SI:Sec(H) for details).

Final states of these simulations are often assumed to be similar. However, the path taken through the thermodynamic states is quite different. In order to highlight the fundamental differences between MC and EDMD simulations of steric objects, however, it is useful to consider a typical densification cycle in both approaches under the same object inflation rate. In EDMD, the particles grow continuously between collisions. This physical phenomena translates into a non-constant rate of compression. By contrast, in MC simulations, polygons change size by a discrete inflation and only after all moves have been accepted (under the appropriate weight), the inflation procedure repeats. This discrete step mimics a system under constant compression and since the stochastic system has no internal force structure, the constant compression is a constant rate of volume change. This fundamental difference is reflected in the two different effective densification curves, i.e., linearly for MC and exponentially for EDMD (see Fig. 1(c)). This is a very delicate issue in comparing approaches, as the densification rate is a key parameter in both MC and EDMD simulations. It is often the main control of the state of order in the equilibrium structure. Generally speaking, the faster the densification rate is, the less crystalline the outcome becomes, and larger the probability of the system will be caught in a metastable state where simulations can become unstable.

2.2. Comparing large number of simulations will remove sampling bias

Comparing different simulation runs of steric molecules stemming from either different initial conditions or between methods is frequently performed by comparing one or a few simulation outcomes [51]. Possible unintentional selection bias from such an approach can be overcome by instead adopting a statistical approach, where a large number of copies under the same initial conditions are examined [7,40]. This can allow determination of, for example, protocols that preferentially determine metastable states in the system, and provide an unbiased approach to comparing different simulation protocols. The set of all initial parameters required for the simulation to uniquely generate an ensemble of configurations is what we define as a protocol. All protocols used for the simulations discussed in the following sections can be found in the supporting information (SI:Sec(B)).

Such a statistical approach allows for a comprehensive analysis of the way phase space is sampled under a particular simulation protocol. However, a fully exhaustive enumeration of all possible microstates for a protocol may be impractical, especially when the most probable outcomes are of interest. Substantially comprehensive ensembles will generate internally reproducible morphologies, such that for the same protocol, the same configuration has a chance to be sampled more than once. When there is variance between outcomes within the ensemble, the resulting morphologies can be reduced into a set of averaged localized attributes to allow for the global comparison between simulation methods and protocols. In the following sections, single configurations are presented to illustrate the local structural descriptions and the related ensemble averaged parameter are used in the comparison of simulation approaches.

2.3. Making statistical ensembles of dense polycrystalline disordered configurations

We have chosen as a statistical ensemble size the smallest one for which the probability distribution of the molecular area fraction (i.e. the fraction of simulation area covered by molecules, ϕ) does not change significantly with further increases in ensemble size. Additionally, the ensemble size should be high enough to find low probability configurations without

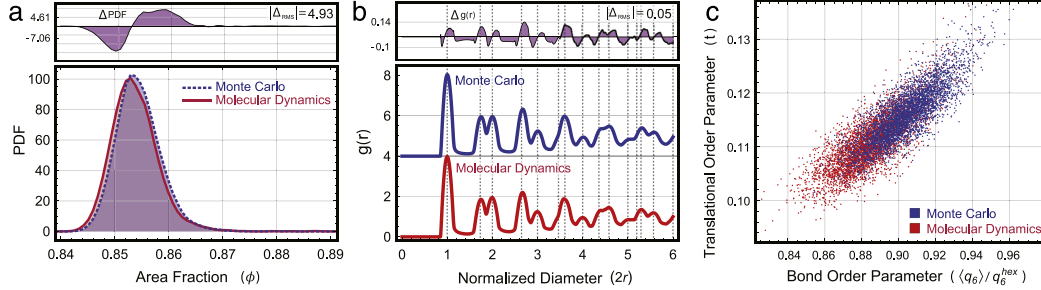


Fig. 2. (Color online) Comparison of different metrics for bulk systems (1024 molecules) with periodic boundary conditions. (a) Probability density functions for the covering area fractions ϕ of the ensembles of 4032 configurations. (b) Ensemble-averaged pair correlation function (offset for clarity). Gridlines indicate peak positions of hexagonal close-packed disks. In each case, the difference spectrum is plotted on top along with the root mean square difference. (c) Order map, i.e., translational order parameter t as a function of normalized average local bond-order parameter $(q_6)/q_6^{\text{hex}}$.

having to over-sample the most probable outcomes. For MC, ensembles with 4032 (full runs) configurations satisfied these conditions [7] and thus, the same number was set for both methods.

In order to provide a stringent comparison between the two methods, we have chosen to focus on protocols that produce very dense yet polycrystalline configurations. In the case of MC, we have achieved this by implementing a biased approach to MC simulations where k moves per particle are tried in an effort to increase the acceptance rate [52–55]. We found this protocol combined with a constant inflation rate at each step favored dense disordered states [7]. These protocols can be transferred between bulk and confined systems to generate the desired configurations [7]. EDMD simulations structures are directed by controlling the expansion rate, number of events per cycle, and the internal pressure. Dense disordered configurations were achieved by sequentially generating multiple ensembles with slightly varying initial conditions. The probability of area fraction was compared to the MC ensemble distribution at each iteration of protocols. The set of protocols that produced the lowest difference were kept and set as the next input for slight variation. This fractal-like protocol search allowed for the unbiased convergence of similarly dense configurations from both simulation techniques. However, there is no guarantee that the ensemble we report on will exactly match; only that is the best converged. It is possible that these could be a local minimum in protocol space.

3. Structural characterization of bulk systems of planar molecules

3.1. Determining a qualitative set of disordered configurations for comparison by matching the probability density functions of the area fraction

Bulk systems are most commonly explored by setting periodic boundary conditions on the simulation box to avoid boundary effects. Statistical ensembles of systems with 1024 molecules were simulated using both EDMD [45] and MC methods. To determine which protocols would be suitable for comparison across simulation methods, the surface coverage of molecules (ϕ) was the initial criterion.

$$\phi = N \frac{A_o}{A_{\text{box}}}. \quad (1)$$

The parameter ϕ , also referred to as the area fraction, represents the fraction of simulation area (A_{box}) covered by N objects having area (A_o), within the unit box of area $A_{\text{box}} = (1 \times 1)$ (see Fig. 1(a) and (b)).

The area fractions are extracted from each configuration in the ensemble and used to build probability density function (PDF) distributions, denoted as $f(\phi)$. These are shown in Fig. 2(a). In order for the configurations from each method to be comparable, as described above, we focus our results on producing ensembles with similar probabilities of area fraction. Optimized protocols were those that produced the smallest deviation in the PDF for the full ensemble (4032 configurations).

As can be seen, the two distributions overlay almost entirely and are roughly Gaussian in shape, suggesting that both simulation techniques are producing similarly dense patterns at the same probability. The mean of these distributions are approximately $\phi = 0.854$. This density is comparable to systems of planar colloids in the hexatic phase [56]. Table 1 shows that the ensemble averaged mean area fraction and standard deviation are identical to three significant figures. However, slight differences remain. The top inset of this graph shows the difference spectrum between the two PDFs,

$$(\Delta \text{PDF}) \approx \|f(\phi_{\text{EDMD}}) - f(\phi_{\text{MC}})\|.$$

A quantitative figure of merit, Δ_{RMS} , can be derived based on a root mean squares analysis of the residual function when one distribution is subtracted from the other. Exact similarity would provide an $\Delta_{\text{RMS}} = 0$. For bulk systems, this difference

Table 1

Ensemble average values (over 4032 bulk configurations) of the covering area fraction ϕ , the first minimum of the pair correlation function $g(r)_{\min}^1$, the normalized average local bond order parameter for hexagonal and square symmetries $\langle q_6 \rangle / q_6^{\text{hex}}$ and $\langle q_4 \rangle / q_4^{\text{sq}}$, the mean translational order parameter $\langle t \rangle$, and percentage of Voronoi areas with deviation under 5%, ($A_{\text{vor}}^{\leq 5\%}$). Systems with 1024 molecules with periodic boundary conditions were used to simulate the bulk. In each case the uncertainty is given by the standard deviation.

	$\langle \phi \rangle$	$\langle q_6 \rangle / q_6^{\text{hex}}$	$\langle q_4 \rangle / q_4^{\text{sq}}$	$\langle g(r)_{\min}^1 \rangle$	$\langle t \rangle$	$A_{\text{vor}}^{\leq 5\%}$
MC	0.854 ± 0.004	0.9046 ± 0.0023	0.4597 ± 0.0002	1.43 ± 0.04	0.116 ± 0.005	57.7%
EDMD	0.854 ± 0.004	0.8846 ± 0.0025	0.4611 ± 0.0002	1.44 ± 0.04	0.110 ± 0.005	51.9%

metric, calculated between optimized protocols for MC and EDMD, was $\Delta_{\text{RMS}} = 4.93$. However, taking the root mean square of the difference will over-estimate the error, allowing for sections with more deviation to become pronounced.

As the probability density function is by definition the derivative of the cumulative distribution function (CDF), with a probability of one over all packing fractions, the CDF for a range of ϕ can also be utilized as a metric of comparison. In the case where the PDF's are completely dissimilar, the cumulative probability would be 2. For those that are completely overlapped, the value would be expected to be 0. Integrating over the residuals, ΔPDF , approximates the difference in CDF.

To approximate this residual function, we integrate the root mean square difference over the range of ϕ similar to a full width half max method, where in residual spectrum difference Δ_{RMS} is the height:

$$(\Delta\text{PDF}) \int d\phi \approx (\Delta_{\text{RMS}})(\phi_{\text{max}} - \phi_{\text{min}}).$$

For our optimized protocols for dense, polycrystalline, disordered configurations, this yielded

$$(4.93)(\phi_{\text{max}} - \phi_{\text{min}}) \approx 0.192.$$

This value was deemed to be sufficiently low to justify the conclusion that these ensembles are representative of configurations with statistically similar densities and have a broad distribution of possible outcomes.

3.2. Quantifying the local structure of configurations with varying density using the pair correlation function, translational & bond-order parameters, and Voronoi tessellations

Having established a suitable ensemble of configurations for comparison, the configurations themselves can now be compared. For this study, dense polycrystalline, disordered states were purposely sampled to draw information on how protocols influence the outcomes in each simulation method. With protocols aimed to produce crystalline patterns, the hexagonally close-packed state (triangular lattice) is the expected configuration of highly ordered circular disks in the bulk. This limits the comparison between simulation approaches to a very small subset of configurations. If simulations, on the other hand, produce disordered systems, there are a wealth of configurations to choose from upon which to base a comparison. Reproducible and reliable metrics for disorder are therefore necessary to compare different approaches.

The PDFs of the area fractions described in the previous section offer a coarse view of the overall outcomes for the structure as predicted from MC and EDMD simulations. A more detailed view of local and long-range ordering is furnished by the pair correlation function $g(r)$ which provides the probability to find another molecule within a certain distance r . The description used in this analysis comes from the spatial distribution of Ripley's K function (described in SI:Sec(C)), which is the cumulative pair separation of all neighbors. The pair correlation function is the distance normalized spatial derivative of Ripley's K function, [57,58].

Fig. 2(b) shows the (4032 full runs) ensemble average of the $g(r)$'s. The one for MC has been offset for clarity and distances were normalized by the diameter of the molecules to allow for direct comparison. As with the PDFs of the area fractions, a more quantitative figure of merit is given by the RMS of the differences between the MC and EDMD predicted $g(r)$'s. Short and long range order are quite similar among configurations in the ensembles as indicated by the peak positions showing only slight deviation and the number of the peaks remaining constant between methods while the distance is increased. When applying the same root mean square metric to these functions, the $\Delta g(r)_{\text{RMS}} = 0.05$ emphasizing that there is sparse deviation.

The $g(r)$ function can be used to define the translational order parameter t [59,60],

$$t = \int_0^{s_c} |g(s) - 1| ds, \quad (2)$$

where $s = r/d$ is a dimensionless distance based on the diameter of the molecules d . In this case, s_c was taken to be six times the object diameter. For polycrystalline disordered systems, this maximum distance incorporates the most prominent components of the $g(r)$ while neglecting uncorrelated long-range structural order. For a completely uncorrelated system, $g(s) = 1$, and thus $t = 0$. For systems with long-range order, $g(s)$ will oscillate over large distances rendering t large as a consequence. The parameter t quantifies the pair-distance distribution, that is, the preferential molecular separations [61].

A complementary account of the local structures can be obtained by analyzing the local orientational order of the molecules with respect to its "nearest neighbors" [62]. Among the many different ways to define nearest neighbors, here

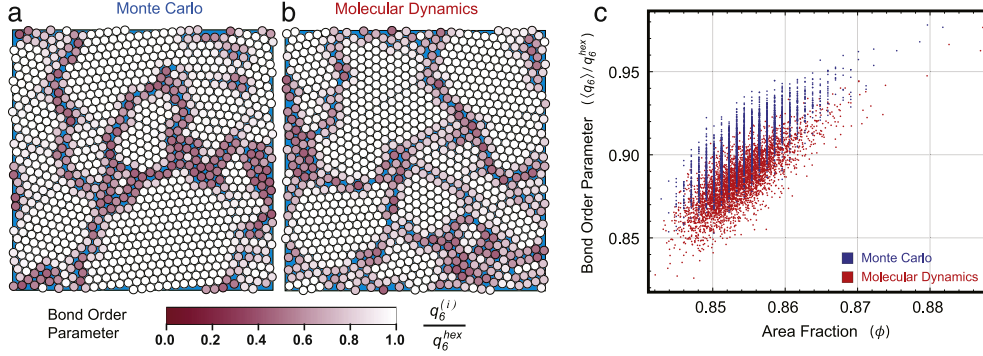


Fig. 3. (Color online) Most probable configurations as predicted by (a) Monte Carlo and (b) event driven molecular dynamics for 1024 molecules with periodic boundary conditions. Each molecule is colored by the value of its normalized local bond-order parameter, $q_6(i)/q_6^{\text{hex}}$. (c) Normalized average local bond-order $\langle q_6 \rangle / q_6^{\text{hex}}$ as a function of covering area fractions ϕ .

we shall consider nearest neighbors those molecules within a fixed cut off radius, which is uniquely defined for each microstate in the statistical ensemble by solving the first minimum of the pair correlation function. In this way, we arrive to a local bond-order parameter $q_\ell(i)$ assigned to each molecule i defined as follows [63]:

$$q_\ell(i) = \left[\frac{4\pi}{2\ell + 1} \sum_{m=-\ell}^{\ell} |Y_{\ell m}|^2 \right]^{1/2}, \quad (3)$$

where $Y_{\ell m}$ is spherical harmonic function with degree ℓ and order m . A configurational average local bond-order parameter can be defined as:

$$\langle q_\ell \rangle = \frac{1}{N} \sum_{i=1}^N q_\ell(i), \quad (4)$$

where N is the number of molecules in the simulation box. Limiting value of Eq. (4) occurs when the molecules are arranged in the hexagonal ($q_6^{\text{hex}} = 0.741$) lattice. Other lattice configurations can be classified in a similar way using the appropriate symmetry parameter i.e. a square lattice would have a $q_4^{\text{sq}} = 0.829$.

Projecting this information into the $t - q_6^{\text{hex}}$ plane provides a useful and systematic approach to study the structural order in partially disordered systems. This representation of both orientational and translational order is known as an “order map” [64]. Fig. 2(c) shows the order map of the full 4032-runs for bulk systems (1024 molecules in a box with periodic boundary conditions) for both MC and EDMD. It is interesting to observe that both MC and EDMD overlap over large part of the map, with MC displaced towards larger t and q_6^{hex} values, i.e., configurations are slightly more ordered than those coming from EDMD.

It can also be instructive to illustrate how the local bond-order parameter can manifest at the molecular level within microstates. Fig. 3 shows two of the “most probable” configurations, i.e., two microstates at the peak of the PDF of the area fractions for both MC and EDMD simulations. Each molecule i has been colored relative to its local bond-order parameter $q_6(i)$. This visualization method highlights grain boundaries between crystallites, appearing as large white domains while boundaries show up as darker red molecules. Expanding the bond-order parameter to the level of the ensemble removes unintentional confirmation bias when comparing simulation methods. Each configuration provides its own unique value, giving us a range of values for molecular orientational order. Instead of just one value calculated for a single configuration, this distribution is what is characterized to gauge the similarity between methods. In Fig. 3(c), the local bond-order parameter is averaged and normalized for each configuration then plotted against the covering area fraction. The nature of discretized inflation of the MC method can be clearly seen as stripes along constant density ϕ . For configurations with the same density, the MC method tends towards patterns that have more hexagonal order. The lower q_6 for EDMD can be interpreted at the microstate level as a decrease in hexagonal order due to more stacking defects in-between and internally to crystallite regions. These can be seen in the center of Fig. 3(b).

Voronoi tessellations provide another efficient and powerful way to analyze the local structure of each molecule as a bridge to understand the macroscopic properties of the system. A Voronoi tessellation or Voronoi diagram can be constructed for a set of points (the center of mass for each molecule) with a cell area of A_{vor} . Voronoi cell areas represent the amount of free volume available for each molecule to occupy. In particular, it is useful to consider the deviation of A_{vor} from the expected area of a hexagonal cell $A_{\text{hex}} = (2\sqrt{3})r$ (corresponding to the Voronoi cell of hexagonally closed-packed disks of lattice constant $2r$). The Voronoi area associated with a configuration forms the lowest free volume state for objects. The

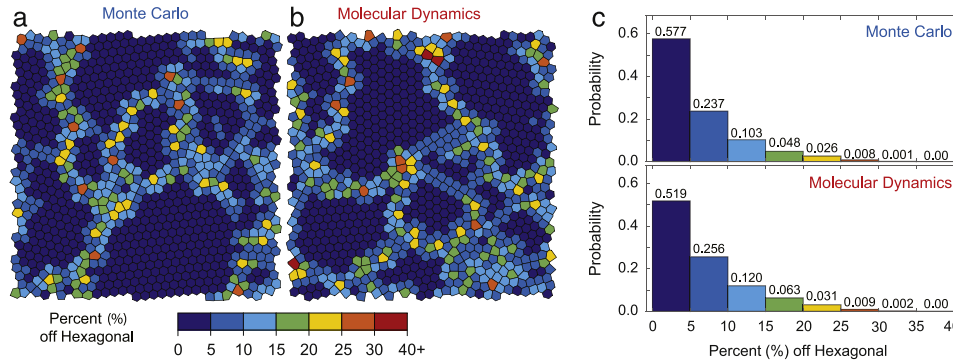


Fig. 4. (Color online) Sample Voronoi tessellation for bulk systems (1024 molecules) with periodic boundary conditions. (a) Voronoi tessellation of the configuration in Fig. 3 corresponding to having the most probable density in the ensemble. Each cell is colored by percent deviation off the expected cell produced from hexagonal packing. (b) Histograms of Voronoi deviations for the entire ensemble of 4032 configurations.

higher this deviation becomes, the larger the distance between neighbors, and thus, the greater likelihood that the molecule is in a disordered state.

Fig. 4(a) and (b) show the Voronoi tessellations of the configurations in Fig. 3(a) and (b), respectively. The color map is based on the percent deviation from the hexagonally close-packed state. Histograms for the entire ensemble are shown in Fig. 4(c) for both MC and EDMD simulations. Each simulation method contains over half of their molecules within 5% deviation from hexagonal configurations, dropping off by about half with each sequential binning of +5%. Again, MC is shown to sample higher crystalline states more often than EDMD, for the same reason, due to stabilized defects within the configuration that would be avoided with trial moves approach of MC.

Overall, structural signatures of bulk systems are similar over the range of these four separate methods of measuring configurational order. This evidence suggests that a stochastic system under constant rate of compression will have static patterns that are structurally similar to equilibrium states of dynamical systems at the same density. This underscores the importance of the entropy in driving the realized morphologies.

4. Structural characterization of planar disks in containers with hard walls

4.1. Differences between static and dynamical sampling of confined dense disordered patterns

Extended systems are ideal ground to understand structural phenomena due to the simplicity in the treatment (i.e., there is periodicity in all directions). In reality, however, all systems have boundaries and a finite number of molecules. Surface and finite-size effects add new dimensions to the structural analysis, as most of the order metrics require modifications to account for the lack of translational symmetry in one or more directions. Confinement, that is, the interplay between surface and finite size, also brings new possibilities to direct self-assembly by stabilizing unique configurations that otherwise are inaccessible to bulk systems. Thus, comparing the equilibrium structures predicted by Monte Carlo and molecular dynamics under confinement provides another avenue for benchmarking the simulation approaches.

Such cases are also interesting from an electronic device point of view. Under confinement effects, the walls impose anisotropic frustration between molecules, which can be utilized to direct the self-assembly of planar molecules [65]. Confinement is a critically important route to controlling morphology in a variety of organic systems [66–68]. Particularly for organic transistors, the channel can have length scales on the order of a few molecular diameters [68], and the optimal morphologies are heavily influenced by confining effects [69]. Predicting these configurations from simulation and optimizing the channel widths to ones which result in highly desirable patterns can be an effective strategy to improve efficiency for new electronic devices.

As in the case of periodic boundaries, an exploration of protocol space to determine suitable ensembles is important to have a meaningful comparison. Dense polycrystalline disordered states in confined systems are not a trivial case to sample. The competition between the frustration from the symmetry of the confining container and the objects' own symmetry yields a wealth of crystalline states. Previous work has shown that dense disordered states can be purposely sampled with the Monte Carlo method by holding protocols constant from bulk systems [7]. The same parameters used for bulk periodic systems can be transferred directly to confined systems with a finite number of molecules and still produce disordered states. However, it is unclear if EDMD simulations can similarly transfer protocol parameters to confined systems with low particle numbers. To examine this, the parameter space of EDMD (expansion rate, number of events, and pressure) at each system size were explored and the resultant PDFs of the area fraction compared against the previously derived MC states. To minimize the deviation from the PDF of area fraction for MC, as was described for the bulk systems, the initial conditions for

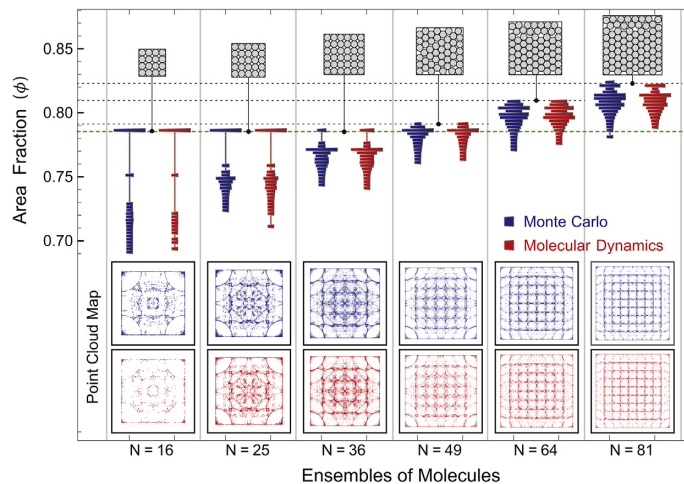


Fig. 5. (Color online) Probability density histogram profiles of covering area fraction ϕ for 16, 25, 36, 49, 64, 81 circular molecules inside hard walls using ensembles of 4032 configurations. The green dashed line is included to represent the covering ratio of the square lattice configuration at $\phi = \pi/4$. Configurations with the highest density are included above showing that the $N \times N$ lattice is not the most dense in systems of $N > 36$. Below are Point Cloud maps to show the collective result of 4032 simulations by plotting all molecular centroids together. (top/blue) Monte Carlo, (bottom/red) event-driven molecular dynamics.

EDMD needed to be modified (SI:Sec(B,F)). This modification allows for the systems to evolve entropically towards a set of configurations that possess the same density and further emphasizes the complexity and non-trivial nature of transferring simulation protocols, even within the same method.

Metastable states rely on the internal pressure being equal in magnitude to the pressure imposed by the container. For the EDMD method, pressure is dependent on the trajectories of the particles. One simulation pattern might provide a force balance through contact networks of the particles. However, if we move the simulation forward with another event step, a loose particle (rattler) can traverse the box during that time and provide the necessary momentum to break the global jammed state. This then cascades into a transition to a new metastable state. After a sufficient amount of time, this pattern tends towards its densest state. With MC, any rattlers in the metastable state will not transfer momentum. Since MC simulations sample static states, there is effectively no pressure from the molecules and container. This is one of the reasons that protocols can be easily transferred among simulation environments. Metastable states are commonly sampled with Monte Carlo.

4.2. Using the density of confined microstates to quantify the probability of disordered morphologies

When a system is under confinement, the walls impose an anisotropic frustration between molecules, which can disrupt the hexagonal close packing of bulk systems [7]. This competition between the symmetry of the container and the excluded-volume frustration of molecules in can be utilized for directing self-assembled systems, similar to that observed experimentally [68,69].

We have compared EDMD and MC simulations for confined systems on square containers with $n \times n$ number of molecules. As with our previous work [7], the focus on $n \times n$ was deliberate, as was the focus on circular objects in square containers, due to their tendency to form easily recognizable patterns under confinement [31]. As the order metrics used for extended systems become less descriptive with increasing confinement, as described in Section 4.3, the use of systems with easily recognizable patterns allows us to take advantage of real-space descriptions to classify disorder.

Fig. 5 shows a distribution chart of the area fraction probability histograms (cf. Fig. 2(a)) for a variety of system sizes. In the case of confined systems, the mean and standard deviation of ϕ are not enough to accurately describe the behavior of molecular arrangement. Confinement imposes specific patterns which are in pressurized equilibrium with the container (i.e. metastable). This causes a localized probability around the area fraction ϕ of that metastable state as it becomes frequently sampled. In Fig. 5, thicker widths of these bins correlate to a higher probability of configurations at those densities. This representation allows a gauge across ensembles with varying numbers molecules at a glance. The effects of confinement result in the same net overall outcome such that Monte Carlo and event driven molecular dynamics can both be tuned to generate disordered states for low numbers of molecules. While not exactly the same, there exists a high degree of similarity in the distribution of probabilities. Both techniques have protocols that can produce a similar probability of configurations of a given area fraction within an ensemble of 4032 runs (SI:Fig(3)).

The expected densest patterns [31] are included in Fig. 5 along the top of the histograms, scaled to have the same molecular diameter for easy comparison. Dotted horizontal lines connect the patterns to the area fraction associated with it to highlight the place where these patterns are found in the probability distribution. For instance, in systems $N \leq 36$, the $n \times n$ lattice is a distinct state from all other patterns, and in fact, forms the densest possible configuration. The disordered states are clearly separate microstates with lower area fraction. When the system increases $N > 36$, the correlation between expected area fraction and the lattice microstate becomes blurred. The molecules have enough volume to rearrange into states denser than the $n \times n$. As is well known and documented for circles under square confinement [31], these objects can densify by re-positioning into non-trivial sections of hexagonal sub-patterns with disordered grain boundaries.

These highest density patterns are also a good benchmark to confirm if the chosen simulation method is accurately modeling natural patterns. If these patterns are never sampled within an ensemble, then the protocol is not accurately representing all possible physical states, and could be nonphysical. Both MC and EDMD are able to sample these expected patterns using the optimized protocols.

4.3. The discontinuous morphology in confined systems causes failures in structural classification using bulk techniques and forces classifying individual configurations into equivalent patterns using shape-matching techniques

Most of the analytical tools described previously are not well suited to characterize the structure of finite systems under confinement. Edge effects dominate as the number of molecules decreases. This poses a large problem when trying to define neighbors to those molecules on the boundaries. For larger confined systems, this error can be reduced by neglecting those in contact with the boundary. However, as the number of objects in confined systems decreases, this error will dominate.

In the case of the pair correlation function, the issue comes from the assumption of molecular positioning outside the simulation box. In periodic boundaries, each molecule can be moved by the periodic translational basis vectors as many times as needed. This approximation implies that density outside the simulation space is the same as inside. However, in confined systems, there are no molecules outside the boundary. As the distance around the molecule increases, a significant portion of the area sampled by the pair correlation function will lie outside the simulation box, causing large errors. Because of this, the pair correlation function is only accurate to the first diameter (or less if the molecule is in a corner). This issue translates over to the translational-order parameter, as it is directly related to the $g(r)$. The bond-order parameter suffers from the same shortcoming as well. Molecules that populate the container walls will only have neighbors inside the box. Highly ordered systems of finite size can be misclassified with a lower average local bond order parameter to the system, attributed solely to the edge effects.

However, small confined molecular systems have the advantage of allowing direct real-space methods to characterize their state of ordering. The presence of square walls introduce a reference frame against which molecule positions can be measured. In the case of periodic boundaries, rotational and translational symmetry prevent such an absolute reference frame from being utilized between configurations in the ensemble, requiring the more probabilistic approach to structure described previously.

We have applied a method of shape matching to classify and collect the different patterns appearing in the statistical ensembles [70,71]. A point-matching descriptor using the center positions of the molecules were used to partition the data into parcels, that is, all microstates consistent with the same pattern. We deliberately chose the set of $n \times n$ molecules due to their tendency to form $n \times n$ square lattices. The square lattice is a configuration that can be pattern matched with the most accuracy, since it is exactly the same under all symmetry operations. This sets the confidence interval for the precision of the pattern matching routine.

We considered three primary cases for the comparison of MC and EDMD approaches, as expressed in Table 2: the densest patterns as predicted by literature [31], the $n \times n$ square lattice, and the most probable pattern. The parcel with the most members can be considered as the most probable pattern. If the $n \times n$ configuration is the most probable, the table reports the parcel size of the next most populous disordered state.

Across the board, we notice that molecular dynamics tends towards more densified states. In pattern matching the $n \times n$ and densest configurations, MC consistently shows fewer counts. However, these expected states are consistently sampled, albeit with low probability. Given that MC is more likely to yield metastable states for systems under confinement, sampling of these states supports the notion that MC is accurately modeling realistic systems.

As the number of molecules increases so too does the configurational entropy associated with the ensemble. This results in more variation between each outcome, where similarly dense patterns can have many different positional permutations. Above ($N \geq 49$), the square lattice is overtaken by a new configuration as the most dense (cf. Fig. 5). Even though this lattice is still an available static state, the probability of sampling it drops heavily. This phenomena is captured by both simulation methods, where $n \times n$ configurations are virtually unsampled above ($N \geq 49$) (see Table 2). As the number of matched states drop by increasing N , the most probable pattern sampled by each simulation method can also vary. In this case, both methods will generate similar patterns but with different yields.

Each ensemble is comprised of dense disordered configurations. To remove unintentional bias of favoring one microstate over any other, we combine the positions of all patterns together to show the confinement space most traversed by the molecules. The centroids of all configurations in the ensemble can be plotted together to produce a point cloud map, i.e., a visual description of all positions visited by every molecule in the ensemble of configurations. To focus solely on disordered states, the $n \times n$ and/or most dense state patterns parceled are removed from this point cloud map.

Table 2

Number of patterns classified from shape-matching routines using a tolerance similarity criteria of (0.975). Ensembles contain 4032 dense disordered patterns confined in square container.

	Pattern	4 × 4	5 × 5	6 × 6	7 × 7	8 × 8	9 × 9
MC	Densest [31]	3157	1543	154	2	6	49
EDMD		3778	1683	380	5	247	193
MC	$n \times n$	3157	1543	154	0	0	0
EDMD		3778	1683	380	3	0	3
MC	Most probable	231	475	165	121	41	56
EDMD	(non $n \times n$)	61	212	119	197	191	194

As can be seen in Fig. 5(c), not all the available space in the simulation box is sampled during the simulations. The excluded volume of the molecule causes specific spaces to be physically forbidden (i.e. unable to come within one radius of the wall) and leads to a similar type of geometric frustration of molecules in the interior. For all system sizes, the point clouds are consistently similar for both simulation methods. Even though the most probable pattern can differ between simulations, the global result of confinement remains constant between simulation methods.

5. Noticeable differences between simulation approaches and summary of statistics: are they really the same?

In order to systematically compare Monte Carlo and event driven molecular dynamics, in this study, we focused on a simplified system of circular objects with hard-core potential interactions. Based on an analysis of order metrics in extended systems of 1024 molecules, and on positional classification of confined systems of up to 81 molecules, we can conclude that when the probability density of covering area fractions are matched, the ensembles produced from MC and EDMD will show the same level of structural disorder and positional patterns. Though they are based on a fundamentally different conceptual basis – static vs dynamic – in a statistical large set of simulations, the overall outcomes are indeed similar. Though this might not be unexpected from the perspective of the central limit theorem, drawing an accurate comparison across methods was not trivial, requiring careful selection of parameters, establishment of appropriate metrics, and examination of many configurations.

Table 1 summarizes the values of the order metrics as extracted from the full set of 4032 configurations for both MC and EDMD approaches. The global expectation values for all these parameters are within the variance, accurately predicting that the systems will develop a mostly hexagonal close-packed configuration ($q_6 \approx 90\%$ of a triangular lattice), with some disordered grain boundaries that reduce the overall surface covering fraction ($\approx 95\%$ density of a full dense triangular lattice with no defects). Voronoi analysis also supports this claim. Both methods have just over half of all molecules possessing Voronoi area deviation to within 5% of the hexagonal expectation value. The pair wise distances distributions of molecules has an almost identical $g(r)$, with a Δ_{RMS} of only 0.05. Given the same density, MC slightly tends more towards organized systems than EDMD, as seen by the order map in Fig. 2(c), and local bond order Fig. 3(c). However, there is still a large degree of overlap between the two approaches which indicates similar structural signatures across methods.

Though all the parameters examined are quite similar for the two approaches, there is one difference in the observed morphology that rests on the fundamental difference between the two approaches. There are specific morphologies that arise from the EDMD method that are unseen in MC configurations. This is mainly in the form of monovacancies (i.e., point defects) and stacking faults. This leads to a tendency to sample with greater frequency slightly more organized configurations in extended bulk-like systems due to the lack of stabilized defects. In MC, random displacements will cause molecules to move into free space, preventing the stabilization of this particular configuration. This results in a probability for less than one defect in 4032 samples. In contrast, these are highly probable to find in EDMD, varying from zero to six point defects in a single configuration. However, this lack of internal pressure, means that for confined systems, there is a tendency to form less dense metastable states. One simulation pattern might provide a force balance through a contact networks of particles. However, loose particles (rattlers) can traverse the box and transfer the necessary momentum to break the global jammed state. This then cascades into a transition into a new metastable state. After a sufficient amount time, this pattern tends towards its densest state. With MC, any rattlers in the metastable state will not transfer momentum. Since MC simulations sample static states, there is effectively no pressure from the molecules and the container. This is one of the reasons that protocols can be easily transferred among simulation environments. Therefore, Monte Carlo as an approach is slightly better suited to modeling systems when the desired morphology is represented by a metastable state (i.e. low probability morphologies that can be directed by manipulating the object); molecular dynamics on the other hand is more suited to finding defects that can arise in morphologies.

For directed self-assembly of finite systems of molecules, Fig. 5 summarizes the similarities between the two approaches in finding global outcomes. Though protocol parameters of bulk EDMD simulations could not be transferred to confined systems, it was possible to find a suitable population of configurations for comparison through an examination of the parameter space for EDMD. Once the probability density of area fractions are matched, the ensembles produced from MC and EDMD do show the same positional patterns in square confinement. Though the direct pattern matching yielded different frequencies of a particular configuration (cf. Table 2) being sampled, the global effects were the same for both approaches.

Occurrence of specific patterns can be low or hard to classify, but the structures of the point clouds indicate that all are sampled within both ensembles. Additionally, after the molecular number goes above 36, there is a drop in the number of $n \times n$ lattice configurations found. This can be explained by the frustration between the effects of confinement and the self-assembly of the molecules favoring less free area. At this size, the competition between square and hexagonal patterns manifests as additional disordered states that are more dense than $n \times n$ but less than the known densest pattern. In the case of both MC and EDMD, this pattern all but disappears (3 and less per 4032) for molecule numbers greater than 49.

The discrepancy in the frequency of configurations in the most dense and most probable parcels in Table 2 between MC and EDMD can have two possible explanations. One, as described above, is related to the dynamic nature of EDMD. The collective vibration of particles that are very close allows for the simulation to explore the localized free area in a relatively small amount of time. This allows the particles to slip into the densest states, which are easily classifiable. Another is related to the polygonal nature of the circular renderings in MC. Slight deviations in the molecular centroids can have an impact on the accuracy of the pattern matching routine. Minimizing the difference between the radius and apothem of the regular polygon is critical in producing accurate positions for the centroids used to pattern match. In contrast, EDMD objects are defined by an exact radius, which creates less variation between neighboring particle distances, simplifying their classification. For confined MC simulations, 100-sided polygons are used to mimic circles. In bulk systems, where there is much more computational stress due to the large number of molecules, a polygon of 40 sides was used. The covering area fraction, in particular, was found to be sensitive to these differences [7]. While this difference was not significant for global metrics (40-sided and 100-sided regular polygons will produce similar distributions of structural parameters $g(r)$, q_6 , and t), this was seen to affect the number of configurations assigned to particular parcels in the pattern matching algorithm (see SI:Sec(H)). A combination of both effects could be magnifying the differences between individual configuration during the comparison.

Such an effect also underscores the need to compare protocols and simulation methods on a statistical scale, rather than at the limit of one or a few configurations. In general, the focus on a few patterns makes the comparison unreliable. By scaling up to a statistical ensemble, unintentional selection bias is eliminated and the true similarities and differences are highlighted.

A final general finding comparing the two approaches links back to the concept of reproducibility of simulation results. Reliability and repeatability hinges on simulation stability. As noted previously, protocol parameters of bulk EDMD simulations could not be transferred to confined systems and still produce dense disordered configurations. This can be attributed to the growth rate. When the simulations have low-molecule numbers, particles can expand so rapidly that their radius expands outside of the hard container. These overlaps cannot be resolved by repositioning of the particles along their trajectories, and thus, the program can crash. On the other hand, the MC method is based on rejected moves. This allows it to sample the same nonphysical states as static objects but continue after rejecting the move. This makes it much easier to achieve a meaningfully large ensemble of configurations from MC than from EDMD, where the simulation has to be restarted continuously or a high number set initially in the hopes that sufficient numbers are able to fully densify (in one instance over 3 million configurations were started to achieve a set of 4032 configurations). However, this leads to another caveat regarding computational resources. Computational time becomes important when dealing with large ensembles, especially when the execution time for each method is quite different. Due to the stochastic nature of the MC method, it will require many rejected trial moves before converging to a solution. Each random displacement requires the polygon clipping routine to check over all other molecules in the simulation. This begins to stack quite heavily for bulk systems of several thousands of molecules. Conversely, EDMD numerically integrates the deterministic equations of motion which is much less computational work. We note here that to generate ensembles within a reasonable time, MC method needed to be distributed among modern high performance computing centers, whereas EDMD could be generated on consumer grade computers.

The major advantage of using MC lies in its ability to directly explore molecules with exceedingly complex geometric descriptions (polygons) by using the same implementation and protocols as with circles. Rotation and anisotropic descriptions of particle dynamics are complex to solve analytically, making EDMD less attractive as shapes become more complicated. Sampling free areas by random rotations and translations with polygons can remove the complexity. The order metrics described throughout this contribution are also broad enough that, if a different shape is used, the same tools can be utilized against the crystalline configuration of that shape (i.e. square molecules can be compared against square lattice configurations). This provides a robust, reliable and stable approach to simulating complex morphologies.

6. Concluding summary

We report that stochastic and dynamic simulations of hard-core circular molecules will have the same structure if they have the same density, driven by the configurational entropy. In this contribution, we systematically compared the outcomes from event driven molecular dynamics and Monte Carlo approaches to investigate the reproducibility and validation between methods. Ensembles of 4032 configurations were gathered to generate statistical sets to compare how the influence of simulation directives affects the physical properties of outcomes. To emphasize the need for reproducible simulations, the positional data obtained from these two simulation methods has been made freely available (see the SI:Sec(A)).

Monte Carlo explores systems with slowly varying density, which is a weak but constant pressure. Event-driven molecular dynamics has a varying pressure, meaning a non-constant rate of compression. Each method explores different

paths through the thermodynamic landscape; however, dense arrays of planar molecules were shown to produce similar outcomes in bulk periodic systems, as well as in confining square boundaries. Structural classification of these systems (averaged pair correlation function, bond-order parameter, translational order parameter, and Voronoi diagrams) shows that stochastic and dynamic approaches do not alter the morphology of the steric molecules. Similar morphologies with a fixed density are a result of entropic packing. The role of the entropy in driving self-assembly can be exploited to produce novel morphologies for the next generation of organic devices.

Acknowledgments

The authors would like to thank the staff at Compute Canada in helping with and providing the computational resources that were essential to this study. This work was made possible by the facilities of the Shared Hierarchical Academic Research Computing Network (SHARCNET: www.sharcnet.ca) and Compute/Calcul Canada. The authors also thank A. Diaz-Ortiz for helpful discussions and suggestions. This research was supported by 436100-2013 RGPIN and 384889-2010 CREAT.

Appendix A. Supplementary data

Supplementary material related to this article can be found online at <http://dx.doi.org/10.1016/j.physa.2016.12.075>.

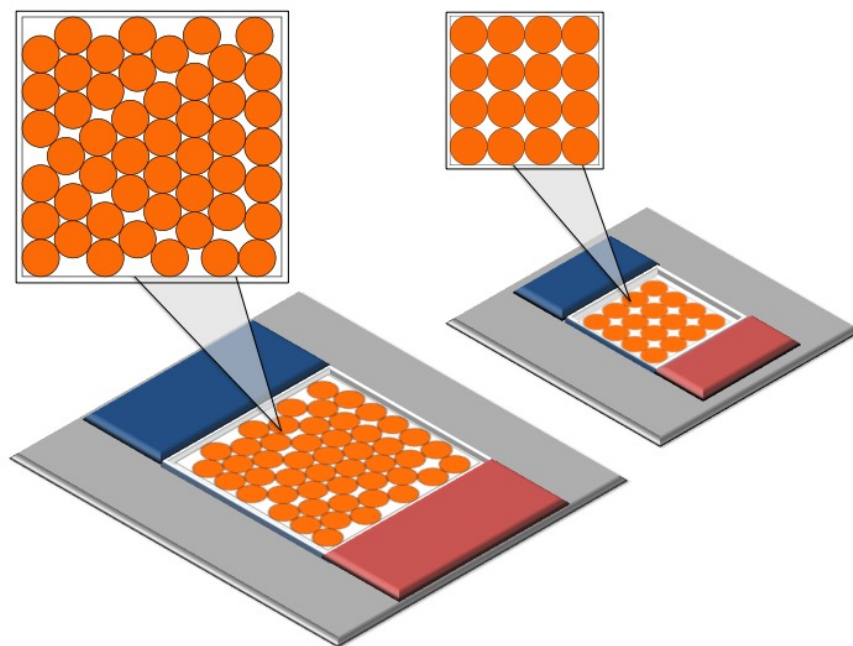
References

- [1] Z.B. Henson, K. Mullen, G.C. Bazan, Design strategies for organic semiconductors beyond the molecular formula, *Nature Chem.* 4 (2012) 699–704.
- [2] A. Turak, M. Nguyen, F. Maye, J. Heidkamp, P. Lienerth, J. Wrachtrup, H. Dosch, Nanoscale engineering of exciton dissociating interfaces in organic photovoltaics, *J. Nano Res.* 14 (2011) 125–136.
- [3] S.H. Park, A. Roy, S. Beaupre, S. Cho, N. Coates, J.S. Moon, D. Moses, M. Leclerc, K. Lee, A.J. Heeger, Bulk heterojunction solar cells with internal quantum efficiency approaching 100%, *Nat. Photonics* 3 (2009) 297–303.
- [4] H.-C. Chen, Y.-H. Chen, C.-C. Liu, Y.-C. Chien, S.-W. Chou, P.-T. Chou, Prominent short-circuit currents of fluorinated quinoxaline-based copolymer solar cells with a power conversion efficiency of 8.0%, *Chem. Mater.* 24 (2012) 4766–4772.
- [5] Y. Liang, Z. Xu, J. Xia, S.-T. Tsai, Y. Wu, G. Li, C. Ray, L. Yu, For the bright future—bulk heterojunction polymer solar cells with power conversion efficiency of 7.4%, *Adv. Energy Mater.* 22 (2010) E135–E138.
- [6] S.A. Ayoub, J.B. Lagowski, Optimizing the performance of multilayered organic polymer devices using computational dimer approach a case study, *J. Phys. Chem. C* 120 (2016) 496–507.
- [7] A. Díaz Ortiz, B. Arnold, M. Bumstead, A. Turak, Steric self-assembly of laterally confined organic semiconductor molecule analogues, *Phys. Chem. Chem. Phys.* 16 (2014) 20228.
- [8] T.J. Roussel, E. Barrena, C. Ocal, J. Faraudo, Predicting supramolecular self-assembly on reconstructed metal surfaces, *Nanoscale* (2014) 7991–8001.
- [9] M. Yoneya, M. Kawasaki, M. Ando, Molecular dynamics simulations of pentacene thin films: The effect of surface on polymorph selection, *J. Mater. Chem.* 20 (2010) 10397.
- [10] P. Clancy, Application of molecular simulation techniques to the study of factors affecting the Thin-Film morphology of small-molecule organic semiconductors, *Chem. Mater.* 23 (2011) 522–543.
- [11] S. Reddy, V.K. Kuppala, Molecular dynamics simulations of organic photovoltaic materials: Investigating the formation of π -stacked thiophene clusters in oligothiophene/fullerene blends, *Synth. Met.* 162 (2012) 2117–2124.
- [12] T. Neumann, D. Danilov, C. Lennartz, W. Wenzel, Modeling disordered morphologies in organic semiconductors, *J. Comput. Chem.* 34 (2013) 2716–2725.
- [13] T.J. Roussel, L.F. Vega, Modeling the self-assembly of nano objects: Applications to supramolecular organic monolayers adsorbed on metal surfaces, *J. Chem. Theory Comput.* 9 (2013) 2161–2169.
- [14] I.G. Kaplan, Model potentials, in: *Intermolecular Interactions*, John Wiley & Sons, Ltd., 2006, pp. 183–254.
- [15] I.G. Kaplan, Nonadditivity of intermolecular interactions, in: *Intermolecular Interactions*, John Wiley & Sons, Ltd., 2006, pp. 141–182.
- [16] N.G. Fytas, V. Martín-Mayor, M. Picco, N. Sourlas, Phase transitions in disordered systems: The example of the random-field Ising model in four dimensions, *Phys. Rev. Lett.* 116 (2016) 227201.
- [17] G. Korniss, C.J. White, P.A. Rikvold, M.A. Novotny, Dynamic phase transition, universality, and finite-size scaling in the two-dimensional kinetic Ising model in an oscillating field, *Phys. Rev. E* 63 (2000) 016120.
- [18] A.M. Ferrenberg, R.H. Swendsen, New monte carlo technique for studying phase transitions, *Phys. Rev. Lett.* 61 (1988) 2635–2638.
- [19] D. Boulatov, V. Kazakov, The Ising model on a random planar lattice: The structure of the phase transition and the exact critical exponents, *Phys. Lett. B* 186 (1987) 379–384.
- [20] I. Nakamura, A.-C. Shi, Study of entropy-driven self-assembly of rigid macromolecules, *Phys. Rev. E* 80 (2009) 021112.
- [21] Y. Miyake, T. Nagata, H. Tanaka, M. Yamazaki, M. Ohta, R. Kokawa, T. Ogawa, Entropy-controlled 2D supramolecular structures of N,N'-bis(n-alkyl)naphthalenediimides on a HOPG surface, *ACS Nano* 6 (2012) 3876–3887.
- [22] P.P.F. Wessels, B.M. Mulder, Entropy-induced microphase separation in hard diblock copolymers, *Phys. Rev. E* 70 (2004) 031503.
- [23] D. Frenkel, Entropy-driven phase transitions, *Physica A* 263 (1999) 26–38.
- [24] D. Görl, X. Zhang, V. Stepanenko, F. Würthner, Supramolecular block copolymers by kinetically controlled co-self-assembly of planar and core-twisted perylene bisimides, *Nature Commun.* 6 (2015) 7009.
- [25] A.D. de Zerío Mendaza, A. Melianas, S. Rossbauer, O. Bäcke, L. Nordstierna, P. Erhart, E. Olsson, T.D. Anthopoulos, O. Inganäs, C. Müller, High-entropy mixtures of pristine fullerenes for solution-processed transistors and solar cells, *Adv. Mater.* 27 (2015) 7325–7331.
- [26] R. Dattani, J.T. Cabral, Polymer fullerene solution phase behaviour and film formation pathways, *Soft Matter* 11 (2015) 3125–3131.
- [27] D. Banerjee, M. Dadmun, B. Sumpter, K.S. Schweizer, Theory of the miscibility of fullerenes in random copolymer melts, *Macromolecules* 46 (2013) 8732–8743.
- [28] C.I. Wang, C.C. Hua, Solubility of C60 and PCBM in Organic Solvents, *J. Phys. Chem. B* 119 (2015) 14496–14504.
- [29] L. Xu, L. Yang, L. Cao, T. Li, S. Chen, D. Zhao, S. Lei, J. Ma, Effect of bulky substituents on the self-assembly and mixing behavior of arylene ethynylene macrocycles at the solid/liquid interface, *Phys. Chem. Chem. Phys.* 15 (2013) 11748–11757.
- [30] N. Hauptmann, K. Scheil, T.G. Gopakumar, F.L. Otte, C. Schtt, R. Herges, R. Berndt, Surface control of alkyl chain conformations and 2D chiral amplification, *J. Am. Chem. Soc.* 135 (2013) 8814–8817.
- [31] E. Specht, Packomania, ("28-Oct-2015"). URL <http://www.packomania.com/> (accessed: 10.08.16).
- [32] D. Gruznev, A. Matetskiy, I. Gvozdz, A. Zotov, A. Saranin, {C60} adsorption onto the one-atomic-layer in films on si(111) surface, *Surf. Sci.* 605 (2011) 1951–1955.

- [33] P. Song, B.K. Olmsted, P. Chaikin, M.D. Ward, Crystallization of micrometer-sized particles with molecular contours, *Langmuir* 29 (45) (2013) 13686–13693.
- [34] A. Morin, J. Urban, P.D. Adams, I. Foster, A. Sali, D. Baker, P. Sliz, Shining light into black boxes, *Science* 336 (2012) 159–160.
- [35] V. Stodden, F. Leisch, R.D. Peng (Eds.), *Implementing Reproducible Research*, first ed., Chapman and Hall/CRC, 2014.
- [36] S. Buck, Solving reproducibility, *Science* 348 (2015) 1403.
- [37] B. Alberts, R.J. Ciccerone, S.E. Fienberg, A. Kamb, M. McNutt, R.M. Nerem, R. Schekman, R. Shiffrin, V. Stodden, S. Suresh, M.T. Zuber, B.K. Pope, K.H. Jamieson, Self-correction in science at work, *Science* 348 (2015) 1420–1422.
- [38] B.A. Nosek, G. Alter, G.C. Banks, D. Borsboom, S.D. Bowman, S.J. Breckler, S. Buck, C.D. Chambers, G. Chin, G. Christensen, M. Contestabile, A. Dafoe, E. Eich, J. Freese, R. Glennerster, D. Goroff, D.P. Green, B. Hesse, M. Humphreys, J. Ishiyama, D. Karlan, A. Kraut, A. Lupia, P. Mabry, T. Madon, N. Malhotra, E. Mayo-Wilson, M. McNutt, E. Miguel, E. Levy Paluck, U. Simonsohn, C. Soderberg, B.A. Spellman, J. Turitto, G. VandenBos, S. Vazire, E.J. Wagenmakers, R. Wilson, T. Yarkoni, Promoting an open research culture, *Science* 348 (2015) 1422–1425.
- [39] V. Stodden, S. Miguez, Best practices for computational science: Software infrastructure and environments for reproducible and extensible research, *J. Open Res. Softw.* 2 (2014) 1–6.
- [40] V. Stodden, Reproducing statistical results, *Ann. Rev. Stat. Appl.* 2 (2015) 1–19.
- [41] M. Allen, D. Frenkel, J. Talbot, Molecular dynamics simulation using hard particles, *Comput. Phys. Rep.* 9 (1989) 301–353.
- [42] S. Miller, S. Luding, Event-driven molecular dynamics in parallel, *J. Comput. Phys.* 193 (2003) 306–316.
- [43] A. Donev, S. Torquato, F.H. Stillinger, Neighbor list collision-driven molecular dynamics simulation for nonspherical hard particles. i. algorithmic details, *J. Comput. Phys.* 202 (2005) 737–764.
- [44] A. Donev, S. Torquato, F.H. Stillinger, Neighbor list collision-driven molecular dynamics simulation for nonspherical hard particles. ii. applications to ellipses and ellipsoids, *J. Comput. Phys.* 202 (2005) 765–793.
- [45] M. Skoge, A. Donev, F.H. Stillinger, S. Torquato, Packing hyperspheres in high-dimensional euclidean spaces, *Phys. Rev. E* 74 (2006) 041127.
- [46] M. Skoge, A. Donev, F.H. Stillinger, S. Torquato, Publisher's note: Packing hyperspheres in high-dimensional euclidean spaces, *Phys. Rev. E* 75 (2007) 029901(E).
- [47] L. Filion, M. Marechal, B. van Oorschot, D. Pelt, F. Smalenburg, M. Dijkstra, Efficient method for predicting crystal structures at finite temperature: Variable box shape simulations, *Phys. Rev. Lett.* 103 (2009) 188302.
- [48] J. de Graaf, R. van Roij, M. Dijkstra, Dense regular packings of irregular nonconvex particles, *Phys. Rev. Lett.* 107 (2011) 155501.
- [49] J. de Graaf, L. Filion, M. Marechal, R. van Roij, M. Dijkstra, Crystal-structure prediction via the floopy-box monte carlo algorithm: Method and application to hard (non)convex particles, *J. Chem. Phys.* 137 (2012) 214101.
- [50] D. Frenkel, B. Smit, *Understanding Molecular Simulation*, second ed., Academic Press, 2001.
- [51] S. Torquato, Y. Jiao, Robust algorithm to generate a diverse class of dense disordered and ordered sphere packings via linear programming, *Phys. Rev. E* 82 (2010) 061302.
- [52] D. Frenkel, G.C.A.M. Mooij, B. Smit, Novel scheme to study structural and thermal properties of continuously deformable molecules, *J. Phys.: Condens. Matter* 3 (1991) 3053–3076.
- [53] J.I. Siepmann, D. Frenkel, Configurational bias monte carlo: A new sampling scheme for flexible chains, *Mol. Phys.* 75 (1992) 59–70.
- [54] J.J. de Pablo, M. Laso, U.W. Suter, Estimation of the chemical potential of chain molecules by simulation, *J. Chem. Phys.* 96 (1992) 6157–6162.
- [55] M. Laso, J.J. de Pablo, U.W. Suter, Simulation of phase equilibria for chain molecules, *J. Chem. Phys.* 97 (1992) 2817–2819.
- [56] A.H. Marcus, S.A. Rice, Phase transitions in a confined quasi-two-dimensional colloid suspension, *Phys. Rev. E* 55 (1997) 637–656.
- [57] A. Baddeley, R. Turner, spatstat: An r package for analyzing spatial point patterns, *J. Stat. Softw.* 12 (6) (2005) 1–42. URL <http://www.jstatsoft.org/v12/i06/>.
- [58] R Core Team, R: A Language and Environment for Statistical Computing, R Foundation for Statistical Computing, Vienna, Austria, 2013. URL <http://www.R-project.org/>.
- [59] T.M. Truskett, S. Torquato, P.G. Debenedetti, Towards a quantification of disorder in materials: Distinguishing equilibrium and glassy sphere packings, *Phys. Rev. E* 62 (2000) 993–1001.
- [60] J.R. Errington, P.G. Debenedetti, Relationship between structural order and the anomalies of liquid water, *Nature* 409 (2001) 318–321.
- [61] Z. Yan, S.V. Buldyrev, N. Giovambattista, H.E. Stanley, Structural order for one-scale and two-scale potentials, *Phys. Rev. Lett.* 95 (2005) 130604.
- [62] P.J. Steinhardt, D.R. Nelson, M. Ronchetti, Bond-orientational order in liquids and glasses, *Phys. Rev. B* 28 (1983) 784–805.
- [63] Y. Wang, S. Teitel, C. Dellago, Melting of icosahedral gold nanoclusters from molecular dynamics simulations, *J. Chem. Phys.* 122 (2005) 214722.
- [64] A.R. Kansal, S. Torquato, F.H. Stillinger, Diversity of order and densities in jammed hard-particle packings, *Phys. Rev. E* 66 (2002) 041109.
- [65] D.G. de Oteyza, E. Barrena, H. Dosch, Y. Wakayama, Nanoconfinement effects in the self-assembly of diindenoperylene (dip) on cu(111) surfaces, *Phys. Chem. Chem. Phys.* 11 (2009) 8741–8744.
- [66] S. Himmelberger, J. Dacuña, J. Rivnay, L.H. Jimison, T. McCarthy-Ward, M. Heeney, I. McCulloch, M.F. Toney, A. Salleo, Effects of confinement on microstructure and charge transport in high performance semicrystalline polymer semiconductors, *Adv. Funct. Mater.* 23 (2013) 2091–2098.
- [67] X. Yang, A. Alexeev, M.A.J. Michels, J. Loos, Effect of spatial confinement on the morphology evolution of thin poly(p-phenylenevinylene)/methanofullerene composite films, *Macromolecules* 38 (2005) 4289–4295.
- [68] T.-S. Kim, S. Hyun Kim, M. Jang, H. Yang, T.-W. Lee, Charge transport and morphology of pentacene films confined in nano-patterned region, *NPG Asia Mater.* 6 (2014) e91.
- [69] M. Aryal, K. Trivedi, W.W. Hu, Nano-confinement induced chain alignment in ordered P3HT nanostructures defined by nanoimprint lithography, *ACS Nano* 3 (2009) 3085–3090.
- [70] A.S. Keys, C.R. Iacovella, S.G. Glotzer, Characterizing structure through shape matching and applications to self-assembly, *Ann. Rev. Condens. Matter Phys.* 2 (2011) 263–285.
- [71] A.S. Keys, C.R. Iacovella, S.G. Glotzer, Characterizing complex particle morphologies through shape matching: Descriptors, applications, and algorithms, *J. Comput. Phys.* 230 (2011) 6438–6463.

Chapter 6

Directing Self-Assembly with Confinement



As electronic components become smaller, so does the amount of volume available for molecules to self-assemble within. The influences from both the container walls and interior quantized space impose restrictions onto molecules to prefer particular arrangements within the box. The series of possible metastable molecular dispersions can be enumerated for confining systems with low numbers of molecules and their probability of occurrence can be approximated by how frequently similar patterns reoccur within the ensemble.

6.1 My Contributions

My contributions to this publication were from actively collaborating to develop methods to test the effects of confinement and evaluated edits to drafts with author Dr. Ayse Turak. Dr. Alejandro Diaz Ortiz is the main author of the manuscript and Bjorn Arnold had input on initial development coding for the Monte Carlo simulation method used (named “gransim” - for granular simulation). My main focus for this publication was to develop ways for improving the pattern matching scheme we used to classify the big data sets. My work has been to analyze and expand the use of the dataset presented here by using it in another publication shown in Chapter 5. I added to the value of this set of data by sharing what we acquired using the computational resources at the Texas Advanced Computing Center.

My work focused on improving the speed of this algorithm, expanding its capabilities to classify systems of more particles. This has allowed us to explore the role that molecule shape has on directing the formation of patterns within a box. Classifying these datasets were too time consuming for studying systems with more particles under confinement. For example, I worked to reduce the time required for the pattern-matching routine to classify all configurations within an ensemble of $N=36$ molecules down from the previous acceptable time-limit of a week, to completing within an hour on consumer grade desktop computers. Because of this improvement, we opened up the number of new systems that can be explored. This pattern matching routine included and fully integrated into the “disLocate” analysis package (Chapter 4).

It also allowed me to uncover a deficiency in the original “gransim” algorithm which produced unclassifiable patterns for certain shapes. The way I found it was to analyze the simulated ensembles using complex (non-circular) shaped particles with the pattern matching tool. Initial observations suggested that similar parcels were classified as different patterns, leading to the possibility that low recurrence of expected patterns could be the result of off-center molecules instead of miscalculations within the pattern matching routine. My work revealed that the “gransim” algorithm was internally redefining the shape of the molecules, resulting with particles with displaced molecular centre of mass. This caused an unnoticeable skew to the output polygon shape (which went undetected by human perception in renderings of configurations) but caused enough deviation to the centroids for common patterns to be mismatched. If this error was not caught, it could have propagated out into the data used in Chapter 7 and would have provided incorrect results for all analysis methods that rely on molecular centroids to classify dispersion. This would not have been found if this pattern matching tool was not used. Detecting and correcting this numerical deficiency was the result of my contribution toward improving the routines used in the manuscript. These changes allowed us to expand our research into simulating complex molecules with confidence that the resulting morphologies will be generated with accurate representations of molecules.

6.2 Overview of Manuscript (PCCP - 2014)

Self-assembly takes advantage of the natural thermodynamic pathway that molecules take on their way to producing planar patterns. The resulting patterns of particles are a product of the initial preparation methods and various environmental influences, such as temperature, deposition rate, and number of objects in the system. One external influence we explore here is the role confinement has on the possible intermolecular structures allowable for molecules to assemble within.

Large ensembles of simulated morphologies with many particles were generated to gauge the bulk properties of steric molecules. The simulations were then changed from periodic boundaries into a hard square container. The influence becomes clear as the container produces a shift toward morphologies with densities lower than the unconstrained bulk system. We then reduce the number of particles allowed to self-assemble together within the container to observe the effect of the box. What was observed is that there is a competition between the steric hindrance of the walls and the intermolecular frustration of neighbouring particles. Particles align themselves along the walls of the box, which form specific boundary conditions and this influence propagates into the centre of the channel as particles condense. Wall particles tend to impose a square lattice

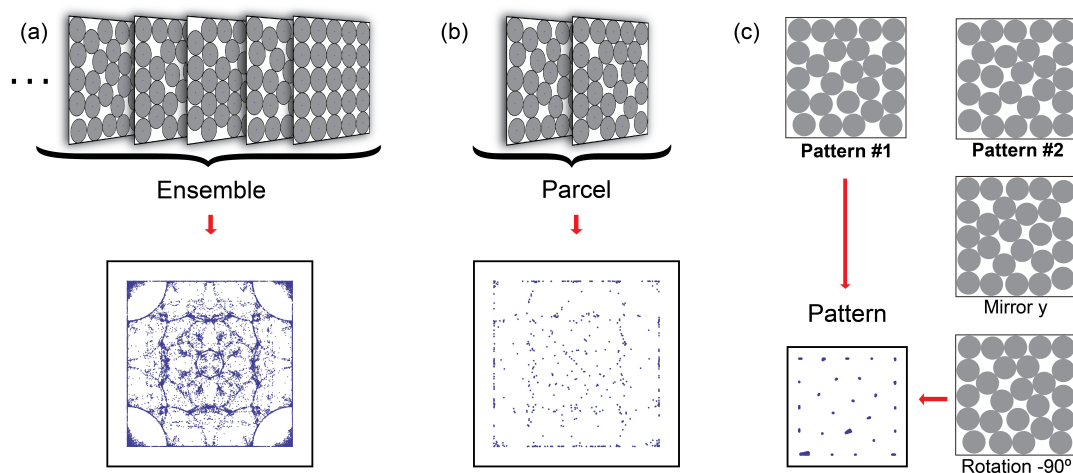


Figure 6.1: Reducing an ensemble of configurations into parcels of patterns. (a) Global effect of confinement can be seen in the point cloud where all centroids of all molecules of all configurations are combined and plotted together. (b) Individual configurations which were successfully classified as similar by pattern matching are grouped together into a parcel. These configurations can still be jumbled (i.e. pre-symmetry operations). (c) Configurations in the parcel are rotated and mirrored relative to each other so their positions have the lowest amount of deviation. Finally, the characteristic parcel pattern emerges at the end, showing the spatial distributions molecules are directed into by confinement effects.

packing which comes into conflict against the densest packing of circles, the hexagonal lattice. This interplay between influences causes metastable states to appear, limiting the number and probability for variations in disordered states.

These states provide a basis for understanding the breadth of possible arrangements that molecules can self-assemble into. The manuscript details the resulting probability distributions of particle densities, positional probability, and frequency of pattern occurrences as a function of varying particle numbers from bulk systems of $N=1024$ particles to the highly contained system of $N=9$ particles through the series of decreasing square numbers ($N = n^2$). We find the emergence of finite and repeated microstates within ensembles of 4032 independently generated Monte Carlo simulations of circular particles of numbers less than $N = 5^2$.

The sections below highlight portions of my research that did not appear in the manuscript and/or were part of the supporting information associated with this publication. Chapter 6 starts with a brief overview of the manuscript in Section 6.2. Section 6.3 highlights the pattern matching algorithm and the optimizations I made to the routine. It also outlines the relevance of these point cloud probability maps and frames them in terms of a visual representation of the partition function. Section 6.4 discusses the confinement effects in relation to a varying molecule shape. The system is held at a constant 49 molecules while the self-assembly of regular polygons and 6-sided molecules are analyzed. The error that caused centres of mass for complex polygons is outlined here.

6.3 Pattern Matching Microstates into Parcels

A pattern matching scheme is an appropriate method to search for similar configurations in statistically large datasets. Figure 6.1 a) shows how the point cloud is built from configurations within the ensemble of confined molecules. All physically sampled states are combined into a single plot by fixing the container size between configurations so the centroids can be overlaid

together. This visually outlines the global probability for N molecules to arrange themselves into finite sets of patterns when confined in a square. It represents a type of identifier or fingerprint that is specific to the molecular shape and number.

Briefly, as shown schematically in Figure 6.1, our point-matching approach classifies the geometric centres of all microstates into patterns where the identity of the particles has been removed (Figure 6.1(a)). A series of symmetry operations consistent with the boundary conditions of the simulation box are then performed on the candidate patterns (Figure 6.1(b)). This limits the parcelling to only be usable with confined configurations inside the 1x1 box and applies the 8 different symmetry operations from the hard square boundaries. This process is applied to all the elements of the ensemble. A major improvement in this routine was found from pre-calculating the symmetry operations of each pattern into the ensemble prior to the shape-matching routine. A mean-square-root distance of the geometric centres is measured after every symmetric transformation for every pair of candidate patterns. If the difference between two patterns is less than a user set threshold for the matching criteria, then these are considered similar patterns and are grouped together into a parcel.

Notwithstanding its conceptual simplicity, the point-matching method is not without subtleties. The most important one is that structural characterization is based on patterns and not on microstates. Finding matches among the latter would be the simplest of tasks, amounting at a trivial point-by-point distance calculation. Such an approach will render two identical $n \times n$ structures as different because of a different indexing of the particles (see, for instance, Figure 6.1(a)). Thus, a point-matching descriptor requires an assignment of coordinates to determine the optimal correspondence between particles' centre of mass for all structures to be compared. In other words, all structures to be matched should have the particles indexed in a way that, for instance, the particle located at the lower left corner of the cavity, always has the same assigned index. The pattern matching routine has been optimized to attempt multiple sortings of particle index to improve accuracy. As such, the number of configurations that are parcelled into a pattern can prove a first order approximation to the probability of microstates.

One important aspect is that of the similarity criterion to classify the different structures. The similarity or cut-off criterion needs to be stringent enough to not miss similar structures and yet lax enough to allow for small distortions. In our case, we have used the mean-square-root distance as the similarity measure between structures. As can be seen in Figure 6.1(c), relaxation of the acceptance criterion allows recognition of patterns that would otherwise be wrongly classified due to the existence of rattlers (i.e., mobile particles in a defect cavity of an otherwise rigid structure). Interested readers are directed to Ref. [107] for a current review on structure matching in self-assembled systems and to Refs. [108, 109, 110, 111] for more technical accounts.

Each final configuration in the ensemble samples the allowable energy microstates within the confining channel. The frequency of each pattern can be explicitly enumerated by pattern matching and can be used as the probability for this microstate. The partition function Z describes the probability of each state has energy E_i in the statistical ensemble.

$$Z = \sum_i e^{-\beta E_i} \quad (6.1)$$

The pattern matching gives the energetic microstate (Ω_i) and the probability of it appearing in the statistical ensemble $P(\Omega_i)$. The complete summation of all parcels and probability gives the thermodynamic partition function of confined molecules.

$$Z = P(\Omega_1)e^{-\beta E_1} + P(\Omega_2)e^{-\beta E_2} + \dots \quad (6.2)$$

One thing that is quantifiable is the percent yield of repeated configurations. When the number of particles is increased, there is more availability for different configurational permutations.

Figure 6.2 shows an example of the registry maps and sample configurations of the parcels found within the ensemble of $N=25$ confined circular molecules. The registry maps show histogram data of the places within the container where particle centroids are more likely to be constrained to. It is used here instead of the probability map because the pattern matched parcels contain precise positions of molecule centroids and would remain unseen. The colour

Pattern:	1	2	3	4	5	6	All Else
Count	1543	481	160	134	128	76	1510
Probability	0.3826	0.1192	0.0396	0.0332	0.0317	0.0188	0.3745

Table 6.1: Enumeration and probability for microstates shown in the top row of Fig 6.2 (left to right \rightarrow 1 to 6). Data is from ensembles of 4032 randomly generated microstates of $N=25$ circular molecules in a square container.

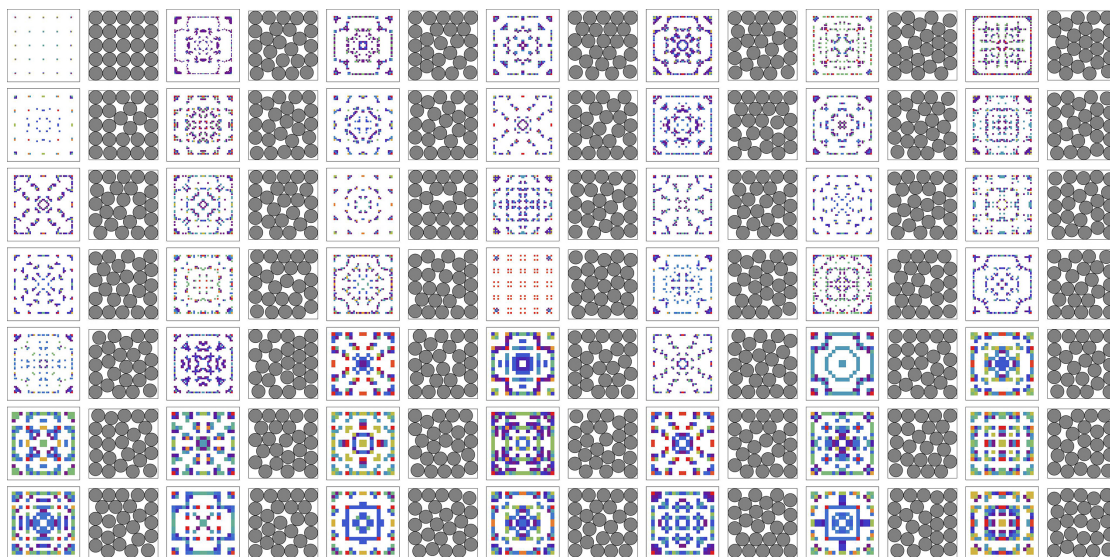


Figure 6.2: Enumeration of microstates with non-zero parcel sizes for $N=25$ circular molecules confined within a box. The pattern with the most parcel members is in the top left - the square packed configuration. Parcels decreasing in size are shown left to right, where the bottom right has the fewest members. The registry map to the left of the configuration shows the planar probability of centroids for that parcel as coloured histograms.

of each square indicates how probable it is to find a centroid in that area. Darker Purple and Blue tones suggest low probability, where Red indicates a higher probability. The free area is indicated as White and shows places with zero probability to find molecule centroids.

As can be seen, the pattern that has the most entries is the square lattice (in the top left) and is also enumerated in Table 6.1. The results are for the top six panels in Figure 6.2, outlining the more probabilistic parcels. The trend gives a clear decline in number of entries within each parcel, as the square lattice pattern dominates with 1543/4032, while the sixth most probable parcel has only 76/4032 entries. As the number of particles within the area increases, so does the number of different positional arrangements each particle can take. This increase in positional entropy is manifested here as a decrease in the number of entries within each parcel.

6.4 Confined Molecules of Varying Shape

A series of complexly shaped molecules confined within a box were simulated with the same self-assembly protocols used for circular particles. Figure 6.3 (a-f) shows these shapes and their most probable configuration with colours mapping to the local bond order parameter q_6 . The row below shows the point clouds for each ensemble of 4032 configurations. One noticeable feature is that these point clouds are relatively similar between molecular analogs, except for Figure 6.3 (f) the Rodonea shape. This is caused the interdigitation of its arms and results in morphologies that have more disorder within the area. The result is interpreted as the Rodonea

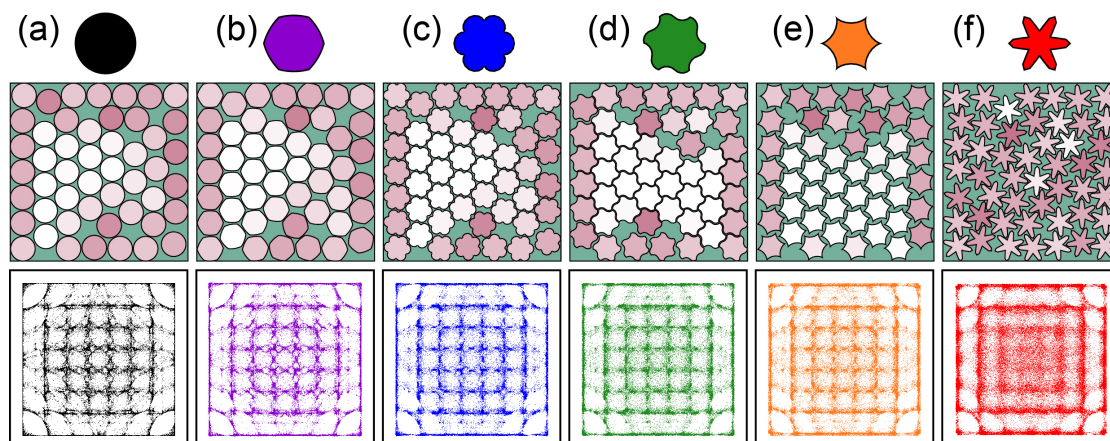


Figure 6.3: The influence of confinement on 49 complexly shaped molecules confined within a square box. Polygons include: (a) Circle, (b) Reuleaux, (c) Epicycloid, (d) Alhambra, (e) Hypocycloid, (f) Rodonea. The most common pattern found within the ensemble is shown on top. Point clouds of superimposed molecular centroids from 4032 configurations are plotted below.

shape influencing its own self-assembly by resisting the confinement effect of the walls (localized positions at the center of the box) and retaining an intermolecular dispersion that resembles a confined fluid.

The pattern matching algorithm was applied to these datasets to enumerate recurring patterns. Table 6.2 details the numbers of patterns inside the most populated parcel (plotted in Figure 6.3) for these complex shapes. The Rodonea shape shows that no two configurations in the ensemble that were similar enough to be patterned matched. All other molecule shapes produce ensembles which contain repeating patterns, however they are also quite sparse.

(a) Circle	(b) Reuleaux	(c) Epicycloid	(d) Alhambra	(e) Hypocycloid	(f) Rodonea
45	22	18	5	7	1

Table 6.2: Enumeration of the most probable microstate shown in Figure 6.3. Data is from ensembles of 4032 randomly generated microstates of 49 complexly shaped molecules in a square container.

6.5 Publication: “Steric self-assembly of laterally confined organic semiconductor molecule analogues” (PCCP - 2014)

PCCP



PAPER

View Article Online

View Journal | View Issue



Cite this: *Phys. Chem. Chem. Phys.*,
2014, 16, 20228

Steric self-assembly of laterally confined organic semiconductor molecule analogues†

Alejandro Díaz Ortiz,^{a,b} Björn Arnold,^c Matt Bumstead^a and Ayse Turak^{*a}

Self-assembly of planar molecules can be a critical route to control morphology in organic optoelectronic systems. In this study, Monte Carlo simulations were performed with polygonal disc analogues to planar semiconducting molecules under confinement. By examining statistically the molecular density and configurations of such analogues, we have observed that the symmetry of the confining medium can have a greater impact on the final densified particle configurations than the intramolecular interactions. Using the steric frustration imparted by confinement, novel self-assembled (partially) ordered phases are available. Our Monte Carlo simulations suggest new avenues to control ordering and morphology of planar molecules, which are critical for high-performance organic optoelectronic devices.

Received 27th May 2014,
Accepted 4th August 2014

DOI: 10.1039/c4cp02331e

www.rsc.org/pccp

1 Introduction

The control of supramolecular self-assembly and morphology, especially of donor–acceptor pairs, is a key feature of molecular electronics.¹ Ideally, long-range ordered molecular arrays with high symmetry and periodicity on the order of typical exciton diffusion lengths (~ 5 – 20 nm) are desired.^{2–6} Tailoring molecular organization can heavily impact the performance of nanostructured devices, such as organic photovoltaics (OPVs), organic light emitting diodes (OLEDs), and organic transistors (OTFTs). OPV device performance, in particular, is heavily influenced by the morphology.^{7–9} While optimal performance in organic devices is often the result of a complex balance of charge carrier flow and emission/absorption locations, many of the recent advances in OPVs have been achieved through morphological tuning.^{10–12}

The assembly of molecules into ordered and continuous phases to yield high charge-collection-efficiency poses a significant challenge. The interplay between molecule–substrate and intermolecular interactions that control molecular self-assembly is most complex in the first monolayer at the substrate surface. The self-assembly on this layer can be tuned by the use of nanostructured surfaces with confinement leading to preferential absorption sites^{13–15} and polymorphic ordering.^{16–18} Exciting new possible directions for developing optimal morphologies for device structures emerge in systems where the substrate

(normal) interactions are negligible and lateral confinement controls the morphology.

Predictive modeling, based only on the steric interactions between molecules, should therefore be an effective tool to examine the range of morphologies that can be obtained and, in future, implemented in a device structure. In this paper, we are motivated by the supramolecular self-assembly of conducting organic molecules on flat and stepped (confined) substrates. As a first approximation, we have used polygonal approximants to circular discs to describe the configurational behavior of symmetric molecules. We have focused on the confinement effects of densified systems that self-assemble into a disordered (random) bulk phase. Introducing a statistical ensemble, *i.e.*, producing a large set of identical copies of the system under the same simulation conditions, allowed us to discriminate the surface and finite-size effects brought about by the confinement from the ordering trends inherent to a monodispersed system of polygonal particles. At the core of our work is the concept of anisotropy in the confinement as imposed by a boundary with inequivalent points (for example, a square boundary where edges are different from corners). We have identified the nature of the confinement, whether it is soft or hard, isotropic or anisotropic, as a key ingredient to direct steric self-assembly.

2 Method

Our method is based on a Monte Carlo simulation where particle shapes are approximated by polygons.¹⁹ The hard-core interaction between polygonal particles is handled by a polygon-overlap detection algorithm.²⁰ This approach has the advantage of modeling particles with both complex and simple shapes on the same footing, including cases where the implementation of

^a Department of Engineering Physics, McMaster University, Ontario, Canada.
E-mail: turaka@mcmaster.ca

^b Synchrotron SOLEIL, L'Orme des Merisiers, Saint-Aubin BP 48,
91192 Gif-sur-Yvette Cedex, France. E-mail: alejandro.diazortiz@gmail.com

^c INTRON GmbH, D-74523 Schwäbisch Hall, Germany, EU

† Electronic supplementary information (ESI) available. See DOI: 10.1039/c4cp02331e

Paper

PCCP

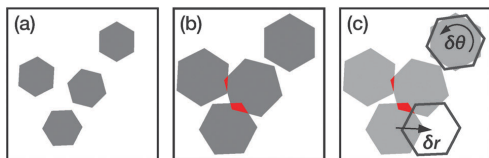


Fig. 1 Schematic representation of the different simulation steps. (a) The systems are prepared in the diluted phase with no overlaps. (b) An increase in density might result in overlapping particles. (c) In such a case, the overlaps are resolved by randomly displacing and rotating all particles according to Gaussian distributions (*cf.*, eqn (2)). Notice that, in principle, rotation or translation Monte Carlo trial moves could increase the overlap between particles. However, only those trial moves that remove overlaps are accepted. The system undergoes cycles of increasing density until there are no more acceptable Monte Carlo moves.

excluded-volume interactions poses serious challenges due to the nonsmooth (*i.e.*, non-analytical) nature of particle shapes – for instance, planar molecules with concave shapes.

The simulations begin by preparing the systems of polygon-rendered particles in the dilute phase, *i.e.*, N particles are randomly deposited in a simulation box of area A while avoiding overlaps (see Fig. 1(a)). For a general polygonal shape, each particle is defined by the position of its geometric center \mathbf{r}_i and its orientation θ_i ($i = 1, \dots, N$). In order to sample the phase space, for a constant number of particles and area of the simulation box, we have implemented two types of Monte Carlo trial moves: translation and rotation of the particles (see Fig. 1(c)). As we are considering systems with only hard-core interactions, the acceptance criterion of our Monte Carlo method is straightforward: all moves are accepted when they do not result in overlaps.[‡]

We have found that changes in the simulation box size can be easily achieved by introducing a rescaled set of coordinates, *i.e.*, mapping the particle positions and polygon vertices to a unit square simulation box. In other words, to increase the particle density each particle is expanded within a fixed simulation box size (see Fig. 1(b)), instead of shrinking the simulation box for a fixed particle size. This rescaling of coordinates greatly simplifies the implementation of the various boundary conditions. Naturally, the rate of compression of the box is directly related to the rate of expansion of the polygonal particles.

The order in which the different steps are applied during the simulations is as follows: first an increase of density is performed. This move is accepted if it does not produce any overlaps between the particles or between the particles and container walls in the case of hard-wall boundary conditions. If the increase in density results in overlaps, all N particles are randomly displaced and rotated in an attempt to remove the existing overlaps:

$$\mathbf{r}_i \rightarrow \mathbf{r}_i + \delta\mathbf{r}_i, \quad \theta_i \rightarrow \theta_i + \delta\theta_i, \quad i = 1, \dots, N, \quad (1)$$

[‡] That is, overlaps between molecules or between a molecule and the container wall.

where $\delta\mathbf{r}_i = (\delta x_i, \delta y_i)$ and $\delta\theta_i$ are random variables following Gaussian distributions

$$p(\delta x_i) = \frac{1}{\sigma_r \sqrt{2\pi}} \exp\left(\frac{-\delta x_i^2}{2\sigma_r^2}\right), \quad (2a)$$

$$p(\delta y_i) = \frac{1}{\sigma_r \sqrt{2\pi}} \exp\left(\frac{-\delta y_i^2}{2\sigma_r^2}\right), \quad (2b)$$

$$p(\delta\theta_i) = \frac{1}{\sigma_\theta \sqrt{2\pi}} \exp\left(\frac{-\delta\theta_i^2}{2\sigma_\theta^2}\right), \quad (2c)$$

with zero mean and standard deviations σ_r and σ_θ , respectively. The rotational move is generated by rotating the particle (*i.e.*, its vertices) along an axis perpendicular to the particle's plane and passing through its geometric center.

The process of increasing the density and removing the overlaps by displacing the particles is repeated until the density cannot be increased further. That is, the density will increase until the total overlap, defined as the sum of overlapping areas between pairs of polygons, cannot be resolved below a given threshold. To determine the overlap polygon, we have used the general polygon clipping library from Murta²⁰ with the area determined using the Shoelace or the Gauss formula.

The values of the trial moves $\delta\mathbf{r}_i = (\delta x_i, \delta y_i)$ and $\delta\theta_i$ are allowed to change during the runs according to the following rule: the initial displacements are maintained until the density cannot be increased further; at this point they are reduced to one tenth of their current values and the simulation continues. This process is repeated until no significant densification between two consecutive reduction cycles is achieved. Usually 4 to 6 reduction cycles, involving *ca.* 10^6 – 10^7 Monte Carlo steps, are necessary to achieve dense configurations.

We have found that random and dense aggregates are consistently obtained for small densification rates when implementing a biased Monte Carlo approach, *i.e.*, biasing the moves by k trial displacements.^{21–24} This approach increases the acceptance rate but also the computational effort. We have found that the biased Monte Carlo approach is effective down to systems with only a few particles. This occurs without the stability complications of the more traditional approach of keeping single-trial moves together with large densification rates in order to produce disordered configurations.²⁵ For very small densification rates, our biased Monte Carlo approach converges to the crystalline state as expected.

It should be noted that similar approaches exist in the literature.^{26–29} The floppy-box Monte Carlo^{27,28} and the adaptive shrinking cell²⁹ schemes share some of the ingredients of our method, *e.g.*, approximating the (complex) particle shape by polygons (two-dimensional systems) or polyhedra (three-dimensional systems) coupled with a Monte Carlo sampling of the phase space.

3 Results

We have applied the method described in Section 2 to simulate disordered aggregates of planar circular molecules on substrates with only steric interactions. For systems with fairly

short-ranged isotropic intermolecular interactions (such as phthalocyanines, coronenes, or perylenes), for the sake of simplicity, we model the intermolecular interaction as a hard-body potential. Due to their planar nature and isotropic symmetry, such conductive molecules can be effectively represented, in a first approximation, by circular disks, *i.e.*, 100-sided polygons in our case.

3.1 Large systems of disordered disk-shaped molecules

Our interest in systematically achieving random and dense aggregates in the bulk stems from the fact that it allows the separation of surface and finite-size effects (confinement-induced ordering, for instance) from the ordering trends inherited from a crystallizing bulk. We have found that using a biased Monte Carlo approach with 1000 trial displacements – Gaussian-distributed with σ in eqn (2) equal to the particle diameter – and a low particle expansion rate of 10^{-5} systematically produced dense disordered systems.

A typical configuration obtained with our method is shown in Fig. 2(a) for a system of 1024 particles. The particles were deposited on a laterally nonconfining substrate, modeled by the use of periodic boundary conditions on the simulation box, and color coded to reflect the distortion of their associated Voronoi cells as a measure of the difference from the crystalline (triangular) state. For instance, particles showing a linear distortion of less than 5% of their hexagonal Voronoi cells are displayed in dark blue. Particles showing distortions between 5 and 10% of their Voronoi cells are colored light blue, and so on for green, yellow and orange. Particles that have Voronoi cells with less or more than six sides are colored red.

Notice that although there are patches of crystalline arrangements (in shades of blue), the configuration is fairly disordered as seen by the extension of the red, orange and yellow disordered patches. In order to gauge the configuration yield of our method, we have estimated the probability distribution function of the particle density distribution from a statistical

ensemble of 4032 (full densification) runs. The resulting probability distribution, shown in Fig. 2(b), has a single peak of a roughly Gaussian profile.

3.2 Finite-size and surface effects: molecules on confining substrates

There are several advantages to adopting a statistical approach for analyzing confinement effects. In the statistical ensemble, a large number of copies of the system under the same conditions are examined. Rather than focusing on a single or a few selected configurations, such an ensemble allows comprehensive analysis of the phase-space sampling under a particular simulation protocol. This can distinguish between, for example, procedures that preferentially determine metastable states in the system. The size of the statistical ensemble should be as large as possible, within the constraints imposed by computational resources and simulation efficiency. We have chosen the ensemble size as the smallest one for which the probability distribution of the particle density does not show significant changes with a further increase of the statistical ensemble size. By testing this pragmatic approach for the smallest and largest system sizes, we found that statistical ensembles with 4032 provide reliable results.

As confinement effects result from the impact of the surface (*i.e.*, the physical boundaries containing the system) commingled with the finite size (*i.e.*, the number of particles in the system), we could further explore confinement effects by systematically changing the number of particles in systems contained by hard walls.

Fig. 3(a) shows the result of confining a system of 1024 particles by setting hard-wall boundary conditions. The shift of the probability distribution towards lower particle densities is due to the frustration brought about by the symmetry of the confining substrate (square) on systems that crystallize on a triangular lattice. However, there is a further shift in the distribution in Fig. 3(b) as a function of the system size, from bulk-like systems of 1024 particles to systems of very few (*e.g.*, nine) particles. This trend is naturally understood in terms of the surface and finite-size effects that dominate in small systems while large systems are controlled by bulk behavior.

For very small systems on confined substrates, there are, however, a series of changes in the particle density distributions that go beyond the mere shifting in particle density. This can be seen clearly for systems with 36 particles, where a satellite peak appears at a particle density of 0.785 (to the right of the dominant part of the distribution). As can be seen, this is a localized state with zero width. For systems with 25 particles, this localized state is comparable in frequency to the main part of the distribution, and for systems with 16 and fewer particles this localized state is the dominant contribution of the particle density distribution. For the smallest systems analyzed here (9 particles), the particle density distribution seems mostly composed of localized states. The localized state appearing at a particle density of $\pi/4 \sim 0.785$ is associated with particle configurations with square symmetry (*i.e.*, an $n \times n$ pattern). Such a confinement induced feature is easily characterized by

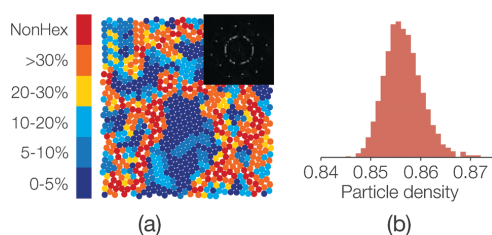


Fig. 2 (a) Typical configuration of a densified system of 1024 particles on a nonconfining substrate (periodic boundary conditions) with a particle density of 0.851. The coloring scheme is such that red (dark blue) signals particles whose local environment departs the most (least) from its ideal 2D triangular crystal structure. Inset: Fourier transform of the particles' geometric centers. (b) Probability density function (arbitrary units) of the particle density distribution as estimated from an ensemble of 4032 densification runs, roughly Gaussian with a mean of 0.857 and standard deviation of 0.004.

Paper

PCCP

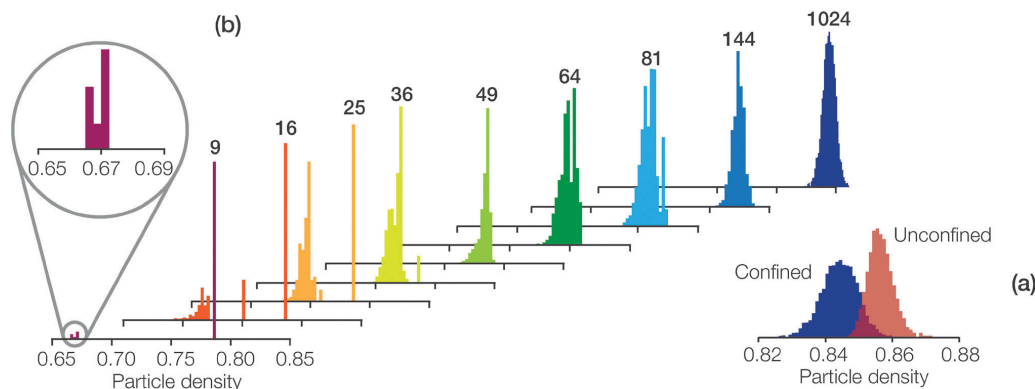


Fig. 3 (a) Probability density histogram (in arbitrary units) of the particle density for systems with 1024 particles on confining (hard-wall boundary conditions) and nonconfining (periodic boundary conditions) substrates. (b) Probability density histogram (in arbitrary units) of the particle density for a number of systems on confined substrates. The number of particles is indicated in each case (bold labels). Very small systems (*i.e.*, with less than 49 particles) show localized states in their probability distributions. For the sake of clarity, the height of the localized states has been clipped out. In each case, the probability distribution was estimated from 4032 densification runs.

examining, therefore, a series of $n \times n$ system sizes. Though the impact of confinement is most easily tracked for such a series, the results are also generally applicable to an arbitrary number of particles. However, the densest configuration for planar disk molecules inside a square cavity for particle numbers less than 49 is in fact $n \times n$.³⁰

The present results bear some resemblance to those obtained for diindenoperylene confined on Cu substrates, where structural polymorphism has been observed.² With the confinement of the molecules to narrow terraces, a transition occurs from the short-range ordered structures seen on wide terraces (roughly triangular) to strong long-range ordered structure (roughly rectangular). Confinement to the terrace forces the molecules into a tightly packed crystalline state to achieve roughly the same molecular density (*i.e.*, particle density) as that observed on the large terraces. As the terrace is narrowed, the molecular density of the short-range ordered structure is reduced due to the poor packing quality required to attach at the edges. The crystal facets of the molecule can nicely follow the step edge, allowing an optimized surface coverage to be obtained by the imposition of long-range order.

It is important to stress, however, the differences between the two physical situations. In the terraces, confinement occurs along one of the two possible directions, the system remaining open (*i.e.*, infinite) along the other one. Additionally, the axial symmetry of the molecules tends to exaggerate the confinement effects on narrow terraces and leads to long-range disorder in the large terraces. In the present system, on the other hand, the self-assembly occurs within a two-dimensional closed cavity whose geometry imposes, in general, symmetry restrictions to the formation of a triangular array upon densification. In our case, finite-size and boundary effects dominate the structural landscape of these quasi-zero-dimensional systems. For large and dense systems, configurations are determined by the competing effects of the square symmetry and the triangular lattice.

A good insight into the configurational space sampling is gained by superimposing the final (*i.e.*, densified) configurations of each of the statistical ensembles (see ESI[†]). Such point clouds (lower halves of Fig. 4) can be interpreted in a probabilistic way, that is, the higher the density of points, the higher the probability of a particle occurring in that position (upper halves of Fig. 4). It is thus interesting to see that for systems with a large number of particles (*i.e.*, 1024 in Fig. 4(a)), there is a density modulation along the walls that dies out at the center of the cavity. Each parallel wall, however, induces its own density-modulation front (hereafter referred to as a layer) without destructive interference from the others.

For lower particle numbers (*e.g.*, $N = 64$ and 81 in Fig. 4(c) and (b), respectively), there is a constructive interference between the different density modulation fronts that renders n high-density nodes along the layer closest to the boundary but $n + 1$ for the rest (the number of particles is $N = n \times n$). The additional nodes in Fig. 4(a)–(e) have two sources. The first one is the tendency of the bulk to accommodate a triangular array of particles to increase density. In other words, by shifting the bulk from square to triangular symmetry, extra rows of nodes are possible. This is apparent when inspecting the high-density nodes between the first (closer to the boundary) and second layers. By the same mechanism, larger systems (with a larger bulk region), for instance, systems with 256–1024 particles (only 1024 shown), can display $n + 2$ high density nodes. The second source of extra nodes is the statistical nature of the point clouds, which associates high density nodes with particle positions *on average*. That is, not all the high-density nodes are associated with particles at the same time. Most interesting is that such a pattern retains the square symmetry of the cavity while attempting to accommodate a triangular array. In other words, the interior of the cavity is not as uniformly visited by the particles as expected in terms of the number of possible microstates.

PCCP

Paper

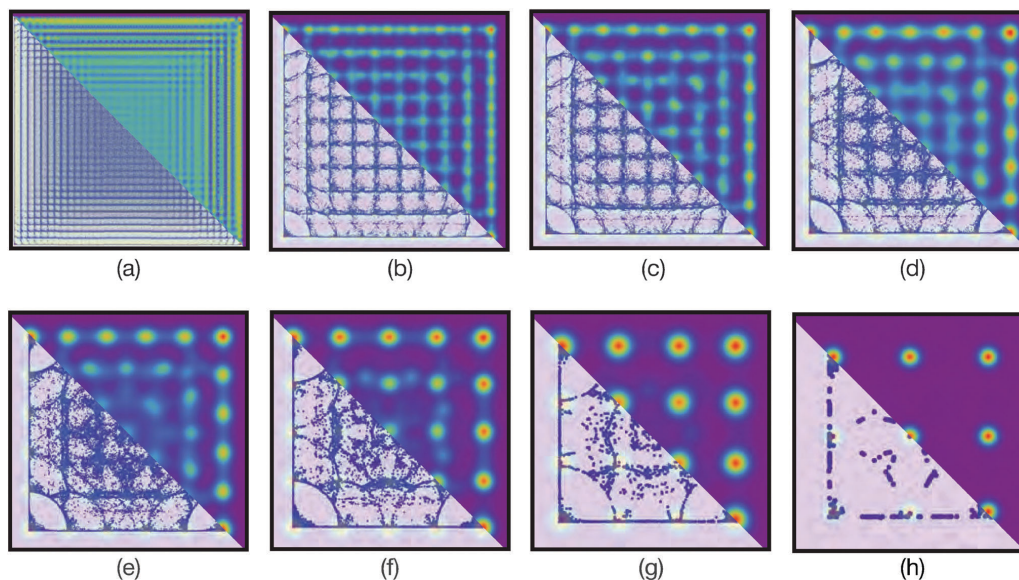


Fig. 4 Point clouds (lower half) and point densities (upper half) of 4032 superimposed densified configurations for (a) 1024, (b) 81, (c) 64, (d) 49, (e) 36, (f) 25, (g) 16, and (h) 9 particles confined in hard-wall cavities (solid square). The point clouds are more localized in space for systems with fewer particles. For systems with particle numbers between 81 and 1024 the point clouds are qualitatively the same (not shown). For point-density plots (upper half), the color scheme is such that red (blue) indicates a high (low) density of points (particle centers). Purple indicates zero or near-zero density.

For even lower particle numbers (*e.g.*, 36 and 25 in Fig. 4(e) and (f), respectively), the point clouds and density plots evolve towards more convoluted patterns where the loci of rolling particles on top of each other are fairly visible around the corners of the cavity. In addition to their complexity, the patterns are more localized in space, in agreement with the structure of their probability distributions (*cf.*, Fig. 3(b)). This is quite clear for the smallest systems investigated here (9 and 16 particles, Fig. 4(h) and (g), respectively), where the densified systems sample only a very small region of the cavity.

The impact of the cavity square geometry is readily seen by the high density spots at the corners, followed by slow decay parallel to the walls. It seems that for confined systems, regardless of the interparticle potential details, the geometry of the container is a key element in understanding the self-assembly of particles.

3.3 Characterization of different structures *via* pattern matching

The probability distribution of the particle density (Fig. 3) and point-cloud data (Fig. 4) offer some clues about the number and type of structures for the different particle configurations. However, with the exception of the localized states that can be easily recognized as the $n \times n$ pattern, the other possible structures are difficult to infer from either representation of configurations.

We have applied the methods of shape matching to classify and collect the different patterns appearing in the statistical ensembles.³¹ A point-matching descriptor (see the ESI[†]) is ideal

for the classification of two-dimensional symmetric molecules where the geometric center contains all the necessary configurational information. Structure matching based on point clouds or sets of coordinates is a conceptually simple yet powerful approach for small systems and/or small-to-moderate sized datasets.

We have used the above point-matching scheme to classify the different patterns appearing in a statistical ensemble of 4032 runs for small confined systems. We have focused on systems with less than 49 particles, since their probability distributions of the particle density show the most interesting features. For the smallest systems, *i.e.*, 9 particles, the distribution of patterns is clearly dominated by the formation of 3×3 arrays, as can be inferred from the particle density distribution (Fig. 3(b)) and point-density (Fig. 4(h)) plots. There is a very small fraction (2%) of structures that make the secondary peak in the probability distribution of the particle density (highlighted in the inset of Fig. 3). Though such a small set of secondary features is not statistically representative, the appearance at particular values suggests confinement strategies to self-assemble distinctive configurations with quantifiable yields.

Such a possibility is realized in larger systems (*i.e.*, systems with 16 and 25 particles), where the occurrence of patterns different from the $n \times n$ motif increases notably. In some cases, for instance systems with 16 particles (the first row in Fig. 5), the secondary patterns are highly symmetric with a relative substantial yield, considering that no attempt was made to direct the self-assembly towards a particular pattern. In some other cases, *e.g.*, systems with 25 particles, the 5×5 and non- 5×5 motifs have

Paper

PCCP

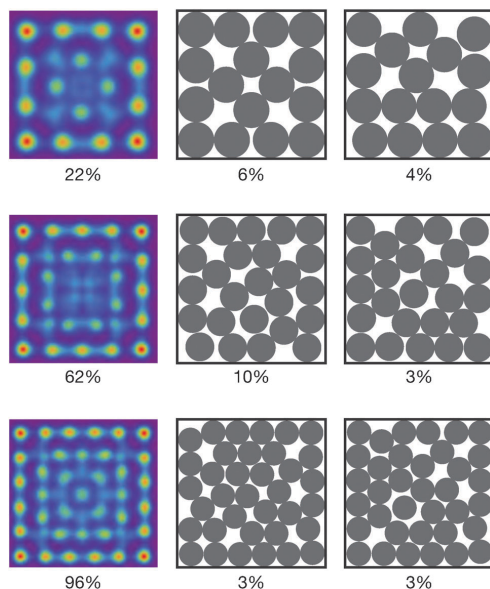


Fig. 5 Point-density plots (first column) and representative structures of the two most frequent non- $n \times n$ patterns (second and third columns) for systems with 16 to 36 particles. The point-density plots were obtained by superposing all the uncorrelated configurations different from the $n \times n$ motif. The frequency (percentage) is indicated below each plot. The $n \times n$ appearance frequency goes from 80% to 4% upon increasing the size of the system from 16 to 36 particles.

comparable proportions, yet highly symmetric patterns appear less frequently (see Fig. 5, second row). For a system with 36 particles, non- 6×6 configurations dominate, occurring 96% of the time, resulting in hundreds of different patterns. Among so many possible configurations, there is a consequent decrease in their frequencies (<5%). Though the 6×6 pattern still has the most frequent occurrence (4%), the next two most frequent patterns (third row in Fig. 5) appear with similar frequency (3%).

4 Discussion

The results presented so far were obtained using a biased Monte Carlo approach that allowed us to successfully transfer the simulation parameters through a large range of system sizes, *i.e.*, from less than 10 particles to several thousands. Our interest was on the impact of confinement, necessitating the examination of disordered systems in the bulk. Had we chosen simulation parameters that consistently produced crystalline or almost crystalline morphologies in the bulk, the true effect of the confinement in encouraging crystalline states would have been masked.

There is a second part of our method that involves the rendering of molecule shapes as polygons. We have used hectogons (*i.e.*, 100-sided regular polygons) to model planar

molecules with only steric interactions. Using finer resolutions, *i.e.*, a larger number of sides (see ESI†) or molecular dynamics with perfect circular discs (see ref. 32), showed that a regular polygon with 100 sides can be considered as a circle for all intents and purposes.

Real conducting molecules, even low-molecular-weight oligomers, tend to have complex, often anisotropic shapes (see for example ref. 2, 4, 33). Thus, the results obtained here, with very little interaction between molecules, suggest that confinement can be even further exploited as a route to directing self-assembly of planar molecules on confining substrates. Though the molecules were approximated by discs as a first approximation, further interesting aspects of confinement are expected as the complexity of the shapes and their ability to interact geometrically increase. Previous results for systems confined in thin two-dimensional channels have the same global behavior (*e.g.*, reentrant layering transitions, orientational and spatial ordering) for a variety of systems with a range of interparticle interactions from hard-core³⁴ to inverse power law $\propto r^{-12}$ (see ref. 35) to magnetic dipolar³⁶ to Coulombic^{37,38} potentials. It is likely that confinement-induced ordering observed in this article is representative of a broader class of systems, since the details of the interparticle interaction are overshadowed by the nature of the confinement.

Whether the confinement is soft or hard, isotropic or anisotropic, seems to play a more important role than the particularities of the interactions or even the scale of the system. For instance, finite Coulomb systems under circular (isotropic) confinement^{39,40} display the same qualitative features as dusty-plasma clusters⁴¹ or colloids in confined geometries.⁴² Anisotropic confinement, as in the square cavities studied here, brings an additional complexity since the probability density is no longer homogeneous for each shell or layer as in the case of isotropic confinement.⁴³ Straight corners act as nucleation sites promoting the formation of intermediate ordered structures, as we have seen in the case of systems with 16 and 25 particles.

This is especially interesting for organic molecules, as the nature of the interactions, either intramolecular or with the substrate, can take on a variety of forms. As the interactions can range from strong covalent linkages to weaker secondary bonding or electrostatic interactions to weak van der Waals interactions, modeling them in real systems is especially challenging. If the confinement medium plays a greater role than the specific intermolecular potentials, as is suggested in this paper, novel morphologies can be controlled purely through geometric frustration. Knowledge of the importance of the steric hard-body interactions in ordering phenomena opens up a new route to self-assembly.

5 Summary and conclusions

A structural analysis of two-dimensional planar molecules on confining substrates has been performed using Monte Carlo simulations. We have found that disordered bulk systems display several degrees of ordering when self-assembled under anisotropic confinement. By investigating statistical ensembles of densified particles under quasi-zero-dimensional confinement,

PCCP

Paper

we were able to gain good insight into the regions in phase space often visited by the system.

The impact of confinement was readily seen through the analysis of point-cloud data, which showed high probability densities at the corners with an oscillating decay in density towards the center of the cavity. The particle density also showed a layered structure parallel to the walls. Within each layer, the particle density decreases monotonically until the midpoint. As a consequence, a grid-like density modulation appears in all but the smallest system (*i.e.*, with less than 49 particles).

The most promising size range to self-assemble symmetric configurations in square cavities is between 16 and 25 particles. In this range, the probability distributions for the particle density show a transition from single- to double-peaked distributions, making it highly probable for the system to crystallize into one of the several possible states. This is a consequence of the fluctuations in small systems that underscore their importance as a variable to direct molecular self-assembly.

We have investigated densified systems, since our interest lies in the self-assembly of conducting two-dimensional molecules. As a first approximation, circular discs, as used in the present study, can describe the ordering behavior driven by steric interactions of symmetric molecules. The strength of the approach described in this contribution lies in the ability to model the more complex steric interactions that arise when the molecular shape is included. By expanding even further into multiple molecule shape types, as would be seen with donor-acceptor mixtures, critical insights into morphology and phase separation can be gained. As morphology is critical to OPV, OTFT, and OLED performance, such insights can allow us to tailor device properties in the next generation devices.

Acknowledgements

Computer resources from the Texas Advanced Computing Center of The University of Texas at Austin are gratefully acknowledged. We would also like to thank Dr Luxat for access to and Dr David Hummel for help with the Engineering Physics Computing Cluster at McMaster University. The authors acknowledge financial support from 436100-2013 RGPIN and 384889-2010 CREAT.

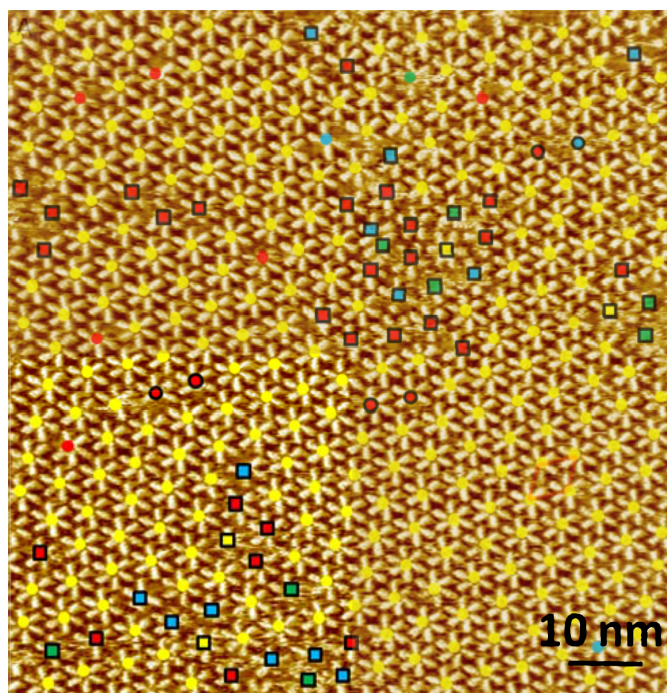
References

- Z. B. Henson, K. Mullen and G. C. Bazan, *Nat. Chem.*, 2012, **4**, 699–704.
- D. G. de Oteyza, E. Barrena, H. Dosch, J. E. Ortega and Y. Wakayama, *Phys. Chem. Chem. Phys.*, 2011, **13**, 4220–4223.
- S. Watanabe, Y. Fukuchi, M. Fukasawa, T. Sassa, M. Uchiyama, T. Yamashita, M. Matsumoto and T. Aoyama, *Langmuir*, 2012, **28**, 10305–10309.
- N. J. Tremblay, A. A. Gorodetsky, M. P. Cox, T. Schiros, B. Kim, R. Steiner, Z. Bullard, A. Sattler, W.-Y. So, Y. Itoh, M. F. Toney, H. Ogasawara, A. P. Ramirez, I. Kyriassis, M. L. Steigerwald and C. Nuckolls, *ChemPhysChem*, 2010, **11**, 799–803.
- J. S. Moon, J. K. Lee, S. Cho, J. Byun and A. J. Heeger, *Nano Lett.*, 2009, **9**, 230–234.
- A. Turak, M. Nguyen, F. Maye, J. Heidkamp, P. Lienerth, J. Wrachtrup and H. Dosch, *J. Nano Res.*, 2011, **14**, 125–136.
- H. Hoppe, T. Glatzel, M. Niggemann, W. Schwinger, F. Schaeffler, A. Hinsch, M. Lux-Steiner and N. Sariciftci, *Thin Solid Films*, 2006, **511–512**, 587–592.
- L. H. Nguyen, H. Hoppe, T. Erb, S. Gunes, G. Gobsch and N. S. Sariciftci, *Adv. Funct. Mater.*, 2007, **17**, 1071–1078.
- J. Peet, A. J. Heeger and G. C. Bazan, *Acc. Chem. Res.*, 2009, **42**, 1700–1708.
- S. H. Park, A. Roy, S. Beaupre, S. Cho, N. Coates, J. S. Moon, D. Moses, M. Leclerc, K. Lee and A. J. Heeger, *Nat. Photonics*, 2009, **3**, 297–303.
- H.-C. Chen, Y.-H. Chen, C.-C. Liu, Y.-C. Chien, S.-W. Chou and P.-T. Chou, *Chem. Mater.*, 2012, **24**, 4766–4772.
- Y. Liang, Z. Xu, J. Xia, S.-T. Tsai, Y. Wu, G. Li, C. Ray and L. Yu, *Adv. Energy Mater.*, 2010, **22**, E135–E138.
- H. L. Zhang, W. Chen, L. Chen, H. Huang, X. S. Wang, J. Yuhara and A. T. S. Wee, *Small*, 2007, **3**, 2015–2018.
- N. Neel, J. Kroger and R. Berndt, *Adv. Mater.*, 2006, **18**, 174–177.
- F. Silly, A. Q. Shaw, K. Porfyrakis, G. Briggs and M. R. Castell, *Appl. Phys. Lett.*, 2007, **91**, 253109.
- D. G. de Oteyza, E. Barrena, H. Dosch and Y. Wakayama, *Phys. Chem. Chem. Phys.*, 2009, **11**, 8741–8744.
- J. O. Osso, F. Schreiber, V. Kruppa, H. Dosch, M. Garriga, M. I. Alonso and F. Cerdeira, *Adv. Funct. Mater.*, 2002, **12**, 455–460.
- R. Otero, Y. Naitoh, F. Rosei, P. Jiang, P. Thostrup, A. Gourdon, E. Loegsgaard, I. Stensgaard, C. Joachim and F. Besenbacher, *Angew. Chem., Int. Ed.*, 2004, **43**, 2092–2095.
- B. Arnold, *Diplomarbeit*, University of Stuttgart, 2009.
- A. Murta, *A General Polygon Clipping Library*, 2009, <http://www.cs.man.ac.uk/~toby/alan/software/>.
- D. Frenkel, G. C. A. M. Mooij and B. Smit, *J. Phys.: Condens. Matter*, 1991, **3**, 3053–3076.
- J. I. Siepmann and D. Frenkel, *Mol. Phys.*, 1992, **75**, 59–70.
- J. J. de Pablo, M. Laso and U. W. Suter, *J. Chem. Phys.*, 1992, **96**, 6157–6162.
- M. Laso, J. J. de Pablo and U. W. Suter, *J. Chem. Phys.*, 1992, **97**, 2817–2819.
- D. Frenkel and B. Smit, *Understanding Molecular Simulation*, Academic Press, 2nd edn, 2001.
- G. Delaney, D. Weaire, S. Hutzler and S. Murphy, *Philos. Mag. Lett.*, 2005, **85**, 89–96.
- L. Filion, M. Marechal, B. van Oorschot, D. Pelt, F. Smalenburg and M. Dijkstra, *Phys. Rev. Lett.*, 2009, **103**, 188302.
- J. de Graaf, L. Filion, M. Marechal, R. van Roij and M. Dijkstra, *J. Chem. Phys.*, 2012, **137**, 214101.
- S. Torquato and Y. Jiao, *Phys. Rev. E: Stat., Nonlinear, Soft Matter Phys.*, 2009, **80**, 041104.
- P. Szabó, M. Markót, T. Csendes, E. Specht, L. Casado and I. García, *New Approaches to Circle Packing in a Square*, Springer, 2007.

- | Paper | PCCP |
|--|--|
| 31 A. S. Keys, C. R. Iacovella and S. G. Glotzer, <i>Annu. Rev. Condens. Matter Phys.</i> , 2011, 2 , 263–285. | 37 L.-W. Teng, P.-S. Tu and L. I, <i>Phys. Rev. Lett.</i> , 2003, 90 , 245004. |
| 32 B. Arnold, M. Bumstead, A. Díaz Ortiz and A. Turak, <i>J. Electrochem. Soc.</i> , submitted. | 38 G. Piacente, I. Schweigert, J. Betouras and F. Peeters, <i>Phys. Rev. B: Condens. Matter Mater. Phys.</i> , 2004, 69 , 045324. |
| 33 B. C. Popere, A. M. Della Pelle, A. Poe and S. Thayumanavan, <i>Phys. Chem. Chem. Phys.</i> , 2012, 14 , 4043–4057. | 39 V. M. Bedanov and F. M. Peeters, <i>Phys. Rev. B: Condens. Matter Mater. Phys.</i> , 1994, 49 , 2667–2676. |
| 34 D. Chaudhuri and S. Sengupta, <i>Phys. Rev. Lett.</i> , 2004, 93 , 115702. | 40 M. Kong, B. Partoens, A. Matulis and F. Peeters, <i>Phys. Rev. E: Stat., Nonlinear, Soft Matter Phys.</i> , 2004, 69 , 036412. |
| 35 A. Ricci, P. Nielaba, S. Sengupta and K. Binder, <i>Phys. Rev. E: Stat., Nonlinear, Soft Matter Phys.</i> , 2007, 75 , 011405. | 41 A. Melzer, M. Klindworth and A. Piel, <i>Phys. Rev. Lett.</i> , 2001, 87 , 115002. |
| 36 R. Haghgooei and P. S. Doyle, <i>Soft Matter</i> , 2009, 5 , 1192–1197. | 42 R. Bubeck, C. Behinger, S. Naser and P. Leiderer, <i>Phys. Rev. Lett.</i> , 1999, 82 , 3364–3367. |
| | 43 W. K. Kegel, <i>J. Chem. Phys.</i> , 2001, 115 , 6538–6549. |

Chapter 7

Morphologies of Molecules with Anisotropic Steric Interactions



Morphology of six-sided complex organic compounds can be explored with STM at molecular resolution. Do molecules with complex shape self-assemble with a dispersion that is similar to ones expected from circular objects? To analyze the role that shape can have at directing particular patterns, the expected intermolecular characteristics of self-assembled morphologies should be classified for many candidate molecules. Adapted with permission from [112]. Copyright (2009) American Chemical Society.

7.1 My Contributions

My contributions to this section include, writing the manuscript, finding and building a library of polygons for potential use, selecting interesting test cases, and running the simulations to acquire the data for this publication. I am the main author of this manuscript. My supervisor Dr. Ayse Turak and I conceptualized this topic together with Dr. Alejandro Diaz Ortiz, who made a major contribution to this topic through thoughtful discussions about the self-assembly differences of pentagonal and circular particles. One goal was to answer the question about how the self-assembled morphology changes when the resolution of sides defining a circular molecule decreases to its minimum (triangle) and what types of order show a deviation from the expected states of circles? I explore this question in the manuscript by quantifying differences in simulated morphologies for a monodisperse set of complex molecular analogs. The expected results for circular particles are also contrasted against the configurations generated using the set of regular polygons for molecular shape.

My work focused on developing the ideas for using complex shapes to represent molecules. One decision I made was to choose a set of images that show molecular dispersions of organic molecules on flat surfaces that could potentially be simulated with a polygonal representation of their observed shape. I did this for the series of regular polygons [113, 114, 115, 116, 117].

Another one of my contributions was to set up the mathematical framework to explore complexly shaped molecular analogs. An overview of literature into simulations and experiments using hard-body particles showed that structural properties are dependent on the density, which is defined in excluded-volume models as the total area of all particles within a measured volume. I pose here a question about how to account for the volume degeneracy between varying shapes, from which I was unable to find a satisfactory solution to within literature. How can the volume fraction account for shape when two distinctly dissimilar molecules have the exact same volume? The reason this problem is that the density is used to predict the global behaviour of the system and expected self-assembled structures, however these predicted outcomes do not change with different molecular (i.e. volume degeneracy). My work was to solve this question so that we could compare morphologies between simulations of several complex six-sided molecules. I did this by defining the global density in terms of local Voronoi area fractions, which decouples the particle volume from density in favour of encoding local structural characteristics instead.

Section 7.2 contains a brief overview of the manuscript. Section 7.3 examines systems of molecules with circular shapes with lowering polygonal resolution. The work regarding complex molecular shapes is contained within the manuscript in Section 7.4. This work is in progress to be submitted before Dec. 15, 2017 to “The European Physical Journal E Soft Matter and Biological Physics” - Special Issue: Advances in Computational Methods for Soft Matter Systems.

7.2 Overview of Manuscript (For Submission - 2017)

All objects that exist will embody volume and this volume is distributed within space. These two conditions define the physical parameter of density which has key importance in describing and predicting the behaviour in self-assembling particles. The excluded-volume model restricts the number of intermolecular potentials to a single repulsive interaction. Allowable microstates are dependent on the “free-volume” or unoccupied space between particles available for objects to move within. This creates a problem when attempting to use the density as a metric to compare dispersions of molecules with same the volume but different structure. An accurate definition for density is needed since any two shapes can be rescaled using geometric transformations to have exactly similar volume. The current excluded-volume model suggests that the macromolecular dispersions produced from particles with different shape but same area fractions will have common morphologies.

To test this behaviour, six-sided symmetric molecular analogs of distorted steric interaction potentials (effective shape) are simulated using a Monte Carlo excluded-volume routine to generate statistical ensembles of disordered morphologies of varying density. Complexly shaped six-sided molecule analog shapes were compared against circular molecules to observe divergences in behaviour associated with small geometric alterations to the circular shape. Structural

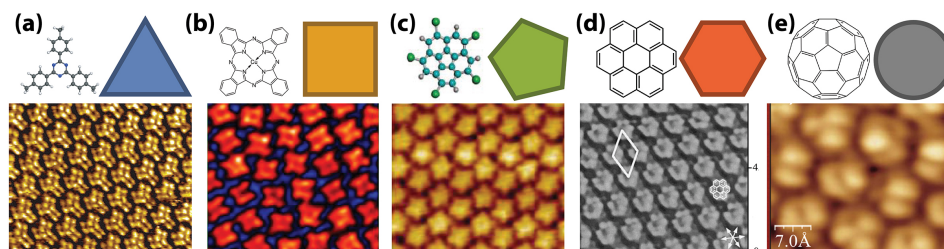


Figure 7.1: Planar configurations of polygonal shaped molecules as viewed using STM. Above each image is the chemical structure associated with that molecule as well as its geometric approximation. Chemical names: a) star-shaped 2,4,6-tris(4,4,4-trimethylphenyl)-1,3,5-triazine [113] b) Copper phthalocyanine [114] c) pentachloro- corannulene derivative [115] d) Coronene [116] e) C60 fullerene [117].

comparisons needed to have the area fraction and intermolecular spacing normalized across simulated morphologies in order to properly determine commonality. In the case of assessing the structural dissimilarity, many of the standard analysis tools can fail to detect differences and thus need finely-grained definitions. We address how modelling molecules not as circles, but as anisotropic shapes, leads to a disconnect between density and structural order. We show that distances between molecular neighbours need to be normalized to allow for a fair comparison of pair correlation functions between molecular analogs. Finally, we conclude with the study of structure metrics with showing that the angular descriptions of neighbouring molecules (i.e. bond order q_6) can fail to detect chirality imposed by geometric frustration.

7.3 Morphology of Circular Molecules with Low Resolution

For many of the molecules that have high symmetry, circles can be used as a first order approximation to describe their interaction volume. This approximation to molecular shape has an isotropic influence on molecule-molecule interactions. To see the effect of introducing shape, the circular approximation can be varied slowly by truncating the number of sides the circle has. A transition in the description of molecular analogs from “almost circular” to being considered a non-circular shape will occur when the resulting morphologies change significantly from one produced from circles.

To quantify this role, we begin by exploring simulated systems of molecules with shapes that resemble regular polygons. Figure 7.1 shows a series of molecules which are possible choices for regular polygons with sides varying from 3 to 6. A geometric analog of each molecule is shown with the chemical structure in Figure 7.1 as well as an example of the molecular morphology when observed from STM. The molecules which are represented in Figure 7.1 are: a) star-shaped 2,4,6-tris(4,4,4-trimethylphenyl)-1,3,5-triazine [113] b) Copper phthalocyanine (CuPC) [114] c) pentachloro-corannulene derivative [115] d) Coronene [116] e) C60 fullerene [117].

The STM images for these molecules often show molecular tilings that are semi-pristine, implying that the molecules arrange into crystalline forms on the surface. These are typically done below room temperature to allow very little molecular movement during the rasterization of the STM image. Thermal agitation of the molecules can cause excessive diffusive motion which prevents single molecule imaging. However, in electronic devices such as photovoltaic cells, the operation temperature is that or above the temperature of the global outside environment. Solar panels are subjected to weather effects which can result in molecules rearranging locally to dissipate the energy of sudden temperature gradients from intense sunlight or small drops of rain water. Disorder in morphology could result within the device by energy transfer through the networks of adjacent molecules. This is why disordered states are just as important to study,

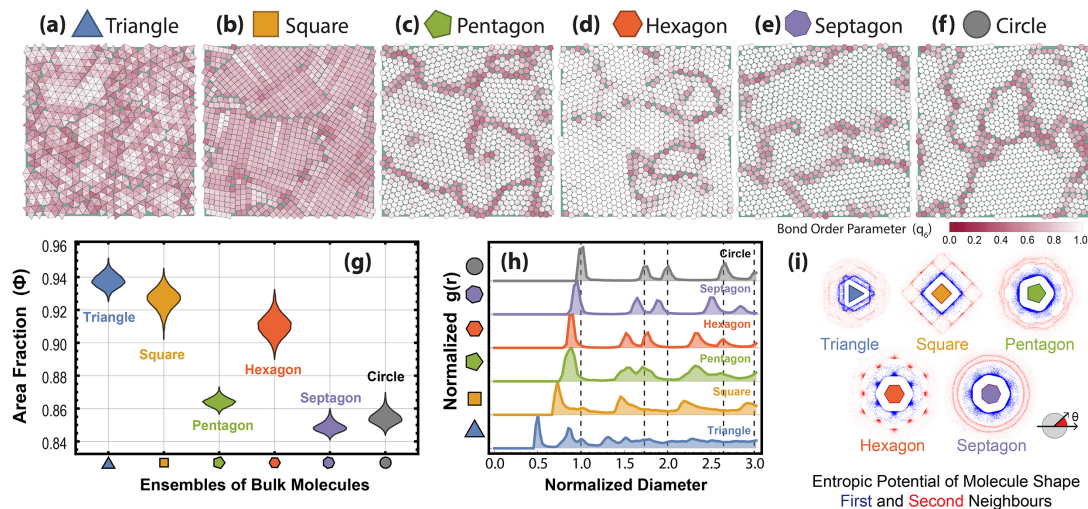


Figure 7.2: Statistics of bulk systems of molecules ($N=1024$) defined by simple steric potentials. (a-f) Simulated configurations of "almost circular" molecules in bulk phase. Colour overlaid as the local bond order q_6 . (e) Probably distribution of area fractions for ensembles with 4032 patterns. (f) Pair correlation functions with intermolecular distances being normalized by the length of the largest distance from the molecular centroid to vertex of the regular polygon.

since their probability of occurring can be higher than crystalline patterns.

To model this disordered state, we used Monte Carlo simulations to explore the steric contribution of the interaction potential on the morphology of organic molecules. The method simulates a set number of rigid molecules which undergo random displacements as the amount of free volume available to molecules is removed at a fixed rate until the morphology forms a glass state [118, 36, 119]. The resulting morphologies are a result of the molecular ability to explore the unoccupied volume which is not embodied by other objects already on the surface and the local geometric frustration caused from the caging influence of surrounding neighbours.

Circles are the simplest shape that provides insight into the mechanisms of planar self-assembly. For organic molecules with symmetric chemical structures (such as fullerene and/or coronene), circles can be used to as a first order approximation to their shape [56, 57]. However, molecules used in photovoltaic devices, such as pentacene [58, 59] and PTCDA (3,4,9,10-perylene-tetracarboxylic-dianhydride) [60], are observed to be elongated and whose shape which resembles an ellipsoid [61, 62]. As a result, molecules of complex shape have the possibility to self-assemble into configurations with localized states that would not be seen in systems of molecules with simple circular shape [63]. To isolate the effect shape has on self-assembled morphology, we start by analyzing dispersions for circles before varying the number of sides toward lower resolutions to observe the influence of limited variation to the shape.

Figure 7.2 shows an example configuration of the regular polygon series: a) triangle b) square c) pentagon d) hexagon e) septagon and (f) circle. Each molecule as been colour coded by its local bond order parameter (q_6) which describes how closely neighbouring molecules are arranged around the central particle relative to a hexagonal lattice. As the molecules loose polygonal, the local angular arrangement stays relatively similar until the molecular shape transitions from being circular into a square. Polycrystalline domains are distinguished using the bond order by the emergence of dark red dislocation lines of molecules along the domain perimeters. Figure 7.2 shows that a) triangles and b) squares both drop in the 6-fold angular order, denoting that the global behaviour has changed from one expected from circles. This intuitively makes sense since square molecules will prefer to self-assemble into square configurations. Triangles will form patterns that have a triangular basis for neighbours, but the six surrounding neighbours do not have equal distances among them like circles do.

The structural characteristics of self-assembled regular polygons have been independently

simulated using discrete element method (DEM) and their structural characterization has been reported on using the same metrics of area fraction and pair correlation function [120] as we show in Figure 7.2. The discrete element method (DEM) is a numerical technique that models particulate matter as hard objects and describes their motion using equations of motion [121]. The momentum of particles is governed by the contact forces, which is calculated using the overlapping areas between colliding objects [122] and can be modified to incorporate non-spherical shapes [123, 124, 120]. In their model, particles of regular polygons pack vertically inside a container with horizontal periodic boundaries and allowed to compact under the influence of gravity and friction [120]. Although their simulation method includes additional interaction potentials, their results for regular polygons show very similar outcomes to ours.

The area fraction (ϕ) for each ensemble is shown in Figure 7.2 g) as probability distributions and contains information from 4032 independently simulated morphologies of bulk ($N=1024$) periodic regular polygons. In this case, each regular polygon produces ensembles with area fraction probability distributions that are similar in shape but with different mean values. It is no surprise that triangles ($\phi = 0.937$), squares ($\phi = 0.926$), and hexagons ($\phi = 0.910$) have the highest mean value of area fraction, since these shapes are known to tile surfaces completely (i.e. $\phi = 1$). However, these results are interesting when compared to the trends reported using DEM, which shows hexagons forming the highest area fraction ($\phi^{\text{DEM}} = 0.93$), followed by squares ($\phi^{\text{DEM}} = 0.92$), then triangles ($\phi^{\text{DEM}} = 0.89$) [120]. This trend runs counter to our results which shows the reverse effect and may be attributed to different condensation protocols between simulation methods (i.e. thermal agitation vs. gravitational compaction).

While our Monte Carlo simulations show the ensemble of circles self-assembling with a mean density of ($\phi = 0.854$), pentagons result in area fraction much higher with ($\phi = 0.864$) and septagons having lowest value at ($\phi = 0.848$). This value of covering area suggests that ensembles of pentagons have self-assembled through their reported first order phase transition at $\phi = 0.84$ into a distorted triangular cell [84, 125]. However, ensembles of septagons suggest that they remain in the hexagonal phase since their phase transition has been reported to occur at $\phi = 0.87$ [125], which is at a density greater than we observed. Both of these support our findings in Figure 7.2, where both c) pentagons and e) septagons globally act as circles when at high density but reveals that pentagons have slightly lower bond order due to this distorted triangular configuration. Further evidence is found from reported simulations of hard pentagons and septagons with these area fractions, which have been observed to have bond order parameters at or above (q_6) = 0.9 [125]. This trend is also seen in the results presented from DEM, although the difference we report here is more profound.

Translational probability is quantified in Figure 7.2 h) showing the pair correlation function for configurations plotted above. To compare across the sets, intermolecular distance was normalized using the largest radius of the regular polygon. The dashed lines denote the expected positions for the peaks associated with the hexagonal lattice. These results are in good agreement with previously reported random packings of regular polygons [120], with pair correlation functions showing similar peak positions and features unique for each polygon. Certain structural features characteristically define circular behaviour and is observed as a splitting of the two peaks at the distances between the first and second nearest neighbour shells. These peaks have been observed experimentally in dispersions of microscale pentagonal tablets undergoing Brownian motion with area fractions as low as 0.74 [126]. This feature is common among the simulated configurations of almost circular shapes, with exceptions being systems of square and triangular particles. Pair correlation functions for planar square colloids have been observed to contain features resembling the merging of the hexagonal first-second shell peaks when in a dilute phase ($\phi = 0.62$), however upon further condensation, the dispersion shifts into one with that produces the unique features associated with square lattice at ($\phi = 0.74$) [127]. Overall, analysis with the pair correlation function suggests that the intermolecular spacing between molecules of circular shape (side > 4) are similar to each other, however, these peaks appear shifted relative to each other when the internal distances are normalized to the largest radius.

In conclusion, the self-assembling behaviours for low resolution circles were analyzed for structural differences within a statistical ensemble of many independently simulated morphologies for each shape. The results show that there is a transition that breaks rotational anisotropy

between simulated septagons (7 sides) and hexagons (6 sides). Another transition occurs between hexagons and pentagons (5 sides), with the collective behaviour acting similarly to circles but also preserving the directional configuration of their crystalline form. Below pentagons, the square (4 sides) and triangle (3 sides) act as unique shapes, preferring tiling patterns which are quantifiably different from expected morphology of circles. Assessment of this lower limit to the circular approximation of molecules can provide justification for utilizing a smaller number of vertices to reduce extraneous computational cycles for routines that use polygons to define objects.

In these cases, the traditional approach to structural quantification leads to a perceived variation in relative dispersion, when in reality, the morphology across samples are relatively similar. For the pair correlation function, similar features are shared with molecules with more than 4 sides but they do not appear at the same intermolecular distance. Also, the distributions of area fractions are relatively similar in shape, however, their means are offset with respect to circular molecules. These two metrics, give conflicting results which suggest that the morphological behaviour of similarly shaped particles should produce different intermolecular structures. Our results show that circular behaviour remains consistent for self-assembled morphologies of regular polygons, with complete divergence occurring when the resolution of a circular approximates has lower than 5 sides.

7.4 Publication: “Similar morphology but different molecule shape: self-assembly simulations with varying steric potentials” (For Submission - 2017)

Similar morphology but different molecule shape: self-assembly simulations with varying steric potentials

Matt Bumstead^{1,*} and Ayse Turak^{1,†}

¹*Department of Engineering Physics, McMaster University, Ontario, Canada*

I. ROLE OF MOLECULAR SHAPE IN SELF-ASSEMBLY

Self-assembly of organic molecules is a complex dynamical process that incorporates many different complex interactions between deposited molecules and the substrate [1]. Advanced imaging techniques with AFM are able to resolve the electronic orbitals of dispersed single molecules [2, 3], revealing the geometric shape of potential candidate molecules for device inclusion. For instance, the same flower shape pattern is seen from STM images from Copper phthalocyanine (CuPc) [4, 5] and Zinc phthalocyanine (ZnPc) [6]. Conversely, organic molecules can have different shapes with the exact same chemical composition. Isomerization of alkene molecules have been investigated with STM and at low temperatures on copper, the trans-cis variation shows distinct differences in observed structure [7]. From this perspective, it is crucial to predict how the effective shape influences the molecular configurations, since it is possible that many semiconducting molecules can not only share a common shape but also have multiple atomistic permutations. If we can understand this phenomena, then it is possible to direct the self-assembly just by choosing correct ratios of donor-acceptor molecules, and/or confining the system in set geometric boundaries (eg. etched surface) to produce morphologies that favour efficient charge separation and transport.

To do this, possible candidate molecules need to be selected for on the basis of how close their observed structure is to interesting complex shape profiles. Experimentally, this is a challenge since molecules of different shape can consist of different chemical elements, resulting in an inconsistent control variable of a commonly controlled interaction between all candidate molecules. Computer simulations can be used to explore self-assembling systems that depend solely on the influence of molecular shape on self-assembly in a way that is challenging to do experimentally. In nano-scale systems such as the organization of organic molecules in devices, many different potential interactions may arise. Intermolecular and substrate interactions within systems of organic molecules can be very complex [1] and this method provides a way to decouple the influences that molecule-molecule interactions and molecule-substrate interactions from the resulting morphologies

A key aspect in numerical modelling molecules is choosing the appropriate interaction potential to accurately reproduce the phenomena of interest. Typically, including as much detail as possible into a system will provide a more accurate representation of the true nature in question. However, it is possible to reduce the complexity and concentrate on only the most important features of the phenomena of study. With the probabilistic nature of quantum phenomena, first principle accounts for interactions may not be able to fully capture all of them.

Systems can be approximated by reducing the number and types of intermolecular interaction potentials into one that captures the main contribution to self-assembly. The excluded-volume model of particle self-assembly provides a way to isolate the influence of molecule-shape interactions and observe its role on morphology using numerical simulations by varying the shape of molecules from simple to arbitrarily complex. The term "excluded-volume" is used to define systems that manifest physical properties mainly as the density of the particles varies. The steric potential simply implies that each entity is rigid with a volume and that particles cannot embody the same regions of space as others.

Our main motivation is to understand how accurately the steric approximation to shape is at describing the self-assembly of intermolecular morphology. This is done by use of excluded-volume Monte Carlo simulations of condensing steric analogs. Since all objects that occupy space have a geometric shape associated with it, these types of simulations should be broad enough to incorporate an arbitrary definition for particle shape while also accurately representing particles of varying length scales. Also, since individual molecules can be resolved in planar monolayer morphologies using STM [8], we can make the assumption that there is a set of molecular orbitals that do not completely overlap and thus represent a steric shape to the molecule. Because of these reasons, it is acceptable to conclude that the steric interaction makes some contribution to the thermodynamic energy potentials [9] and that the molecular shape has an influence on the resulting morphology.

Each organic molecule has a geometric shape that corresponds to its chemical structure. The electronic orbitals of the molecule create an interaction volume that can resemble a shape this is likely similar to its chemical structure. Since it is possible that the influence of the steric potential can extend past the outline of the molecule observed in STM, this calibrated distance explicitly describes the repelling interaction strength be-

* Corresponding author; bumstema@mcmaster.ca

† Corresponding author; turaka@mcmaster.ca

tween molecules. Understanding both of these issues leads to a better framework for which slight differences in the intermolecular morphology caused by varying the organic molecules from simple circular shapes to complex ones.

Physical objects embody volume. Shape manifests as a physical property of objects through partitioning the surrounding volume with geometric contours that confine the spatial distributions of material as a localized aggregate which collectively acts a single body. The interface between the surrounding environment and the excluded-volume of the object defines a conformal outline of the shape. Terms such as *volume* and *area* may sometimes used synonymously here as they both relate to an amount of geometric space that is physically embodied by the molecules in either 3D or 2D systems.

The property of volume exclusion is common within varying length scales, and can be seen from nanometer scale to macroscale objects. Shape is a result of the collective behaviour of all constituents that compose of the material that acts as a single object. Granular material is an example of steric particulates that collectively to from static states with physical properties which depend on excluded-volume fraction of the system.

The simplest geometric shape that embodies volume is a sphere which can interact locally through hard-body collisions. This simplification provides insight into the role of density by minimizing the influence of anisotropic particle volumes. These properties form the basis of the hard-sphere model [10], which is successful in predicting the behaviour of material such as liquid crystals [11], colloidal nanoparticles [12–14], and macromolecular crowding in cells [15].

What happens when the object interactions act at the distance and can a steric potential (shape) still be defined as an excluded-volume interaction? Lenard Jones fluids, and electromagnetic charged fluids show the same behaviour as the hard-body case, and has been theoretically proposed that all these interaction potentials are limiting cases of an overlying potential that manifests through repulsion interactions [16]. Particles that act at a distance through repulsive potentials can have a steric potential drawn using contours of constant energy potentials [9]. Molecular orbital contours are then accessible from experimental techniques since individual molecules can be imaged using scanning tunnelling microscopy [17] There has been a lot of work describing intermolecular potentials that use this function to define physical properties within a system of many particles [18–20]. Models like density functional theory (DFT) calculates a potential by using a correlation function between atoms to form a description of the charge density in molecular orbitals [21]. It is practical importance for organic electronic devices, since it is able to calculate energy states of molecular orbitals such as the highest occupied (HOMO) and lowest unoccupied molecular orbital (LUMO). These energy states act similarly to the conduction and valence band energies for traditional semiconductors [22]. These in-

teraction potentials are calculated based on the distance between pairs of points (i.e. two particle interaction). Work has been done to expand this to incorporate higher orders of pairs using a more general correlation function which is defined as a truncated expansion of the between multiple pairs of particles [23, 24].

In systems of organic molecules with complex shapes, steric interactions between molecules can prevent interdigitation of dangling alkoxy side chains [25], hinder the self-assembly of hydrophobic domains of dendrimers [26], and produce chirality in intermolecular dispersions from rotations caused by increased density [27]. It has also been used explain the observed morphologies of amino acid derivatives [28], the confinement effect of macromolecular crowding in biological systems [29, 30]. Substrates can also cause steric influence on molecules by preventing movement of molecules at step edges [31]. Molecules with chemical structures that in 3D can be sterically influenced by the substrate. The steric interaction between the substrate and molecules' rigid chemical bonds prevent them from laying flat on the surface which can cause parts of molecule to extend out of the plane causing a change to the lateral interaction volume/shape felt by adjacent molecules [17, 26, 32].

To explore complexity, six-sided symmetric molecular analogs of distorted steric interaction potentials (effective shape) are simulated using a Monte Carlo excluded-volume routine to generate statistical ensembles of disordered morphologies of varying density. In the case of assessing the structural dissimilarity, many of the standard analysis tools can fail to detect differences and thus need finely-grained definitions. We address how modelling molecules not as circles, but as anisotropic shapes, leads to a disconnect between density and structural order. We show that distances between molecular neighbours need to be normalized to allow for a fair comparison of pair correlation functions between molecular analogs. Finally, we conclude with the study of structure metrics with showing that the angular descriptions of neighbouring molecules (i.e. bond order q_6) can fail to detect chirality imposed by geometric frustration.

II. MODELLING COMPLEX 6-SIDED MOLECULE

The simplest shape that can be used to model a molecule is shown in Figure 1 a) as the circle. In this case, the molecule is treated as an isotropic steric potential, one in which relative molecular orientation can be neglected. Small variations to the steric potential may break rotational symmetry, resulting in Figure 1 b) Reuleaux Polygon [33]. With odd number of sides (i.e. 3,5,7,...), Reuleaux polygons have the unique ability that allows for the object to rotate freely within a square due to its constant width [33]. The steric potential of a convex molecule does not allow any interconnections between molecules.

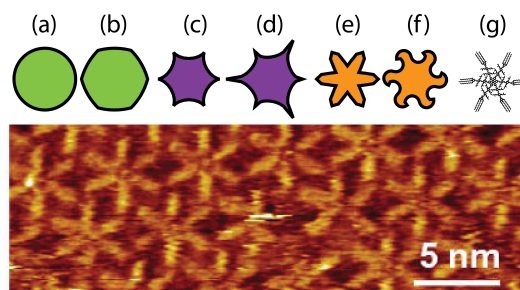


FIG. 1. Steric interaction potentials that might approximate molecular structure seen in STM. The simplest description of the molecule can be done using (a) Circle. Small variations to the steric potential may break rotational symmetry, resulting in (b) Reuleaux Polygon [33]. Angular symmetry is broken from $2\pi/6$ (c) Hypocycloid [34] to $2\pi/3$ (d) Super Ellipse [35] by extending a subset of its sides. Chirality is introduced along molecular arms, breaking mirror symmetry of (e) Rhodonea curve [36] into a (f) Chiral-Alhambra shape and finally the (g) chemical structure for complex 6-fold symmetric organic molecule with STM image below [37].

Another approach is to modify this circular steric potential into one that emancipates possible free volume from between arms, and concave polygons fit this description. The space between the arms of the six-sided symmetric molecules can be approximated in different ways. Long oligamer chains hang off the arms can be distinguished in STM and thought of as being part to the molecules steric potential. This implies that the volume between molecular arms is completely excluded from probe-able space. The hypocycloid [34] is shown in at Figure 1 c) and provides a geometric description which implies less interaction volume at the very ends of the arms and most of the mass is represented in the bulky centre. If there is an additional excluded-volume interactions on the molecule (such as longer 3 ligands longer than the rest) the steric equivalence will cause a change represented in Figure 1 e) as the Super Ellipse [35] which exaggerates the effect of the Hypocycloid arms. The Rhodonea curve [36] in Figure 1 e) is one that most accurately fits outline as seen in STM [37, 38]. This molecule has also been observed to have chiral self-assemblies [39] so we also include a chiral modification to the arms as seen in Figure 1 e) as the Chiral-Alhambra curve. Finally, Figure 1 e) shows the chemical structure of this 6-sided complex molecule.

Consider the Circles and Reuleaux polygons shown in Figure 2 (a-b). The local bond order is mapped directly onto the molecules, where deep red indicate disorder while white represents configurations that are close to having q_6 similar to that of hexagonally closed-packed disks. Both molecular analogs seem to produce similar probabilities of q_6 , however, the neighbour map shows clearly that molecules prefer to be at certain orientations relative to each other. This small deviation in the circular steric potential shows the impact that breaking angular symmetry can direct orientational self-assembly.

One method to explore the influence of molecular orientation is to build a probability map of neighbouring molecules. To start, neighbours are assigned to each molecule if they share a Delaunay connection. The neighbours' vectors are re-orientated around the molecular analog to explore angular and probability over some distance. In Figure 2, the probability maps show the closest molecular centers and are re-orientated around the symmetry axis of each particle. This visual description describes the probability to find molecules at both r and θ directions along a molecular axes. It may be useful to think of these insets as 2d pair correlation $g(r)$ maps [40]. When assessing only the first nearest neighbours, we refer to this as the bond order probability maps.

What can be seen is that shape will break the isotropic angular distribution of neighbours into places that minimize the distance between molecules. The neighbour distribution around the (a) circle is isotropic which should be the cause if we are using a circle to minimize the entropic influence due to shape. It also implies that the circle has no way to tell its relative orientation from the positions of its neighbours and thus chirality is not possible at the particle level. For the case of the (c) hypocycloid, and (f) chiral alhambra, the probability map of neighbours shows packing chirality by having the bright spots slightly off center from the apothem distance. The (b) Reuleaux shape however keeps its symmetric distribution of six neighbours to the middle of molecular analog side. This may be the influence of its convex apothem relative to the convex others.

The (bottom) section of Figure 2 displays the local bond order parameter q_6 being visually mapped onto a sample configuration with the density that is most probable for each ensemble of molecule analogs. The (a) circle and (b) Reuleaux shape show similar dislocation lines within sections of hexagonal domains. Similar features

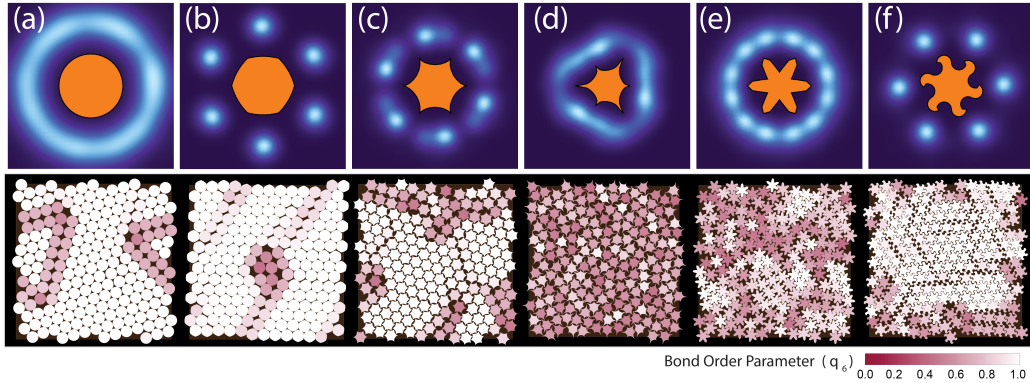


FIG. 2. Bond order parameter comparison of steric molecule analogs as outlined in Figure 1 (a-f). Bright areas indicate high probability for positional arrangement of neighbours relative to molecular structure. Simulations of 200 molecules are coloured with the local bond order q_6/q_6^{hex} below.

are between (c) and (f) which show hexatic behaviour and (d) and (e) which present more disorder than the rest, as indicated with deeper red areas.

III. CHARACTERIZATION OF DENSITY AND INTERMOLECULAR SEPARATION DISTANCES BETWEEN MOLECULAR ANALOGS

Position and orientation of molecules relative to one another can effect charge transport in organic optoelectronics. Simulations have been successful in describing monodisperse systems (only one chemical species) and with the goal being to predict possible morphologies that can arise. Unlike typical semiconducting materials (i.e. point particles), interactions of local neighbours will cause frustration in organic systems which leads to disordered states. In locally disordered regions, there may be a higher probability for the recombination of charge carriers. Conversely, long-range order is needed to extract charges after the disassociation of excitons. As such, robust metrics that can characterize disorder are needed to distinguish subtle morphological differences that result from a change in the effective steric potential.

Figure 3 shows a set of molecules self-assembled on a substrate. All those inside the box (orange) are considered for structural analysis. Molecules outside the box (green) influence the morphology inside, but cannot be fully investigated. Analogous to the frame size of a photo, the box here represents a snapshot of bulk-phase morphology (i.e. periodic boundary conditions). Figure 3 (b) shows Voronoi tessellations are built from centroids of molecules and partition the simulation area into localized amounts for each molecule. Figure 3 (c) shows how using periodic boundary conditions ensures that the

total area of the Voronoi cells will be exactly the same as the square image area. Molecular shape can then be separated from the density. Figure 3 shows how the localized area fraction ϕ_* can be broken up into i) the effective excluded-volume interaction (molecule) and ii) the resulting available free volume (cell). Each Voronoi cell is associated with a localized number density (i.e. only one molecule per cell).

The area fraction ϕ , represents the fraction of simulation area covered by N total objects with the simulation space being a unit box of area $A_{\text{box}} = (1 \times 1)$.

$$\phi = N \frac{A_{\text{mol}}}{A_{\text{box}}}, \quad (1)$$

However, as the geometric shape changes between molecules so does their area. To define the area fraction as general as possible allows it to be utilized to compare across different geometrical descriptions of steric potentials (i.e. polydisperse systems or non-circular shapes). Each candidate molecule i has an excluded-volume potential with area $A_*(i)$. The sum of all objects is the total excluded area $\sum A_*(i)$.

$$\phi = \frac{1}{A_{\text{box}}} \sum_i^N A_*(i) \quad (2)$$

One might notice that two candidate molecules can have different geometric shape but have degenerate area A_* (i.e. different shape, same area). This becomes an issue when trying to describe the density in this manner. A more robust metric is needed to study the intricate details that differentiate candidate molecules.

Voronoi tiles have the property of tessellating the space completely. Instead of using the total simulation box

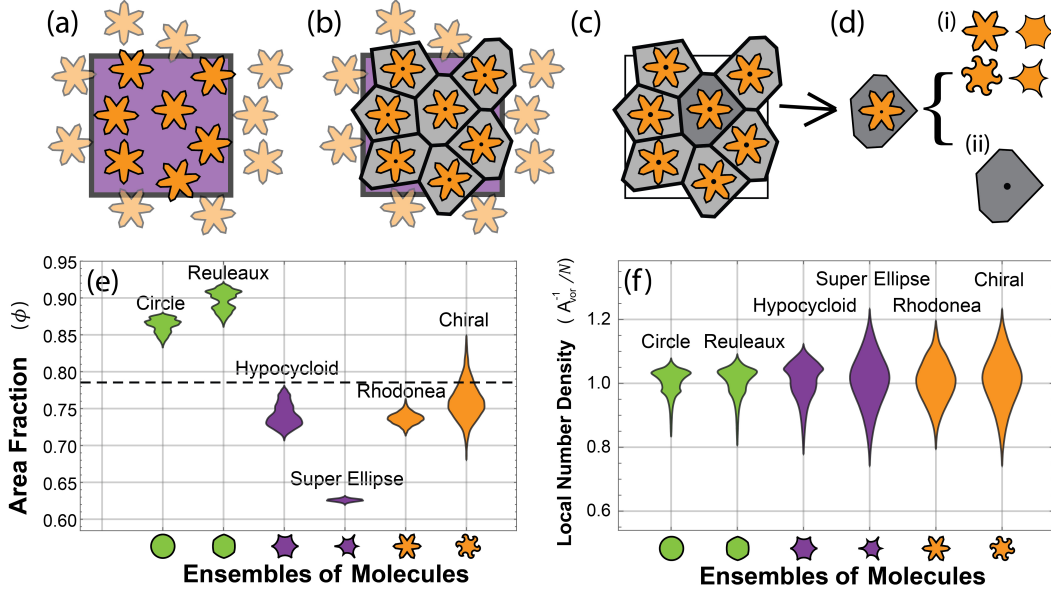


FIG. 3. Separating molecular structure from area fraction using Voronoi tessellations. (a) Molecules self-assemble on a substrate but only those inside the area box (orange) are considered for structural analysis. (b) Voronoi tessellations are built from centroids of molecules. (c) The area of the substrate is partitioned into localized amounts defined by morphology of the surrounding molecules. (d) Molecular shape is separated from the density. Localized area fraction (ϕ_*) can be broken up into the effective excluded-volume interaction (molecule) and the resulting available free volume (cell). Density distributions of molecular analogs: (e) probability distributions of the area fractions ϕ associated with ensembles of molecule analogs. (f) Local number density \mathcal{N} defined by using areas of the Voronoi cells, defined by the centroids of molecular analogs. Number density is normalized by the number of molecules in the system ($N=200$ in simulations) to compare the mean local density rather than the global average.

area, all space is locally partitioned into distributions that are defined by the structural self-assembly of each candidate molecule. In this case, the sum of all Voronoi tiles will return the total simulation area $A_{\text{box}} = \sum A_{\text{vor}}$. For every molecule i in the system, each has a local area fraction ϕ_*

$$\phi = A_* \sum \frac{1}{A_{\text{vor}}}, \quad (3)$$

This can be expressed as a local number density, where $\mathcal{N} = 1/A_{\text{vor}}$:

The sum of the local area fractions returns to the original global area fraction. Normalized by the equipartition of the total area between all objects analyzed. This result tells us that the global area fraction parameter can be partitioned into localized area fluctuations for each molecule instead and that the probability distribution of local number density for each particle in the statistical ensemble will provide information about the internal structure.

What can be seen in Figure 3 (e) is the area fraction probability distribution for each molecular analog using 5000 independently run configurations. The removal of internal excluded-volume from between the ligands that define the complex molecular analogs leads to area fractions have values where their ranges do not overlap with each other. From this, one might conclude that they do not produce the same morphology. However, this is an influence of shape-volume degeneracy. The intermolecular structures can be extracted independently of the molecular shape, using the centre of mass to define the molecules position. Figure 3 (f) shows the probability distributions for the local number density for each of the molecular shape analogs. The results show that similar shapes like the circle and Reuleaux shape collapses into relatively similar distributions for in both range and peak probabilities. The hypocycloids show a similar distribution features to the circles

A. Distance renormalization for determining magnitude of the steric interaction

Self-assembly is numerically modelled by increasing density of molecules while reducing molecular thermal energy. Rather than shrinking the simulation area, molecules are inflated. This is done by mapping the distances inside simulation box onto the size of the molecules [41]. When the simulation stops, stochastic nature of the method imposes that the density of the system will vary between runs. As such, area fraction directly corresponds to molecular radius and distances between neighbours.

There are three ways to normalize distance to allow comparison across ensembles of varying polygonal potentials. This first is use the radius of the molecule as a ruler. The radius (furthest distance from centre to polygon) of all shapes can be set to $r=1$. This implies that the interaction potentials are always contained within what is seen in the STM molecule. The STM probes the electron clouds of the molecule. These can cause a screening effect on electrical potentials, causing truncation of its influence as it penetrates the clouds. The geometric description of these clouds can vary as external influences probe and distort these clouds through complex interactions. Structures seen from this will provide a unique starting point to estimate geometric descriptions of the steric potential.

A circle provides an isotropic steric potential. However, the molecules seen in STM experiments 1 have non-circular shape. Many have 6 branches, but are seen to vary slightly between 5 and 7. Even though this molecule looks 6-sided, the associated steric interaction potential can undertake any shape. To explore this, the molecule analogs in this study are chosen such that most each potential could be argued to be possible candidate. Each shape is subjected to undirected self-assembly simulations. Statistically large sets of results from each outcome are combined and analyzed together. This unbiased approach allows for the most probable morphologies to be compared evenly. The resulting morphologies that differ across simulations is a direct function of the steric potential chosen to represent the molecule. We compare this to a physically representative sample molecule in different interaction potentials.

One main tool to gauge structural order within morphology is the pair-correlation function $g(r)$. This metric describes the probability to find neighbouring molecules within a shell of dr at a radial distance of r from another. Distance between molecules needs to be normalized for an accurate comparison. It is possible that molecules with varying steric potentials could produce similar structure. If a metric is based on the subtraction between pair-correlation functions, then it might mis-classify similar morphology at different length scales. This normalization provides insight into the magnitude of the steric potential required.

To illustrate this, take the example of the case of the hypocycloid and super ellipse in Figure 4. The method

to determine the magnitude of the steric potential. In cases where there is high thermal energy, molecules will undergo rotation, effectively reducing their shape into a circle. This radius of this suggests the physical representation of the molecule that neighbouring objects feel. Average distance between molecules can be larger than the molecule. Similar to a liquid crystal, circular molecules on a substrate might form angularly ordered patterns, but are not hexagonally closed packed (i.e. not touching). In this case, an effective steric potential analog to molecules in this system could be estimated as a disk, extending outside the molecule and fully encapsulating it. Geometry of this effective interactions can vary depending on the environment.

When we want to use the molecular size to normalize the distance, there are different points we can use to define the radius. Fig. 1(a) shows this effective rotation volume when the molecule candidate undergoes a skew to its sides with changes the rotational symmetry. The interaction volume for the hypocycloid extends outside its radius of gyration. In this case, the steric potential of the hypocycloid is not felt. By defining the radius from the hypocycloid, the excluded volume potential is smaller. Fig. 1(b) shows the largest radius of gyration that can be defined that completely encapsulates the hypocycloid.

In simulations, the distance is only a relative scale measure between molecular centroids. Granular and steric objects have a wide range of available length scales in which they hold the same properties. The same possible distributions of planar colloids can be sampled using macroscopic objects such as billiard balls. This length-scale super position places steric objects within the complete range of distances between quantum and gravitational realms. As a result, conclusions drawn from modelling steric objects can be widely transferred between scientific disciplines with ease. By accumulating vast amounts of self-assembled configurations, a data base of all possible configurations can be built. Time dependant flows of steric objects is important when dealing with small macroscopic objects, like gains of sand. However, the steady state configurations is also important. This is the final configurations after the self-assembly of molecules onto a surface, once the thermal energy dissipates and molecules are contained inside the device. At this point, the molecules are fixed at their current locations. Mass production of planar organic electronics is bound to produce slight variations between products. Simulations of disordered states allows for probing these possible deviations without the need to run costly experiments aimed at categorizing the many varying morphologies. By understanding the probability for molecules to arrange into specific configurations, it is possible to engineer and optimize the outcomes to maximize reliability.

Steric molecules are described by the geometric structure, which is a property unique to its chemical species. These can range from being simple (planar disk) or as complex as possible (dendrimers). Here we note that molecules can have very different shapes, but exert

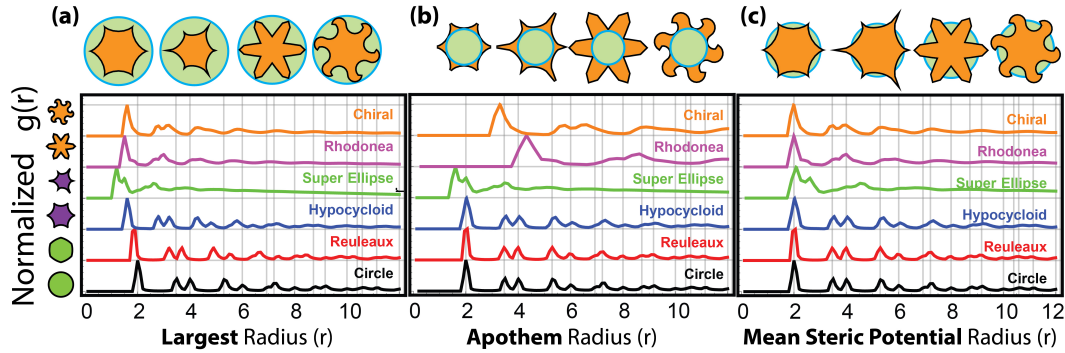


FIG. 4. Renormalization of the intermolecular distance using different magnitudes of steric potential. (a) Intermolecular distance is scaled by the maximum observable diameter, and (b) the minimum internal feature size to define the shape. (c) The mean distance of the centroid-to-perimeter distance integrated over 2π rotational angle.

the same volume. If the resulting configurations modelled by an excluded-volume potential is only a function of volume, then one should expect to see same patterns with different shapes. However, having different shapes changes the gradient of excluded-volume around the molecule, causing the entropic repositioning around molecules to change. We predict that since the simulations are driven by entropic densification and that molecular volumes remove free-volume, then since the molecular geometry defines the volume, resulting morphologies should be influenced by molecular shape.

There are two parts to describe the reduction of interactions into an effective steric potential. The shape of the molecule will influence the distribution of local neighbour molecules. This can be thought of as the angular component of the potential. The second one is the relative scale this effect has on molecules, the magnitude or radius of influence. If it is thought of as a mean field potential, this would encompass the number of influencing neighbours.

The radius of influence is a key parameter to justify steric descriptions of molecules. If geometric descriptions of molecules have no influence on the morphology, then it is quite possible for these simulations to all produce exactly similar morphologies. If the relative distance between molecules is set to produce exactly similar density, then we would expect the resulting structural signatures to collapse across ensembles of varying polygons as well. However, when this was explored, we report that there was indeed differences between ensembles. This indicates shape has an influence on steric frustration.

IV. CONCLUSIONS

Complexly shaped six-sided molecule analog shapes were simulated to observe divergences in behaviour as-

sociated with molecular structural alterations. The circle is altered into a six-sided Reuleaux polygon [33] and compared to other six-sided molecular analogs such as, Hypocycloid [34], Super Ellipse [35], Rhodonea curve [36], Chiral-Alhambra. Structural comparisons needed to have the area fraction and intermolecular spacing normalized across simulated morphologies in order to properly determine commonality.

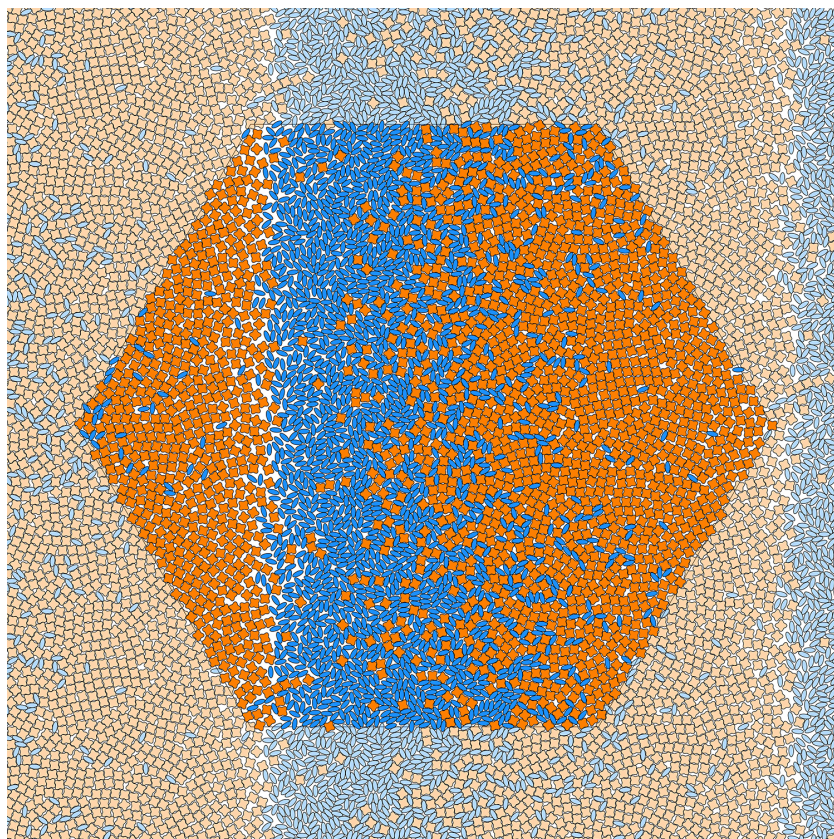
Our results show that density and intermolecular structures commonly seen with dispersions of self-assembled molecular analogs can exemplify circular behaviour in one set of order metrics but deviate once these account for the influence of complex shape. We found that circles and the Reuleaux polygon share a common distribution of probable local Voronoi number densities but this distribution is not shared amongst the other molecular analogs. This would be expected since their shapes have the most similarity. The Hypocycloid does produce a probability distribution which is similar in features to the circle, but it is spread out over a larger range of local number densities. The Super Ellipse, Rhodonea, and Chiral-Alhambra analog share similar probability with the disordered Voronoi distributions of granular particles[], but also that the Rhodonea analogs condense closer than the other two. With the intermolecular distances normalized, the pair correlation functions $g(r)$ of the simulated molecular analogs of the Reuleaux, and Hypocycloid showed similarity in structural of that of circles. The Rhodonea analog could be considered as possibly similar, since the $g(r)$ shows a splitting of the double peak in at the second neighbour shell. We also confirm this by using the correlation cloud, which showed hexatic packing of neighbours with Reuleaux, and Hypocycloid.

-
- [1] R. Otero, J. M. Gallego, A. L. V. de Parga, N. Martín, R. Miranda, *Molecular Self-Assembly at Solid Surfaces*, *Advanced Materials* 23 (44) (2011) 5148–5176.
- [2] C.-S. Guo, M. A. Van Hove, R.-Q. Zhang, C. Minot, Prospects for resolving chemical structure by atomic force microscopy: A first-principles study, *Langmuir* 26 (21) (2010) 16271–16277.
- [3] L. Gross, Recent advances in submolecular resolution with scanning probe microscopy., *Nature chemistry* 3 (4) (2011) 273–8.
- [4] H. Karacuban, M. Lange, J. Schaffert, O. Weingart, T. Wagner, R. Möller, Substrate-induced symmetry reduction of CuPc on Cu(1 1 1): An LT-STM study, *Surface Science* 603 (5).
- [5] A. El-Sayed, P. Borghetti, E. Goiri, C. Rogero, L. Floreano, G. Lovat, D. J. Mowbray, J. L. Cabellos, Y. Wakayama, A. Rubio, J. E. Ortega, D. G. de Oteyza, Understanding Energy-Level Alignment in DonorAcceptor/Metal Interfaces from Core-Level Shifts, *ACS Nano* 7 (8) (2013) 6914–6920.
- [6] F. Chen, X. Chen, L. Liu, X. Song, S. Liu, J. Liu, H. Ouyang, Y. Cai, X. Liu, H. Pan, J. Zhu, L. Wang, Chiral recognition of zinc phthalocyanine on Cu(100) surface, *Applied Physics Letters* 100 (8) (2012) 081602. doi:10.1063/1.3685713. URL <http://scitation.aip.org/content/aip/journal/apl/100/8/10.1063/1.3685713>
- [7] Q. Sun, C. Zhang, L. Wang, Z. Li, A. Hu, Q. Tan, W. Xu, Surface-assisted cis-trans isomerization of an alkene molecule on Cu(110), *Chem. Commun.* 50 (14) (2014) 1728–1730.
- [8] S. Uemura, R. Tanoue, N. Yilmaz, A. Ohira, M. Kunitake, *Molecular Dynamics in Two-Dimensional Supramolecular Systems Observed by STM*, *Materials* 3 (8) (2010) 4252–4276.
- [9] S. Liu, Steric effect: A quantitative description from density functional theory, *The Journal of Chemical Physics* 126 (24) (2007) 244103.
- [10] S. Torquato, F. H. Stillinger, Jammed hard-particle packings: From Kepler to Bernal and beyond, *Reviews of Modern Physics* 82 (3) (2010) 2633–2672. doi:10.1103/RevModPhys.82.2633.
- [11] L. Mederos, E. Velasco, Y. Martínez-Ratón, Hard-body models of bulk liquid crystals, *Journal of Physics: Condensed Matter* 26 (46) (2014) 463101.
- [12] C. L. Phillips, E. Jankowski, M. Marval, S. C. Glotzer, Self-assembled clusters of spheres related to spherical codes, *Physical Review E* 86 (4) (2012) 041124.
- [13] K. Zhao, T. G. Mason, Self-organized chiral colloidal crystals of Brownian square crosses, *Journal of Physics: Condensed Matter* 26 (15) (2014) 152101.
- [14] M. C. Marchetti, Y. Fily, S. Henkes, A. Patch, D. Yllanes, Minimal model of active colloids highlights the role of mechanical interactions in controlling the emergent behavior of active matter, *Current Opinion in Colloid & Interface Science* 21 (2016) 34–43. doi:10.1016/j.cocis.2016.01.003.
- [15] K. a. Sharp, Analysis of the size dependence of macromolecular crowding shows that smaller is better, *Proceedings of the National Academy of Sciences* 112 (26) (2015) 7990–7995. doi:10.1073/pnas.1505396112.
- [16] J. C. Dyre, Simple liquids’ quasiuniversality and the hard-sphere paradigm, *Journal of Physics: Condensed Matter* 28 (2016) 323001. doi:10.1088/0953-8984/28/32/323001.
- [17] L. Grill, Large molecules on surfaces: deposition and intramolecular STM manipulation by directional forces, *Journal of Physics: Condensed Matter* 22 (8) (2010) 084023.
- [18] C. N. Likos, Effective interactions in soft condensed matter physics, *Physics Reports* 348 (4) (2001) 267 – 439.
- [19] H. Hansen-Goos, C. Lutz, C. Bechinger, R. Roth, From pair correlations to pair interactions: An exact relation in one-dimensional systems, *EPL (Europhysics Letters)* 74 (1) (2006) 8.
- [20] C. A. Young, A. L. Goodwin, Applications of pair distribution function methods to contemporary problems in materials chemistry, *J. Mater. Chem.* 21 (2011) 6464–6476.
- [21] R. O. Jones, Density functional theory: Its origins, rise to prominence, and future, *Rev. Mod. Phys.* 87 (2015) 897–923.
- [22] V. Coropceanu, J. Cornil, D. A. da Silva Filho, Y. Olivier, R. Silbey, J.-L. Brédas, Charge transport in organic semiconductors, *Chemical Reviews* 107 (4) (2007) 926–952.
- [23] B. Bhattacharjee, nth-nearest-neighbor distribution functions of an interacting fluid from the pair correlation function: A hierarchical approach, *Phys. Rev. E* 67 (2003) 041208.
- [24] R. D. Rohrmann, E. Zurbriggen, Conditional pair distributions in many-body systems: Exact results for poisson ensembles, *Phys. Rev. E* 85 (2012) 051109.
- [25] L. Xu, L. Yang, L. Cao, T. Li, S. Chen, D. Zhao, S. Lei, J. Ma, Effect of bulky substituents on the self-assembly and mixing behavior of arylene ethynylene macrocycles at the solid/liquid interface, *Phys. Chem. Chem. Phys.* 15 (2013) 11748–11757.
- [26] K. W. Chooi, A. I. Gray, L. Tetley, Y. Fan, I. F. Uchegbu, The Molecular Shape of Poly(propyleneimine) Dendrimer Amphiphiles Has a Profound Effect on Their Self Assembly, *Langmuir* 26 (4) (2010) 2301–2316.
- [27] P. Slezczkowski, N. Katsonis, O. Kapitanchuk, A. Marchenko, F. Mathevet, B. Croset, E. Lacaze, Emergence of chirality in hexagonally packed monolayers of hexapentyloxytriphenylene on Au(111): A joint experimental and theoretical study, *Langmuir* 30 (44) (2014) 13275–13282.
- [28] Y. Fan, L. Cheng, C. Liu, Y. Xie, W. Liu, Y. Li, X. Li, Y. Li, X. Fan, Steric effect on the self-assembly behaviours of amino acid derivatives, *RSC Adv.* 4 (2014) 52245–52249.
- [29] R. Ellis, Macromolecular crowding: an important but neglected aspect of the intracellular environment, *Current Opinion in Structural Biology* 11 (1) (2001) 114–119.
- [30] H.-X. Zhou, G. Rivas, A. P. Minton, Macromolecular Crowding and Confinement: Biochemical, Biophysical, and Potential Physiological Consequences, *Annual Review of Biophysics* 37 (1) (2008) 375–397.
- [31] S. L. Tait, A. Langner, N. Lin, S. Stepanow, C. Rajadurai, M. Ruben, K. Kern, One-Dimensional Self-Assembled Molecular Chains on Cu(100): Interplay between Surface-Assisted Coordination Chemistry and

- Substrate Commensurability, *The Journal of Physical Chemistry C* 111 (29) (2007) 10982–10987.
- [32] F. Rosei, M. Schunack, P. Jiang, A. Gourdon, E. Lægsgaard, I. Stensgaard, C. Joachim, F. Besenbacher, Organic molecules acting as templates on metal surfaces, *Science* 296 (5566) (2002) 328–331.
- [33] F. Reuleaux, *The Kinematics of Machinery*, London, Macmillan, 1876.
- [34] E. W. Weisstein, *CRC Concise Encyclopedia of Mathematics*, Hoboken : CRC Press, 2002.
- [35] J. Gielis, A generic geometric transformation that unifies a wide range of natural and abstract shapes, *American Journal of Botany* 90 (3) (2003) 333–338.
- [36] J. D. Lawrence, *A catalog of special plane curves*, New York: Dover Publications, 1972.
- [37] . Tomovi, J. van Dongen, S. J. George, H. Xu, W. Pisula, P. Leclre, M. M. J. Smulders, S. De Feyter, E. W. Meijer, A. P. H. J. Schenning, Star-shaped oligo(p-phenylenevinylene) substituted hexaarylbenzene: purity, stability, and chiral self-assembly, *Journal of the American Chemical Society* 129 (51) (2007) 16190–16196. doi: 10.1021/ja0765417.
- [38] H. Xu, A. Minoia, v. Tomović, R. Lazzaroni, E. W. Meijer, A. P. H. J. Schenning, S. De Feyter, A multivalent hexapod: Conformational dynamics of six-legged molecules in self-assembled monolayers at a solid-liquid interface, *ACS Nano* 3 (4) (2009) 1016–1024.
- [39] H. Xu, E. Ghijssens, S. J. George, M. Wolffs, Ž. Tomović, A. P. H. J. Schenning, S. De Feyter, Chiral Induction and Amplification in Supramolecular Systems at the Liquid–Solid Interface, *ChemPhysChem* 14 (2013) 1583–1590.
- [40] J. T. Kindt, Grand canonical Monte Carlo using solvent repacking: Application to phase behavior of hard disk mixtures, *The Journal of Chemical Physics* 143 (12) (2015) 124109. doi:10.1063/1.4931731.
- [41] M. Bumstead, B. Arnold, A. Turak, Reproducing morphologies of disorderly self-assembling planar molecules with static and dynamic simulation methods by matching density, *Physica A: Statistical Mechanics and its Applications* 471 (2017) 301–314. doi:10.1016/j.physa.2016.12.075.

Chapter 8

Simulating Morphologies with Multiple Molecular Species



The self-assembled morphology changes with the introduction of different molecular species, boundaries, and interactions. A simulated bulk system of two molecules (CuPC - orange flower and DIP - blue ellipse) is shown here and highlights new features like hexagonal periodic boundaries, and assembly under an external background field.

8.1 Morphological Variation in Organic Electronic Devices

Organic electronic devices can have a large variation in possible candidate molecules as the photon absorption active layer. Tuning the intermolecular structure has been shown to increase the efficiency in photovoltaic devices. Devices like bulk heterojunctions combine two separate donor and acceptor molecules to form the devices active layer [10, 11, 12, 13, 14, 15]. The interface between the donor and acceptor molecules has an influence on how the much of the absorbed photons are converted into energy [10, 69]. The excited charge carriers need to be extracted from the interior organic active layer once the photon energy is collected. To do this, there needs to be an accessible percolation path that allows the charges to move within. To minimize the loss in energy due to recombination, there needs to be a balance between having enough donor/acceptor interfaces to split excited excitons while also limiting the number of interfaces that charges will encounter on its way to the electrodes.

A system of two or more molecules is referred to as polydisperse, while ones that only contain a single molecular species are considered monodisperse. For instance, the molecular combination of CuPc and DIP appear as a four lobed shape and ellipse respectively when imaged using STM [15]. Organic molecules are built from basic chemical building blocks which can have many permutations of atoms and chemical species. In some instances, the replacement of atoms can result in a chemical that has similar bond structure to the original but with different intermolecular interactions with the substrate and other molecules due to the new chemical species. For instance, the same flower shape pattern is seen from STM images from Copper phthalocyanine (CuPc) [70] and Zinc phthalocyanine (ZnPc) [71]. This has the potential to change the electrical properties of a system by selecting different molecule, but keeping the same effective shape of the molecule. Device performance can change by swapping out one molecule for another with favourable electrical properties without changing the tiling pattern. The way that these molecules arrange themselves with respect to each others geometric shape is something that has yet to be explored with excluded-volume simulations.

This opens up a different question when we plan to simulate polydisperse particles. The definition of density depends on the covering area of the molecule. In a system of two or more molecules, each species can have a very different and complex shape, however the total volume they occupy can be exactly similar. In this case, relying on the density to determine the expected morphology can be a challenge. We hypothesize that these interactions manifest as a change to the geometry of the molecule and its “effective steric shape” is what drives the manifested arrangement seen in STM.

8.2 Expansions to the Monte Carlo Simulation Method

Monte Carlo methods are a common simulation approach that utilizes random numbers to simulate complex phenomena. The main problem that my thesis explores is how to incorporate this method for modelling molecules as steric objects and to quantify how close this approximation can be. Simulations are used to predict the self-assembly, reducing the need to perform costly and time consuming experiments. However, it is possible that other interactions effect the self-assembly of planar organic molecules. STM images currently are the best way to verify the positional order of molecules we use to build devices. Simulation outcomes can be compared to directly with experiment, suggesting that we can link a polygonal shape directly to model that molecule.

One of the main motivations for developing a new version of this software was the desire to simulate multiple types of molecules, each defined by their unique shape. An example of polydisperse simulations that would be previously inaccessible is shown in Figure 8.1. In Figure 8.1 (a), the the two particle model of CuPc and DIP has been simulated inside a hexagonal homeotropic boundary. The internal patches of donor/acceptor molecules makes this a good example to show off the motivation for developing this simulation method. Charge extraction is a key component to optimizing organic photovoltaic devices. The path the charge carries

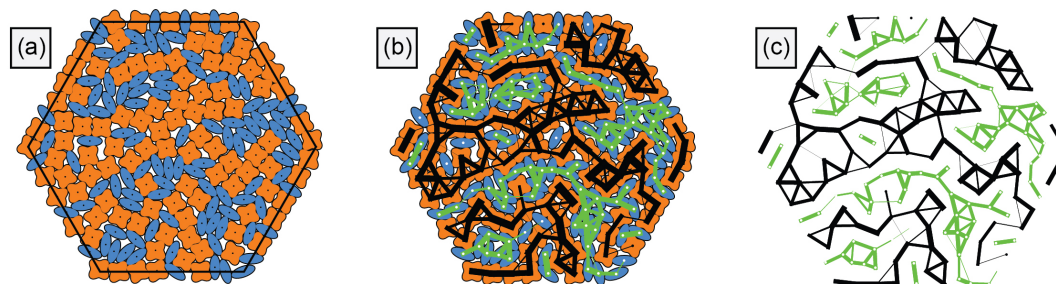


Figure 8.1: Example output configuration from simulating CuPc + DIP molecules ($N=100$ each) inside a hexagonal container with homeotropic boundary walls. (a) Rendered configuration with CuPc in orange and DIP in blue. (b) Charge percolation paths for each molecular species is plotted on top of the configuration. Black indicates the donor path while green is the acceptor. (c) Objects are removed for clarity, showing the regions of charge favourability and donor/acceptor interfaces. Thicker percolation paths indicate higher steric overlap - leading to a higher probability for charges to transfer between those molecules.

take after being generated by photon absorption will effect the efficiency. Charges that meander throughout the device not only take longer to reach the electrodes but also have a higher chance of recombination at the donor/acceptor interface. Both of these reduce the amount of electricity that can possibly be harvested.

In Figure 8.1 (b) the percolation paths for this configuration has been solved and plotted over top. The black colours indicate the path of the CuPc charges, which green lines show the route for DIP. The thickness of these lines show the relative probability for charges to jump from one molecule to another; where thick lines are interpreted as having higher steric-force interactions with its neighbour, and therefore suggests an increased probability to hop locally between these molecules.

In Figure 8.1 (c), the molecules are removed from the background for clarity. Here we can now observe the preferred path of charge carriers, having some long paths which connect from one edge to the other. The understanding the movement of charge inside the device is a key component to increasing the efficiency in photovoltaic devices and the overlap network gives a quick visual description into the likely pathways that are possible for a given morphology.

To fully produce useful results that can extrapolated for use in photovoltaic devices, the simulation needs to be able to handle more than one molecular shape at the same time. The addition of multiple molecular shapes into the simulation would be a powerful tool to fully understand the self-assembly of donor/acceptor organic molecules.

8.2.1 Types of Systems that can be Simulated

Initial version of the code (entitled “gransim”) kept a very rigid subset of simulatable conditions, forcing users to simulate monodisperse particles inside either periodic or hard square boundaries. One major limitation of this program is that it is only able to simulate monodisperse morphologies. Generating configurations for polydisperse monolayers is currently not possible for the “gransim” versions of the software. The solution for this was a new application (entitled “Morphologies”) that builds upon the previous work of Bjorn Arnold and expands the base capability to explore a more realistic description of molecular environments within photovoltaic devices. A list of the changes made to this program is outlined in Table 8.1. There have been 3 major releases of this program with each iteration adding more features. The last release was written from the ground up to include polydispersity in the simulations. Many sections of the original code were improved upon within the new framework of exploring new environments with polydisperse particles. The core of this code was patched by me in version 1.11 to accommodate the user input of non-square boundaries as well as an automatic repacking stage (denoted as cooling at jamming). However, we soon found that patching in expansions would take much

Release Info	gransim 1.0.9	gransim 1.11	Morphologies 1.0
Developer:	Bjorn Arnold	Matt Bumstead	Matt Bumstead
Year:	2009	2014	2017
Published Data:	Papers [36, 119]	Chapter 7	Chapter 8
External Codes			
Overlap Library:	Murta Clip. Lib.[128]	Murta Clip. Lib.[128]	Boost Geometry [129]
RNG Library:	Intel	Intel	Boost Random [129]
Matrix Library:	MKL	MKL	None (removed)
Compiler:	icc	icc	icc/gcc/clang
Molecules	Monodisperse	Monodisperse	Polydisperse
Boundary			
Hard	Square	Polygonal	Variable Polygonal
Homoeotropic	Square	Polygonal	Variable Polygonal
Periodic	Square	Square	Square / Hexagonal
Interactions	Thermal Agitation	Thermal Agitation Glass Transition	Thermal Agitation Glass Transition Background Potential

Table 8.1: List of major release features and their limitations over various iterations of our Monte Carlo simulation method.

more effort than re-writing the simulation code with polydispersity in mind. As such, the new code was designed with optimization in mind, with quick rejections and fast clipping methods to reduce computational cost associated with Monte Carlo trials. This improvement in speed allowed for development of additional features like interactions and complex boundaries that would be impractical otherwise. Without the test implementations as patches to the source code, many of the key efficiencies may have easily been overlooked.

Sections of Table 8.1 display the external routines, codes, and compilers needed to run the simulations. The initial version of the code random number generator and linear algebra libraries are propriety libraries of Intel. These were removed and replaced with the open source Boost Library [129]¹ to ensure more accessibility to researchers who do not own these licences. Initial testing also suggested that the Intel linear algebra routines used to translate and rotate the polygon vertices were also slower than expected because they have been optimized for large array manipulations. These were removed and replaced with similar a function without optimization. Overall, this change focuses more on improving the autonomy of the code while not having to sacrifice computation time in the process.

Sections of Table 8.1 outline the progress on the types of environments that molecules can be simulated under. Another limitation of the initial source code was that the systems were confined to having a simulation area that was always defined to be in a 1x1 unit square. We explored the effect of these square boundaries on how finite numbers of particles arrange themselves with its available volume (Chapter 6). This is fine for basic simulations but it limits the type of results that can be explored in a laboratory setting. In the realm of nano electronics, channels for charge transport can be etched out to create a cavity on a substrate [130]. These cavities are not necessarily square and might have much geometric complexity to them. The patch to the initial code expanded the boundary conditions to include any arbitrary shape which can be defined as a polygon. A new periodic boundary using hexagonal basis translations were developed for reducing CPU calculation cycles and are included within the new code.

The final expansion to the initial code was the inclusion of non-steric interaction potentials between simulated particles. The initial source code only simulates particles acting through

¹Module used on Sharcnet: boost/intel1503-openmpi187std/1.59.0

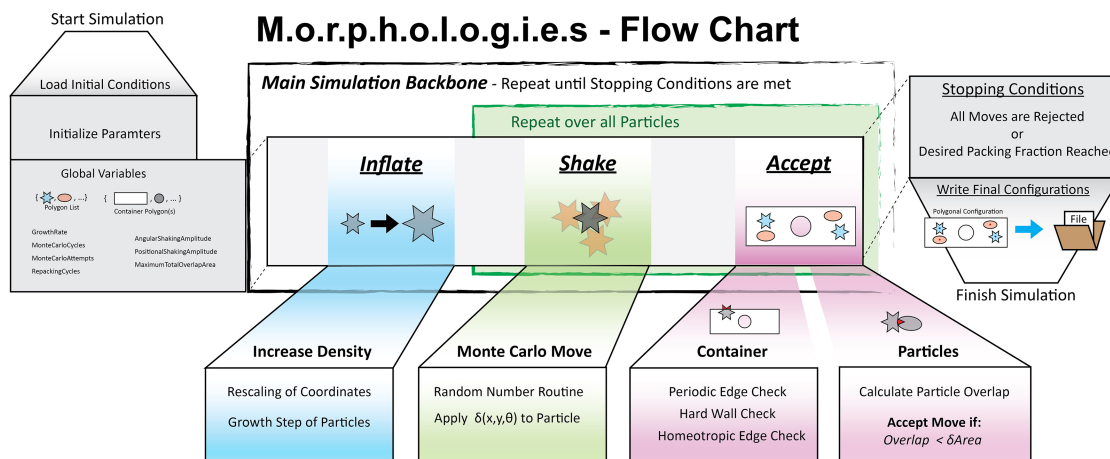


Figure 8.2: Flow chart of the “Morphologies” simulation procedure.

repulsive interactions that occur when the molecules in the system overlap. This defines an infinite interaction potential inside the molecule and zero potential outside the boundary of the polygon. Thermal agitation is modelled as a series of randomized trial displacements with equal probability to move in any direction. Once overlaps are detected, the move is rejected and the object is repositioned with a different randomized displacement. The new simulation includes a way to model additional interaction potentials through biasing the Monte Carlo moves. The system can mimic interaction potentials by biasing the probability to pick random displacements in the direction of the net force on the particle. This allows for particle-particle interactions and also model for forces that are imposed by an external field.

8.2.2 Overview of the Main Algorithm

Figure 8.2 shows a flowchart for the “Morphologies” simulation algorithm. It is based heavily on the work developed by Bjorn Arnold in his Masters thesis [118]. As such, the method will be briefly outlined with a focus on new implementations or key developments while additional information can be found in our previous published work [118, 36, 119].

The exact summary of the newest implementation is outlined in Table 1. This algorithm table describes (in words) how the simulation is coded and provides a quick reference that outlines the procedure for those who might not be as computational savvy. The first thing needed to use the simulation is to set initial conditions within the input files. These parameters tell “Morphologies” the types of environment to simulate. Properties such as: the rate of condensation, the spatial and angular range for thermal motion, the amount of allowable molecular overlap, the type of boundary conditions, and the number of Monte Carlo trials are all set within this document. An additional input file is needed to link in the polygons that are intended to be simulated. This link file is a text file that consists two columns: the number of particles and the directory path to the polygon file to be read. Since any number of different particles can be input as shapes, keeping this separate from “defaults.dat” seemed the easiest to implement while maintaining ease of use for the user. Input abbreviations for user inputs are kept over from Bjorn as common colloquia associated with each variable.

There are three basic components to this simulation routine: to inflate the particles, then to shake them until a move is accepted. The first inflation step is key to the self-assembly, since it represents the densification of the molecules (reduction of free volume) and sets the path particles take through static equilibrium states. The inflation represented in Figure 8.2 (blue) and shows the change in molecule size from one simulation step to the next. The second is the shaking portion and this simulates the movement of the particle. The molecular shaking is represented in Figure 8.2 (green) and shows a set of possible Monte Carlo moves that the grey molecule can take, with the choices in opaque red. External influences and other potentials that depend on particle position can be included or modified in this section. The final step is to check the resulting move from shaking for physical validity. The acceptance criteria is represented in Figure

8.2 (pink) and shows the two conditions that need to be met to be physical. The main criteria for acceptance is to check if particles satisfy the boundary conditions; which can be periodic, homeotropic, or hard walls. I have paid special attention into ways that each type of boundary condition works and have implemented many functions that are designed to quickly reject moves before unneeded overlap calculations are done between particles. This was done in order to reduce the time of each simulation and works quite well at limiting calculations. Finally, any move that results in an unallowable amount of overlap between two objects is rejected and a new move is sampled. This rejection function needs to be looped over all particles in the simulation, which is why it is checked last. These procedures are repeated for every simulation step until the simulation cannot generate anymore acceptable moves wherein which the simulation writes the final details regarding the morphology to data files and then halts.

Procedure of “Morphologies”

The algorithm is the backbone of the simulation method. It has been developed with both speed and large-scaling of particle number in mind. The main focus has been emphasize routines that determine the rejection criteria, so that unnecessary computations are skipped instantly if overlaps are detected. Reducing computational time it is possible to run more complex systems.

```

Input: Total Number of Molecule ( $N_{tot}$ ), Molecule Steric Potential ( $P$ ), Number of
Molecules of Shape ( $N_p$ ), Number of Monte Carlo Attempts ( $\omega$ ), Ensemble
Number ( $ens$ )
1 Begin Simulation from Terminal:
2 ./RunMorphologies
3 Initialize(); Import: defaults.dat and polygons.dat
4 Imported Correctly? → (true || false) → if (false) then Halt
5 Start: Morphologies
6 while Molecule Moves → ? Accepted do
7   Inflate(); Update → SimStep++;
8   Update Current BoostPolygon List → Apply Inflation;
9   QuickRejection(); if (Global Overlap < Allowable) → Skip Shaking and Inflate
   Again
10  Shake(); Test Random Movement of Molecules
11  for Monte Carlo Cycles do
12    for Molecule Index (i) → 1 to  $N_{tot}$  do
13      RandomizedInteraction();
14      Generate ( $\omega$ ) Random Displacements:  $\partial r = \{\partial x, \partial y, \partial \theta\}$ 
15      for Monte Carlo Attempts → 1 to  $\omega$  do
16        PositionDisplacedMolecule();  $\{x \rightarrow x + \partial x\}, \{y \rightarrow y + \partial y\}, \{\theta \rightarrow \theta + \partial \theta\}$ 
17        TestForSatisfiedBoundaries();
18        for translations  $\subseteq \vec{v}_{pbc}$  do
19          for All Boundary Edges do
20            Homeotropic → (true || false)
21            Hard Wall → (true || false)
22          if (Any Boundaries  $\neq$  Satisfied) then
23            Reject Move
24          else
25            ParticleOverlap();
26            for particle ( $j \neq i$ )  $\leftarrow$  1 to  $N_{tot}$  do
27               $\sum$  Overlapping Area
28              if (Overlap < Allowable) then
29                Accept Move and Break (Monte Carlo Cycles) Loop
30      Accept();
31      if (Overlap < Allowable) then
32        Update Accepted Centroids;
33      else
34        Reset to Previous Accepted Move
35        Reduce Shaking Amplitude → Increase Repacking Step
36      if (RepackingStep > Allowable) then
37        Halt;
38 Final Halt
Output: Files: “conf_1.dat” - Positional Centroids, “container.dat” , Boundary Polygon,
“polygon_1.dat” Molecule Polygons

```

Algorithm 1: “Morphologies” Algorithm

8.3 Molecular Confinement and Boundary Conditions

Boundary conditions are crucial components in numerical experiments. This parameter sets the limits on what can be simulated and dictates the type of phenomena that can be observed and modelled. “Morphologies” has two types of possible boundary choices: confining walls and simulated particle edges. Confining walls disallow any Monte Carlo move that displaces a molecule outside of its bounds. A subset of this boundary is called homeotropic boundaries, where instead of the complete molecular area being confined, it is instead the molecular centroid that must remain inside [131]. While being procedurally similar, the homeotropic boundary condition has been shown to produce drastically different morphologies than purely hard walls when elongated (ellipsoidal) particles were simulated inside the cavities [132, 133, 134]. In reality, both these methods are specific types of confinement effects that manifest their influence by changing steric interactions at the boundary edge. The simulated particle edge boundary is more commonly known as periodic boundary conditions, which is implemented to remove as much influence as possible from the limitations of simulated self-assembly. These differences in outcomes builds the basis for a hierarchy of steric influences that the simulation walls have on the internal molecules.

The boundary with the most influence on particles is the hard boundary, which produces large steric frustration against any movement by disallowing any excluded-volume of the molecule from leaving the box. The second is the homeotropic boundary, where molecules are confined by their center of masses. This allows them to have more rotational freedom, since parts of the molecule may leave the box to find steric relaxation from the internal molecular pressure. The third is the periodic boundary. This type of boundary is used to minimize any influence from the numerical simulation container by allowing molecules that leave the box to be translated back to the opposite periodic edge. This hierarchy of steric influence is what allows for quick rejection algorithms that appear in morphologies. In the following sections, the case will be made for how the morphology from each subcategory can be reproduced using a geometric transform of the boundary with more steric influence.

In Chapter 5, we showed that if steric simulations produce ensembles where the density is matched, the structural metrics will be (on average) similar. We expand this idea to benchmark “Morphologies”. This simulation should be able to reproduce everything that the initial simulation “gransim” will when under the same restrictions (i.e. thermal motion and monodisperse particles). In the next sections, we highlight the types of boundaries and compare the configuration outcomes using initial conditions which are as close as possible to each other.

“Morphologies” also needs to be benchmarked against comparable systems from “gransim” to authenticate physical validity. To benchmark each method, we create large ensembles of typical outcomes from varying initial positions. These ensembles represent a large statistical framework from which comparison of physical properties is possible. This is done to remove unintentional bias of comparing metastable and/or rare configurations as commonly sampled states. False classification of similar/dissimilar states can result in erroneous falsification between methods. Large statistical ensembles of many outcomes can be gathered from simulations to obtain a set of typical outcomes that are possible. This section outlines the benchmarking as the boundaries are varied.

8.3.1 Hard Boundary Condition - (hard)

The most influence is the hard boundary condition, where any Monte Carlo moves that result in the molecule moving outside are rejected. This sets very large restrictions on the translational and rotation degrees of freedom, essentially removing about half the total allowable movements. In the “Morphologies” procedure, this boundary condition is checked first. This is because of the rigorous rejection of anything that lands outside the boundary. When this is checked first, a move has the potential to be rejected before any unneeded computations are done. An example of an unoptimized procedure would be to check the overlap between all particles first. Any move can satisfy the particle-particle overlap but all of the overlap calculations are done in waste if it results in a boundary overlap. By selecting the hard condition first, the method cuts down

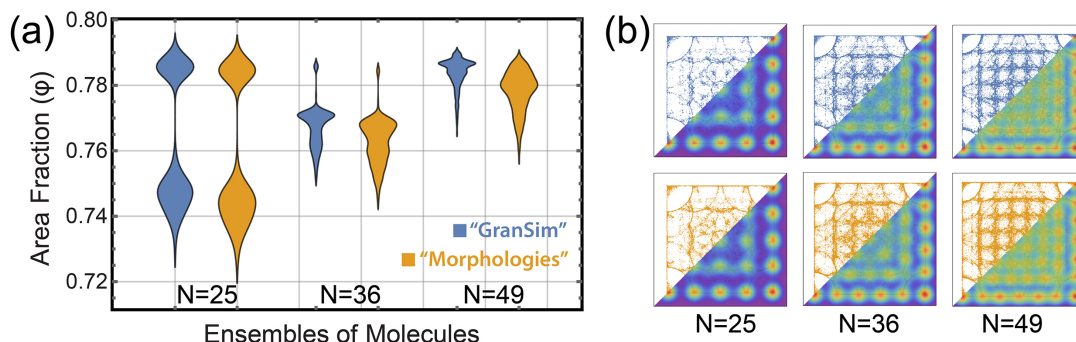


Figure 8.3: Comparing Monte Carlo simulations under confined boundaries. (a) Area fraction distributions of confined circular particles. (b) Point clouds associated each distribution. Ensembles contain 4032 configurations.

on computational time and allows for more particles to be simulated in the time frame as the inefficient method.

A comparison of the different Monte Carlo simulations are shown in Figure 8.3. These simulations were run with the same initial conditions to provide as much consistency between each implementation as possible. In Figure 8.3 a), the area fraction probability distributions are plotted together, similarly to the comparison in Chapter 5. These probability distributions match fairly well. However it does seem that for $N = 49$, “gransim” produces configurations where are denser, as indicated by a thicker section at higher packing fractions. This can be attributed to the different acceptance criteria in “gransim” which favours acceptance rather than rejections. In Figure 8.3 b) the point clouds are plotted with the density map overlaid. In this case, the two methods produce planar probabilities which seem identical.

8.3.2 Homeotropic Boundary Condition - (soft)

A weaker set of confinement is the homeotropic boundary conditions, which allow molecules more freedom by only confining them by their center of mass. This boundary accounts for a force normal perpendicular to the walls which acts on the molecular centroid [131] and detaches the rotational and translational steric influence of the container by changing the how pressure is applied to the system [135]. In this case, the system equalizes the pressure by preferring configurations that maximize density at the container-molecule interface. This liberates the rotational degree of freedom, putting only the restrictions on translational motion. Since the thermal agitation randomly rotates the molecules around their center of mass, this homeotropic boundary mimics a “pinning effect”, where the molecule looks as if held down in the center but allowed to rotate by the steric force of its neighbours [133].

A comparison between from “gransim” and “Morphologies” is shown in Figure 8.4 a) as probability distributions from ensembles of homeotropic boundaries. The shape of each distribution is similar, however, “Morphologies” shows a slightly higher density. Figure 8.4 b) shows final configurations of molecules and how this boundary pins the centroids of molecules. The area fraction is calculated using only the molecules within the box area and is highlighted with blue. In both simulations, the molecules pack tight at the edges with a large portion of their volume outside of the container, however, the area fractions suggest that molecules simulated with “Morphologies” prefer to distribute themselves inside the box rather than outside. In Figure 8.4 (c), the centroids of circular molecules are confined within a square container but extend toward the edges. This result highlights the hierarchical confinement effect of homeotropic boundaries, since the point clouds show the same features of hard boundary confinement when compared to the point clouds of Figure 8.3 b). Another explanation for this difference would come from the “gransim” data used for this comparison. The data shown here was collected prior to the inclusion of the repacking method used in “Morphologies”. This repacking allows for the molecules to expand

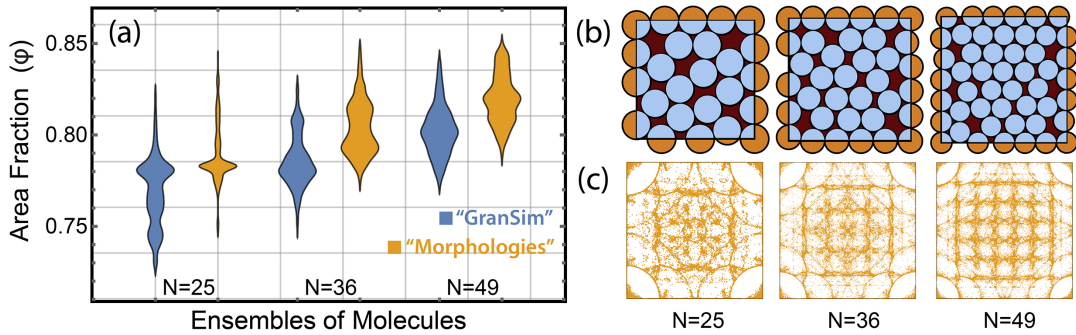


Figure 8.4: Comparing Monte Carlo simulations under homeotropic boundaries. (a) Area fraction distributions for 25, 36, and 49 circular particles. (b) Example of the most probable configuration from “Morphologies”. Area fractions are calculated using only the portions of molecules contained within the square box, denoted as blue sections. (c) Point clouds from “Morphologies”. Ensembles contain 4032 configurations.

to reduce spurious area between them without changing the internal structure by reducing the thermal agitation such that the Monte Carlo moves sample displacements that are closer to their centroid. Taking this into account would suggest that these two routines are fairly similar under homeotropic boundaries.

8.3.3 Periodic Boundary Condition

Periodic boundaries are often thought of as having least influence on particles and being the best representation of large systems. In simulation, this periodic boundary is a subset of the homeotropic boundary that results in multiple instances of virtual particles that reside on the opposite side of the soft boundary. For every set of periodic translations, there is always exactly one movement that results in the molecular centroid being contained within the original simulation area. This is the reason it is a subset of the homeotropic boundary.

Square Periodic Boundaries - (periodic)

Square periodic boundaries are the most commonly used boundary conditions. Any objects close to a periodic edge cause a virtual particle to be placed with the boundary causing an opposite influence. This means that the boundary produces an influence onto the molecules by conservation of volume. In Figure 8.6 (a), the orange molecule close to the periodic container edge causes eight (8) virtual particles. Periodic boundaries have the most influence on the system when molecules land the corners. When a molecule translates outside the container, the system adjusts to an equalization equilibrium by reducing the available volume for other molecules equal to that of the molecular volume outside. This results in three (3) virtual particles in the mirror-edge corners that all influence relatively spatially separated parts of the simulation area. The method is to test all possible translations and accept the one that successfully moves the molecule without overlapping any neighbours. This allows for the wrapping around effect of molecules moving their center of mass outside the container.

Figure 8.5 shows the results from benchmarking bulk systems of circular particles. The covering area distributions in Figure 8.5 a) shows that for “Morphologies”, the covering area is lower than “gransim” which implies the configurations are less dense. Figure 8.5 b) shows the pair correlation function of the configuration that has a mean area fraction that is at the peak of the distribution (i.e. most probable). The difference spectrum between the two curves indicates that these patterns are actually quite similar in translational order even with different density. Angular order of neighbours is outlined in Figure 8.5 c) with the bond order parameter (q_6) displayed in histograms and locally coloured Voronoi tessellations. Higher amounts of angular order for

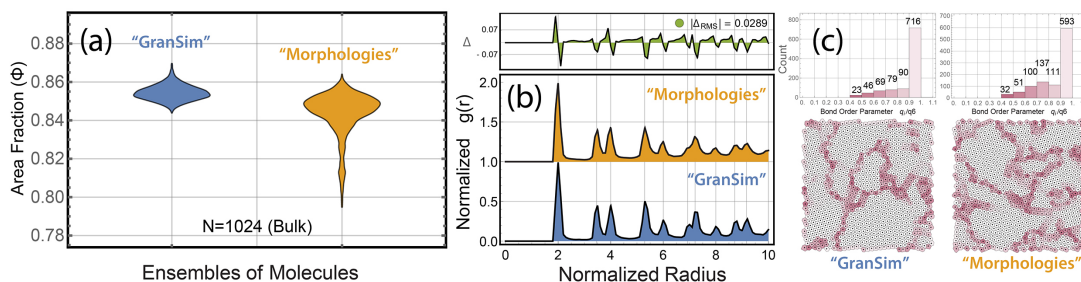


Figure 8.5: Comparison between Monte Carlo simulations of 1024 circular molecules within periodic boundaries. (a) Density profile of the covering area. (b) Pair correlation function and (c) Voronoi tessellations with bond order colouring for the most probable configuration

Number of Molecules:	25	36	49	1024 (pbc)
Time (sec):				
- gransim	711.7	2119.2	2410.2	42866.6
- morphologies	418.7	679.3	1005.8	27916.8
RAM (MB):				
- gransim	11.9	11.1	10.1	9.0
- morphologies	9.1	8.6	8.5	12.1

Table 8.2: Examining execution time and RAM usage for Monte Carlo simulations of circular molecules inside both a hard and periodic square.

“gransim” can be interpreted from the histograms. The lower angular order in “Morphologies” can be attributed to the lower density of the ensemble, since high hexagonal order depends on high density. The looser the particles, the more chance for slight positional fluctuations which causes deviation in the hexagonal bond order.

Hexagonal Periodic Boundaries - (hexagonal)

The hexagonal periodic boundary condition has many computational benefits over the traditionally used square boundary. One reported advantage these have over square boundaries is that artifacts will form at large packing fractions due to the corner translations [136]. This causes the excluded volume of the virtual molecule to be split between periodic mirror edges. If one were to examine at the amount of orange volume that extends outside of the dark gray container and compare it to the total volume of the both green molecules inside the container, you will notice that they are the same. Another benefit is that it requires two less translation basis vectors, which immediately removes 1/4 of the calculations needed to calculate a particle interaction and Monte Carlo displacement rejection. Reduction in computational complexity comes from the reduction of virtual particle interactions. In Figure 8.6 (b), the orange molecule close to the periodic container edge causes only six (6) virtual particles. The four (4) gray virtual molecules are translated outside the range to sterically interact with the particles at the boundary edge and can be removed from the calculations. Even with the benefits over traditional square boundaries, hexagonal tiles have not seen wide use in planar simulations.

8.3.4 Benchmarking CPU Times for Confined Monodisperse Systems

It is important to compare the execution time and RAM usage in between simulations which can be seen in Table 8.2. The goal is to produce a faster and more streamlined version of

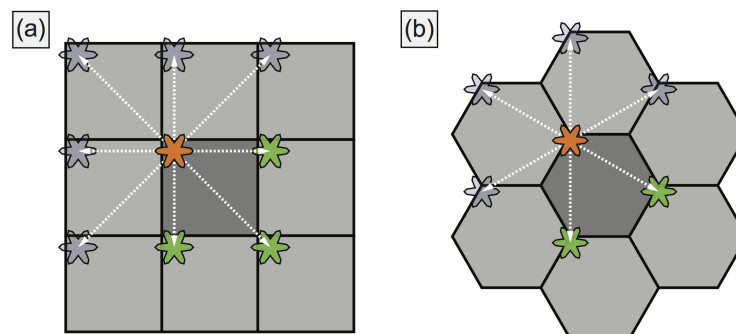


Figure 8.6: Periodic boundaries that are available in “Morphologies”. (a) Square and (b) Hexagonal periodic tiling. The orange particle inside the centre dark gray areas are translated by a set of basis vectors, adding and placing virtual particles that influence the rejection criteria for the Monte Carlo displacement. Note that only the green virtual particles influence the molecules inside the container, with the opaque gray particles being translated too far outside the system to interact sterically and thus can be ignored.

“gransim” which can reproduce the same phenomena. In previous sections, we quantified that the morphologies are similar in confined and bulk systems. When comparing across computational times, “Morphologies” has a drastic reduction in simulation time almost by a factor of 2. This reduction in simulation time can allow for larger numbers of particles to be simulated together for the same amount of time “gransim” would take. Secondly, we notice that both methods are quite light on RAM usage and are practically similar among each other. This information is beneficial for our use on super cluster computers since it allows us to schedule jobs with lower RAM meaning shorter queue wait times.

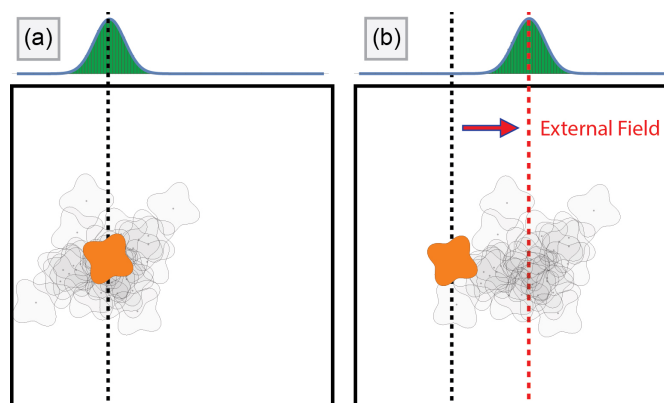


Figure 8.7: Example of how the probability distribution of possible Monte Carlo trial is spatially displaced to incorporate the effect of a constant background field (along the x-axis). a) No field. b) Constant field.

8.4 Molecular Monte Carlo Interactions

A major part of the new simulation being built is one that can incorporate different interactions. All sorts of different interaction potentials are possible. To describe the new method, we can relate this to the mean-field Ising model. The Ising model is one in which neighbouring particles influence individual particles. A Monte Carlo in the Ising model step is one where a) the energy required to flip a spin is calculated from the states of its neighbours then b) a random number is selected from an exponential distribution of possible outcomes. This random number is considered to be the thermal energy of the particle at that specific time. If this random number is above the energy required to change its spins (as dictated by the neighbours), the move is accepted and flipped.

Now consider a single Monte Carlo step proposed for new molecular modelling scheme. A molecule in the simulation is selected for the Monte Carlo move. The first step is to calculate the energy (or force) that this molecule will experience. This can be a sum of interaction potentials from neighbours (i.e. Lennard-Jones or Coulomb interactions) but is not limited to this. An arbitrary amount of potentials can be included, given by the user. The addition of each interaction changes the spatial distribution of possible probabilities for random number generation. Figure 8.7 displays a schematic for possible types of interactions. Monte Carlo sample displacements are in transparent, while solid colours indicate current positions of molecules. The current description of thermal motion is in Figure 8.7 (a) with the probability distribution above the real-space simulation. Random samples have a higher probability to move the object small deviations from the center, while the farther moves tail off in the probability distribution. External fields are introduced in Figure 8.7 (b). Consider a charged particle in an electric field. The molecule will move in the direction of that field. If the field is on the same order of that thermal energy, the molecule will continue to move randomly (Brownian motion), but will also be pulled by the field. The net result of having both types of motion will manifest as described in Figure 8.7 (b). It is possible to model this by shifting the probability distribution.

Molecule-molecule interactions can be included the same way. The magnitude and direction of the interaction potential can be calculated by an arbitrary number of neighbours. The result is a net force/interaction as defined by the state of the neighbouring molecules. A super position of these interactions are then built, and manifests as a change in the random number distribution. Figure 8.7 (c) shows that the sum of two oppositely charged molecules (blue) results in a force that is in the direction directly between them. The magnitude is proportional to the calculated interaction. By including the thermal motion, we include the possibility for the molecule to move opposite of the field. This effect is similarly seen in devices using organic molecules, where charge percolations can temporarily move opposite to the field in order for current to flow.

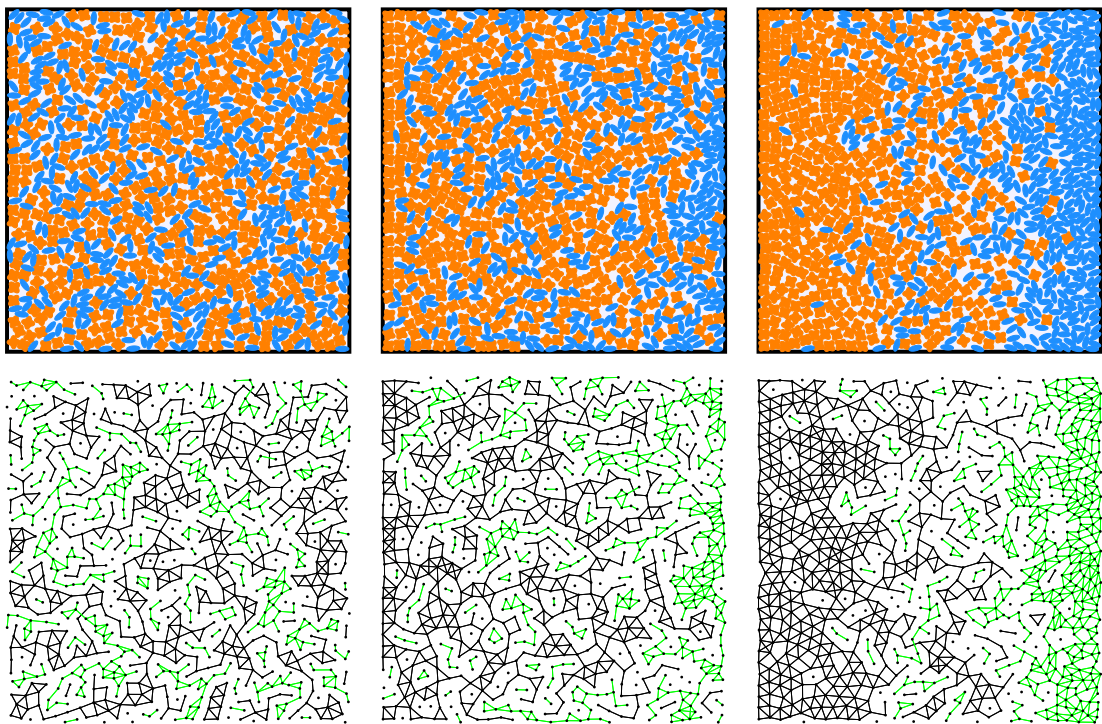


Figure 8.8: Example configuration with a constant background field (along the x-axis) with $N=1024$ molecules (512:512). Blue particles have an opposite charge to the Orange ones, hence the segregation of molecules. Field strengths relative to the thermal agitation: (a) Zero field (b) 0.1 kT, (c) 0.2 kT

Chapter 9

Summary and Outlook

9.1 Concluding Remarks

This thesis brings together many aspects of self-assembly in attempt to understand the role of molecular shape on the resulting morphology. The ability to accurately detect differences in these systems has been investigated by building and applying tools to characterize the localized disorder of molecules relative to a highly ordered hexagonal state. This quantification allows for the extraction of hidden structural subtleties that can be missed by causal observers. Excluded-volume of simulations were built to explore the effect of shape by isolating the steric interaction potential within systems dictated by the density. We show that Monte Carlo methods can produce the same morphology as event-driven molecular dynamics for bulk and confined systems. In these confined systems, morphologies are statistically quantized into parcels of similar patterns. When the particle number decreases, we observe the emergence of quantized patterns in a metastable equilibrium state. The shape of molecules were explored in relation to steric molecular analogs that have geometries that resemble those observed in scanning tunnelling microscopy. Finally, polydispersity is touched on by highlighting the features of the new excluded-volume simulation code.

The entirety of this thesis incorporates many different aspects of self-assembly from various scientific fields. Due to the limited nature of the project, some of the possible research directions were unable to be fully explored. A few different parts were discussed internally, however, they are not currently fully implemented as complete sections. As such, this chapter is dedicated to projects that were researched from literature surveys, quickly implemented with crude algorithms, and tests on small sample sets of data.

Although the ground-work for classifying dispersion is outlined here, there are many other tools that provide very interesting analysis. Many build upon the methods utilized in the thesis by adding or combining different order metrics to produce a finely-grained description of morphology. In last section of the thesis, some of the initial research on these topics are presented.

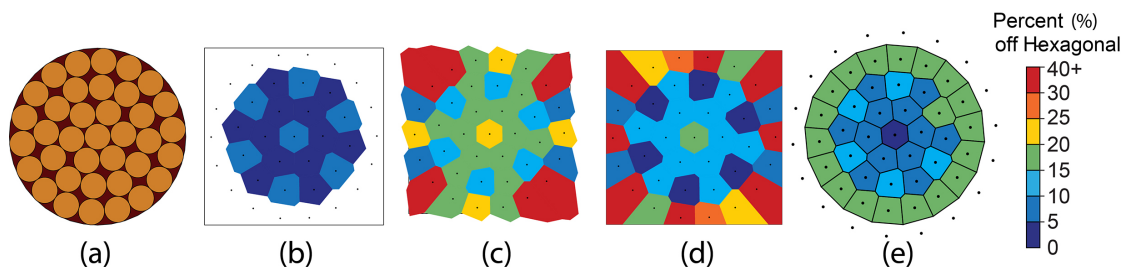


Figure 9.1: Examples of Voronoi tessellations and boundary corrections. (a) Configuration of 37 circular particles simulated inside a circularly confining boundary. (b) Truncated boundaries are applied as usual, with tiles extending outside the automatically detected bounding box being excluded. This removes the outer particles in touch the channel walls, causing the particles under steric frustration to be neglected. (c) Periodic boundaries introduces large Voronoi tiles at the corners, causing errors in both the expected shape and expected number density. (d) Regular image charge boundaries within “disLocate” explicitly assume a rectangular confinement space. (e) The general routine for image charge boundaries is applied showing that Voronoi edges approximate the box at the boundary.

9.2 Expanding Upon this Research

9.2.1 Image Charge Boundary and Circular Confinement

Image charge boundaries have provided quite a robust way to circumvent the limitations of categorizing morphology in confined areas. This routine assumes neighbours outside of the confining space by placing virtual particles an equidistant length away from the box edge. The result is that Voronoi tessellations are forced to have edges exactly at the container edge. In the “disLocate” package (see Chapter 4), image charge boundaries are implemented assuming that the box is rectangular. In reality, the boundaries that confine particles in can be quite complex. In Figure 9.1, we show how this boundary can be expanded into a more general method. A circular confining box was chosen to hold simulated molecules and does well at illustrating the details of the method.

9.2.2 Voronoi Coordination Shells and the Pair Correlation

The pair correlation function is a one metric that essentially collapses all translational order into a one-dimensional function of distance. It describes a global average of the particle arrangement. A portion of this thesis was to quantify local disorder in planar systems and to quantify the variance. Disordered systems create broad peaks in the pair correlation function, implying that there is less positional order at specific positions than a hexagonal lattice with the same mean intermolecular spacing. The methods that we developed really focus on the first shell of neighbours. These neighbours cause local frustration and cage the internal particle. This effect is analogized as a main influence in the glass transition. When the particles are cooled too fast, they do not have time to relax and thus the caging particles lock in their positions as disordered states.

One tool we have begun exploring is the separating the pair correlation function as a function of the neighbour shells [137]. As the distance expands radially from the centre, the caging molecules become the ones who are contained in the next layer directly behind them. This effect is outlined in Figure 9.2 (a). Defining each shell is a trivial task once the Delaunay triangulation has been calculated. This function assigns neighbours to every particle in the system. To start, the Delaunay triangulation is the first shell of neighbours. The next step can be repeated as many times as desired to obtain the influence of the “n-th” neighbour shell. Here we describe how to calculate the second shell. For all particles in the first shell, assign a group of particles that form the Delaunay neighbours for those particles in the first shell. Then, remove all the particle which

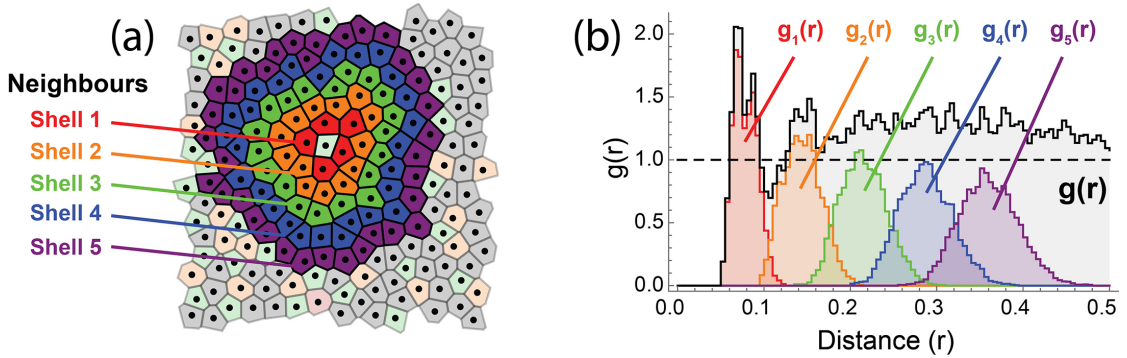


Figure 9.2: (a) Voronoi tessellations of a disordered packing. The central particle is surrounded by a series of “neighbour shells”. (b) The pair correlation function can be subdivided to capture the information about specific caging influences. Colours of the shells in the Voronoi diagram represent the $g(r)$ of the same colour.

are in the previous group (i.e. the first shell particles) and then delete any duplicate entries. Particles on either side of each member will generate a group with two entries that are similar, since each particle inside the second shell has two neighbours directly beside each other. That is it. Continue this process of assigning groups to the full coordination neighbours and removing the previous entries or shells.

Once groups of neighbouring particles are defined, the pair correlation function can be solved using only that subset of neighbours. This can allow for a high degree of accuracy when trying to determine the influences of self-assembly. To see how this works, consider the pair correlation function as an infinite sum of shells. Each shell (i) adds to the total probability of particles in the system.

$$g(r) = \sum_{i=1}^{\infty} g_i(r) \quad (9.1)$$

At some point the function is truncated, either due to the limited information of particles within an image (finite number effect) or no more useful information is gained as we expand outward (disorder turns into gas phase). This will produce an estimated function of the $g(r)$ that is quite close to the global definition. For instance, if we consider the first 3 shells, then $g(r)$ becomes:

$$g(r) = g_1(r) + g_2(r) + g_3(r) + \dots \quad (9.2)$$

Figure 9.2 (b) shows the pair correlation function as well as the split between neighbour shells. One interesting thing to note is that the shells will often cause the tail-ends of the functions to blend into each other. This can be interpreted as a breaking of radial translational symmetry. If you follow a shell angularly around the central particle, you might notice that the disordered morphologies have shells which are not exactly circular. They vary in both distance and angular separation from what might be expected in hexagonal packing. When particles are disordered, the ability to determine which shell it is in becomes quite unclear. This is important if we want to quantify other parameters. For example, the bond order parameter commonly uses the first minimum of the pair correlation function to define neighbours. If this was used with the global $g(r)$, it is possible that particles from the second shell will leak into our numerical analysis and disturb the true result. With this method we can easily extract coordination shells unambiguously and use only those particles of interest.

Rights and Licenses for Reuse of Publications

**ELSEVIER LICENSE
TERMS AND CONDITIONS**

Jun 06, 2017

This Agreement between Matt Bumstead ("You") and Elsevier ("Elsevier") consists of your license details and the terms and conditions provided by Elsevier and Copyright Clearance Center.

License Number	4123161053598
License date	Jun 06, 2017
Licensed Content Publisher	Elsevier
Licensed Content Publication	Physica A: Statistical Mechanics and its Applications
Licensed Content Title	Reproducing morphologies of disorderly self-assembling planar molecules with static and dynamic simulation methods by matching density
Licensed Content Author	M. Bumstead,B. Arnold,A. Turak
Licensed Content Date	Apr 1, 2017
Licensed Content Volume	471
Licensed Content Issue	n/a
Licensed Content Pages	14
Start Page	301
End Page	314
Type of Use	reuse in a thesis/dissertation
Portion	full article
Format	both print and electronic
Are you the author of this Elsevier article?	Yes
Will you be translating?	No
Order reference number	
Title of your thesis/dissertation	Simulating Self-Assembly of Organic Molecules & Classifying Intermolecular Dispersion
Expected completion date	Aug 2017
Estimated size (number of pages)	150
Elsevier VAT number	GB 494 6272 12
Requestor Location	Matt Bumstead Room A328, John Hodgins Engineering McMaster University 1280 Main St W Hamilton, ON L8S 4L7 Canada Attn: Matt Bumstead
Total	0.00 CAD

[Terms and Conditions](#)**INTRODUCTION**

1. The publisher for this copyrighted material is Elsevier. By clicking "accept" in connection with completing this licensing transaction, you agree that the following terms and conditions apply to this transaction (along with the Billing and Payment terms and conditions established by Copyright Clearance Center, Inc. ("CCC"), at the time that you opened your Rightslink account and that are available at any time at <http://myaccount.copyright.com>).

GENERAL TERMS

2. Elsevier hereby grants you permission to reproduce the aforementioned material subject to the terms and conditions indicated.

3. Acknowledgement: If any part of the material to be used (for example, figures) has appeared in our publication with credit or acknowledgement to another source, permission must also be sought from that source. If such permission is not obtained then that material may not be included in your publication/copies. Suitable acknowledgement to the source must be made, either as a footnote or in a reference list at the end of your publication, as follows:

"Reprinted from Publication title, Vol /edition number, Author(s), Title of article / title of chapter, Pages No., Copyright (Year), with permission from Elsevier [OR APPLICABLE SOCIETY COPYRIGHT OWNER]." Also Lancet special credit - "Reprinted from The Lancet, Vol. number, Author(s), Title of article, Pages No., Copyright (Year), with permission from Elsevier."

4. Reproduction of this material is confined to the purpose and/or media for which permission is hereby given.

5. Altering/Modifying Material: Not Permitted. However figures and illustrations may be altered/adapted minimally to serve your work. Any other abbreviations, additions, deletions and/or any other alterations shall be made only with prior written authorization of Elsevier Ltd. (Please contact Elsevier at permissions@elsevier.com). No modifications can be made to any Lancet figures/tables and they must be reproduced in full.

6. If the permission fee for the requested use of our material is waived in this instance, please be advised that your future requests for Elsevier materials may attract a fee.

7. Reservation of Rights: Publisher reserves all rights not specifically granted in the combination of (i) the license details provided by you and accepted in the course of this licensing transaction, (ii) these terms and conditions and (iii) CCC's Billing and Payment terms and conditions.

8. License Contingent Upon Payment: While you may exercise the rights licensed immediately upon issuance of the license at the end of the licensing process for the transaction, provided that you have disclosed complete and accurate details of your proposed use, no license is finally effective unless and until full payment is received from you (either by publisher or by CCC) as provided in CCC's Billing and Payment terms and conditions. If full payment is not received on a timely basis, then any license preliminarily granted shall be deemed automatically revoked and shall be void as if never granted. Further, in the event that you breach any of these terms and conditions or any of CCC's Billing and Payment terms and conditions, the license is automatically revoked and shall be void as if never granted. Use of materials as described in a revoked license, as well as any use of the materials beyond the scope of an unrevoked license, may constitute copyright infringement and publisher reserves the right to take any and all action to protect its copyright in the materials.

9. Warranties: Publisher makes no representations or warranties with respect to the licensed material.

10. **Indemnity:** You hereby indemnify and agree to hold harmless publisher and CCC, and their respective officers, directors, employees and agents, from and against any and all claims arising out of your use of the licensed material other than as specifically authorized pursuant to this license.

11. **No Transfer of License:** This license is personal to you and may not be sublicensed, assigned, or transferred by you to any other person without publisher's written permission.

12. **No Amendment Except in Writing:** This license may not be amended except in a writing signed by both parties (or, in the case of publisher, by CCC on publisher's behalf).

13. **Objection to Contrary Terms:** Publisher hereby objects to any terms contained in any purchase order, acknowledgment, check endorsement or other writing prepared by you, which terms are inconsistent with these terms and conditions or CCC's Billing and Payment terms and conditions. These terms and conditions, together with CCC's Billing and Payment terms and conditions (which are incorporated herein), comprise the entire agreement between you and publisher (and CCC) concerning this licensing transaction. In the event of any conflict between your obligations established by these terms and conditions and those established by CCC's Billing and Payment terms and conditions, these terms and conditions shall control.

14. **Revocation:** Elsevier or Copyright Clearance Center may deny the permissions described in this License at their sole discretion, for any reason or no reason, with a full refund payable to you. Notice of such denial will be made using the contact information provided by you. Failure to receive such notice will not alter or invalidate the denial. In no event will Elsevier or Copyright Clearance Center be responsible or liable for any costs, expenses or damage incurred by you as a result of a denial of your permission request, other than a refund of the amount(s) paid by you to Elsevier and/or Copyright Clearance Center for denied permissions.

LIMITED LICENSE

The following terms and conditions apply only to specific license types:

15. **Translation:** This permission is granted for non-exclusive world **English** rights only unless your license was granted for translation rights. If you licensed translation rights you may only translate this content into the languages you requested. A professional translator must perform all translations and reproduce the content word for word preserving the integrity of the article.

16. **Posting licensed content on any Website:** The following terms and conditions apply as follows: Licensing material from an Elsevier journal: All content posted to the web site must maintain the copyright information line on the bottom of each image; A hyper-text must be included to the Homepage of the journal from which you are licensing at <http://www.sciencedirect.com/science/journal/xxxxx> or the Elsevier homepage for books at <http://www.elsevier.com>; Central Storage: This license does not include permission for a scanned version of the material to be stored in a central repository such as that provided by Heron/XanEdu.

Licensing material from an Elsevier book: A hyper-text link must be included to the Elsevier homepage at <http://www.elsevier.com>. All content posted to the web site must maintain the copyright information line on the bottom of each image.

Posting licensed content on Electronic reserve: In addition to the above the following clauses are applicable: The web site must be password-protected and made available only to bona fide students registered on a relevant course. This permission is granted for 1 year only. You may obtain a new license for future website posting.

17. **For journal authors:** the following clauses are applicable in addition to the above:

Preprints:

A preprint is an author's own write-up of research results and analysis, it has not been peer-reviewed, nor has it had any other value added to it by a publisher (such as formatting, copyright, technical enhancement etc.).

Authors can share their preprints anywhere at any time. Preprints should not be added to or enhanced in any way in order to appear more like, or to substitute for, the final versions of articles however authors can update their preprints on arXiv or RePEc with their Accepted Author Manuscript (see below).

If accepted for publication, we encourage authors to link from the preprint to their formal publication via its DOI. Millions of researchers have access to the formal publications on ScienceDirect, and so links will help users to find, access, cite and use the best available version. Please note that Cell Press, The Lancet and some society-owned have different preprint policies. Information on these policies is available on the journal homepage.

Accepted Author Manuscripts: An accepted author manuscript is the manuscript of an article that has been accepted for publication and which typically includes author-incorporated changes suggested during submission, peer review and editor-author communications.

Authors can share their accepted author manuscript:

- immediately
 - via their non-commercial person homepage or blog
 - by updating a preprint in arXiv or RePEc with the accepted manuscript
 - via their research institute or institutional repository for internal institutional uses or as part of an invitation-only research collaboration work-group
 - directly by providing copies to their students or to research collaborators for their personal use
 - for private scholarly sharing as part of an invitation-only work group on commercial sites with which Elsevier has an agreement
- After the embargo period
 - via non-commercial hosting platforms such as their institutional repository
 - via commercial sites with which Elsevier has an agreement

In all cases accepted manuscripts should:

- link to the formal publication via its DOI
- bear a CC-BY-NC-ND license - this is easy to do
- if aggregated with other manuscripts, for example in a repository or other site, be shared in alignment with our hosting policy not be added to or enhanced in any way to appear more like, or to substitute for, the published journal article.

Published journal article (JPA): A published journal article (PJA) is the definitive final record of published research that appears or will appear in the journal and embodies all value-adding publishing activities including peer review co-ordination, copy-editing, formatting, (if relevant) pagination and online enrichment.

Policies for sharing publishing journal articles differ for subscription and gold open access articles:

Subscription Articles: If you are an author, please share a link to your article rather than the full-text. Millions of researchers have access to the formal publications on ScienceDirect, and so links will help your users to find, access, cite, and use the best available version.

Theses and dissertations which contain embedded PJAs as part of the formal submission can be posted publicly by the awarding institution with DOI links back to the formal publications on ScienceDirect.

If you are affiliated with a library that subscribes to ScienceDirect you have additional private sharing rights for others' research accessed under that agreement. This includes use for classroom teaching and internal training at the institution (including use in course packs and courseware programs), and inclusion of the article for grant funding purposes.

Gold Open Access Articles: May be shared according to the author-selected end-user license and should contain a [CrossMark logo](#), the end user license, and a DOI link to the formal publication on ScienceDirect.

Please refer to Elsevier's [posting policy](#) for further information.

18. **For book authors** the following clauses are applicable in addition to the above:

Authors are permitted to place a brief summary of their work online only. You are not allowed to download and post the published electronic version of your chapter, nor may you scan the printed edition to create an electronic version. **Posting to a repository:** Authors are permitted to post a summary of their chapter only in their institution's repository.

19. **Thesis/Dissertation:** If your license is for use in a thesis/dissertation your thesis may be submitted to your institution in either print or electronic form. Should your thesis be published commercially, please reapply for permission. These requirements include permission for the Library and Archives of Canada to supply single copies, on demand, of the complete thesis and include permission for Proquest/UMI to supply single copies, on demand, of the complete thesis. Should your thesis be published commercially, please reapply for permission. Theses and dissertations which contain embedded PJAs as part of the formal submission can be posted publicly by the awarding institution with DOI links back to the formal publications on ScienceDirect.

Elsevier Open Access Terms and Conditions

You can publish open access with Elsevier in hundreds of open access journals or in nearly 2000 established subscription journals that support open access publishing. Permitted third party re-use of these open access articles is defined by the author's choice of Creative Commons user license. See our [open access license policy](#) for more information.

Terms & Conditions applicable to all Open Access articles published with Elsevier:

Any reuse of the article must not represent the author as endorsing the adaptation of the article nor should the article be modified in such a way as to damage the author's honour or reputation. If any changes have been made, such changes must be clearly indicated.

The author(s) must be appropriately credited and we ask that you include the end user license and a DOI link to the formal publication on ScienceDirect.

If any part of the material to be used (for example, figures) has appeared in our publication with credit or acknowledgement to another source it is the responsibility of the user to ensure their reuse complies with the terms and conditions determined by the rights holder.

Additional Terms & Conditions applicable to each Creative Commons user license:

CC BY: The CC-BY license allows users to copy, to create extracts, abstracts and new works from the Article, to alter and revise the Article and to make commercial use of the Article (including reuse and/or resale of the Article by commercial entities), provided the user gives appropriate credit (with a link to the formal publication through the relevant DOI), provides a link to the license, indicates if changes were made and the licensor is not represented as endorsing the use made of the work. The full details of the license are available at <http://creativecommons.org/licenses/by/4.0>.

CC BY NC SA: The CC BY-NC-SA license allows users to copy, to create extracts, abstracts and new works from the Article, to alter and revise the Article, provided this is not done for commercial purposes, and that the user gives appropriate credit (with a link to the formal publication through the relevant DOI), provides a link to the license, indicates if changes were made and the licensor is not represented as endorsing the use made of the

work. Further, any new works must be made available on the same conditions. The full details of the license are available at <http://creativecommons.org/licenses/by-nc-sa/4.0>.

CC BY NC ND: The CC BY-NC-ND license allows users to copy and distribute the Article, provided this is not done for commercial purposes and further does not permit distribution of the Article if it is changed or edited in any way, and provided the user gives appropriate credit (with a link to the formal publication through the relevant DOI), provides a link to the license, and that the licensor is not represented as endorsing the use made of the work. The full details of the license are available at <http://creativecommons.org/licenses/by-nc-nd/4.0>. Any commercial reuse of Open Access articles published with a CC BY NC SA or CC BY NC ND license requires permission from Elsevier and will be subject to a fee.

Commercial reuse includes:

- Associating advertising with the full text of the Article
- Charging fees for document delivery or access
- Article aggregation
- Systematic distribution via e-mail lists or share buttons

Posting or linking by commercial companies for use by customers of those companies.

20. Other Conditions:

v1.9

Questions? customercare@copyright.com or +1-855-239-3415 (toll free in the US) or +1-978-646-2777.

From: **CONTRACTS-COPYRIGHT (shared)** <Contracts-Copyright@rsc.org>
Subject: RE: Copyright Request for Reuse in Thesis/Dissertation
Date: July 5, 2017 at 6:44 AM
To: MATTHEW BUMSTEAD <bumstema@mcmaster.ca>



Dear Matt

The Royal Society of Chemistry (RSC) hereby grants permission for the use of your paper(s) specified below in the printed and microfilm version of your thesis. You may also make available the PDF version of your paper(s) that the RSC sent to the corresponding author(s) of your paper(s) upon publication of the paper(s) in the following ways: in your thesis via any website that your university may have for the deposition of theses, via your university's Intranet or via your own personal website. We are however unable to grant you permission to include the PDF version of the paper(s) on its own in your institutional repository. The Royal Society of Chemistry is a signatory to the STM Guidelines on Permissions (available on request).

Please note that if the material specified below or any part of it appears with credit or acknowledgement to a third party then you must also secure permission from that third party before reproducing that material.

Please ensure that the thesis states the following:
Reproduced by permission of PCCP Owner Societies
and include a link to the paper on the Royal Society of Chemistry's website.

Please ensure that your co-authors are aware that you are including the paper in your thesis.

Regards
Gill Cockhead
Publishing Contracts & Copyright Executive

Gill Cockhead
Publishing Contracts & Copyright Executive
Royal Society of Chemistry,
Thomas Graham House,
Science Park, Milton Road,
Cambridge, CB4 0WF, UK
Tel +44 (0) 1223 432134

Follow the Royal Society of Chemistry:
www.rsc.org/follow

Winner of The Queen's Award for Enterprise, International Trade 2013

From: **MATTHEW BUMSTEAD** <mailto:bumstema@mcmaster.ca>
Sent: 01 July 2017 14:12
Date: CONTRACTS-COPYRIGHT (shared) <Contracts-Copyright@rsc.org>
Subject: Copyright Request for Reuse in Thesis/Dissertation

Hello,

I am completing a Ph.D. thesis at McMaster University entitled "Simulating Self-Assembly of Organic Molecules & Classifying Intermolecular Dispersion". I would like your permission to reprint the following journal articles in my thesis:

Alejandro Díaz Ortiz, Björn Arnold, Matt Bumstead, and Ayse Turak, "Steric self-assembly of laterally confined organic semiconductor molecule analogues", *Phys. Chem. Chem. Phys.*, 2014, 16, 20228. DOI: 10.1039/C4CP02331E

Please note that I am a coauthor of this work. The Rightslink website declared my request to be not allowed and redirected me to this email address.

I would also like to request that you grant irrevocable, nonexclusive license to McMaster University and to the National Library of Canada to reproduce this material as a part of the thesis. Proper acknowledgement of your copyright of the reprinted material (including the authors, title, date and publisher) will be given in the thesis.

If these arrangements meet with your approval, please let me know.
Thank you very much. I look forward to hearing from you.

Matt Bumstead
Department of Engineering Physics
McMaster University
e-mail: bumstema@mcmaster.ca
website: <http://organicelectronics.mcmaster.ca/>

This communication is from The Royal Society of Chemistry, a company incorporated in England by Royal Charter (registered number RC000524) and a charity registered in England and Wales (charity number 207890). Registered office: Burlington House, Piccadilly, London W1J 0BA. Telephone: 0207 4378 6556, Facsimile: 0207 4490 3393 (Head Office). This communication (including any attachments) may contain confidential, privileged or copyright material. It may not be relied upon or disclosed to any person other than the intended recipient(s) without the consent of The Royal Society of Chemistry. If you are not the intended recipient(s), please (1) notify us immediately by replying to this email and delete all copies from your system and (2) note that disclosure, distribution, copying or use of this communication is strictly prohibited. Any advice given by The Royal Society of Chemistry has been carefully formulated but is necessarily based on the information available, and The Royal Society of Chemistry cannot be held responsible for accuracy or completeness. In this respect, any views or opinions presented in this email are solely those of the author and may not represent those of The Royal Society of Chemistry. The Royal Society of Chemistry owes no duty of care and shall not be liable for any resulting damage or loss as a result of the use of this email and/or attachments. The Royal Society of Chemistry acknowledges that a disclaimer cannot restrict liability at law for personal injury or death arising through a finding of negligence. The Royal Society of Chemistry does not warrant that its emails or attachments are Virus-free: Please rely on your own screening.

Bibliography

- [1] A TANAKA. Toxicity of indium arsenide, gallium arsenide, and aluminium gallium arsenide. *Toxicology and Applied Pharmacology*, 198(3):405–411, aug 2004. doi: 10.1016/j.taap.2003.10.019.
- [2] Peter Reiss, Marie Carrière, Christophe Lincheneau, Louis Vaure, and Sudarsan Tamang. Synthesis of Semiconductor Nanocrystals, Focusing on Nontoxic and Earth-Abundant Materials. *Chemical Reviews*, 116(18):10731–10819, sep 2016. doi: 10.1021/acs.chemrev.6b00116.
- [3] M.C. Scharber and N.S. Sariciftci. Efficiency of bulk-heterojunction organic solar cells. *Progress in Polymer Science*, 38(12):1929–1940, dec 2013. doi: 10.1016/j.progpolymsci.2013.05.001.
- [4] Mikkel Jørgensen, Jon E. Carlé, Roar R. Søndergaard, Marie Lauritzen, Nikolaj A. Dagnæs-Hansen, Sedi L. Byskov, Thomas R. Andersen, Thue T. Larsen-Olsen, Arvid P.L. Böttiger, Birgitta Andreasen, Lei Fu, Lijian Zuo, Yao Liu, Eva Bundgaard, Xiaowei Zhan, Hongzheng Chen, and Frederik C. Krebs. The state of organic solar cellsA meta analysis. *Solar Energy Materials and Solar Cells*, 119:84–93, dec 2013. doi: 10.1016/j.solmat.2013.05.034.
- [5] Tatsuo Saga. Advances in crystalline silicon solar cell technology for industrial mass production. *NPG Asia Materials*, 2(3):96–102, jul 2010. doi: 10.1038/asiamat.2010.82.
- [6] F. Meillaud, M. Boccard, G. Bugnon, M. Despeisse, S. Hänni, F.-J. Haug, J. Persoz, J.-W. Schüttauf, M. Stuckelberger, and C. Ballif. Recent advances and remaining challenges in thin-film silicon photovoltaic technology. *Materials Today*, 18(7):378–384, sep 2015. doi: 10.1016/j.mattod.2015.03.002.
- [7] Zachary B. Henson, Klaus Mullen, and Guillermo C. Bazan. Design strategies for organic semiconductors beyond the molecular formula. *Nature Chemistry*, 4:699–704, 2012.
- [8] C.W. Ow-Yang, J. Jia, T. Aytun, M. Zamboni, A. Turak, K. Saritas, and Y. Shigesato. Work function tuning of tin-doped indium oxide electrodes with solution-processed lithium fluoride. *Thin Solid Films*, 559:58–63, may 2014. doi: 10.1016/j.tsf.2013.11.035.
- [9] Ayse Turak, Minh Nguyen, Felix Maye, Johnathan Heidkamp, Peter Lienerth, Jorg Wrachtrup, and Helmut Dosch. Nanoscale engineering of exciton dissociating interfaces in organic photovoltaics. *Journal of Nano Research*, 14:125–136, 2011.
- [10] Ji Sun Moon, Jae Kwan Lee, Shinuk Cho, Jiyun Byun, and Alan J Heeger. Columnlike Structure of the Cross-Sectional Morphology of Bulk Heterojunction Materials. *Nano Letters*, 9(1):230–234, jan 2009. doi: 10.1021/nl802821h.
- [11] Sung Heum Park, Anshuman Roy, Serge Beaupre, Shinuk Cho, Nelson Coates, Ji Sun Moon, Daniel Moses, Mario Leclerc, Kwanghee Lee, and Alan J Heeger. Bulk heterojunction solar cells with internal quantum efficiency approaching 100%. *Nature Photonics*, 3(5):297–302, may 2009. doi: 10.1038/nphoton.2009.69.

- [12] Noah J Tremblay, Alon a Gorodetsky, Marshall P Cox, Theanne Schiros, Bumjung Kim, Rachel Steiner, Zachary Bullard, Aaron Sattler, Woo-Young So, Yoshimitsu Itoh, Michael F Toney, Hirohito Ogasawara, Arthur P Ramirez, Ioannis Kymissis, Michael L Steigerwald, and Colin Nuckolls. Photovoltaic Universal Joints: Ball-and-Socket Interfaces in Molecular Photovoltaic Cells. *ChemPhysChem*, 11(4):799–803, mar 2010. doi: 10.1002/cphc.200900941.
- [13] Carsten Deibel and Vladimir Dyakonov. Polymerfullerene bulk heterojunction solar cells. *Reports on Progress in Physics*, 73(9):096401, 2010.
- [14] Yongye Liang, Zheng Xu, Jiangbin Xia, Szu-Tsing Tsai, Yue Wu, Gang Li, Claire Ray, and Luping Yu. For the bright future—bulk heterojunction polymer solar cells with power conversion efficiency of 7.4%. *Advanced Energy Materials*, 22:E135–E138, 2010.
- [15] Dimas G. de Oteyza, Esther Barrena, Helmut Dosch, J. Enrique Ortega, and Yutaka Wakayama. Tunable symmetry and periodicity in binary supramolecular nanostructures. *Phys. Chem. Chem. Phys.*, 13:4220–4223, 2011.
- [16] Afaf El-Sayed, Duncan J. Mowbray, Juan M. Garca-Lastra, Celia Rogero, Elizabeth Goiri, Patrizia Borghetti, Ayse Turak, Bryan P. Doyle, Martina DellAngela, Luca Floreano, Yutaka Wakayama, Angel Rubio, J. Enrique Ortega, and Dimas G. de Oteyza. Supramolecular environment-dependent electronic properties of metalorganic interfaces. *The Journal of Physical Chemistry C*, 116(7):4780–4785, 2012.
- [17] Wei Chen, Dong-Chen Qi, Han Huang, Xingyu Gao, and Andrew T S Wee. Organic-Organic Heterojunction Interfaces: Effect of Molecular Orientation. *Advanced Functional Materials*, 21(3):410–424, feb 2011. doi: 10.1002/adfm.201000902.
- [18] Esther Barrena, Dimas G de Oteyza, Helmut Dosch, and Yutaka Wakayama. 2D Supramolecular Self-Assembly of Binary Organic Monolayers. *ChemPhysChem*, 8(13):1915–1918, sep 2007. doi: 10.1002/cphc.200700494.
- [19] Minxuan Kuang, Jingxia Wang, and Lei Jiang. Bio-inspired photonic crystals with super-wettability. *Chem. Soc. Rev.*, 45(24):6833–6854, 2016. doi: 10.1039/C6CS00562D.
- [20] Navid Kashaninejad, Nam-Trung Nguyen, and Weng Kong Chan. The three-phase contact line shape and eccentricity effect of anisotropic wetting on hydrophobic surfaces. *Soft Matter*, 9(2):527–535, 2013. doi: 10.1039/C2SM26963E.
- [21] Robert N. Wenzel. RESISTANCE OF SOLID SURFACES TO WETTING BY WATER. *Industrial & Engineering Chemistry*, 28(8):988–994, aug 1936. doi: 10.1021/ie50320a024.
- [22] A. B. D. Cassie and S. Baxter. Wettability of porous surfaces. *Transactions of the Faraday Society*, 40(5):546, 1944. doi: 10.1039/tf9444000546.
- [23] M. Ramiasa-MacGregor, A. Mierczynska, R. Sedev, and K. Vasilev. Tuning and predicting the wetting of nanoengineered material surface. *Nanoscale*, 8(8):4635–4642, 2016. doi: 10.1039/C5NR08329J.
- [24] Lichao Gao and Thomas J. McCarthy. How Wenzel and Cassie Were Wrong. *Langmuir*, 23(7):3762–3765, mar 2007. doi: 10.1021/la062634a.
- [25] H. Yildirim Erbil. The debate on the dependence of apparent contact angles on drop contact area or three-phase contact line: A review. *Surface Science Reports*, 69(4):325–365, dec 2014. doi: 10.1016/j.surfrep.2014.09.001.
- [26] Anaïs Gauthier, Marco Rivetti, Jérémie Teisseire, and Etienne Barthel. Finite Size Effects on Textured Surfaces: Recovering Contact Angles from Vagarious Drop Edges. *Langmuir*, 30(6):1544–1549, feb 2014. doi: 10.1021/la403744b.

- [27] Alexandros Askounis, Khellil Sefiane, Vasileios Koutsos, and Martin E.R. Shanahan. Effect of particle geometry on triple line motion of nano-fluid drops and deposit nano-structuring. *Advances in Colloid and Interface Science*, 222:44–57, aug 2015. doi: 10.1016/j.cis.2014.05.003.
- [28] G.G. Alexander, S.M. King, R.M. Richardson, and H. Zimmermann. Determination of the translational order parameter for smectic liquid crystals using small-angle neutron scattering. *Liquid Crystals*, 37(6-7):961–968, jul 2010. doi: 10.1080/02678292.2010.481902.
- [29] Luis Mederos, Enrique Velasco, and Yuri Martínez-Ratón. Hard-body models of bulk liquid crystals. *Journal of Physics: Condensed Matter*, 26(46):463101, nov 2014.
- [30] James P. Mithen and Richard P. Sear. State between Liquid and Crystal: Locally Crystalline but with the Structure Factor of a Liquid. *Crystal Growth & Design*, 16(6):3049–3053, jun 2016. doi: 10.1021/acs.cgd.6b00209.
- [31] J S Langer. Theories of glass formation and the glass transition. *Reports on Progress in Physics*, 77(4):042501, apr 2014. doi: 10.1088/0034-4885/77/4/042501.
- [32] Masaharu Isobe. Hard sphere simulation in statistical physics methodologies and applications. *Molecular Simulation*, 42(16):1317–1329, nov 2016. doi: 10.1080/08927022.2016.1139106.
- [33] M. D. Shattuck, R. A. Ingale, P. M. Reis, Masami Nakagawa, and Stefan Luding. Granular Thermodynamics. In *AIP Conference Proceedings*, volume 1145, pages 43–50. AIP, 2009. doi: 10.1063/1.3179956.
- [34] XiaoMing Chen, Wei Dong, and XianRen Zhang. Self-assembly of amphiphilic molecules: A review on the recent computer simulation results. *Science China Chemistry*, 53(9):1853–1861, sep 2010. doi: 10.1007/s11426-010-4064-2.
- [35] Carlos-andres Palma, Marco Cecchini, and Paolo Samorì. Predicting self-assembly: from empirism to determinism. *Chemical Society Reviews*, 41(10):3713, 2012. doi: 10.1039/c2cs15302e.
- [36] Alejandro Díaz Ortiz, Björn Arnold, Matt Bumstead, and Ayse Turak. Steric self-assembly of laterally confined organic semiconductor molecule analogues. *Physical Chemistry Chemical Physics*, 16(37):20228, aug 2014. doi: 10.1039/C4CP02331E.
- [37] Boris D. Lubachevsky and Frank H. Stillinger. Geometric properties of random disk packings. *Journal of Statistical Physics*, 60(5/6):561–583, 1990.
- [38] Daan Frenkel and Berend Smit. *Understanding Molecular Simulation*. Academic Press, second edition, 2001.
- [39] H. Hoppe, T. Glatzel, M. Niggemann, W. Schwinger, F. Schaeffler, A. Hinsch, M.Ch. Lux-Steiner, and N.S. Sariciftci. Efficiency limiting morphological factors of mdmo-ppv:pcbm plastic solar cells. *Thin Solid Films*, 511-512:587–592, 2006.
- [40] Le Huong Nguyen, Harald Hoppe, Tobias Erb, Serap Gunes, Gerhard Gobsch, and N. Serdar Sariciftci. Effects of Annealing of the Nanomorphology and Performance of Poly(alkylthiophene):Fullerene Bulk-Heterojunction Solar Cells. *Advanced Functional Materials*, 17:1071–1078, 2007.
- [41] Kar Wai Chooi, Alexander I Gray, Laurence Tetley, Yuling Fan, and Ijeoma F Uchegbu. The Molecular Shape of Poly(propylenimine) Dendrimer Amphiphiles Has a Profound Effect on Their Self Assembly. *Langmuir*, 26(4):2301–2316, feb 2010. doi: 10.1021/la9027282.
- [42] Christos N. Likos. Effective interactions in soft condensed matter physics. *Physics Reports*, 348(4):267 – 439, 2001.

- [43] H. Hansen-Goos, C. Lutz, C. Bechinger, and R. Roth. From pair correlations to pair interactions: An exact relation in one-dimensional systems. *EPL (Europhysics Letters)*, 74(1):8, 2006.
- [44] Callum A. Young and Andrew L. Goodwin. Applications of pair distribution function methods to contemporary problems in materials chemistry. *J. Mater. Chem.*, 21:6464–6476, 2011.
- [45] R. O. Jones. Density functional theory: Its origins, rise to prominence, and future. *Rev. Mod. Phys.*, 87:897–923, Aug 2015.
- [46] Shubin Liu. Steric effect: A quantitative description from density functional theory. *The Journal of Chemical Physics*, 126(24):244103, June 2007.
- [47] Leonhard Grill. Large molecules on surfaces: deposition and intramolecular STM manipulation by directional forces. *Journal of Physics: Condensed Matter*, 22(8):084023, mar 2010.
- [48] Makoto Yoneya, Masahiro Kawasaki, and Masahiko Ando. Molecular dynamics simulations of pentacene thin films: The effect of surface on polymorph selection. *Journal of Materials Chemistry*, 20(46):10397, 2010. ISSN 0959-9428. doi: 10.1039/c0jm01577f.
- [49] Paulette Clancy. Application of Molecular Simulation Techniques to the Study of Factors Affecting the Thin-Film Morphology of Small-Molecule Organic Semiconductors. *Chemistry of Materials*, 23(3):522–543, February 2011. ISSN 0897-4756. doi: 10.1021/cm102231b.
- [50] S.Y. Reddy and Vikram K. Kuppaa. Molecular dynamics simulations of organic photovoltaic materials: Investigating the formation of π -stacked thiophene clusters in oligothiophene/fullerene blends. *Synthetic Metals*, 162(23):2117–2124, December 2012. ISSN 03796779. doi: 10.1016/j.synthmet.2012.09.020.
- [51] Tobias Neumann, Denis Danilov, Christian Lennartz, and Wolfgang Wenzel. Modeling disordered morphologies in organic semiconductors. *Journal of computational chemistry*, 34(31):2716–25, December 2013. ISSN 1096-987X. doi: 10.1002/jcc.23445.
- [52] Thomas J. Roussel and Lourdes F. Vega. Modeling the Self-Assembly of Nano Objects: Applications to Supramolecular Organic Monolayers Adsorbed on Metal Surfaces. *Journal of Chemical Theory and Computation*, 9(5):2161–2169, May 2013. ISSN 1549-9618. doi: 10.1021/ct3011248.
- [53] S Atkinson, Y Jiao, and S Torquato. Maximally dense packings of two-dimensional convex and concave noncircular particles. *Physical Review E*, 86(3):1–11, 2012. doi: 10.1103/PhysRevE.86.031302.
- [54] Artur Ciesielski, Silvia Colella, Leszek Zalewski, Bernd Bruchmann, and Paolo Samorì. Nanopatterning the graphite surface with ordered macrocyclic or ribbon-like assemblies of isocytosine derivatives: an STM study. *CrystEngComm*, 13(18):5535, 2011. doi: 10.1039/c1ce05521f.
- [55] D. Choudhary, P. Clancy, R. Shetty, and F. Escobedo. A Computational Study of the Sub-monolayer Growth of Pentacene. *Advanced Functional Materials*, 16(13):1768–1775, September 2006. ISSN 1616-301X. doi: 10.1002/adfm.200500148.
- [56] Brett J Gyarfás, Bryan Wiggins, Monica Zosel, and K W Hipps. Supramolecular Structures of Coronene and Alkane Acids at the Au(111)Solution Interface: A Scanning Tunneling Microscopy Study. *Langmuir*, 21(3):919–923, feb 2005.
- [57] Chun-Sheng Guo, Michel A. Van Hove, Rui-Qin Zhang, and Christian Minot. Prospects for resolving chemical structure by atomic force microscopy: A first-principles study. *Langmuir*, 26(21):16271–16277, 2010.

- [58] Paul V. Pesavento, Reid J. Chesterfield, Christopher R. Newman, and C. Daniel Frisbie. Gated four-probe measurements on pentacene thin-film transistors: Contact resistance as a function of gate voltage and temperature. *Journal of Applied Physics*, 96(12):7312–7324, 2004.
- [59] Paul V. Pesavento, Kanan P. Puntambekar, C. Daniel Frisbie, John C. McKeen, and P. Paul Ruden. Film and contact resistance in pentacene thin-film transistors: Dependence on film thickness, electrode geometry, and correlation with hole mobility. *Journal of Applied Physics*, 99(9):094504, 2006.
- [60] Veaceslav Coropceanu, Jrme Cornil, Demetrio A. da Silva Filho, Yoann Olivier, Robert Silbey, and Jean-Luc Brdas. Charge transport in organic semiconductors. *Chemical Reviews*, 107(4):926–952, 2007.
- [61] Qing Hua Wang and Mark C Hersam. Room-temperature molecular-resolution characterization of self-assembled organic monolayers on epitaxial graphene. *Nature Chemistry*, 1(3):206–211, June 2009.
- [62] Leo Gross. Recent advances in submolecular resolution with scanning probe microscopy. *Nature chemistry*, 3(4):273–8, 2011.
- [63] Shinobu Uemura, Ryota Tanoue, Neval Yilmaz, Akihiro Ohira, and Masashi Kunitake. Molecular Dynamics in Two-Dimensional Supramolecular Systems Observed by STM. *Materials*, 3(8):4252–4276, aug 2010.
- [64] eljko Tomovi, Joost van Dongen, Subi J. George, Hong Xu, Wojciech Pisula, Philippe Leclre, Maarten M. J. Smulders, Steven De Feyter, E. W. Meijer, and Albertus P. H. J. Schenning. Star-shaped oligo(p-phenylenevinylene) substituted hexaarylbenzene: purity, stability, and chiral self-assembly. *Journal of the American Chemical Society*, 129(51):16190–16196, 2007. doi: 10.1021/ja0765417.
- [65] Riccardo Gatti, Jennifer M. MacLeod, Josh A. Lipton-Duffin, Andrey G Moiseev, Dmitrii F Perepichka, and Federico Rosei. Substrate, Molecular Structure, and Solvent Effects in 2D Self-Assembly via Hydrogen and Halogen Bonding. *The Journal of Physical Chemistry C*, 118(44):25505–25516, nov 2014. doi: 10.1021/jp507729w.
- [66] Adrian Kitai. *Principles of Solar Cells, LEDs and Diodes*. Wiley-Blackwell, 2011.
- [67] Christopher M. Proctor, Martijn Kuik, and Thuc-Quyen Nguyen. Charge carrier recombination in organic solar cells. *Progress in Polymer Science*, 38(12):1941–1960, dec 2013. doi: 10.1016/j.progpolymsci.2013.08.008.
- [68] Satoshi Watanabe, Yasumasa Fukuchi, Masako Fukasawa, Takafumi Sassa, Masanobu Uchiyama, Takashi Yamashita, Mutsuyoshi Matsumoto, and Tetsuya Aoyama. Electron Donor and Acceptor Spatial Distribution in Structured Bulk Heterojunction Photovoltaic Devices Induced by Periodic Photopolymerization. *Langmuir*, 28(28):10305–10309, jul 2012. doi: 10.1021/la3005618.
- [69] Samuel D Collins, Niva A Ran, Michael C Heiber, and Thuc-quyen Nguyen. Small is Powerful: Recent Progress in Solution-Processed Small Molecule Solar Cells. *Advanced Energy Materials*, 7(10):1602242, may 2017. doi: 10.1002/aenm.201602242.
- [70] H. Karacuban, M. Lange, J. Schaffert, O. Weingart, Th Wagner, and R. Möller. Substrate-induced symmetry reduction of CuPc on Cu(1 1 1): An LT-STM study. *Surface Science*, 603(5), 2009.
- [71] Feng Chen, Xiu Chen, Lacheng Liu, Xin Song, Shuyi Liu, Juan Liu, Hongping Ouyang, Yingxiang Cai, Xiaoqing Liu, Haibing Pan, Junfa Zhu, and Li Wang. Chiral recognition of zinc phthalocyanine on Cu(100) surface. *Applied Physics Letters*, 100(8):081602, 2012. ISSN 00036951. doi: 10.1063/1.3685713.

- [72] Esther Barrena, Dimas G. de Oteyza, Helmut Dosch, and Yutaka Wakayama. 2d supramolecular self-assembly of binary organic monolayers. *ChemPhysChem*, 8(13):1915–1918, 2007. doi: 10.1002/cphc.200700494.
- [73] Nicolas Estrada, Emilien Azéma, Farhang Radjai, and Alfredo Taboada. Identification of rolling resistance as shape parameter in sheared granular media. *Physical Review E*, 84:011306, 2011.
- [74] Ana M. Vidales, Luis A. Pugnaroni, and Irene Ippolito. Pentagon deposits unpack under gentle tapping. *Physical Review E*, 77:051305, 2008.
- [75] Paul J. Steinhardt, David R. Nelson, and Marco Ronchetti. Bond-orientational order in liquids and glasses. *Physical Review B*, 28:784–805, 1983. ISSN 01631829. doi: 10.1103/PhysRevB.28.784.
- [76] T M Truskett, S Torquato, and P G Debenedetti. Towards a quantification of disorder in materials: Distinguishing equilibrium and glassy sphere packings. *Physical Review E*, 62(1):993–1001, jul 2000. doi: 10.1103/PhysRevE.62.993.
- [77] K. Lochmann, A. Anikeenko, A. Elsner, N. Medvedev, and D. Stoyan. Statistical verification of crystallization in hard sphere packings under densification. *The European Physical Journal B*, 53(1):67–76, sep 2006. doi: 10.1140/epjb/e2006-00348-9.
- [78] Walter Mickel, Sebastian C. Kapfer, Gerd E. Schröder-Turk, and Klaus Mecke. Shortcomings of the bond orientational order parameters for the analysis of disordered particulate matter. *The Journal of Chemical Physics*, 138(4):044501, 2013. ISSN 00219606. doi: 10.1063/1.4774084.
- [79] BORIS A. KLUMOV. How to quantify solidliquid phase transition: LennardJones system case study. *Journal of Plasma Physics*, 79(06):1125–1128, dec 2013. doi: 10.1017/S0022377813001098.
- [80] F. W. Dyson, A. S. Eddington, and C. Davidson. A determination of the deflection of light by the sun’s gravitational field, from observations made at the total eclipse of may 29, 1919. *Philosophical Transactions of the Royal Society of London A: Mathematical, Physical and Engineering Sciences*, 220(571-581):291–333, 1920. doi: 10.1098/rsta.1920.0009.
- [81] Duo Li, FengChao Wang, ZhenYu Yang, and YaPu Zhao. How to identify dislocations in molecular dynamics simulations? *Science China Physics, Mechanics & Astronomy*, 57(12):2177–2187, dec 2014. doi: 10.1007/s11433-014-5617-8.
- [82] Christina a. Knapek. *Phase Transitions in Two-Dimensional Complex Plasmas*. Springer Berlin Heidelberg, Berlin, Heidelberg, 2011. ISBN 978-3-642-19670-6. doi: 10.1007/978-3-642-19671-3.
- [83] Yuta Komatsu and Hajime Tanaka. Roles of Energy Dissipation in a Liquid-Solid Transition of Out-of-Equilibrium Systems. *Physical Review X*, 5(3):031025, aug 2015. doi: 10.1103/PhysRevX.5.031025.
- [84] Y. Limon Duparcmeur, A. Gervois, and J. P. Troadec. Dense Periodic Packings of Regular Polygons. *Journal de Physique I*, 5(12):1539–1550, dec 1995. doi: 10.1051/jp1:1995112.
- [85] V. Senthil Kumar and V. Kumaran. Voronoi cell volume distribution and configurational entropy of hard-spheres. *Journal of Chemical Physics*, 123(11), 2005. doi: 10.1063/1.2011390.
- [86] Matthias Schröter, Daniel I. Goldman, and Harry L. Swinney. Stationary state volume fluctuations in a granular medium. *Physical Review E*, 71(3):030301, mar 2005. doi: 10.1103/PhysRevE.71.030301.

- [87] Silke Henkes, Corey S. O'Hern, and Bulbul Chakraborty. Entropy and temperature of a static granular assembly: An ab initio approach. *Physical Review Letters*, 99(3):1–4, 2007. doi: 10.1103/PhysRevLett.99.038002.
- [88] BorisD. Lubachevsky, FrankH. Stillinger, and ElliotN. Pinson. Disks vs. spheres: Contrasting properties of random packings. *Journal of Statistical Physics*, 64(3-4):501–524, 1991. ISSN 0022-4715. doi: 10.1007/BF01048304.
- [89] Larysa Burtseva and Frank Werner. Modeling of Spherical Particle Packing Structures Using Mathematical Tessellation. *researchgate.net*, pages 1–29, mar 2015. doi: 10.13140/2.1.2664.7840.
- [90] J B Parse and J A Wert. A geometrical description of particle distributions in materials. *Modelling and Simulation in Materials Science and Engineering*, 1(3):275–296, apr 1993. doi: 10.1088/0965-0393/1/3/003.
- [91] Valerio Lucarini. From Symmetry Breaking to Poisson Point Process in 2D Voronoi Tessellations: the Generic Nature of Hexagons. *Journal of Statistical Physics*, 130(6):1047–1062, mar 2008. doi: 10.1007/s10955-007-9475-x.
- [92] Stanislav O. Yurchenko, Nikita P. Kryuchkov, and Alexei V. Ivlev. Pair correlations in classical crystals: The shortest-graph method. *The Journal of Chemical Physics*, 143(3):034506, jul 2015. doi: 10.1063/1.4926945.
- [93] Leo Radzihovsky, Erwin Frey, and David R. Nelson. Novel phases and reentrant melting of two-dimensional colloidal crystals. *Physical Review E*, 63(3):031503, feb 2001. doi: 10.1103/PhysRevE.63.031503.
- [94] Thomas Palberg. Crystallization kinetics of colloidal model suspensions: recent achievements and new perspectives. *Journal of Physics: Condensed Matter*, 26(33):333101, aug 2014. doi: 10.1088/0953-8984/26/33/333101.
- [95] Hajime Tanaka. Roles of bond orientational ordering in glass transition and crystallization. *Journal of Physics: Condensed Matter*, 23(28):284115, jul 2011. doi: 10.1088/0953-8984/23/28/284115.
- [96] Pallop Karnchanaphanurach, Binhua Lin, and Stuart A. Rice. Melting transition in a quasi-two-dimensional colloid suspension: Influence of the colloid-colloid interaction. *Physical Review E*, 61(4):4036–4044, apr 2000. doi: 10.1103/PhysRevE.61.4036.
- [97] Yanting Wang, S Teitel, and Christoph Dellago. Melting of icosahedral gold nanoclusters from molecular dynamics simulations. *The Journal of chemical physics*, 122(21):214722, June 2005. doi: 10.1063/1.1917756.
- [98] M. Isobe and B. J. Alder. Generalized bond order parameters to characterize transient crystals. *The Journal of Chemical Physics*, 137(19):194501, nov 2012. doi: 10.1063/1.4767061.
- [99] David J. Griffiths. *Introduction to Electrodynamics*. Reed College: Pearson, 1999.
- [100] Monica Skoge, Aleksandar Donev, Frank Stillinger, and Salvatore Torquato. Packing hyperspheres in high-dimensional Euclidean spaces. *Physical Review E*, 74(4):041127, October 2006. ISSN 1539-3755. doi: 10.1103/PhysRevE.74.041127.
- [101] Adrian Baddeley and Rolf Turner. Spatstat: An R Package for Analyzing Spatial Point Patterns. *Journal of Statistical Software*, 12(6):1–42, 2005. ISSN 1548-7660. doi: 10.18637/jss.v012.i06.
- [102] Boris D. Lubachevsky and Frank H. Stillinger. Geometric properties of random disk packings. *Journal of Statistical Physics*, 60(5-6):561–583, sep 1990. doi: 10.1007/BF01025983.

- [103] J. A. van Meel, B. Charbonneau, A. Fortini, and P. Charbonneau. Hard-sphere crystallization gets rarer with increasing dimension. *Physical Review E*, 80(6):061110, dec 2009. doi: 10.1103/PhysRevE.80.061110.
- [104] Bjoern Arnold. *Geometric Packing in Two-Dimensional Systems with Competing Length Scales*. Diplomarbeit, University of Stuttgart, 2009.
- [105] A. Libál, C. Reichhardt, and C. J. Olson Reichhardt. Point-defect dynamics in two-dimensional colloidal crystals. *Phys. Rev. E*, 75:011403, Jan 2007. doi: 10.1103/PhysRevE.75.011403.
- [106] Wolfgang Lechner, David Polster, Georg Maret, Peter Keim, and Christoph Dellago. Self-organized defect strings in two-dimensional crystals. *Phys. Rev. E*, 88:060402, Dec 2013. doi: 10.1103/PhysRevE.88.060402.
- [107] Aaron S. Keys, Christopher R. Iacovella, and Sharon G. Glotzer. Characterizing structure through shape matching and applications to self-assembly. *Annual Reviews in Condensed Matter Physics*, 2:263–285, 2011.
- [108] Arthur M. Lesk. A Toolkit for Computational Molecular Biology. II. On the Optimal Superposition of Two Sets of Coordinates. *Acta Crystallographica A*, 42:110–113, 1986.
- [109] A. Shapiro, J. D. Botha, A. Pastore, and A. M. Lesk. A Method for Multiple Superposition of Structures. *Acta Crystallographica A*, 48:11–14, 1992.
- [110] Richard Blankenbecler, Mattias Ohlsson, Carsten Peterson, and Markus Ringnér. Matching protein structures with fuzzy alignments. *Proceedings of National Academy of Sciences USA*, 100:11936–11940, 2003.
- [111] Aaron S. Keys, Christopher R. Iacovella, and Sharon G. Glotzer. Characterizing complex particle morphologies through shape matching: Descriptors, applications, and algorithms. *Journal of Computational Physics*, 230:6438–6463, 2011.
- [112] Hong Xu, Andrea Minoia, Željko Tomović, Roberto Lazzaroni, E. W. Meijer, Albertus P H J Schenning, and Steven De Feyter. A multivalent hexapod: Conformational dynamics of six-legged molecules in self-assembled monolayers at a solid-liquid interface. *ACS Nano*, 3(4):1016–1024, 2009.
- [113] Fabien Sully. Two-Dimensional Self-Assembly of 2,4,6-Tris(4,4,4-trimethylphenyl)-1,3,5-triazine Star-Shaped Molecules: Nanoarchitecture Structure and Domain Boundaries. *The Journal of Physical Chemistry C*, 118(22):11975–11979, jun 2014. doi: 10.1021/jp5013957.
- [114] Afaf El-Sayed, Patrizia Borghetti, Elizabeth Goiri, Celia Rogero, Luca Floreano, Giacomo Lovat, Duncan John Mowbray, Jose Luis Cabellos, Yutaka Wakayama, Angel Rubio, Jose Enrique Ortega, and Dimas G. de Oteyza. Understanding Energy-Level Alignment in Donor/Acceptor/Metal Interfaces from Core-Level Shifts. *ACS Nano*, 7(8):6914–6920, aug 2013.
- [115] Tobias Bauert, Leo Merz, Davide Bandera, Manfred Parschau, Jay S. Siegel, and Karl Heinz Ernst. Building 2D crystals from 5-Fold-Symmetric molecules. *Journal of the American Chemical Society*, 131(10):3460–3461, 2009.
- [116] Soichiro Yoshimoto, Ryuji Narita, Mitsuru Wakisaka, and Kingo Itaya. The structure of a coronene adlayer formed in a benzene solution: Studies by in situ STM and ex situ LEED. *Journal of Electroanalytical Chemistry*, 532(1-2):331–335, 2002.
- [117] Katharina J Franke and Jose Ignacio Pascual. Effects of electronvibration coupling in transport through single molecules. *Journal of Physics: Condensed Matter*, 24(39):394002, oct 2012.

- [118] Bjoern Arnold. Geometric packing in two-dimensional systems with competing length scales. Diplomarbeit, University of Stuttgart, 2009.
- [119] M. Bumstead, B. Arnold, and A. Turak. Reproducing morphologies of disorderly self-assembling planar molecules with static and dynamic simulation methods by matching density. *Physica A: Statistical Mechanics and its Applications*, 471:301–314, April 2017. ISSN 0378-4371. doi: 10.1016/j.physa.2016.12.075.
- [120] Chuncheng Wang, Kejun Dong, and Aibing Yu. Structural characterization of the packings of granular regular polygons. *Physical Review E*, 92(6):062203, dec 2015. doi: 10.1103/PhysRevE.92.062203.
- [121] P. A. Cundall and O. D. L. Strack. A discrete numerical model for granular assemblies. *Geotechnique*, 29(1):47–65, 1979. doi: 10.1680/geot.1979.29.1.47.
- [122] Yongxin Song, Richard Turton, and Ferhan Kayihan. Contact detection algorithms for DEM simulations of tablet-shaped particles. *Powder Technology*, 161(1):32–40, jan 2006. doi: 10.1016/j.powtec.2005.07.004.
- [123] G. Lu, J.R. Third, and C.R. Müller. Discrete element models for non-spherical particle systems: From theoretical developments to applications. *Chemical Engineering Science*, 127:425–465, may 2015. doi: 10.1016/j.ces.2014.11.050.
- [124] Kejun Dong, Chuncheng Wang, and Aibing Yu. A novel method based on orientation discretization for discrete element modeling of non-spherical particles. *Chemical Engineering Science*, 126:500–516, apr 2015. doi: 10.1016/j.ces.2014.12.059.
- [125] Tanja Schilling, Sander Pronk, Bela Mulder, and Daan Frenkel. Monte Carlo study of hard pentagons. *Physical Review E - Statistical, Nonlinear, and Soft Matter Physics*, 71(3):036138, mar 2005. doi: 10.1103/PhysRevE.71.036138.
- [126] Kun Zhao and Thomas G. Mason. Frustrated Rotator Crystals and Glasses of Brownian Pentagons. *Physical Review Letters*, 103(20):208302, nov 2009. doi: 10.1103/PhysRevLett.103.208302.
- [127] Kun Zhao, Robijn Bruinsma, and Thomas G Mason. Entropic crystal-crystal transitions of Brownian squares. *Proceedings of the National Academy of Sciences*, 108(7):2684–2687, feb 2011. doi: 10.1073/pnas.1014942108.
- [128] Alan Murta. A general polygon clipping library, 2009. URL <http://www.cs.man.ac.uk/~toby/alan/software/>.
- [129] Boris Schling. *The Boost C++ Libraries*. XML Press, 2011. ISBN 0982219199, 9780982219195. URL <http://www.boost.org/>.
- [130] Vladimir Svrček, Ivan Turkevych, and Michio Kondo. Photoelectric Properties of Silicon Nanocrystals/P3HT Bulk-Heterojunction Ordered in Titanium Dioxide Nanotube Arrays. *Nanoscale research letters*, 4(11):1389–1394, January 2009. ISSN 1931-7573. doi: 10.1007/s11671-009-9410-y.
- [131] Daniel A. Beller, Mohamed A. Gharbi, and Iris B. Liu. Shape-controlled orientation and assembly of colloids with sharp edges in nematic liquid crystals. *Soft Matter*, 11:1078–1086, 2015.
- [132] Daniel de las Heras and Enrique Velasco. Domain walls in two-dimensional nematics confined in a small circular cavity. *Soft Matter*, 10:1758–1766, 2014.
- [133] Thomas Geigenfeind, Sebastian Rosenzweig, Matthias Schmidt, and Daniel de las Heras. Confinement of two-dimensional rods in slit pores and square cavities. *The Journal of Chemical Physics*, 142(17):174701, 2015.

-
- [134] Ioana C. Garlea and Bela M. Mulder. Defect structures mediate the isotropic-nematic transition in strongly confined liquid crystals. *Soft Matter*, 11:608–614, 2015.
- [135] Andriy V. Kityk, Mark Busch, Daniel Rau, Sylwia Calus, Carole V. Cerclier, Ronan Lefort, Denis Morineau, Eric Grelet, Christina Krause, Andreas Schonhals, Bernhard Frick, and Patrick Huber. Thermotropic orientational order of discotic liquid crystals in nanochannels: an optical polarimetry study and a landau-de gennes analysis. *Soft Matter*, 10:4522–4534, 2014.
- [136] S C Kapfer, W Mickel, F M Schaller, M Spanner, C Goll, T Nogawa, N Ito, K Mecke, and G E Schrder-Turk. Local anisotropy of fluids using minkowski tensors. *Journal of Statistical Mechanics: Theory and Experiment*, 2010(11):P11010, 2010.
- [137] N. L. Lavrik and V. P. Voloshin. Calculation of mean distances between the randomly distributed particles in the model of points and hard spheres (the method of voronoi polyhedra). *The Journal of Chemical Physics*, 114(21):9489–9491, 2001.